Studies for current and future high-intensity operation of CERN's secondary M2 beamline

Dissertation
zur
Erlangung des Doktorgrades (Dr. rer. nat.)
der
Mathematisch-Naturwissenschaftlichen Fakultät
der
Rheinischen Friedrich-Wilhelms-Universität Bonn

von
Fabian Metzger
aus
Düren

Bonn, Februar 2024

Angefertigt mit Genehmigung der Mathematisch-Naturwissenschaftlichen Fakultät der Rheinischen Friedrich-Wilhelms-Universität Bonn.

Gutachter / Betreuer:	Prof. Dr. Bernhard Ketzer
Gutachter:	Prof. Dr. Alexander Gerbershagen
Tag der Promotion:	01.07.2024
Erscheinungsjahr:	2024

Für Mama und Papa

Abstract

The AMBER experiment is aiming at studying the fundamental QCD processes generating the hadronic degrees of freedom by measuring the excitation spectra of strange mesons, as well as the valence and sea quark, and gluon contributions in the kaon and pion. For these physics measurements high-intensity pion and kaon beams are important. The M2 secondary beamline at CERN's SPS can operate in high-intensity, high-energy hadron and muon mode, and it can also deliver low-intensity, low-energy electron beams. As the mixed hadron secondary beam is produced from protons on target, kaons are a minority. Therefore, it is important to increase their relative abundance or to make maximal use of the low fraction.

To achieve the former, the RF separation technique is investigated, which makes use of the velocity difference that distinct particle species have for the same momentum. Studies and proposed developments of the beam optics are discussed resulting in an optimised beam transmission and species separation. The performance of such a system is simulated and evaluated in terms of kaon rate and purity in the beam.

The optimal use of the kaon fraction is studied in terms of a conventional beam approach. A limiting factor of the current beam performance is multiple scattering that complicates particle identification. Improvements concerning vacuum upgrades and beam optics are estimated with simulations. With those beam performance improvements, simulations of the AMBER strange-meson spectroscopy campaign have been performed to estimate the needed time for the measurement.

The NA64 experiment is another user of the M2 line. It explores the muon beam for dark matter searches, for which the knowledge of any background is crucial. One of the major sources is the in-flight decays of hadrons that are wrongly identified as muons. Therefore, a precise determination of the number of hadrons in the muon beam is essential. To estimate their contribution, variance reduction techniques in Monte Carlo simulations are employed. With those the hadron contamination is evaluated.

A potential future user of the muon beam is the MUonE experiment studying the hadronic contribution to the electromagnetic coupling constant in elastic muon-electron scattering. During a test campaign a calorimeter has been calibrated with the available electron beam. The simulation of the beamline model, which has been used to estimate the electron spectrum, is validated and benchmarked with the collected data.

Several parts of this thesis have been published in:

A. Gerbershagen, F. Metzger et al., *Design of beam optics for RF-separated kaon and antiproton beams in the M2 beam line of the CERN North Area*,
Nuclear Instruments and Methods in Physics Research Section A: Accelerators, Spectrometers, Detectors and Associated Equipment (2022) 168004, ISSN: 0168-9002,
URL: https://doi.org/10.1016/j.nima.2022.168004.

F. Metzger et al.,
Kaon beam simulations employing conventional hadron beam concepts and the RF separation technique at the CERN M2 beamline for the future AMBER experiment,
Journal of Physics: Conference Series **2687** (2024) 052023,
URL: https://doi.org/10.1088/1742-6596/2687/5/052023.

F. Metzger, F. W. Stummer and L. J. Nevay,
Automatic building of 3D models of beamlines, (2024), Publication in progress.

F. Metzger et al., *Hadron contamination studies in CERN's secondary M2 muon beam*, (2024), Publication in progress.

Parts of the content of this thesis have been presented at the following occasions:

F. Metzger et al., *RF separated beams: Beam optics and tracking results*,
Talk at RF-separated beams for AMBER – Kick Off Meeting, 2021,
URL: https://indico.cern.ch/event/1069879/contributions/4499716/subcontributions/351863.

F. Metzger et al., *Conventional Hadron Beam Optimization: Beam Optics and Vacuum*,
RF-separated beams for AMBER – Follow-up Workshop, 2022,
URL: https://indico.cern.ch/event/1133376/contributions/4786345/.

F. Metzger et al.,
Beam dynamics aspects of RF separated beams at the CERN M2 secondary beam line,
Talk at German Physical Society (DPG) Spring Meeting, 2022.

F. Metzger et al.,
RF separated and conventional hadron beam in CERN's secondary M2 beam line,
Talk at International Workshop on Hadron Structure and Spectroscopy, 2022,
URL: https://indico.cern.ch/event/1121975/contributions/4989715/.

F. Metzger et al., *RF separated beams: Status*,
Talk at Physics Beyond Colliders Annual Workshop, 2022,
URL: https://indico.cern.ch/event/1137276/contributions/4950759/.

F. Metzger et al., *Kaon beam studies employing conventional hadron beam concepts at the CERN M2 beam line for the future AMBER experiment*,
Talk at German Physical Society (DPG) Spring Meeting, 2023.

Acknowledgements

Now, after five years at uni and another three years at CERN, it is the time for me to say thank you to all the people that supported me during this time.

First of all, I want to thank my supervisor Prof. Dr. Bernhard Ketzer for all the years from my Bachelor degree towards the PhD making all the various projects I worked on possible. All the discussions in various group meetings in Bonn and lunches and dinners at CERN have been a pleasure. You have always been asking the right questions paving the way to the answer. Thank you for all your support for various applications like the BCGS, CERN Doctoral Student Programme and Fellowship.

Secondly, I want to say thanks to Prof. Dr. Alexander Gerbershagen. Having you as a supervisor at CERN made my start here so easy and enjoyable. I am thankful for all the discussions we had on the corridor, over coffee or during meetings. I do not know how many times I knocked on your door and you always took your time helping me moving on. Even after you left CERN, you were still available for any question I had. So, just thank you; of course also for being available for the second review of my thesis. It is so nice that we can finish the whole project, as we started it, together.

I also want to thank Priv.-Doz. Dr. Bastian Kubis and Prof. Dr. Jürgen Gall for agreeing to review my thesis.

There are two more people. Without them this work would have been impossible. I would like to say thank you to Dr. Dipanwita Banerjee for taking over the role as my supervisor. I was worried, where my project would go during the changeover, but you got me back on track. Thanks for all the funny discussions not only about M2-related, but all the various topics, especially dogs. Thank you for pushing me to do all the interesting studies that we did together, also the ones that did not make it into this thesis. Of course, many thanks for your support for my Fellowship application!

Thank you Dr. Laurie Nevay for your help with any kind of software, especially BDSIM. Thanks for all the time you took for introducing me to Python and debugging any code that I produced with it in the beginning. You have always been available for any kind of all kinds of questions and discussions that I can gladly say I had two supervisors. I am looking forward to the future and interesting projects that are ahead of us.

I would also like to thank Dr. Johannes Bernhard who made the whole projects I worked on possible. Thanks for giving me the chance to come to CERN. It was a pleasure working in such a nice team and I am happy to continue working in this great environment.

I want to express my gratitude to Dr. Lau Gatignon for always being available for the fruitful

discussions we had on any physics related topic. Thank you for all your help and explanations of the various beam physics and experimental aspects and for your support here during my time at CERN.

Of course, without a great group of friends, university studies and a PhD are impossible. So, thanks to Karl, Hakan, Lars, Pierre and Tobias. Without you all the courses would have been so much more boring and getting through to the end would not have been possible. I hope that we can stay in contact in or the other way as loosing it is not an option for the future. Danke Karl, for also sharing the time here at CERN making life so much easier and more enjoyable. I am also happy that I found new good friends at CERN making life here more fun. Thank you Florian, Filipa, Laurie, Gian Luigi and Celia. I am grateful that I had the chance to meet you all and share the time here with you. I really hope that we will be able to see each other again every now and then even if we will be spread all over the world.

I want to say thank you to everyone in EA-LE. It was a great experience working in an international environment like CERN and it was a pleasure being able to interact with so many different characters and nationalities. Also thanks to everyone in Bonn for the funny DPG trips and evening activities. I would like to specially thank Henri Pekeler for helping me with the AMBER-studies and of course for the various cocktail evenings.

Last, but most importantly, I am deeply grateful for my family. I do not know how to express, what you did for me. I would need another book to say all of it. Thank you for making everything I wanted possible, supporting and helping me in every situation. Getting where I am, was only possible because I knew I can count on you. I want to say thanks for doing this journey and thesis together with me! This work was our effort!

Contents

CHAPTER 1

Introduction

Up to now, The Standard Model of Particle Physics predicts experimental results with the highest precision. With the discovery of the Higgs boson [1, 2] in 2012 [3, 4], which explains the masses of fundamental particles like quarks and leptons, it is believed to be complete. Still, it is known that it cannot be a fundamental theory because there are observations that cannot be predicted by the Standard Model.

As quarks cannot be observed freely due to confinement, it is challenging to measure their masses precisely. Still, they have been evaluated to be of the order of MeV/c^2 for the light u- and d-quarks, and $O(100\,\mathrm{MeV}/c^2)$ for the s-quark [5]. Considering the lightest hadronic states like pions, kaons or protons in the so-called constituent quark model, their total masses cannot come from the quark masses alone, but there need to be other processes responsible for creating masses of the order of 0.1 to 1 GeV/c^2. Literally, these processes create the overwhelming amount of mass in the visible universe as the Higgs mechanism can only explain a few % of the visible mass. In the particle physics community it is referred to as the "**E**mergence of the **H**adron **M**ass" (EHM) [6]. These phenomena generating mass are summarised in Fig. 1.1.

Nearly 60 years ago, the theoretical work by Gell-Mann [8] and Zweig [9] paved the way towards **Q**uantum **C**hromo**D**ynamics (QCD). They considered a SU(3) symmetry group being the basis of a model that has been able to describe, for example, characteristics of the nucleons. In this model the proton and neutron are not point-like but made of elementary particles. Such a much more complicated internal structure has been first experimentally confirmed at the Standford Linear Collider SLAC by the SLAC-MIT collaboration [10, 11] in deep-inelastic electron-proton scattering. But only after Bjorken's work concerning "scaling" in deep-inelastic scattering [12] the correct understanding, i.e. the interpretation that smaller particles form the nucleons, has been possible. Later, the particles forming this substructure have been named quarks. Still, such a long time after the discovery it is puzzling why the simplest particles made of quarks, the proton, and the π- and K-mesons are so different in terms of mass. In the constituent quark model it is assumed that the pion is made of up and down quarks, the two lightest ones, while in the kaon case the down quark is replaced by a strange quark. One

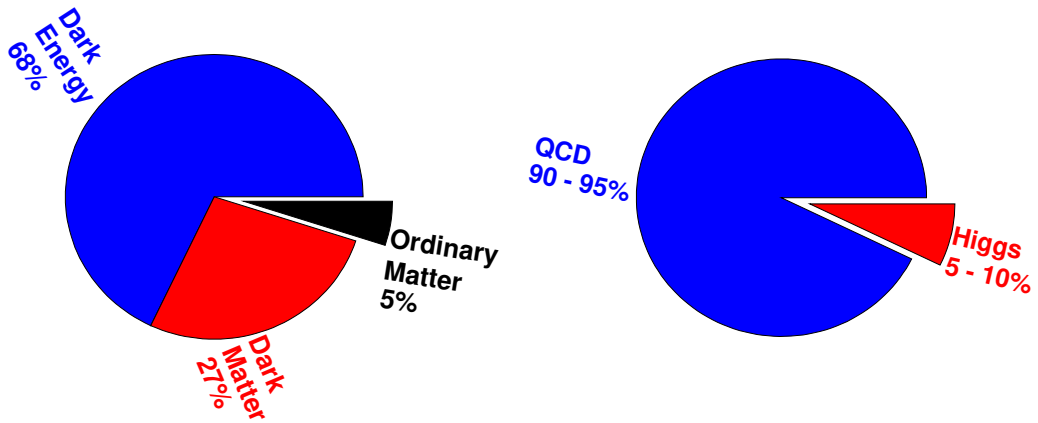

(a) (b)

Figure 1.1: Fig. 1.1(a) shows the distribution of mass in the universe. Ca. 70 % are Dark Energy (blue) and only the smallest amount is ordinary matter (black), while the rest is Dark Matter (red) [7].The process generating only again a small portion of the mass of ordinary matter is currently fully understood, which is illustrated by Fig. 1.1(b). The known Higgs mechanism (red) accounts for about 5 to 10 % (when summing the quark masses in the proton), whereas the majority is dynamically generated by QCD processes (blue).

down and two up quarks form the proton. Therefore, one would assume that the pion weighs about $\frac{2}{3}$ of the proton mass. Considering $(139.57039 \pm 0.00018)\,\mathrm{MeV}/c^2$ for the pion and $(938.272081 \pm 0.000006)\,\mathrm{MeV}/c^2$ for the proton [5], the mass difference is striking because one adds only one up quark to get from pion to proton. It is puzzling how this mass difference comes up. In the simplified constituent quark model, the large mass of the proton can be explained through the gluon fields that bind the constituents together to form the proton. But it is not clear why the contribution is smaller in the pion. Due to the pion's Nambu-Goldstone nature [13, 14] it is expected to be massless without the Higgs mechanism. But due to explicit chiral symmetry breaking, i.e. quarks have a small, non-zero mass as they couple to the Higgs field, one observes massive pions. The same argument holds for the kaon because it is a Nambu-Goldstone boson, too. Of course, with a mass of $(493.677 \pm 0.016)\,\mathrm{MeV}/c^2$ it is much heavier than the pion, but still much lighter than the proton. The underlying processes responsible for these different mass scales are important input to QCD. In addition, comparing the pion and kaon, the huge mass difference is striking again because only the down quark in the pion is replaced by a strange quark in the kaon. Therefore, by comparing both particles it might be possible to study the interplay between the Higgs mechanism and QCD.

Of course, the mass is not the only parameter describing the mentioned particles. Other examples, the longitudinal momentum distributions of the partons, the so-called **P**arton

Distribution **F**unctions (PDF), are important input to understand how the constituents form the larger, observable particles. Therefore, they are tools to test QCD at energies, at which perturbative approaches are impossible [15, 16].

After over 20 years of a successful run time, the fixed target experiment COMPASS [17] located at CERN's secondary M2 beamline has come to an end in 2022. It delivered important input towards the understanding of the characteristics of the proton. The lessons learned about the proton need to be extended to other particles in the large zoo. Investigations of pion states led to an increased interest of spectroscopy of strange mesons. These experimental efforts are going to be combined in the AMBER experiment [18, 19] being the successor of COMPASS. During its running time, it is hoped that one gets an insight into various of the aforementioned described phenomena, which all come back to the emergence of hadronic degrees of freedom. In order to be able to perform all the anticipated measurements, various beams parameters are needed, i.e. different beam momenta, intensities and ultimately, compositions. Compared to the beams available for the COMPASS experiment, several characteristics need substantial improvement. During COMPASS's time, both, muon and hadron beams, have been the essential ingredient for exploring protons, deuterons and more. With the increased interest in the phenomena in the meson sector, pion and especially kaon beams will take over this role.

The hadron beams, produced in interactions of protons with a fixed target, consist of various kinds of particles. Of course, depending on the charge these include protons, positive kaons and pions, or antiprotons, negative pions and kaons, and leptons, mostly muons at the studied energies. Clearly, for investigations of the kaon and pion internal structures having these particles in the beam is key. As it will be shown later in this thesis, in the negative beam the pion component is dominant compared to the other particles, while in the positive beam pions and protons form the vast majority. Consequently, for both beam charges the kaon is a minority part meaning one needs to ensure its optimal exploitation. Several options concerning this issue have been proposed with the most prominent one being a radio-frequency separated beam. This is a method to increase the relative share of one particle type in the mixed beam of different species. Another possibility, not affecting the beam composition itself, are upgrades of the conventional hadron beam[1]

A main part of this thesis is focused on those possibilities to improve the performance of the hadron beam available at the M2 line. In order to understand the presented concepts, the M2 beamline and its specialties are introduced in chapter 2. As it is located at CERN, the whole research center including the accelerators and beamlines serving the various experimental areas is discussed. Light is shed on the AMBER experiment as the main user of the upgraded facility connected to the M2 line. The anticipated measurements of AMBER are discussed in chapter 3. The studies investigating the possible improvements rely on various kinds of software and simulation suites. The tools used and developed to perform those simulations are reviewed in chapter 4.

The RF separated beam concept is introduced in chapter 5. Following its discussion,

[1] The conventional hadron beam has served the COMPASS experiment.

optimisations concerning total particle rates provided by the RF beam technique are performed. Those performance gains are estimated and put into context. Because the RF beam is not the only possible upgrade, the potential improvements of the conventional hadron beam are investigated throughout chapter 6.

As the AMBER collaboration will not be the only user of the beamline, there are also needs for investigations concerning the other possible beam options available at M2. Those are on the one side muon beams, and on the other side electron beams. Future users of the muon beam option are the NA64 [20] and MUonE collaborations [21] with the latter one being also interested in the electron beam. Therefore, those two options have been studied in simulation, too, including for the first time a complete validation of the detailed beamline models for all beam modes with data. The muon beam including the development of the whole geometry, later on referred to as 3D model, are explored in chapter 7 with a special focus on the hadronic contamination in the beam that has been measured by NA64. Following a test beam campaign of MUonE, the electron beam is investigated in chapter 8 focusing on benchmarking the simulation with data taken throughout the beam time.

In chapter 9, time is taken to put the obtained results in a bigger context drawing possible conclusions towards the future high-intensity operation of CERN's secondary M2 beamline.

The work of this thesis involved the development of beam optics and their optimisation for the RF separated beam in M2 and the investigations of possible other upgrades to the conventional beam. The 3D models of the M2 beamline and the presented simulations and results are the author's own contributions.

CHAPTER 2

Secondary beams at CERN

In this chapter, the general CERN research complex and acceleration process are discussed. This leads to an introduction into secondary beamlines that one can find at many accelerator facilities, whereas the focus is on the M2 line in CERN's **N**orth **A**rea (NA). General aspects like beam optics, matrix formalism, magnets and beam instrumentation are described. Production of secondary beams at CERN, so production of pions, kaons and mouns from primary protons, is discussed. These different concepts and aspects are related to M2 describing the different purposes they fulfill to achieve the beam parameters required for conducting the envisaged physics experiments.

2.1 CERN accelerator complex

The acronym CERN comes from the name of the founding organisation, which was called "**C**onseil **E**uropéen pour la **R**echerche **N**ucléaire" [22]. Nowadays, one can find it under its French name, which is "Organisation européenne pour la recherche nucléaire", or the English translation, i.e. "European Organization for Nuclear Research". It has a unique infrastructure in terms of particle accelerators serving various physics experiments. A general overview of the whole accelerator complex and the experimental facilities is given in Fig. 2.1.

In Fig. 2.1 one can see that CERN offers a broad variety of accelerators and experimental facilities. During most of the time of the year, one will find protons that are accelerated through nearly the whole chain. Starting with negative hydrogen ions H^- at the **Lin**ear **Ac**celerator LINAC4 (final kinetic energy is 160 MeV) [24], they get converted into protons while injected into the **P**roton **S**ynchrotron **B**ooster PSB by stripping off the two accompanying electrons. In the PSB, the protons are accelerated up to 2 GeV kinetic energy [25] and extracted towards the **P**roton **S**ynchrotron PS. The PS has a circumference of 628 m and a maximum final kinetic energy of 26 GeV [26, 27]. At extraction, the protons can be either sent to experimental facilities in the East Area or at the Antimatter Facility or to the **S**uper **P**roton **S**ynchrotron SPS, where they are accelerated further. In the SPS, which has a circumference of nearly 7 km, protons reach final momenta of 450 GeV/c when extracted towards the **L**arge **H**adron **C**ollider LHC

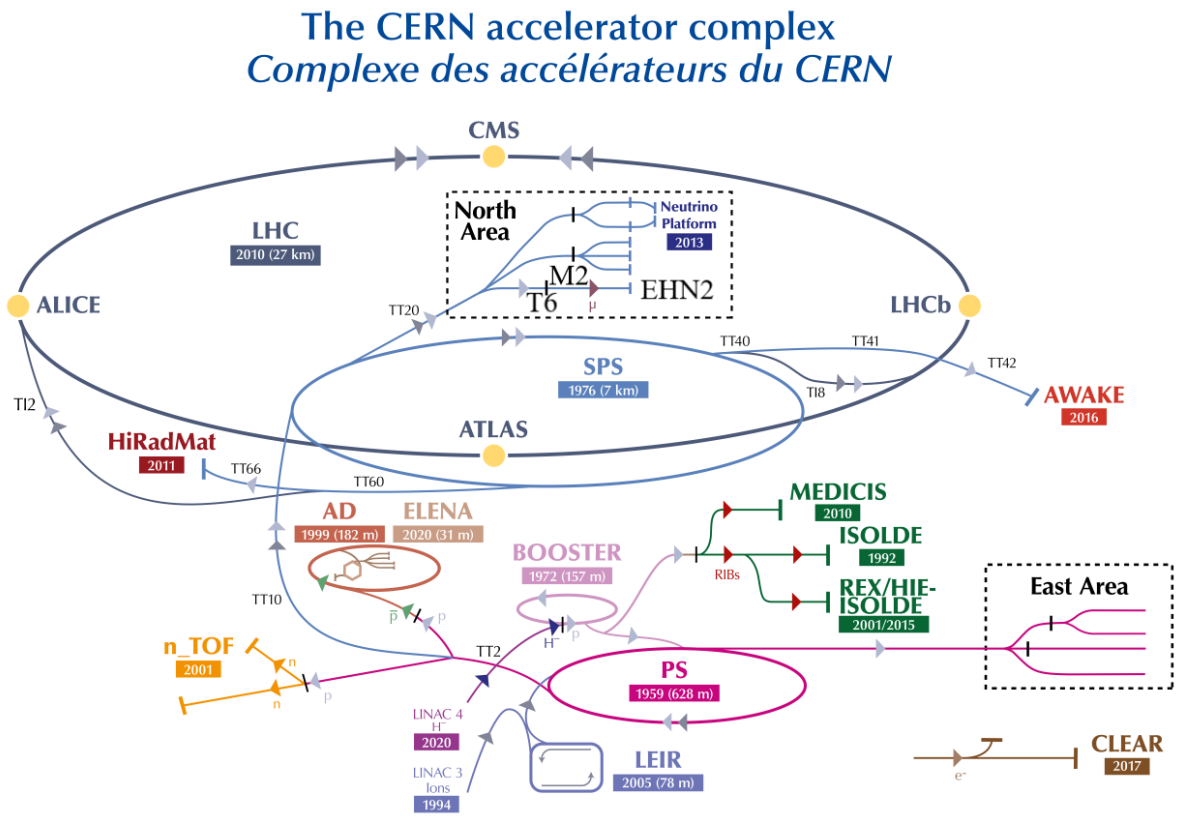

Figure 2.1: Layout of the full CERN accelerator complex including the experimental facilities. Most important for this thesis is the M2 line in the North Area served by the SPS. From [23]; modified.

[28] or 400 GeV/c when sent to CERN's North Area to serve fixed-target experiments [29, 30]. In the LHC, the last part in the accelerator chain, the protons can reach up to 6.8 TeV/c [31, 32]. One collides two protons beams of the same energy in LHC. Therefore, in total 13.6 TeV are available in the center-of-mass system that can be used to produce other particles.

In the case of ion runs, the chain does not start with LINAC4, but with LINAC3 that starts accelerating the ions and sends them to the **L**ow **E**nergy **I**on **R**ing LEIR. In the LEIR ring, the continuous ion beams are bunched, accelerated from 4.2 to 72 MeV kinetic energy per nucleon and sent to the PS [33, 34]. From there on, they follow the same way as the protons. Maximum momentum at SPS extraction is 400 Z GeV/c with the ion charge Z. In the LHC, they can reach 6.4 Z TeV/c. During these runs, typically lead ions are accelerated, i.e. $Z = 82$. Also, xenon ions have been used as beam particle already. It is possible to have p + Pb collisions, too.

As the focus of this work is on the M2 line in the North Area, this unique facility will be discussed in more detail. The primary protons from the SPS, accelerated to momenta of 400 GeV/c, can be sent to various production targets and beamlines. A general overview of the North Area is given in Fig. 2.2.

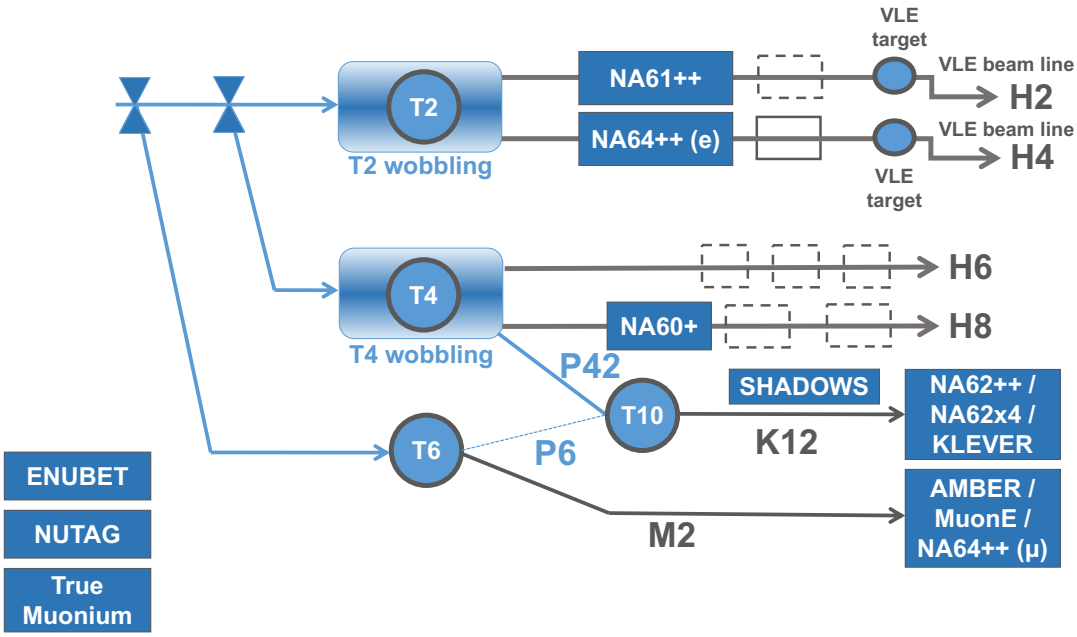

Figure 2.2: Schematic layout of CERN's North Area [35]. The beam traverses several splitter magnets to achieve the wanted sharing of protons between the targets. The lines H2 to H8 are mostly used for test beam activities. P42 and K12 serve the NA62 experiment. Most important for this thesis are the T6 target and the M2 beamline transporting the beam to the experiments.

The protons are transported via the transfer lines TT20 to TT25 to the primary production targets T2, T4 and T6 located in an underground cavern. The slowly extracted proton beam from the SPS needs to serve three production targets. To be able to do so, the proton beam gets divided by so-called splitter magnets [36, 37]. In short, those magnets have a dipole design, with a hole in the yoke. To split the beam, it is sent on the magnet, where some parts of the beam go through the hole, which is nearly field-free, and are not deflected, whereas the other part traverses the dipole field region and gets deflected. Schematically, this is indicated in Fig. 2.2 in the top left corner. The first splitter section, divides the beam into a part going to T6, followed by another section, splitting it between T2 and T4.

Following Fig. 2.2, several experiments are served by the beamlines following the aforementioned production targets. Most important for this thesis is the M2 line that transports secondary beams produced in interactions of protons from the SPS with the T6 target to several experiments that share beam time over the year. Following the end of the **C**ommon **M**uon and **P**roton **A**pparatus for **S**tructure and **S**pectroscopy COMPASS in 2022, currently most of the time, the **A**pparatus for **M**eson and **B**aryon **E**xperimental **R**esearch AMBER [18, 19] (cf. chapter 3) is using the various beam options available (cf. section 2.3). Besides AMBER, there is the NA64μ experiment [38] looking for dark matter candidates using a high-energy muon beam (cf. chapter 7) and doing a missing-momentum approach. Lastly, the **MU**on **on** **E**lectron

elastic scattering experiment MUonE [21] aims at measuring the hadronic contribution to the electromagnetic coupling constant by conducting elastic muon-electron scattering.

Until 2023, it has been possible to guide the protons that have not interacted in the T6 target via the P6 line towards the T10 target serving the K12 beamline, which currently transports beam to the NA62 experiment [39] located in the so-called **E**xperimental **C**avern **N**orth 3 ECN3. Now, this primary proton line has been dismantled and beam can only be sent via the primary proton line P42 to T10. Again, those are protons that have not interacted in the production target, which is T4. Of course, secondary beams are also produced in T4 that can be sent via H6 and H8 to the **E**xperimental **H**all **N**orth **1** EHN1 in the North Area. It needs to be mentioned that the momenta of the beams of those beamlines and of the primary protons guided via P42 are strongly coupled due to the so-called wobbling system [40]. This consists of three bending sections, two upstream and one downstream of the target that deflect the primary beam in such a way that secondary beams of wanted momenta can be transported via the mentioned beamlines, which have an angle relative to the nominal proton direction.

Around T2, one will also find a wobbling system that ensures operation of both lines H2 and H4 at the same time. Those four beamlines are typically used for detector tests and calibrations, but one can also find permanent setups of certain experiments, for instance NA61/SHINE [41] or NA64 operating in electron-mode [38].

2.2 Design principles of secondary beams

Normally, protons are the particles that are accelerated in the various machines. Therefore, it is necessary to let them interact with matter to be able to produce other particles, like unstable pions and kaons, or stable electrons and positrons. In the following, the production of secondary particles, their transport to the experiments and the elements needed for the transport are discussed.

2.2.1 Particle production

The primary proton beam from the SPS is guided towards various production targets serving the secondary beams in CERN's North Area. Those targets consist of various beryllium plates with different lengths [42]. Beryllium is used as it has an acceptable particle production rate while being able to sustain high beam intensities and energies without melting (which happens at 1 560 K [43]). In inelastic processes of the protons with the target material a spray of secondary particles like pions, kaons, neutrons and many more is produced. Of course, protons can also traverse the beryllium plates without interacting. The spectra and rates of the produced particles determine the maximal rate an experiment can expect without considering any losses due to decays or beamline acceptance. In 1980, a measurement has been conducted at the H2 line in the North Area to determine the production rates of several particle species. This will be referred to as the Atherton parameterisation [44]. The production of protons, antiprotons, kaons and pions has been estimated depending on their momenta (absolute value and direction) for

400 GeV/c protons impinging on beryllium. The obtained parameterisation is given in Eq. (2.1) for antiprotons, kaons and pions and in Eq. (2.2) for protons. The latter one takes the incoming proton into account. N describes the number of particles, p their momentum, Ω is the solid angle considering the direction of the secondaries, p_0 the primary proton momentum and θ is the production angle. A, B and C are constants that are determined by a fit to the data and are given in Tab. 2.1 for the various particles. The formulas are visualised in Fig 2.3.

$$\frac{\mathrm{d}^2N}{\mathrm{d}p\,\mathrm{d}\Omega} = \frac{ABCp^2}{p_0\pi}\exp\left(-\left(\frac{Bp}{p_0} + C\left(p\theta\right)^2\right)\right). \tag{2.1}$$

$$\frac{\mathrm{d}^2N}{\mathrm{d}p\,\mathrm{d}\Omega} = \frac{A\left(B+1\right)Cp_0}{\pi}\left(\frac{p}{p_0}\right)^{B+2}\exp\left(-C\left(p\theta\right)^2\right). \tag{2.2}$$

Particle	A in GeV$^{-2}\,c^2$	B	C in GeV$^{-2}\,c^2$
π^+	1.2	9.5	5.0
π^-	0.8	11.5	5.0
K^+	0.16	8.5	3.0
K^-	0.10	13.0	3.5
p	0.8	−0.6	3.5
$\bar{p}$	0.06	16.0	3.0

Table 2.1: Values for the parameters used in the Atherton parameterisation to calculate the production rates for the given particles [44].

The Atherton formula is valid for secondary momenta above 60 GeV/c and accurate to $O(10\,\%)$[1] and describes the production of pions, kaons and (anti-)protons. Production of muon and electron/positron beams works differently at the considered proton energies at CERN. For M2 one makes use of the produced pions. By ensuring a beamline that is long enough, a fraction of these pions will decay into muons and the corresponding neutrinos. Those muons are used to form the tertiary beam sent to the experimental area. Electron or positron beams are coming from high-energy π^0s that are produced in the interactions of the primary protons with the target material. These π^0s decay into two high-energy photons that produce electron-positron pairs.

To be able to calculate a beam rate that can be expected at the location of an experiment, one needs to account for the beamline acceptance, both longitudinally and transversely, which is described by $\mathrm{d}p$ and $\mathrm{d}\Omega$, respectively. Clearly, in the case of unstable particles, their decays need to be considered, too. Another important parameter is the so-called target efficiency yielding the number of protons that interact with the target material. But some protons might traverse the target without producing secondaries. Therefore, not the full number of protons is available for production of secondaries, but only a fraction. An important quantity for the

[1] The data has been collected only down to 60 GeV/c

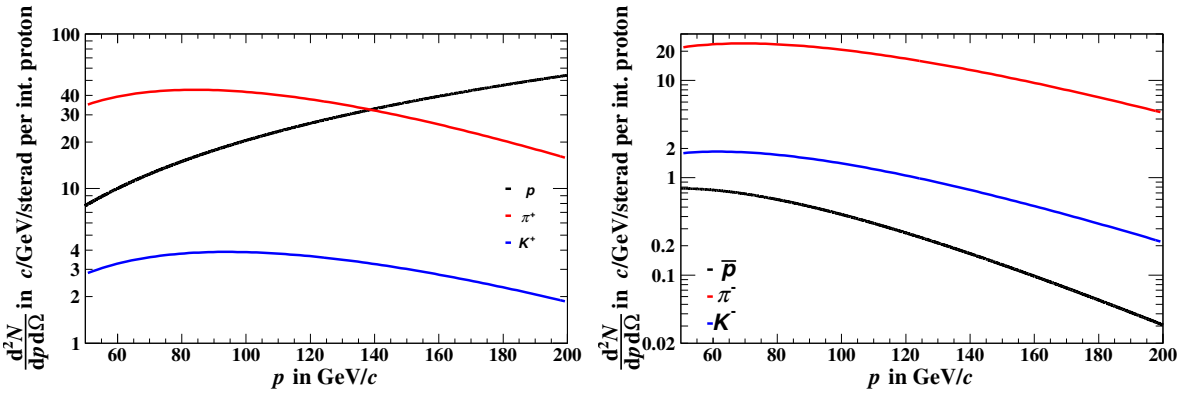

(a) (b)

Figure 2.3: Production of various particles in forward direction described by the Atherton parameterisation given in Eq. (2.1) and (2.2). It yields the spectra of hadrons in a given solid angle. 2.3(a) shows the production of protons in black, positive pions in red and positive kaons in blue. 2.3(b) illustrates the spectra of antiprotons in black, negative pions in red and negative kaons in blue.

target efficiency is the nuclear interaction length λ_n, which defines a length scale, over which a proton on average interacts with the target. Therefore, the number of protons that have not interacted decreases exponentially. It also defines a length scale, over which particles that have been produced interact with the target. Finally, the fraction of protons that interact and produce hadrons that escape the target and can in principle be transported by the beamline can be written as

$$\epsilon\left(L\right) = \frac{L}{\lambda_n} \exp\left(-\frac{L}{\lambda_n}\right), \tag{2.3}$$

with L being the target length. This is known as the target efficiency ϵ. It is maximal for $\frac{L}{\lambda_n} = 1$ with $\epsilon = e^{-1} \approx 0.37$ [45]. In the case of beryllium, the nuclear interaction length is 42.1 cm [43], meaning the maximal hadron rate can be expected for the T6 target head 500 mm. Other target lengths are available for controlling the particle rate. Those are 300 mm, 180 mm, 100 mm and 40 mm. It is also possible to let the beam pass through air yielding the lowest flux of secondaries.

The particle production has also been studied with simulations. The relevant software packages and codes used will be explained in chapter 4. In 2022, the proton beam shape in front of T6 has been measured, which is shown in Fig. 2.4. The shown distribution has been used to simulate the particles emerging from the interactions with a 500 mm beryllium plate. The transverse dimensions of the target plate are 160 mm × 2 mm [42]. The results have been scored 10 mm behind the target on an area of 4 m × 4 m and are shown in Fig. 2.5. Throughout this thesis, the abbreviation *pot* is used for **p**rotons **o**n **t**arget. If not stated otherwise, the quoted and plotted errors correspond to the statistical uncertainty.

Clearly, the results are not directly comparable with the Atherton parameterisation as they

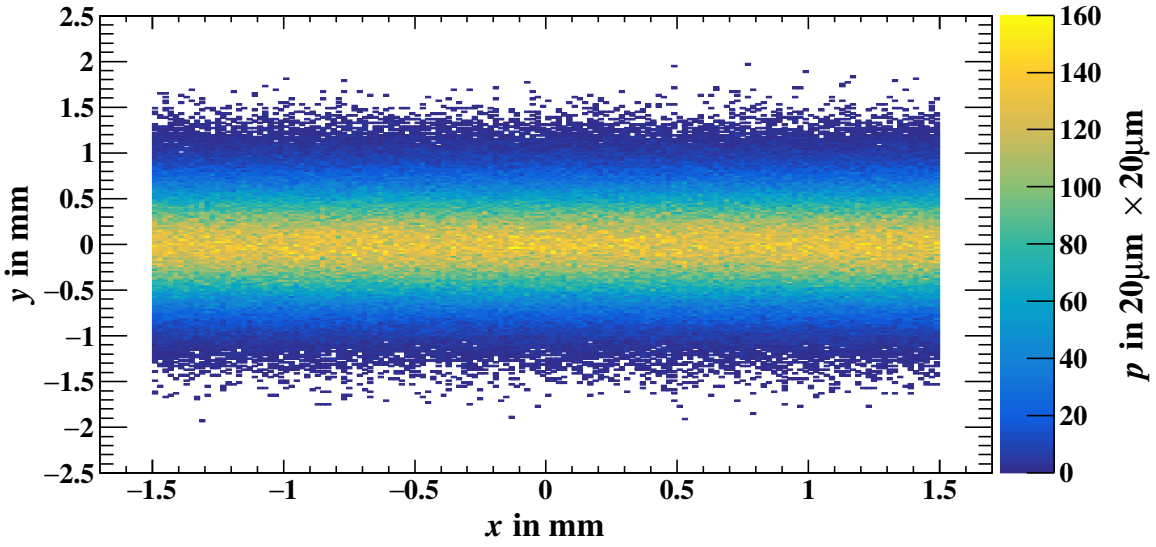

Figure 2.4: The spatial distribution of primary protons in front of T6 is shown. It is used for the simulations presented throughout this thesis. The input is described by a uniform distribution in the horizontal between ±1.5 mm and a Gaussian distribution with $\sigma = 0.414$ mm in the vertical direction. The data is based on a measurement that can be found in [46].

include the integrated rate over the covered solid angle. Nevertheless, it is clear from the plots 2.3 and 2.5 that pions are the particles that are produced the most in the momentum range up to 120 GeV/c, which is comparable with the Atherton formula. For higher energies, the production of secondary protons gets dominant until at momenta around 350 GeV/c the primary protons start becoming relevant with a clear peak at the primary momentum of 400 GeV/c. Neutrons are produced in large numbers, too, which is not relevant here, but important under radiation-protection aspects.

2.2.2 Particle transport

The particles that have been produced from the interactions of the 400 GeV/c primary proton beam coming from the SPS on the target material, need to be transported to the experimental areas, where the actual physics experiments and test beams are located. To do so, several elements placed along the beamlines are needed to guide and shape the beam. All these elements can be found at accelerator facilities around the world, including transfer lines and actual accelerators and will be discussed below.

Magnets

The most common beamline elements one will find are magnets, which can come in the form of dipole, quadrupole or even higher-order magnets. The presented concepts have been taken

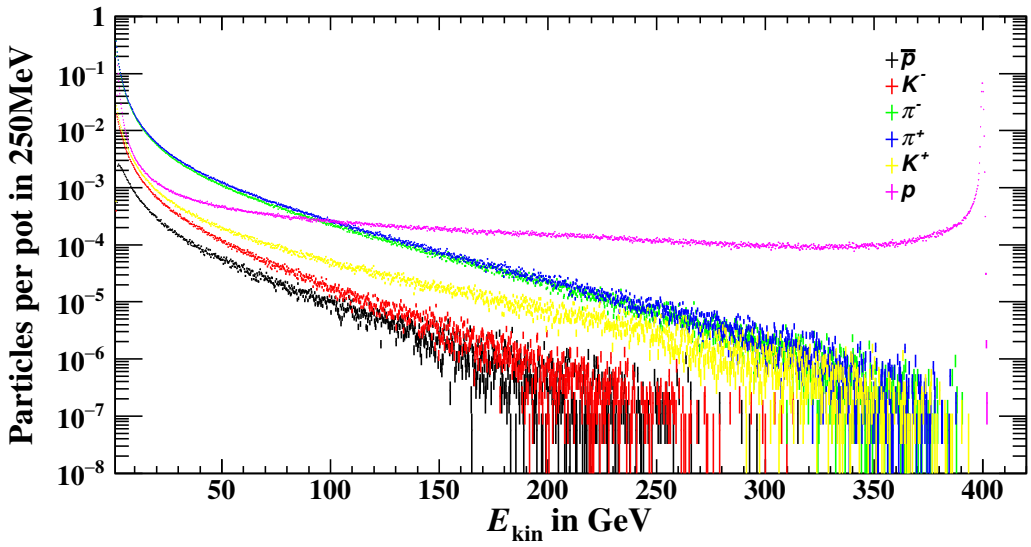

Figure 2.5: Spectra of particles produced in interactions from 400 GeV/c protons with 500 mm beryllium. It is simulated with BDSIM version 1.5.1 and Geant4 version 10.07.02 with the *FTFP_BERT* physics list. The results have been scored 10 mm behind the beryllium plate on an area with 4 m × 4 m.

from [47], but can be found in various text books about accelerator physics.

A particle with charge q traversing a general electromagnetic field described by its electric field $\vec{E}$ and magnetic field $\vec{B}$ is accelerated by the Lorentz force $\vec{F}_L$, i.e.

$$\vec{F}_L = q\left(\vec{E} + \vec{v} \times \vec{B}\right) . \tag{2.4}$$

In purely magnetic fields, the electric field of course vanishes. One can deduce that the force acts perpendicular to the direction of motion and perpendicular to the direction of the $\vec{B}$-field. The purpose of magnets at accelerator facilities is typically to keep the beam on the so-called ideal orbit. From Eq. (2.4) one can immediately see, why magnetic and not electric fields are used to fulfill this task. For a high-energy particle its velocity $\left|\vec{v}\right|$ is close to the speed of light c. In this case, the latter term dominates the first one in most cases as electric fields of the order of GV m^{-1} are non-trivial to achieve and to keep stable.

In transfer lines, one will typically find two different types of magnets: dipoles, also referred to as bends, and quadrupoles. Rarely, sextupoles are also placed. Those and even higher-order magnets are used to correct field errors in imperfect magnets or to account for a non-vanishing momentum spread in the beam. This is important in circular accelerators as the beam passes through those elements millions of times. But as those non-linear magnets are not used in the beamlines of interest, they will not be discussed here.

Dipole magnets consist of two poles, north and south, as the name already implies. A picture can be seen in Fig. 2.6.

Figure 2.6: Picture of a vertical dipole magnet installed in the M2 line. The arrows indicate the magnetic field lines. The good field region is not to scale; in reality, it is smaller. The magnet is 2 m long with a full aperture of 192 mm × 140 mm.

The dipoles found in the beamlines feature a quite homogeneous field in the region the beam passes through. Considering the indicated field direction in Fig. 2.6 and a particle traversing the magnet (direction into the plane), it gets deflected upwards or downwards depending on its charge (positive/negative) according to the Lorentz force (2.4). In the described example, one has $\vec{v} \perp \vec{B}$ meaning that the particle gets forced on a circular trajectory. Considering centripetal force

$$\left|\vec{F}_Z\right| = \frac{pv}{\rho}\,, \tag{2.5}$$

with p being the particle momentum, and ρ the magnetic bending radius, which equals the Lorentz force, one can find the magnetic rigidity

$$B\rho = \frac{p}{q} . \tag{2.6}$$

Eq. (2.6) can also be rewritten to specify the bending angle of a beam with a given momentum traversing the defined magnetic field. The result is given in (2.7) considering small angle approximation, with the length of the magnet L_{M}.

$$\theta = \frac{L_{\mathrm{M}}}{\rho} = q\frac{BL_{\mathrm{M}}}{p} . \tag{2.7}$$

Often, BL_{M} is referred to as the integrated field. In practical units, (2.7) can be expressed as

$$\theta/\mathrm{mrad} = 299.79\frac{BL_{\mathrm{M}}/\mathrm{T\,m}}{p/\mathrm{GeV}\,c^{-1}} , \tag{2.8}$$

with the numerical factor coming from expressing the speed of light in the unit $\mathrm{m\,ns}^{-1}$.

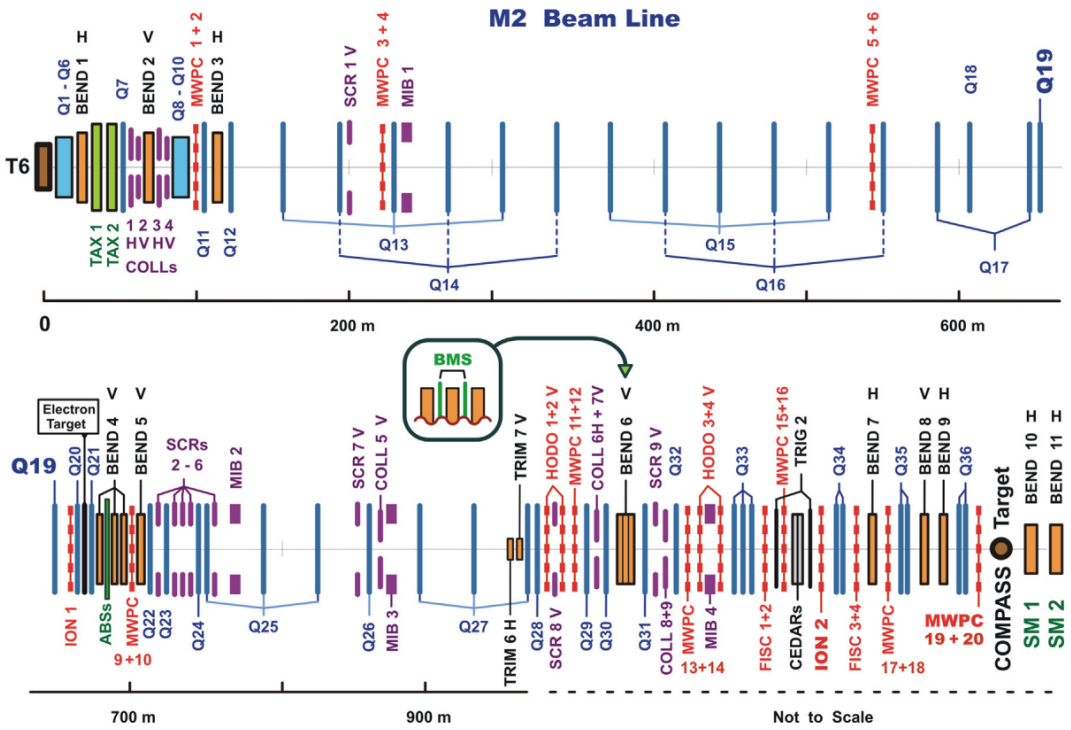

Figure 2.7: Schematic layout of the M2 beamline including the naming of all beamline elements [48]. H corresponds to a horizontal bend, while V refers to a vertical one.

In M2, which is schematically shown in Fig. 2.7 including the naming of the various beamline elements, one can find several types of dipole magnets fulfilling different purposes. In total,

there are nine bending stations, where a station can consist of more than one magnet. Most of the bends act as vertical ones to guide the beam upwards from the SPS towards the **E**xperimental **H**all **N**orth **2** EHN2. Two of the vertically bending stations also have additional functions. One can move several hadron absorbers into bend4 (ca. 700 m downstream of T6), which is a C-shaped dipole. Those are used for cleaning the muon beam that is available in M2 (cf. section 2.3 and chapter 7). The deflection in bend6 (ca. 1.03 km downstream of T6), which is H-shaped, is used by experiments to measure the momenta of muons that are sent to the experimental areas [17]. As the beam is still going up coming out of bend6, bend8 (1.11 km after T6) is used to make the beam parallel to the ground. Bend7 (1.1 km) and bend9 (1.12 km) have been formerly used by COMPASS to have a beam hitting the polarised target with a horizontal angle. As the beam traversed the solenoid magnet around the target it has been going parallel to the nominal beam axis through the COMPASS spectrometer. As this so-called chicane is not needed anymore for AMBER, those magnets do not fulfill any purposes anymore, too, but one can still find them in the beamline. The first set of dipoles that are horizontally deflecting and are located about 30 m behind T6 bend the secondaries such that they follow the beamline while the primary protons that barely interacted in the target are deflected in a way that they hit a dedicated collimator (cf. section 2.2.2) called **T**arget **A**ttenuator E**X**perimental Areas TAX. Clearly, at all bending stations the beam momentum is defined, but the first one cleans the beam from the primaries and secondaries that come out of the target with the wrong momentum. After the TAX, other bends together with collimators further define the momentum. In addition, one can also find corrector magnets, which are dipoles. Those are used to correct the beam track. This is necessary as elements can be misaligned meaning that the beam would not go through their centre.

The second important class of magnets are the quadrupoles, also called lenses. An example is given in Fig. 2.8.

A beam that travels along the line consists of many particles. The positions and angles with respect to the beam axis, the so-called divergence, follow certain probability distributions. To contain the beam in a usable size so that it is guided along the beamline over long distances of several 100 m [2] focusing elements are needed, like optical lenses in light optics. A field that is proportional to the amplitudes in both transverse directions

$$B_x = gy, \qquad B_y = gx\,, \tag{2.9}$$

can fulfill this requirement. g is called the magnetic field gradient. Calculating the Lorentz force with Eq. (2.4) and the described field distribution, one can deduce that the force is repelling in one transverse direction, while focusing in the other one[3]. This is in contrast to light optics with concave lenses that have a focusing effect in the full transverse plane. Therefore, one needs systems consisting of several quadrupoles with opposite polarities to get an overall net-focusing

[2] As the apertures of magnets are of the order of cm to dm, this can be considered as a reasonable size of the beam, which can still be transported.

[3] Of course, the directions can be interchanged by flipping the the polarity of the field and therefore of the gradient g.

Figure 2.8: Picture of a quadrupole magnet of type **Q**uadrupole **W**est Area **L**ong QWL installed in the M2 line. It is 2.948 m long with a beam pipe of 100 mm diameter.

in both transverse directions.

For optics calculations, one does not use the field gradient g itself but the focusing strength k such that the optics are momentum-independent, i.e.

$$k = \frac{qg}{p}\,, \tag{2.10}$$

or again, in practical units

$$k/\mathrm{m}^{-2} = 0.29979 \frac{g/\mathrm{T\,m}^{-1}}{p/\mathrm{GeV}\,c^{-1}}\,. \tag{2.11}$$

For ideal quadrupoles, g can be expressed as the ratio of the field at pole tip and half-aperture.

In M2 different types of quadrupoles are employed. One has 36 (de)focusing stations in total, where again a station can consist of more than one magnet. Following the target, six high-gradient quadrupole magnets are installed. With those a large transverse beamline acceptance is achieved. Having a large acceptance guarantees an optimal collection of the secondary particles produced in T6. Going along the beamline, one typically finds quadrupoles with large apertures. Those are needed for the muon mode as it is characterised by its large transverse extent, which is due to it being a tertiary beam. Q33 (1.075 km downstream of T6) is used to define the beam size and divergence in the CEDAR area, where beam particle identification detectors are installed (cf. section 2.2.3 and chapter 6). Q35 (1.11 km) and Q36 (1.12 km) define the beam divergence and size at the AMBER target.

A well-known, highly used approach to efficiently transport particle beams over long distances are so-called FODO-cells. An example is given in Fig. 2.9.

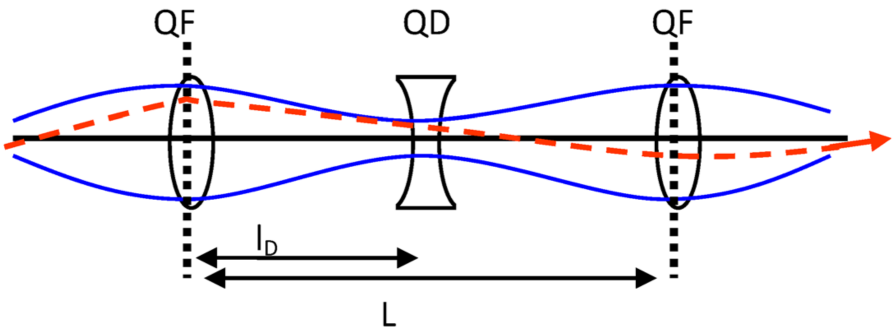

Figure 2.9: Example of a symmetric FODO-cell [49], which is made by two half focusing and one defocusing quadrupole separated by two drifts of the same length l_D. The period, when several cells are placed, is from center to center of the focusing quadrupoles.

Such a system consists of **F**ocusing and **D**efocusing lenses in alternating order with free drifts **O** in between (FODO). An important example is the symmetric FODO-cell, meaning $k_{QD} = -k_{QF}$ and $l_D = 0.5L$, with l_D being the distance from focusing to defocusing magnet and L the length of the whole cell. In thin-lens approximation, one can easily calculate the phase-advance φ per FODO-cell yielding the rotation in trace space (which is the space spanned by position and angle of- the beam particles; cf. 2.2.2). One will find

$$\sin\frac{\varphi}{2} = \frac{L}{4f}\,, \tag{2.12}$$

with the magnetic focal length f, which is connected with the focusing strength via $f = \frac{1}{kL_M}$ with L_M being the magnetic length.

The FODO-concept is also applied in M2, where one can find nine unit cells in total. As its design also features the muon beam option, it is necessary to make the beamline as long as possible as the muons come mostly from decays of pions that are produced at T6. Therefore, it

is important to provide enough distance from T6 to the experiment, where the beam can move nearly without any influence. One also needs to ensure proper transportation of the produced muons together with the hadrons that have not yet decayed. This is achieved by FODO-cells with large-aperture quadrupoles. Those ensure that the beam is contained within the beamline. The phase advance per cell of the parent, higher momenta pions is set to 60° to guarantee the simultaneous transmission of the lower momenta muons, too. As the remaining hadrons are removed by the mentioned absorber, only muons of one defined momentum need to be guided afterwards. Therefore, the argument to transmit a broad-momentum beam does not need to be respected anymore.

Collimators

Collimators are devices that are put in the way of the beam on purpose to define the beamline acceptance and momentum spread. They consist of blocks of material with a large stopping power, typically iron with a defined and adjustable aperture for the passage of the beam. If a particle is within the collimator aperture, the collimator can be considered as a drift in free space. But if the particle hits the aperture, it interacts with the collimator material. Because the block is about six nuclear interaction lengths long [50] ($\lambda = 16.77\,\text{cm}$ [51]), the particle will get absorbed. A picture of a large two-block collimator used in the M2 line is shown in Fig. 2.10(a). The Geant4 model of a standard four-block collimator is depicted in Fig. 2.10(b).

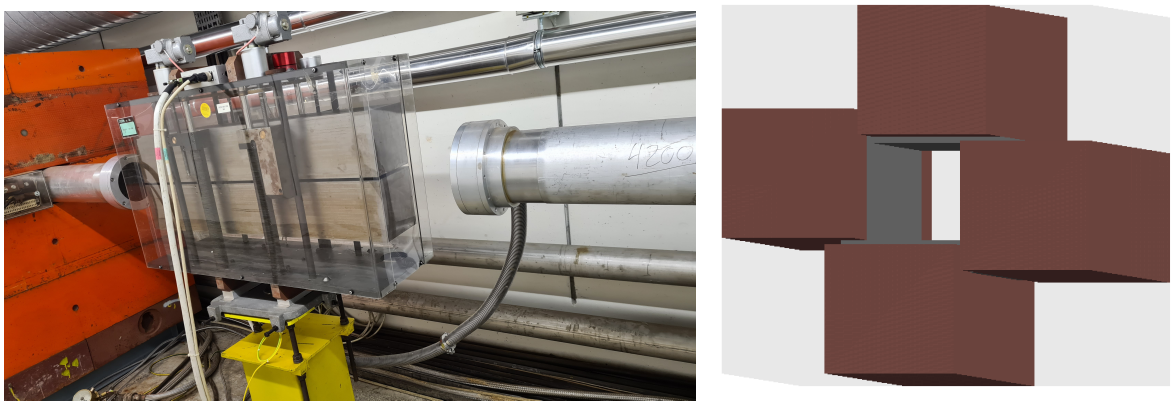

(a) (b)

Figure 2.10: Two types of collimators used in CERN's North Area beamlines. Fig. 2.10(a) shows the large two-block collimator called XCBV, which is 1.2 m long. It can be found only in M2. Fig. 2.10(b) shows the Geant4 model of a standard four-block collimator called XCHV, which is 1 m long. These can be found in every beamline including M2.

The blocks need to be able to contain the hadronic shower created by an impacting particle. Therefore, one will find in the standard two- and four-block collimators additional tungsten cladding on the inside of the iron blocks as it provides a higher stopping power and smaller skin depth [52]. Besides that in the high-energy regime one is dealing with in the North Area at

CERN one will always have particles created in the shower that escape the collimator and would contribute to backgrounds for experiments. Therefore, one typically places other so-called cleaning collimators, or even magnets behind it.

Two different types of collimators are installed in M2. The downstream four-block ones (six to nine) are used for cleaning the beam from hadrons outside of the core. C2 and C4 define the vertical acceptance of M2, while C1 and C3 define the momentum bite of the secondary hadron beam used for muon mode operation. The large two-block collimator is employed for momentum-definition purposes in hadron and electron beam mode, while it is fully open during muon beam operation, where it is used as a source of multiple scattering for halo particles helping to remove them.

Collimation of neutral particles is a more advanced topic, which will not be discussed here. Instead, additional information can be found for instance in [53].

Muon beam collimation is not possible with passive material as muons lose minimal amounts of energy in contrast to electrons, photons and hadrons. Therefore, it is necessary to use so-called sweeper magnets. In the M2 beamline one will find magnetic collimators that clean the muon beam, i.e. scraper magnets (XCM) and magnetised iron blocks (MIB). Both are typically powered with currents of 100 A. Those devices have a toroidal magnetic field of the order of 1 T, inside the iron yoke and are nearly field-free inside the aperture, which is shown in Fig. 2.11. Such fields help collimating a muon beam sweeping out halo muons that interacted with beamline material as they did not go through the aperture of the elements. An example for each can be seen in Fig. 2.12.

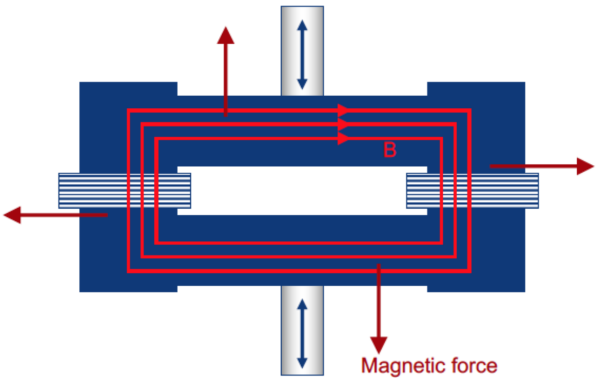

Figure 2.11: Schematic sketch of a magnetic collimator with its toroidal field pulling positively charged particles towards the center while negatively charged ones get pushed outwards [53].

The field configuration results in a radially out-going Lorentz-force for one type of muons, while the corresponding anti-muons will get pushed towards the beam axis. This is still useful as anyway only one charge gets transported along the beamline. Therefore, the polarity of the field can be chosen accordingly.

The scrapers four and five serve as momentum defining slits for the muon beam in M2 while the other ones clean the beam from halo muons.

(a) (b)

Figure 2.12: The two types of magnetic collimators used in the M2 beamline. Fig. 2.12(a) highlights the scraper magnet. Those are 5 m long and have a movable aperture. Fig. 2.12(b) shows a magnetised iron block, which is 1.6 m long with a beam pipe of 200 mm diameter. Both magnetic collimators provide a toroidal field of the order of 1 T.

Linear transverse beam dynamics

There is no general analytical approach to solve the equations of motion in an arbitrary accelerator or beamline as the specific outline including magnets, beam instrumentation and free drifts needs to be known. This might include non-linear devices like high-orders magnets. As such elements are not installed in the studied beamline configurations, only linear beam dynamics will be investigated in the following. In addition, the focus is especially on transverse linear beam dynamics because it is only dealt with beamlines without longitudinal acceleration. The presented theoretical concepts are based on [54].

To describe the evolution of single particles or the full beam, it is necessary to define an appropriate coordinate system. The coordinate system is following the so-called reference particle, which is a nominal-momentum particle that traverses every element in its center parallel to the elements nominal axis. It is described by the three coordinates $(x,\ y,\ s)$ with s being tangential to the reference orbit in the direction of the particle's movement. x and y are the transverse coordinates spanning an orthogonal right-handed coordinate system. This is summarized in Fig. 2.13.

Considering that beam sizes and angles are of the order of mm and mrad, one is typically only interested in small deviations from this reference orbit. Therefore, one can follow approaches known from geometric light optics. In geometric light optics, every ray is described by its transverse positions x and y. In addition, changes to these positions along the beamline are given

$$x' = \frac{\mathrm{d}x}{\mathrm{d}s}, \qquad y' = \frac{\mathrm{d}y}{\mathrm{d}s}\,. \tag{2.13}$$

As one deals only with small deviations from the reference orbit, the angle with respect to this axis will be small and can therefore be linearized, which is known as paraxial optics. With this at hand, one can describe a particle by four coordinates, i.e. $(x,\ x',\ y,\ y')$.

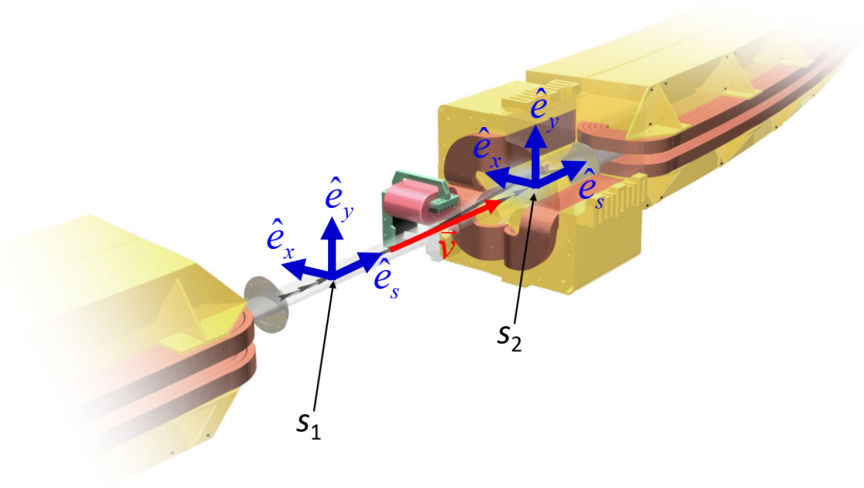

Figure 2.13: Definition of the coordinate system that follows the reference orbit [54]. s is pointing in beam direction while x and y construct the plane transverse to that direction.

In a free space, without any magnets, a particle will keep its direction of movement, but changes its transverse coordinates if it has a non-zero angle to the reference axis. This can be described by

$$x = x_0 + Lx', \qquad y = y_0 + Ly', \tag{2.14}$$

with x_0, y_0 being the initial displacements, L the length of the drift and x', y' the angles with respect to the s-axis. This can be described conveniently by a two-dimensional matrix for each transverse coordinate. The matrix reads

$$M_{\text{Drift}} = \begin{pmatrix} 1 & L \\ 0 & 1 \end{pmatrix}. \tag{2.15}$$

An ideal dipole magnet bends the particle independent of its transverse displacement. As the system of reference is the one following the ideal particle, a bend acts the same way as a free drift. This changes when a particle traverses a quadrupolar field. The magnetic field changes the transverse angle of the particle depending on the transverse offset, i.e.

$$x' = x'_0 \left(1 - \frac{x_0}{f}\right), \qquad y' = y'_0 \left(1 + \frac{y_0}{f}\right), \tag{2.16}$$

with the focal length f. In a thin-lens approximation, $L \ll f$, in which the kick is applied after traversing the magnet without any action while passing, the transverse positions remain unchanged. Again, those equations can be summarized in a matrix, which reads

$$M_{\text{Quad}} = \begin{pmatrix} 1 & 0 \\ \mp kL & 1 \end{pmatrix} = \begin{pmatrix} 1 & 0 \\ \mp\frac{1}{f} & 1 \end{pmatrix}. \tag{2.17}$$

Recall, the sign-flip accounts for the effect that a magnetic lens is focusing in one direction but defocusing in the other. With those matrices at hand, it is possible to describe the effect of a full beamline lattice, by multiplying the matrices for each element and applying the final matrix to the initial coordinates of a beam particle. Clearly, those matrices do not cover neither the coupling of the two transverse directions, nor the coupling of the beam direction with the two transverse ones. This is achieved by introducing the 6D space, spanned by the vector $\left(x,\, x',\, y,\, y',\, -c\Delta t,\, \frac{\Delta p}{p}\right)$, with Δt being the time difference to the reference particle and Δp a small deviation from the nominal momentum p. Working in this reference frame, one can write down 6D matrices made of the presented 2D ones considering additional cross-directional coupling terms. Coupling between the two transverse directions happens for example when rotating a bending or quadrupole magnet by angles different to $n\frac{\pi}{2}$ around the beam axis, which are known as skew magnets. Coupling between the longitudinal and one of the transverse directions is very common as according Eq. (2.7) the bending depends on the particle's momentum meaning having a slightly different momentum results in a different transverse angle and displacement. Throughout this thesis, coupling of the transverse directions is zero as there are no skew magnets. So, one will find mostly terms of the 6D transport matrix, called R_{11}, R_{12}, R_{16}, R_{21}, R_{22} and R_{26}. Those are the matrix elements describing the horizontal position of the particle after an element as a function of its horizontal position before, horizontal angle before and momentum deviation; similarly, they describe the horizontal angle as a function of horizontal position, angle and momentum deviation. In the same way one will find the terms describing the vertical direction with the indices 3, 4 and 6.

Following a more general, but still linear approach, it is possible to derive the equations of motion for particles in an arbitrary lattice. For the derivation it is referred to [47, 54]. The resulting linear equations of motion read

$$\begin{aligned} x''(s) + \left(\frac{1}{\rho^2(s)} - k(s)\right) x(s) &= \frac{1}{\rho(s)}\frac{\Delta p}{p}, \\ y''(s) + k(s)y(s) &= 0. \end{aligned} \tag{2.18}$$

In the derivation, it has been assumed that the machine stays in the xs-plane, so there is no vertical bending. $\rho(s)$ is the bending radius of the machine at a given location s and $k(s)$ the (de)focusing strength. Especially, the term describing effects on off-momentum particles is of importance as it contains the different bending of particles for different momenta. This is known as dispersion, similar to light optics with a wave-length dependent index of refraction. In beamlines one makes actual use of this effect when defining the nominal momentum of the

beam. When having a broadband beam, one can place a dipole magnet in the way of the beam that bends the particles depending on their momenta. By placing a collimator downstream of the dipole and closing the jaws to a given opening, one can choose the momentum bite of the beam and create a monochromatic beam as only the particles with the appropriate momentum will pass through the collimator. Clearly, the energy-spread of the beam depends on the opening of the momentum-defining collimator.

Until now, only single particles have been investigated. At CERN generally and in M2 in particular, one is dealing with intensities of the order of 10^{12} to 10^{13} for primary protons and of the order of 10^3 to 10^9 for secondary and tertiary beams. Therefore, it is useful to define statistical quantities, like the beam size and divergence and ultimately the emittance. The beam size and divergence are given by the variances

$$\sigma_x^2 = \frac{1}{N}\sum_{i=1}^{N} x_i^2, \qquad \sigma_{x'}^2 = \frac{1}{N}\sum_{i=1}^{N} x_i'^2\,, \tag{2.19}$$

when assuming that the beam center is at the reference orbit and follows it exactly (similarly, this holds for y). Those quantities yield the so-called transverse beam emittance ϵ

$$\epsilon_x = \sigma_x \sigma_{x'}, \qquad \epsilon_y = \sigma_y \sigma_{y'}\,, \tag{2.20}$$

which is strongly connected to the area the beam fills in the trace space. The trace space is spanned by the transverse displacement and angle, i.e. x and x'. Every particle in the beam describes a point in trace space. It is connected to the phase space as the transverse momenta are directly proportional to the angles with respect to the reference orbit. Therefore, one can also write

$$\epsilon_x = \frac{1}{\pi}\int \mathrm{d}x \int \mathrm{d}x'\,. \tag{2.21}$$

According to Liouville's theorem [55] the phase space area is constant under application of conservative forces. As the emittance is directly linked to the trace space (and therefore to the phase space) area, it is a conserved quantity. This manifests in the fact that magnets and drifts placed along the beamline only change the form of the ellipse in phase space, but not its area. Ultimately, one only applies transforms in phase space when having such elements in the line. This is demonstrated in Fig. 2.14. Considering a trace space distribution illustrated in Fig. 2.14(a) and applying a drift over 20 m, the shape of the ellipse changes, which can be seen in Fig. 2.14(b). But the area stays constant.

The situation changes as soon as one collimates the beam, either with a collimator or with cutting the beam at the magnet or beam pipe apertures. As this is not a conservative transformation, the emittance will change.

The emittance and application of Liouville's theorem are important for M2 generally and this thesis in particular. One finds several parts of the beamline, e.g about 100 m, where the beam

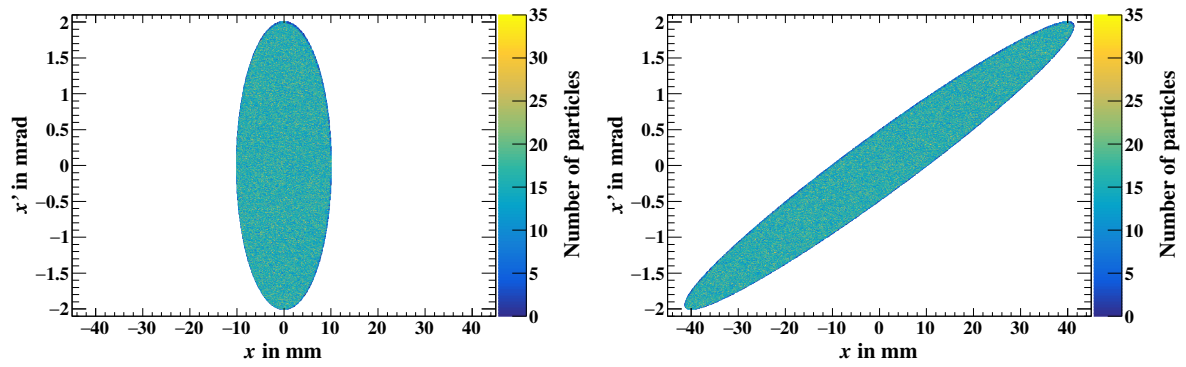

(a) (b)

Figure 2.14: Illustration of the transformation of the trace space coming from a drift. 2.14(b) is the trace space distribution after drifting the distribution 2.14(a) over 20 m. Calculating the areas of both ellipses yields the same emittance due to Liouville's theorem.

traverses air at atmospheric pressure (cf. chapter 6). Those locations are sources of multiple scattering leading to an uncontrollable increase of the beam emittance. This results in a larger beam size and divergence even when imposing a focus for the former or a parallel beam for the latter.

The fact that the emittance is constant under the application of conservative forces is applied later on in chapters 5 and 6. There, the fact that the beam divergence is small for a large beam and vice versa, is used to optimise the beam optics for the described purposes of beam separation or particle identification.

2.2.3 Beam instrumentation

Depending on the beam characteristics that one wants to measure there are several beam intercepting devices one can employ. The most common ones are beam profile monitors, typically wire chambers in the North Area beamlines, scintillators and ionisation chambers for intensity measurements, and particle identification systems [45]. The detectors described in the following are specific to CERN's experimental area beamlines, but they can be found similarly at other facilities, too.

Particle identification

To be able to identify the different species in the beam, one can follow several approaches. The two common ones are time-of-flight measurements on the one hand, and identification based on Čerenkov light emission. Particle differentiation using time-of-flight is based on measuring differences in travel time from one point in space to another one. This approach gets quite sophisticated for momenta larger than 10 GeV/c as the differences in the particles velocities get

smaller with increasing beam energy. Therefore, one needs more precise time measurements of the order of ps and smaller. That is why one will typically find Čerenkov detectors in the North Area beamlines.

Those detectors make use of the Čerenkov effect. Particles that travel at a speed v faster than the local speed of light in the medium $\frac{c}{n}$, i.e.

$$v > \frac{c}{n}\,, \tag{2.22}$$

with n being the index of refraction of the traversed medium, emit electromagnetic radiation [56]. The light is emitted on a cone with opening angle

$$\cos\theta = \frac{1}{\beta n}\,, \tag{2.23}$$

with $\beta = \frac{v}{c}$ [57].

In the North Area one can find two types of Čerenkov-detectors, so-called Threshold Čerenkov Counters (XCET) and Čerenkov Detectors with Achromatic Ring Focus (CEDAR). Both are gas-filled detector types.

Threshold counters make use of the fact that one can set the pressure of the gas in such a way that only particles up to a given threshold pressure will be above the Čerenkov limit and emit light while heavier particles do not. By slowly increasing the pressure one can measure the relative content of each single species. The threshold pressure can be calculated as follows: Assume $n = 1 + k_{\text{gas}}P$ with P being the gas pressure and k_{gas} a gas constant that varies only slightly with wavelength. Considering the Čerenkov condition (2.22), this can be translated into the threshold pressure, above which all particles fulfilling it will emit light, i.e.

$$P > \frac{m^2c^2}{2p^2k_{\text{gas}}}\,. \tag{2.24}$$

For typical gases used in Čerenkov counters the parameter k_{gas} is of the order of 10^{-4} to $10^{-3}\,\text{bar}^{-1}$. Typically, one can identify particles up to momenta of the order of 20 GeV/c with those, which comes from safety limits on the gas pressure. Hence, for identifying particles in beams with larger momenta a different detector type is needed, which are CEDARs in the present case.

Ideally, CEDARs will only give a trigger signal for one particle type in contrast to threshold counters. A schematic view is presented in Fig. 2.15.

A particle traversing the gas-filled tank that fulfills the Čerenkov condition (2.22) emits light that is reflected by a mirror close to the end caps and focused on the photo-multiplier tubes (PMTs). On the way, there are optical elements correcting for chromaticity. Most importantly, in front of the PMTs, there is a so-called diaphragm with a central diameter of 20 mm and an adjustable width of that slit. As every particle has a specific Čerenkov angle for a fixed momentum and refractive index, one can tune the pressure in a way that the particle of interest

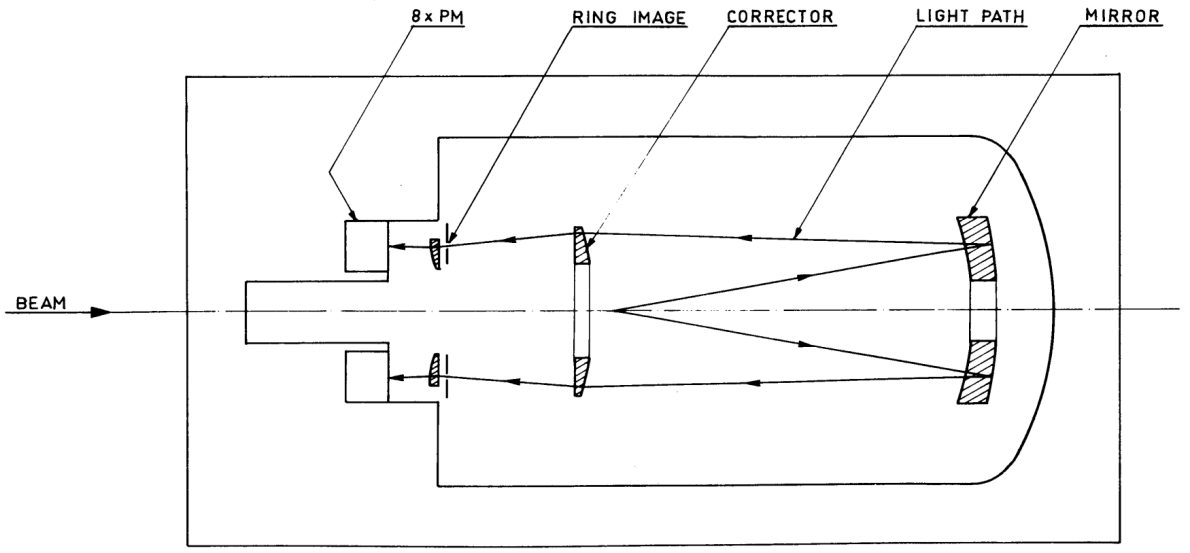

Figure 2.15: Schematic design of a CEDAR detector [58]. If a beam particle that fulfills the Čerenkov-condition (2.22) traverses the gas volume, it emits light that gets reflected close to the end-caps and guided towards a ring of PMTs.

will create a light ring with the right opening angle. When having the diaphragm fully open the light cones of several particles will be accepted. Therefore, to be able to reject particle species to only accept the one of interest, one needs to make the diaphragm smaller taking into account multiple scattering and the ring size of the particle emitting light under an angle closest to the tagged one. Clearly, a critical parameter is the beam divergence as the light is emitted relative to the direction of travel of the particle. A particle traversing the CEDAR with a non-zero angle relative to the beam axis might emit the light in such a way that it creates a cone with a part going through the diaphragm and creating a trigger signal. That is why one typically requires a coincidence of several PMTs (one has eight of them in a circle). Unfortunately, one cannot achieve a perfectly parallel beam (cf. Liouville's theorem) meaning that one will lose the parts of the beam that are too divergent. The maximal divergence for still being able to differentiate particle species is shown in Fig. 2.16.

Such an approach leads to a reduced particle identification efficiency, especially at high beam momenta as the Čerenkov angles of the various particles come closer. Therefore, a more sophisticated offline-analysis technique has been developed by the COMPASS collaboration making use of the track information obtained with the full spectrometer [59–61]. The beam position and angle are propagated backwards to the location of the beam particle identification in order to correct for the divergence of the reconstructed beam particle. With such an approach, kaon identification efficiencies of the order of 85 % have been achieved [59–61].

At CERN, two types of CEDARs are used that feature different gases and maximal pressures. The CEDAR-West operates with nitrogen and can separate kaons from pions up to 150 GeV/c [62]. The CEDAR-North is flushed with helium and differentiates pions from kaons up to

300 GeV/c [62]. In M2, the CEDAR-N type is employed due to it being capable to still tag pions beyond 190 GeV/c. Those are installed ca. 1.1 km downstream of T6 and about 50 m upstream of the AMBER target. As it is a gaseous detector, temperature changes influence its performance. This is another reason for the CEDAR-N as those are stabilized to 0.1 K [58].

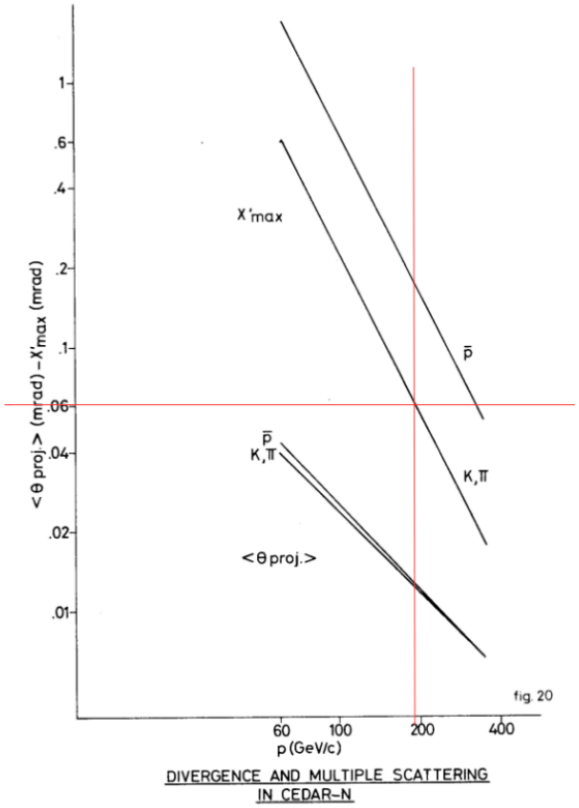

Figure 2.16: Contribution to the beam divergence coming from multiple scattering of the beam in the CEDAR gas as well as maximal beam divergence to differentiate certain particle types [63]. The maximal divergence is shown more clearly in Fig. 6.7.

Profile monitors

Beam profile monitors are detectors measuring the beam shape and size at various locations along the beamline. Typically, one will find gas-filled multi-wire proportional chambers (MWPC) in the North Area [64]. An example of a chamber that is installed in the beamlines is shown in Fig. 2.17.

Wire-chambers make use of ionisation processes happening in a gas when an ionising particle traverses it. Along the trajectory, electron-ion pairs are created. By applying a potential difference between the wires and the outer electrodes (typically, the wires are on positive potential), an electric field is generated. Due to this field, the electrons move towards the anode

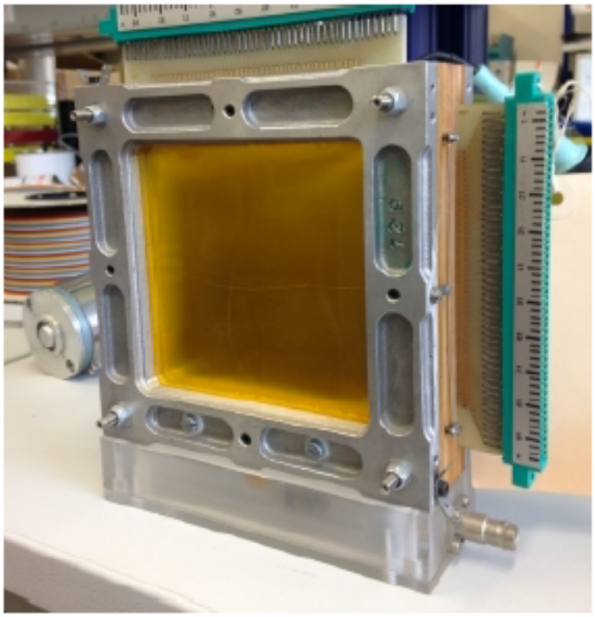

Figure 2.17: An analog wire chamber XWCA. The active area is 10 cm × 10 cm and the wire spacing is 1 mm [45]. The other profile monitors look similar, but they have different distances between the wires.

wires. Close to the wires ($r \approx a$, with a being the wire diameter), the electric field gets high enough such that electrons start an avalanche process and create further electron-ion pairs[4]. This avalanche leads to a signal that can be easily read-out electronically. By knowing which wire has fired, one can measure the point the beam passed through[5]. In M2, the standard wire spacing is 2 mm [45]. It is foreseen to replace the MWPCs by scintillating fibre detectors [65, 66], which have the advantage to be incorporated in beam pipes, so in vacuum.

The beam divergence can be measured with so-called filament scanners that feature a 200 µm wide scintillator filament that can be moved through the beam, typically on a spill-by-spill basis [45]. By requiring the coincidence of two horizontal or vertical scanners (depending on which divergence should be measured), where one is kept at the same position while the other one is moved relative to it, one can estimate the parallelism of the beam.

Beam intensity

For the estimation of the beam rate, one can find two detector types in CERN's experimental areas of the North and East Areas. For intensities up to some MHz [45] scintillators are used that yield the total number of particles per spill that traversed the active area. Typically, one also determines the beam composition by placing two of them around a Čerenkov detector

[4] The electric field is proportional to r^{-1} with r being the distance to the wire.

[5] Often, one can profit from the signal being induced in several wires. By calculating the center-of-gravity, it is possible to measure the position more precise than just $\frac{d}{\sqrt{12}}$ with the distance between the wires d.

and requiring a coincidence signal. The two scintillators yield the total beam flux while the convolution with the Čerenkov detector signal gives the flux of a particle species (or several in the case of a threshold counter). For intensities above a few MHz and up to several 100 MHz [45] the rate is estimated with ionisation chambers that give a charge signal proportional to the number of ionising particles that traversed the sensitive gas volume.

Both of those types are also installed in M2. If even higher intensities need to be measured, for instance the rate of primary protons sent on production targets, secondary emission monitors are used. For more information about those, it is referred to [45].

2.3 The M2 beamline

Originally, as the abbreviation implies, the M2 beam has been implemented as a muon beamline. Therefore, it served the CERN muon program since the beginning, with all the adjoined experiments being located in the overground EHN2 experimental hall in the North Area. To get into its current shape it has been lastly, majorly modified in the 90's for the COMPASS experiment [17, 67, 68]. Nowadays, it can run in three different beam modes: it is possible to have high-intensity and high-energy hadron and muon beams ($I_{\max} \approx 10^8$, $p_{\max} = 280\,\mathrm{GeV}/c$), and low-intensity, low-energy electron beams ($I_{\max} \approx 10^4$, $p_{\max} = 50\,\mathrm{GeV}/c$) [45]. A schematic view including the bending angles of the various dipoles is shown in Fig. 2.18.

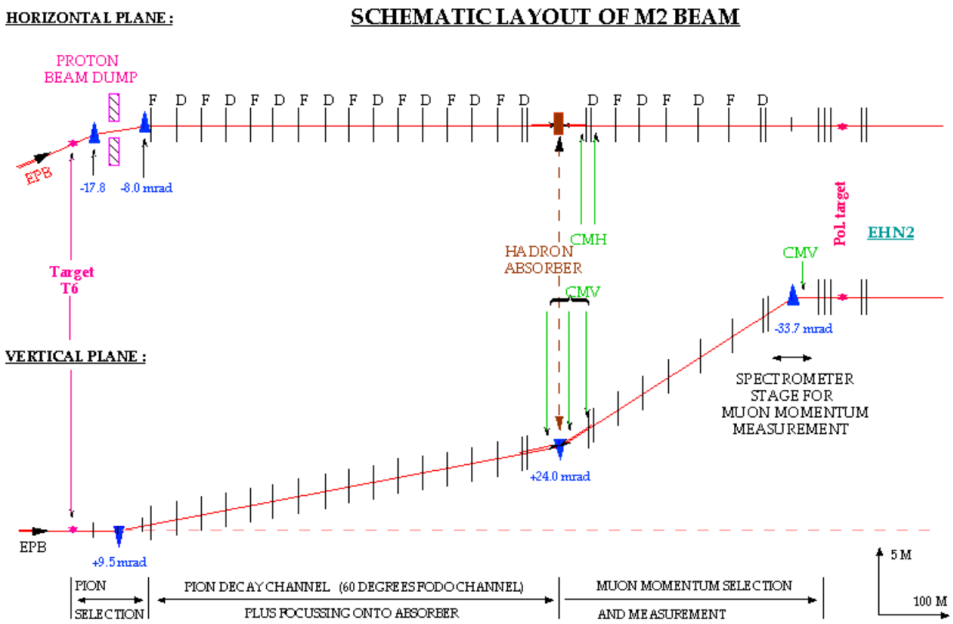

Figure 2.18: Schematic layout of the M2 beam [45]. From the underground target area, where the production target T6 is located, the beam gets transported to the overground hall EHN2. The height difference is about 17 m. The different bending sections and scraper magnets are highlighted.

Following Fig. 2.18, the beamline can be divided into two main sections: the hadron section and the muon section. The hadron section can be characterised by its large transverse and longitudinal acceptance to make maximal use of the hadron content produced in the T6 target, which is typically set to 500 mm beryllium to produce the maximum flux of hadrons. Following the acceptance defining part, there is a long FODO-section to efficiently transport the hadron beam. In this part of the beamline parts of the pion and kaon components in the beam will decay and produce muons, which will become the beam particle in the case it is operated in muon mode. The phase-advance per FODO-cell is tuned in this case to 60° for the mother particles in order to maximize transmission for the higher-momenta hadrons and lower momenta muons. The hadron section ends at the so-called absorber, which acts as the fourth bending section in the beamline ($s \approx 700$ m). It is depicted in Fig. 2.19.

Figure 2.19: Photo of the absorber section in M2. The black arrow indicates the beam direction. Each magnet is 3 m long.

The absorber consists of three C-shaped dipole magnets, which can be optionally filled with nine 1.1 m-long beryllium rods. Those are used to stop hadrons that have not decayed until this point. The upstream produced muons will traverse the absorber material and loose minimal amounts of energy. In case of hadron operation, those beryllium rods can be moved out such that the hadrons will not be absorbed and reach the end of the beamline. In the remaining part of the line, i.e. the muon section, one can mostly find magnetic collimators to clean the muon and hadron beam from muons that are going outside of the beamline apertures and traverse lots of material. This component is called beam halo. For having a momentum resolution of the hadron beam of the order of 1 %, an additional two-block collimator, depicted in Fig. 2.10(a) has been installed. This one will be closed to apertures of the order of 5 to 10 mm in hadron beam operation, but will be open when running in muon mode.

When operating in electron mode, the absorbers are also moved out, but an electron-target is moved in, which is a 5 mm lead plate. In the T6 target, one makes typically use of production

of π^0, decaying into two photons that produce electron-positron pairs. Typically, one makes use of 100 GeV/c electrons and transports them, besides other hadrons and muons of course, towards the electron-target. In this target, electrons will loose large amounts of energy due to bremsstrahlung while hadrons and muons loose much less of their energy. The remaining part of the beamline is set to a much lower momentum, typically 40 GeV/c, to make sure that only electrons and no hadrons are transmitted.

CHAPTER 3

Physics at AMBER

The AMBER experiment [18, 19] is going to investigate several properties of mesons, especially pions and kaons, like their masses, and quark and gluon distributions. Also, the production of antiprotons is going to be measured as important input for dark matter searches.

In the first, already approved phase of running time [19] three major investigations are planned with different particle beams delivered by the M2 beamline. In the second phase, which is currently being defined and still needs approval, the focus is on the exploration with strange mesons, i.e. kaons. Those different experiments are described in the following, in the order as they have been and are planned to be conducted. The setup is illustrated in Fig. 3.1. A schematic view can be seen in Fig. 3.2.

3.1 The Standard Model of Particle Physics

The Standard Model of Particle Physics is currently known to describe the interactions between the fundamental particles shown in Fig. 3.3 with highest precision by quantum field theoretical approaches. It contains three of the four fundamental forces, i.e. the electromagnetic, weak and strong forces mediated by the photon γ, the W- and Z-bosons, and the gluon g, respectively. The fourth force, gravitation, which is the weakest of all those forces, only important on large scales and therefore negligible in the quantum world, has not been incorporated into the Standard Model yet.

The force carriers are exchanged in interactions between the fundamental fermions shown on the left-hand side in Fig. 3.3. Those are sub-divided into quarks and leptons. Quarks are the building blocks of hadrons, meaning strongly interacting particles, and are currently assumed to be fundamental, i.e. point-like. Hadronic particles are divided into mesons like the pion and kaon, and baryons like protons and neutrons. The former have an integer spin, whereas the latter have a half-integer spin. Quarks can interact strongly, weakly and electromagnetically. The quarks in the first row in 3.3 have electric charges of $\frac{2}{3}e$ with the elementary charge e, while the ones in the second row have charges of $-\frac{1}{3}e$. The respective anti-quarks carry the opposite electric charge.

Figure 3.1: Panoramic picture of the AMBER experiment [69]. The beam is entering from the bottom left side.

The leptons illustrated in the two bottom rows in Fig. 3.3 cannot interact via the strong force in contrast to quarks. Electron, muon and tau carry electric charges of $-e$. Their antiparticles carry charges of e. The bottom row, i.e. the so-called neutrinos, are not electrically charged and only interact weakly. Together with the lightest baryons formed by the u- and d-quarks, i.e. protons and neutrons, electrons form stable atoms that are nowadays observed in the universe. Within the Standard Model it is assumed that all quarks and charged leptons acquire mass by coupling to the Higgs field. Neutrino masses cannot be generated through Yukawa coupling to the Higgs, but can be constructed through loops, which has several consequences that are beyond the scope of this thesis [5].

The fundamental fermions are divided into three families of quarks and leptons, where one family is formed by the two particles underneath each other, for example u and d, or μ and ν_μ. The key differences between the different quark families are the masses. For example, the c-quark is the heavier sister of the u-quark. The same holds for the lepton generations, meaning the τ is the heavier sister of μ being the heavier sister of the electron. Transitions inside and between families are possible through weak interactions, which is illustrated by the Feynman diagram of the muon decay 3.4.

The Standard Model is still the theory that predicts experimental results with highest precision. Nevertheless, it is known that it cannot be the full answer because it has several shortcomings. Several experiments have shown that neutrinos oscillate between families requiring massive neutrinos [70]. Studies yield masses $m_{\nu_e} < 1.1\,\mathrm{eV}/c^2$, $m_{\nu_\mu} < 190\,\mathrm{keV}/c^2$

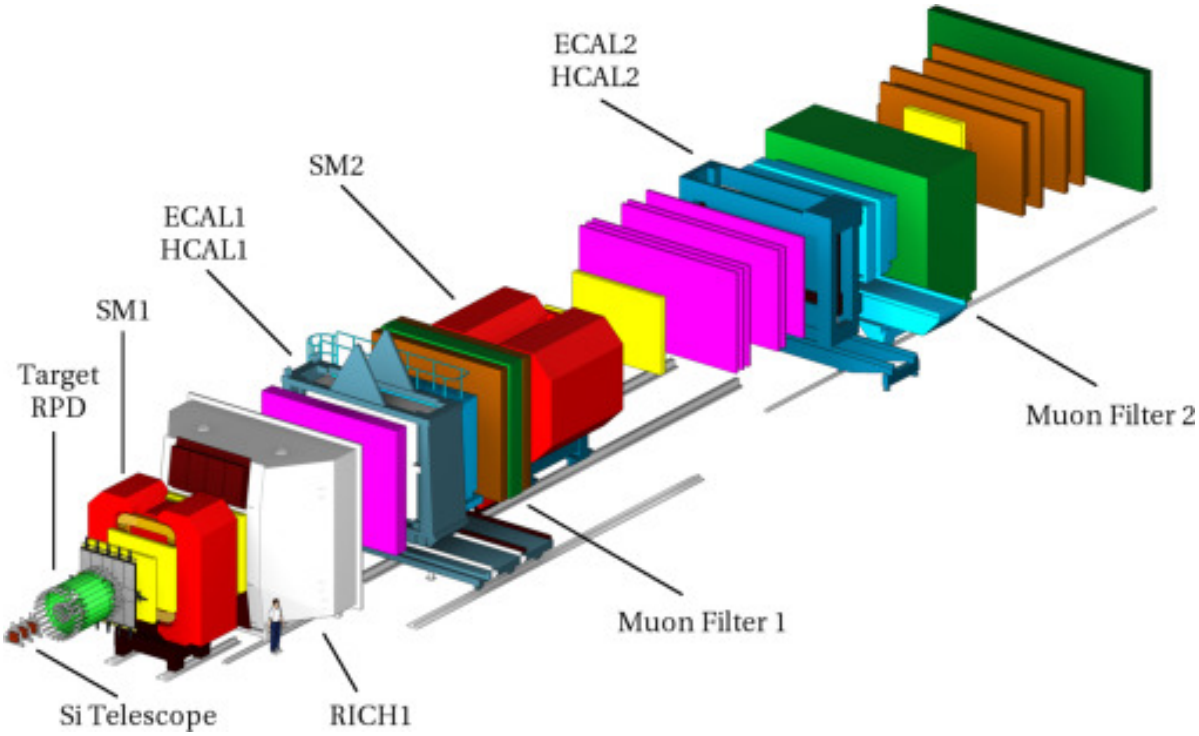

Figure 3.2: Artistic view of the of the setup of the COMPASS experiment [48]. AMBER is going to use a similar setup with upgrades of several detector systems. The beam enters from the bottom left.

and $m_{\nu_\tau} < 18.2\,\mathrm{MeV}/c^2$ [5]. Especially, vanishing neutrino masses cannot be excluded experimentally. Considering masses of the order of eV for ν_e and $(172.69 \pm 0.30)\,\mathrm{GeV}/c^2$ for the t-quark, it is surprising that this is a scale of more than eleven orders of magnitude. In addition, theories dealing with energy ranges beyond the electroweak scale predict heavy neutrinos besides the known three ones. This would mean the Standard Model would be an effective theory describing the low-energy processes [5].

Also, dark matter that is seen in astronomical observations [71] is not a part of the Standard Model. As it makes up about 25 % of the mass in the universe, there needs to be a bigger picture combining the known particles with dark matter. Also, there is no quantum field theory of gravitation. Those are only a few of the topics typically referred to as Beyond Standard Model Physics (BSM). Further aspects and the underlying theoretical concepts of the Standard Model are extensively discussed for instance in [72].

As mentioned in this section, the fundamental particles, i.e. quarks, leptons and the massive bosons W, Z and H, acquire their masses through (self-)coupling to the Higgs field. But the quark masses contribute on the percent-level to the masses of hadrons, only. The proton mass is $(938.272081 \pm 0.000006)\,\mathrm{MeV}/c^2$ [5], whereas the masses of the two u- and one d-quark are on the order of 1 to 5 MeV/c^2, meaning a total mass of about 10 MeV/c^2, which is just 1 % of the total proton mass. Clearly, there must be another process coupled to the strong interaction

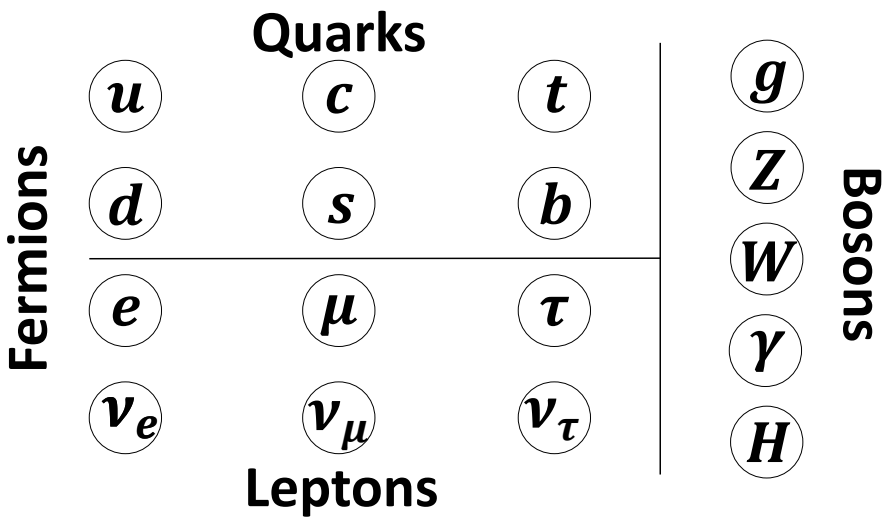

Figure 3.3: Fundamental particles in the Standard Model of Particle Physics. On the left side, there are the fermions (spin is $\frac{1}{2}$), i.e. leptons and quarks. On the right side, the gauge bosons (spin is 1), i.e. the mediators of the electromagnetic, weak and strong forces, and the Higgs boson (spin is 0) giving mass to the elementary particles are drawn.

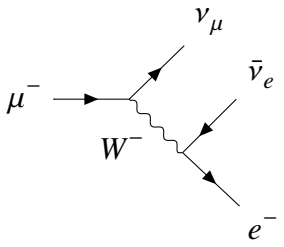

Figure 3.4: Feynman diagram showing the muon decaying into a muon-neutrino, an electron and an electron-anti-neutrino.

generating the overwhelming part of the mass of visible matter. In addition, looking at the proton, pion and kaon masses in the constituent quark model, it is striking that the three quarks in the proton have masses of the order of 300 MeV/c^2, while the pion as a whole has a mass of ca. 140 MeV/c^2 and the kaon of ca. 494 MeV/c^2. With several anticipated measurements, AMBER can help to understand the underlying processes that generate the hadron masses.

3.2 Fixed target experiments

As AMBER is a fixed target experiment, the concept of it and key differences to a collider experiment are pointed out. In particle physics, typically one aims for highest energies and

intensities. Pushing the energy limits might pave the way to new, unknown physics, whereas reaching highest intensities makes precision physics possible.

The energy that is available for producing new particles is determined by the center-of-mass energy. Assuming two symmetrically colliding beams with the same beam particle, i.e the four-vector can be written as $(E, \pm\vec{p}c)$ results in a center-of-mass energy $\sqrt{s} = 2E$. In a fixed target experiment with the target particle being at rest, i.e. $(E, \vec{p}c)$ for the beam and $(m_{\text{Target}}c^2, \vec{0})$ for the target, results in

$$\sqrt{s} = \sqrt{\left(m_{\text{Target}}^2 + m_{\text{Beam}}^2\right) c^4 + 2Em_{\text{Target}}c^2}\,. \tag{3.1}$$

Typically, the beam energies are much larger than the particle masses. Therefore, the energy available by colliding two beams is much higher compared to the energy available in a fixed target experiment. Assuming a beam energy of 100 GeV results in $\sqrt{s} = 200\,\text{GeV}$ for a collider experiment, whereas in a fixed target experiment with a proton at rest, one would only reach about 14 GeV. With those numbers, it is clear that finding new physics at high energies is only possible with collider experiments.

When focusing on precision experiments the situation becomes different. Because the target is typically much larger in the transverse plane than the beam in a fixed target configuration, the actual shape of the beam does not matter and one only needs to take the particle flux into account. Therefore, the instantaneous luminosity $\mathcal{L}_{\text{FT}}$, so the number of particles interacting with the target in a certain period of time per unit of cross section, can be written as

$$\mathcal{L}_{\text{FT}} = \phi_{\text{B}} \cdot \rho_{\text{T}} L_{\text{T}}\,, \tag{3.2}$$

[73], with the beam flux ϕ_{B}, the particle number density of the target ρ_{T} and the length of the target L_{T}. One can easily achieve values of the order of $10^{35}\,\text{cm}^{-2}\,\text{s}^{-1}$.

With colliding beams, the situation is different because the actual shapes of the beams matter. As one needs to have them overlapping in order to generate events, it is obvious that it is much harder to reach high luminosities in collider experiments. With extreme beam focusing techniques, it has been possible to achieve about $2 \times 10^{34}\,\text{cm}^{-2}\,\text{s}^{-1}$ in the LHC run 3 [74].

With the fixed target approach it is also possible to use unstable beam particles, like pions, kaons or muons. Also, interactions of various particles with heavy targets for instance for material studies can be investigated. Therefore, with polarised targets, spin properties can be studied, too.

When having the instantaneous luminosity, it is possible to calculate the total number of events N expected for a certain reaction by integrating it over the time of running and applying the interaction cross section σ, i.e.

$$N = \sigma \int \mathcal{L}\,\mathrm{d}t\,. \tag{3.3}$$

3.3 Antiproton production cross section measurement

Antimatter is still a fascinating field of science, even after over 90 years since Dirac's prediction of the existence of antiparticles [75]. The fascination finds its origin in the fact that according to conservation laws, like lepton- and baryon-number conservation (out of energy, it is only possible to create a particle simultaneously with its antiparticle), equal amounts of matter and antimatter would be created in the big bang. As mankind exists in a universe made of matter, there is the need for an asymmetry between matter and antimatter. There are huge efforts exploring properties of antimatter, like its excitation spectra [76] or behaviour in the earth's magnetic field [77]. Recently, it has been shown that antihydrogen atoms also fall towards the ground [78]. Also spectroscopy experiments with antihydrogen show good agreement with values obtained in precision spectroscopy of ordinary hydrogen [79].

With measurements performed with the **A**lpha **M**agnetic **S**pectrometer AMS [80] on the **I**nternational **S**pace **S**tation ISS showing the flux of antiprotons [81], the need for a better understanding of sources of antiproton production have come up. It is assumed that most of the antiprotons are produced in inelastic scattering processes of cosmic rays with nuclei in the interstellar medium [18]. To be able to find exotic sources, even like anti-stars or dark matter annihilation, the production cross sections in processes including ordinary matter need to be understood well. This is important because the antiproton flux needs to be known for dark matter searches in the astronomy.

The AMBER experiment is measuring the production of antiprotons in proton-proton (usage of a liquid hydrogen target) and proton-helium (usage of a liquid helium target) collisions, which are the dominant processes as those are the main particles and atoms one finds in the universe. Data-taking has already started in 2023 with proton-helium collisions (beam momenta from 60 to 250 GeV/c) and will be continued in 2024 with proton-proton and proton-deuteron collisions making use of the proton component available in the positive hadron beam in M2. The expected results obtained with AMBER are illustrated in Fig. 3.5.

Two important parts to conduct the measurement of antiproton production are the particle identification detectors. Those are shown in Fig. 3.6.

On the one side, there are two CEDAR detectors installed in the beamline ($s \approx 1.1$ km) identifying incoming beam particles and in this case triggering on protons. On the other side, one finds the so-called **R**ing **I**maging **Č**erenkov detectors identifying particles produced in the interactions of the beam particles with the AMBER target. Clearly, the successful identification of antiprotons is of great importance in the present case. So the combined performance of those two detectors is the key ingredient for a successful measurement.

3.4 Proton charge-radius measurement

With the proton being one of the building blocks of atoms and molecules, studying its properties is of general interest. It was discovered by Ernest Rutherford in 1919 [85] with first evidences that it is not a point-like particle found in 1933 by Otto Frisch and Otto Stern [86]. Clearly,

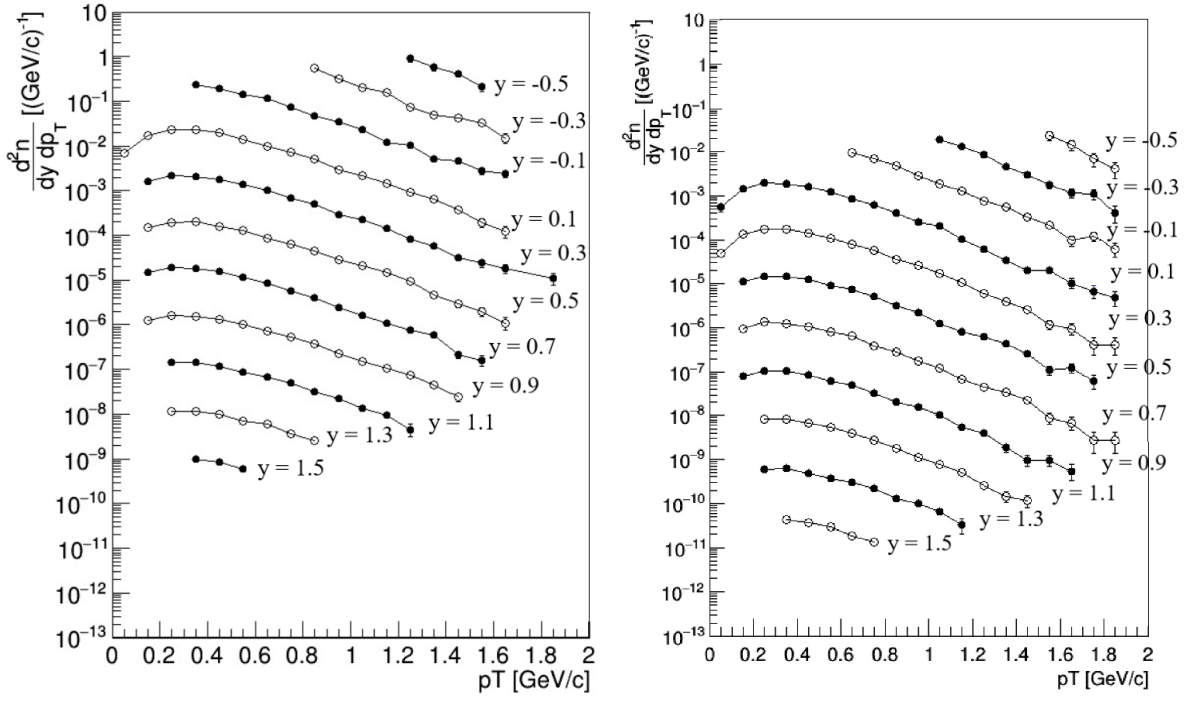

(a) (b)

Figure 3.5: Expected results for antiproton production from AMBER in proton-proton (Fig. 3.5(a)) and proton-helium collisions (Fig. 3.5(b)) with a beam momentum of 190 GeV/c. The transverse momentum spectra are shown for various pseudorapidities y. From [82]; modified.

because it is not a fundamental particle measuring its size is interesting by itself, especially as it makes up all the visible mass in the universe. The size of a proton has been determined via two different approaches: on the one hand, one can estimate the charge-radius by doing lepton-proton scattering, on the other hand, it is possible to measure the radius via laser spectroscopy of hydrogen.

A 2014-CODATA-value of (0.8751 ± 0.0061) fm [87] has been extracted from data collected in elastic electron-proton scattering experiments, which has been in good agreement with the long established value of about 0.88 fm. With spectroscopy of electronic hydrogen a 2014-CODATA-value of (0.8759 ± 0.0077) fm [87] has been established, which is in agreement with radii extracted from electron-proton scattering.

In 2010 the CREMA collaboration measured the Lamb-shift in muonic hydrogen[1] and obtained a result of (0.84184 ± 0.00067) fm [88]. In 2013, the small charge-radius has been confirmed in muonic hydrogen with (0.84087 ± 0.00039) fm [89].

As it has only been measured in electron-proton-scattering so far, but with ordinary and muonic hydrogen, it is naturally interesting to also explore the proton radius in muon-proton

[1] In muonic hydrogen the electron is replaced by a muon. Due to the higher mass of a muon, the center-of-mass of the two body system is closer to the proton. Therefore, the muon is more sensitive to the proton's finite size.

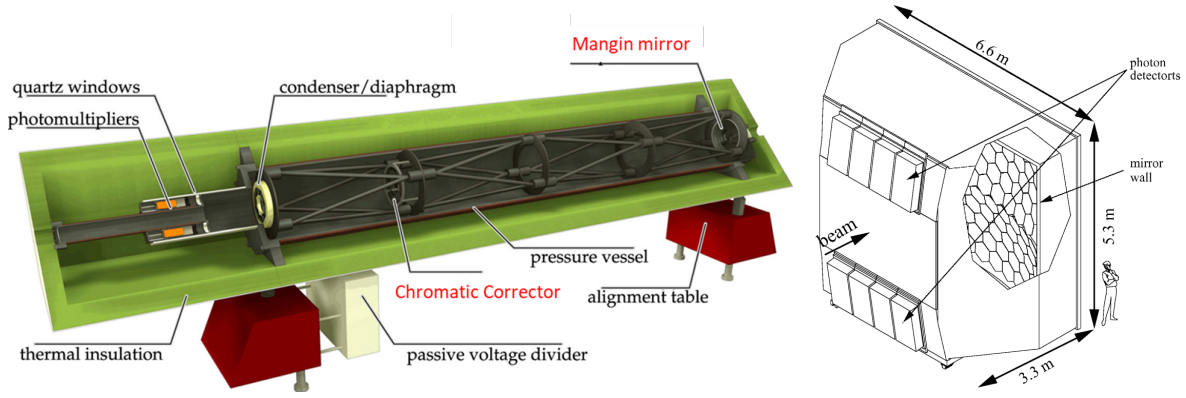

(a) (b)

Figure 3.6: Particle identification systems that have been in use by COMPASS and will be in use by AMBER. A 3D-model of a CEDAR-N is shown in Fig. 3.6(a) [83] that is installed in the beamline to identify the incoming beam particles. The COMPASS RICH-1 detector is illustrated in Fig. 3.6(b) [84] that is used to identify the particles produced in the interactions of the beam with the AMBER target.

scattering, which is depicted in the respective diagram 3.7.

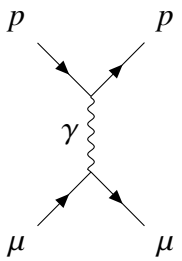

Figure 3.7: Feynman diagram showing the elastic scattering of a muon on a proton. This is the fundamental process to measure the proton charge-radius at AMBER.

It can help to shine a light on possible lepton-flavour asymmetries if it would come out differently to the electron-scattering case. From a systematics point-of-view, it is a more controllable experiment because the radiative corrections concerning the muon are less important than for the electron.

With M2 being able to deliver high-intensity, high-energy muon beams [90] it is an optimal place to conduct such an experiment. Therefore, AMBER is going to measure the proton charge-radius in elastic muon-proton scattering. It is possible to extract the size from the elastic cross section when measured for different four-momentum-transfers. By doing so, one is able to calculate the electric form factor G_{E}, which gives the proton rms charge-radius in the limit $Q^2 \to 0$, i.e.

$$\left\langle r_{\mathrm{p}}^2 \right\rangle = -6\hbar^2 \left. \frac{\mathrm{d}G_{\mathrm{E}}\left(Q^2\right)}{\mathrm{d}Q^2} \right|_{Q^2=0} . \tag{3.4}$$

As it is an elastic process, in principle it is enough to measure one quantity, for example the scattering angle by combining the incoming and outgoing muon tracks. To overconstrain the measurement, the recoil proton's energy will be measured in addition. This is done by employing an active-target Time Projection Chamber [91] filled with hydrogen gas under high pressure with a segmented read-out structure [92]. With overconstraining the full reaction it is easier to control possible background events and to select only elastic events.

3.5 Drell-Yan and charmonium production

For a long part of history, experiments focused on investigations of the structure of baryons, typically the proton, which is easier from an experimental point of view because it is stable. Therefore, one can probe it with point-like particles like muons and electrons. When it comes to mesons like the pion or kaon, both first experimentally observed in 1947 [93, 94], investigations need to be more advanced because those are unstable particles. As they are unstable they need to be probed by being the beam particle itself. As one of the fundamental questions when it comes to the emergence of hadron mass is the large mass difference between protons, pions and kaons, the two latter ones need to be explored in similar detail as it has been done for the proton. The parton distribution functions of the pion and kaon are important to interpret various collected data-sets in scattering processes from a theoretical perspective like hadronic jet production at the LHC [95]. Understanding the inner structure of the pion and kaon can help studying nonperturbative approaches in QCD [15, 16]. Also, comparing pion and kaon will help to understand the interplay between QCD and the Higgs mechanism for generating the hadron mass. Current knowledge of the PDFs comes from early pion-induced Drell-Yan [96, 97] measurements with around 700 events from kaon-induced Drell-Yan processes [98]. AMBER is planning to contribute in both regards by making use of the kaons and pions in the hadron beam in M2 at high energies of about 100 to 190 GeV.

The Drell-Yan process explains the production of dilepton pairs in hadron-hadron interactions.

The respective Feynman diagram 3.8 shows the annihilation of a quark-antiquark pair to produce a lepton-antilepton pair. At AMBER, one will focus on dimuon production. Having such a process at hand, it gets clear that Drell-Yan yields inside views to the valence and sea quark distributions in the pions and kaons. To be able to extract the sea quark distributions, it is necessary to explore both beam charges to have positive and negative pions and kaons available. The predicted uncertainties for the pion-induced Drell-Yan measurement with a carbon target are shown in Fig. 3.9. For the kaon-induced case they are depicted in Fig. 3.10.

Again, beam particle identification is of high importance because AMBER is specifically interested in pion- and kaon-induced Drell-Yan processes. Clearly, differentiating those is

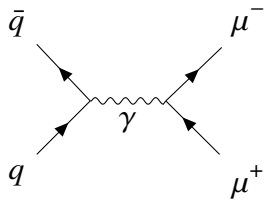

Figure 3.8: Quark-antiquark annihilation producing a muon-pair. This is the relevant Feynman diagram for the Drell-Yan process.

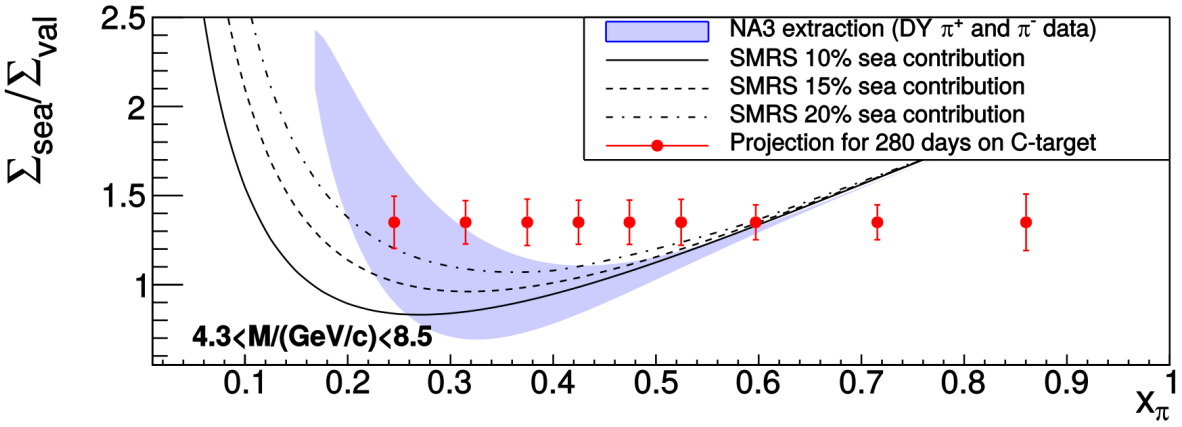

Figure 3.9: The uncertainties expected by AMBER for the pion-induced Drell-Yan campaign are shown together with the data extracted by NA3 and model predictions for various sea quark contributions [18]. The ratio of sea-to-valence quarks is plotted as a function of the momentum fraction carried by the active beam parton, i.e. Bjorken x [99].

extremely challenging when one is looking at kaons specifically. For pions the situation is much easier. In the negative beam, it is fair to assume that the beam consists only of pions. When doing such an assumption, a systematic error needs to be associated. But as the other particles only contribute to around 5 %, at maximum, this is negligible. It is different for the positive beam case as the proton fraction increases with increasing beam momentum. But because the difference in terms of Čerenkov angles of pions and protons is far above the resolution of the CEDARs, this is a manageable task. Again, the kaon contribution to the finally obtained pion sample is negligible and can be treated accordingly.

The situation changes drastically for both beam charges when doing kaon physics. As kaons only contribute to around 2 % in both cases, such approaches similarly as for the pions are not possible. Therefore, it is important to efficiently tag the kaons, which is challenging as their Čerenkov angle is close to the one of pions (cf. Fig. 2.16 showing the maximum beam divergence to differentiate pions and kaons, which is a function of beam momentum because the Čerenkov angles depend on the velocity and therefore ultimately on the momentum). As Drell-Yan is a rare process, one needs to collect high statistics to be able to analyse the obtained

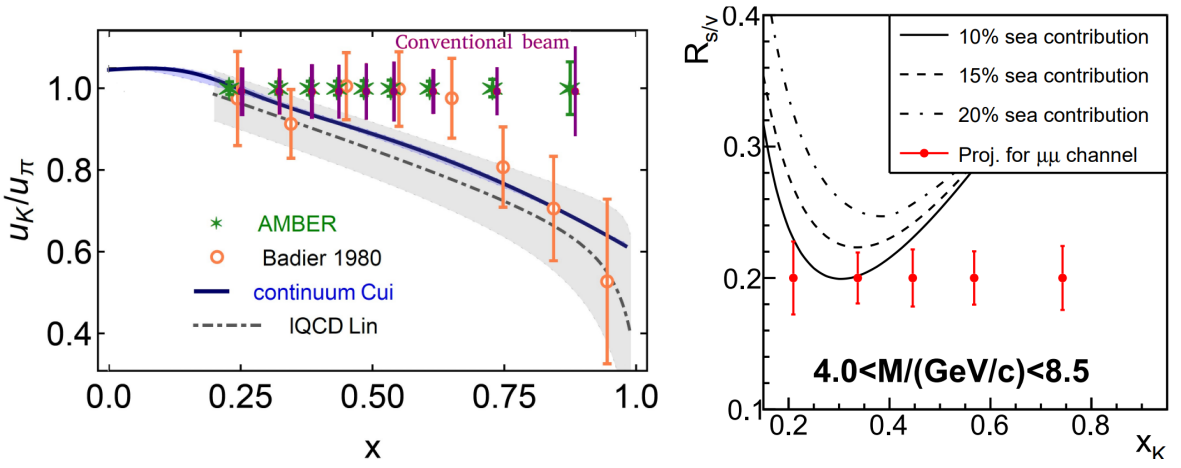

(a) (b)

Figure 3.10: Expected uncertainties for the kaon-induced Drell-Yan experiment at AMBER [100]. In Fig. 3.10(a) the ratio of the up-quark contents in the kaon and pion is plotted as a function of the fractional momentum of the particle carried by the quark as it has been obtained from another measurement and model predictions. Fig. 3.10(b) shows the ratio of sea-to-valence quarks in the kaon as a function of the momentum fraction carried by the active beam parton for different sea quark contributions.

data, which underlines the need for efficient beam particle identification once more.

To operate at even higher intensity, the target will be enclosed by a bunker, similarly as it has been done for the COMPASS experiment [101]. It is illustrated in Fig. 3.11.

With such a shielding, which acts as an absorber for hadronic particles, it will be possible to increase the prompt intensity to 10^9 particles per spill in EHN2 and to an accumulated number of particles of 3.07×10^{14} in one year of running [102]. These increases clearly help collecting larger data-sets featuring the described low-probability Drell-Yan reaction.

Drell-Yan is not the only process that is happening in the interactions of the hadron beam with the target. Especially in lower dilepton-mass ranges one will observe the dominant production of J/Ψ [103, 104]. The J/Ψ is a bound state of a c- and $\bar{c}$-quark. It is another approach towards the PDFs of pions and kaons. At the energies available at AMBER, $q\bar{q}$-annihilation gives a reasonable contribution to the J/Ψ-production. Together with the knowledge gained in Drell-Yan about the valence quark contents, it is finally possible to also extract the gluon distribution functions as gluon-gluon fusion is the other dominant process producing J/Ψ [18].

For the AMBER experiment this is especially interesting because the data can be collected in parallel with the anticipated Drell-Yan campaign.

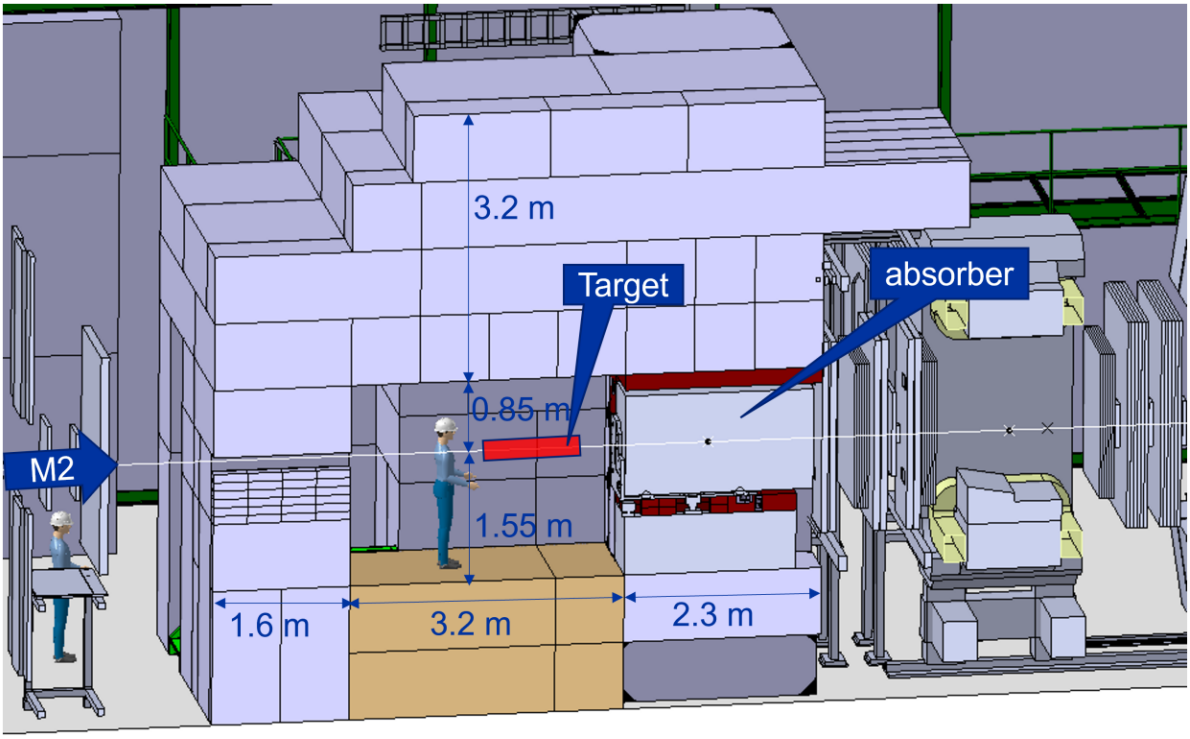

Figure 3.11: Model of the proposed shielding for the AMBER Drell-Yan data-taking [102]. Especially the absorber directly downstream of the target is important to be allowed to sent high beam rates up to 200 MHz to EHN2.

3.6 Kaon spectroscopy

Studying bound systems like the pion or kaon can yield information on the force holding the constituents together, which is the strong interaction in the case of mesons (and baryons, too). With it being one of the four fundamental forces it is important to explore its features. Due to confinement, it is not possible to investigate properties of the quarks alone that form the bound states, but only through conclusions drawn from measurements of those systems. These precise measurements of the hadronic excitation spectra are important input for theoretical models yielding predictions of other features.

The hadronic states are typically described by the underlying quantum numbers specifying the total angular momentum J determined by the spin-state S and the orbital angular momentum L, the parity P and the isospin I[2]. Because kaons are two-quark systems in the constituent quark model, which have $s = \frac{1}{2}$, the total spin of the bound system can have values of zero or one. Therefore, the lowest state of the system is $J = 0$ with no radial excitation. Excited states meaning higher mass states are therefore quantified by $L > 0$ and/or $S = 1$.

With recent developments in lattice QCD, the pion and kaon as a whole can be treated and

[2] Often, the charge conjugation C is given, too.

various characteristics can be calculated. Especially interesting with the theoretical approach are predictions of exotic states, which are states that have quantum numbers forbidden in the simple constituent quark model. With such methods at hand, one has a powerful tool to test fundamental predictions by QCD by comparing the calculated excitation spectra with measurements. The COMPASS experiment for instance measured one of those exotic states of the pion, which is the $\pi_1(1600)$ [105].

Comparing the predictions and measurements of spectra of pions and kaons can help to understand the large mass difference between those two by just exchanging the d- with the s-quark. Therefore, one needs to investigate the different kaon states, too, as it has been done in the past for the pion, which is described in [106].

The currently known spectra of mesons with strangeness are shown in Fig. 3.12.

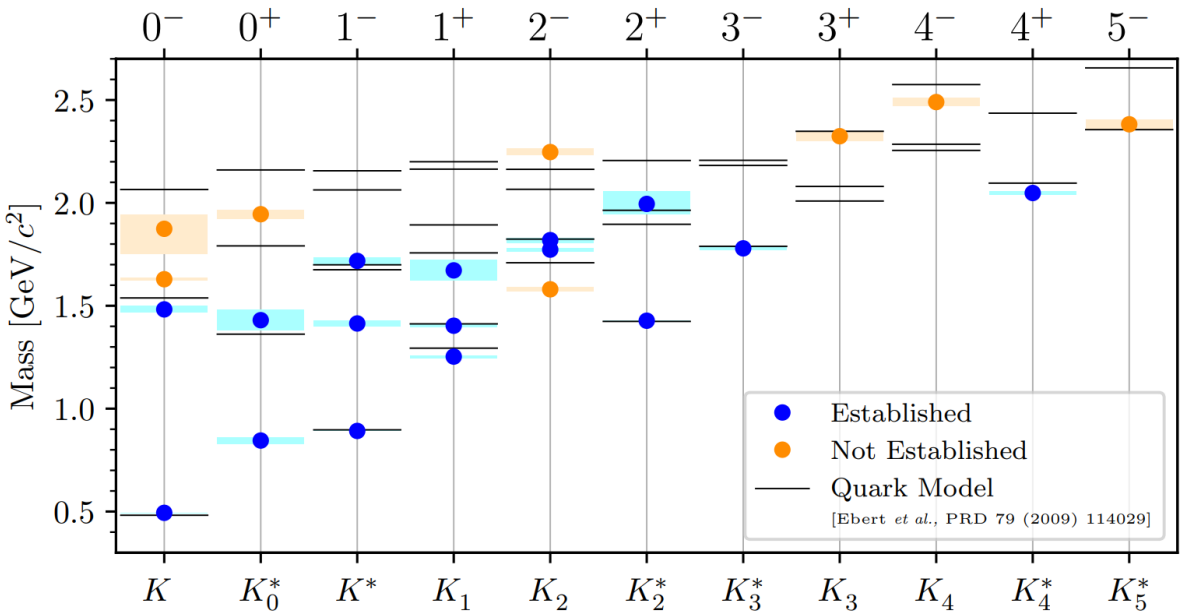

Figure 3.12: Strange meson spectra [59]. Blue data points represent experimentally confirmed states with their uncertainty given by the rectangles around. Orange points show states that are not yet established. The predictions by the quark model are shown by the black lines.

Clearly, besides the already experimentally confirmed excited states, there are still more to explore, where the currently available data is not enough to confirm them. Of course, seeing the black lines, there are even more states that are predicted by theoretical calculations that have not yet been observed in experiments. Here, AMBER comes into play. The COMPASS collaboration measured excitation spectra of light mesons without strangeness via the diffractive reaction $\pi^- + p \rightarrow \pi^-\pi^+\pi^- + p$. Similarly, AMBER is aiming at exploring the strange meson spectra by making use of the kaon component in the M2 hadron beam that interacts with a liquid hydrogen target, which is illustrated in the Feynman diagram 3.13.

As already discussed, particle identification is important again here. It is necessary to clearly identify the incoming beam kaon to keep the pollution by pions as low as possible. In the

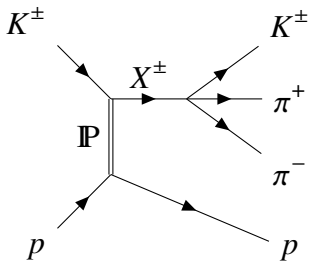

Figure 3.13: Feynman diagram showing the diffractive production of the $K^{\pm}\pi^{+}\pi^{-}$ final-state. The incoming beam kaon is excited into the state $X^{\pm}$ that decays into the studied final-state. Simultaneously, the target proton stays intact and one observes the recoil.

present process, the target proton remains intact and the recoil proton needs to be confirmed by the recoil proton detector (cf. [48]), which is placed around the target. The beam kaon gets diffractively excited into the state $X^{\pm}$ that decays into an outgoing kaon and a pion-pair. Those need to be identified by the RICH-1 detector (cf. Fig. 3.6(b)) in the setup. Finally, by applying so-called Partial-Wave-Analyses (PWA) (cf. [59, 107]) one can extract the quantum numbers of the different resonances X filling up the missing states in Fig. 3.12.

As high-precision is needed for such an experiment, an absorber (cf. Fig. 3.11) like the one for Drell-Yan cannot be installed in those data-taking periods. Therefore, the beam intensity needs to be limited. From a beam identification point of view this is a preferable option because one can ensure lower divergence at the CEDAR location by appropriate collimation upstream removing effectively particles that cannot be identified and would only contribute to an unnecessary increase of the total intensity.

CHAPTER 4

Software

Many simulations for comparison to data are presented in this thesis and therefore accurate modelling and simulations are highly important for the conclusions drawn. Conducting those studies is only possible with appropriate software developed for those purposes. In the present case those are beam optics calculations and optimisations, particle tracking along the beamline and beam-matter interaction when beam, e.g. secondary particle production, or even background particles hit anything along the line. Several softwares have been used in combination to conduct the studies, which will be presented and discussed shortly.

4.1 MAD-X

Methodical **A**ccelerator **D**esign - **X** [108] is a code for optics calculations for particle accelerators and beamlines. It is mainly written in C, C++ and Fortran and interprets text-based input. With various routines it is possible to calculate optical parameters and transfer matrices (cf. section 2.2.2) in circular and linear machines. With several fitting algorithms the user can achieve certain beam parameters like size or divergence. Apart from optical calculations, tracking routines are implemented, too. The tracking gives an insight into particle coordinates at any location in the lattice. It will also cut the beam at given apertures in case the particles are outside of those. Particle-matter interactions are not taken into account. It outputs any information in its own so-called **T**able **F**ile **S**ystem, TFS, but it has also an internal plotting routine.

4.2 Geant4

The **Ge**ometry **an**d **T**racking 4 software package [109–111] enables the user to simulate the interaction of various particles with matter with the help of Monte Carlo techniques. Geant4 is written in a C++ class structure that makes it possible to use it through other software codes. All necessary components are provided in the C++ class library but the users need to write

their own program considering geometry construction using constructive solid geometry (CSG) principles and primitives, constructing the correct physics processes and beam particles[1], and most importantly handling the sensitivity. To make the user's life easier some primitive shapes like cubes, spheres, tubes or extrusions are predefined in Geant4. Those can be combined using boolean operations like intersections or subtractions. Special care needs to be taken to not generate overlapping geometry. In such a case it is ambiguous, in which material the particle is at that specific time. Therefore, one typically works with safety margins for proper geometry navigation in Geant4. An example of an event simulated in Geant4 is shown in Fig. 4.1.

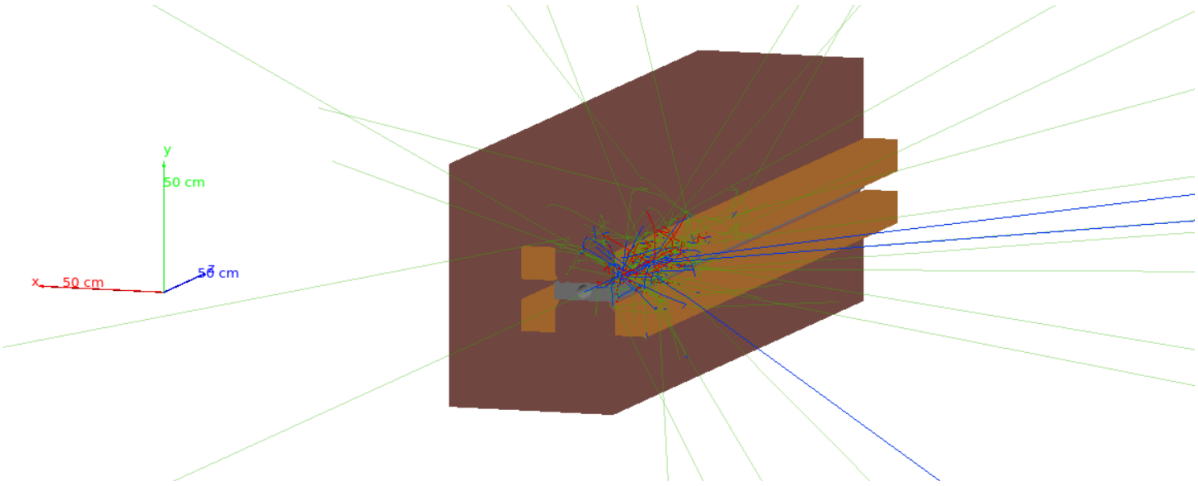

Figure 4.1: A 100 GeV proton impinging on a C-shaped dipole magnet shown in Geant4's internal visualiser. Lines of positive particles are shown in blue, neutral particles are presented in green, and negatively charged particles in red.

It is also possible to import geometry through Geant4's so-called **G**eometry **D**escripting **M**arkup **L**anguage GDML [112] based on XML (E**x**tensible **M**arkup **L**anguage). Besides that one can make use of predefined physics lists that activate the physics models needed for the simulation. Of course, the user can define the necessary models and interactions in case one of the predefined ones is not suitable for the case at hand. It is heavily used in the high-energy physics community, but also finds its application in simulations for instance for medical purposes. The results obtained from a simulation can be written out in various ways. Typically, it is written to a ROOT file [113, 114], either directly in histograms or as raw-data as ROOT's internal Ntuples, or to an ASCII file.

[1] Beam in this context is to be considered in a broader manner. It refers to particles that interact with the geometry and generate events.

4.3 BDSIM

Beam **D**elivery **SIM**ulation BDSIM [115] is a software package that makes use of the Geant4-package and represents a nice and easy interface to it. It comes with many predefined geometries typically used in accelerators, like magnets, collimators or cavities. It simplifies the usage of fields and field maps heavily. The reason for that is the coordinate transformation between a global reference frame and the local coordinate system following the beamline. As this is done automatically throughout the code, there is no need to provide electromagnetic fields in a global manner, but it is enough to define it in the coordinate system of that element generating the field. This is in contrast to Geant4, in which one needs to deal with one Cartesian coordinate system and to ensure the proper transformations. Besides Geant4, it makes use of the CLHEP library [116] and ROOT for the output of data. Combining the functionalities of all these complex software codes, makes BDSIM a tool that is capable of precise tracking of particles over long distances, which is required in accelerators like the LHC, with simulation of interactions of particles with the surrounding material [117]. That is why it is extensively used for simulating and estimating beam distributions and backgrounds not only for physics experiments, but again for medical machines, too [118]. It has also been the basis for most of the presented simulations and studies.

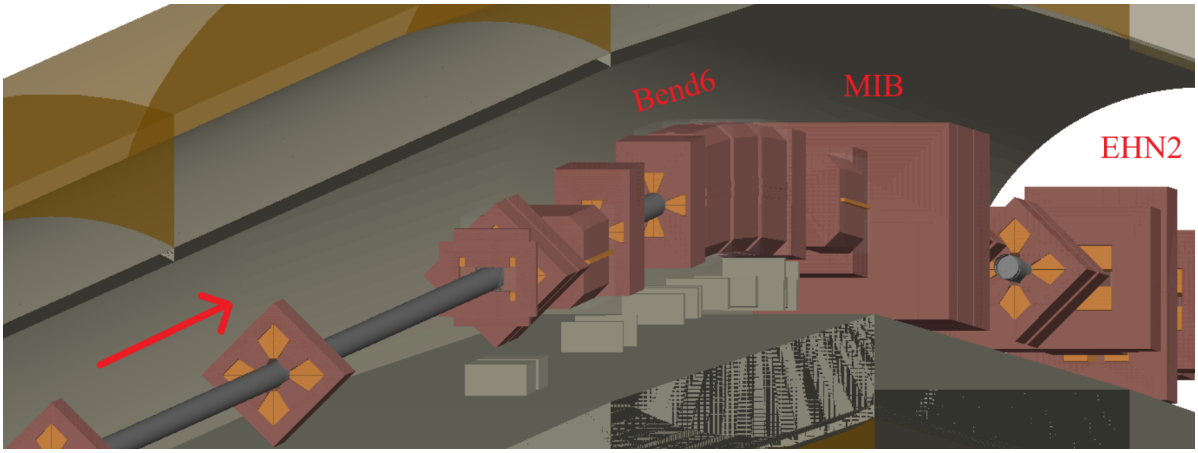

Figure 4.2: Parts of the M2 beamline model shown in the Geant4 visualiser after construction in BDSIM. The direction of the beam is indicated by the arrow. It is the last part before the beam hits the AMBER target.

The form of the output makes it especially powerful. The output is structured such that all information is grouped per event, where one event typically starts with one input particle. This means that particular histories can be investigated because the data is already structured to isolate histories. The exact output data can be chosen and the most common form is an invisible plane, a *sampler*, placed after an element that records the kinematic variables and track IDs of particles in an event at that specific location. An example of a short, fictional beamline including samplers showing the particle hits is shown in Fig. 4.3.

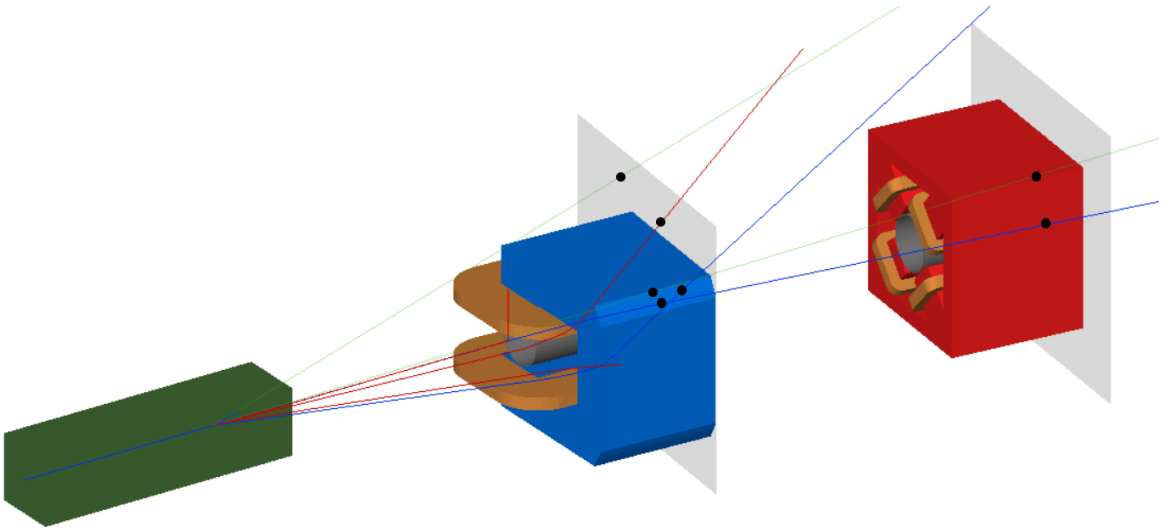

Figure 4.3: The grey, transparent volumes represent *samplers* in BDSIM. At those locations variables like position, energy and particle ID are recorded and written to the output. The hits are indicated by the black dots. The magnets are the available defaults for straight bends and quadrupoles. Lines of positive particles are shown in blue, neutral particles in green and negatively charged particles in red.

Other optional data are *trajectories*, which are a full history of each step of a particle with the ability to filter and select, which particles are stored to limit the data quantity. This is of special interest when it comes to background estimations. The package also comes with an internal analysis tool called **R**OOT **E**vent **BDSIM** REBDSIM. This allows to histogram the recorded data on a per-event basis making rate estimations per initial beam particle possible. Only with a per-event structure the variance and therefore uncertainties can be properly estimated when dealing with aggregate quantities such as energy deposition or fluxes.

4.4 Automatic model building

Preparing a full 3D model of a whole beamline is a long and error-prone process. Therefore, it is convenient to build such a model in an automatic manner based on an optical description of the line as it is done in MAD-X. This is especially important considering that a beamline consists typically of tens of magnets. Of course, each single one can be modelled, but it would be time-consuming to prepare the corresponding BDSIM input syntax for the geometry of every single component. On top of the geometry modelling, one also needs an accurate description of the magnetic fields along the beamline. This is especially important as typically, the physical setup does not change, but often different momenta or particle types are required. To achieve this, different fields are needed. Given these constraints, it is straightforward and optimal to automate the building of the BDSIM input syntax and associated files including geometry and fields. This also ensures reproducibility and eliminates the highly likely human error in such a

large model building. In [119] a tool that achieves this goal is described. The process will be discussed shortly.

With BDSIM, there are a few more software codes written in Python that have been published. Two of them are called *pymadx* and *pybdsim*. pymadx makes the reading of the optical description of a given beamline or ring from MAD-X easy. It allows to get information about the various elements placed in the machine, like name, type (for example quadrupole or collimator), bending angle, or focusing strength, and many more. pybdsim offers the conversion from a MAD-X optical description to BDSIM's GMAD syntax. By default, BDSIM would provide generic geometry with that input. As it is explained in [119], additional codes have been developed for the creation of geometric models of North Area devices like collimators or magnets and their fields. With *pyg4ometry* [120], a database of all those geometries has been setup. It is a Python-based package, with which one can construct a Geant4-geometry and export it to GDML and Fluka [121, 122]. Besides this, another database has been setup containing field maps of various magnets deployed in the North Area. Those field maps have been calculated mostly in Opera-2D [123] and have been provided by the CERN TE-MSC group. For each magnet various field maps have been created at different excitation currents. An example is given Fig. 4.4. The field maps make use of given symmetries. These are also handed over to BDSIM, which offers possible reflections to generate the full field map.

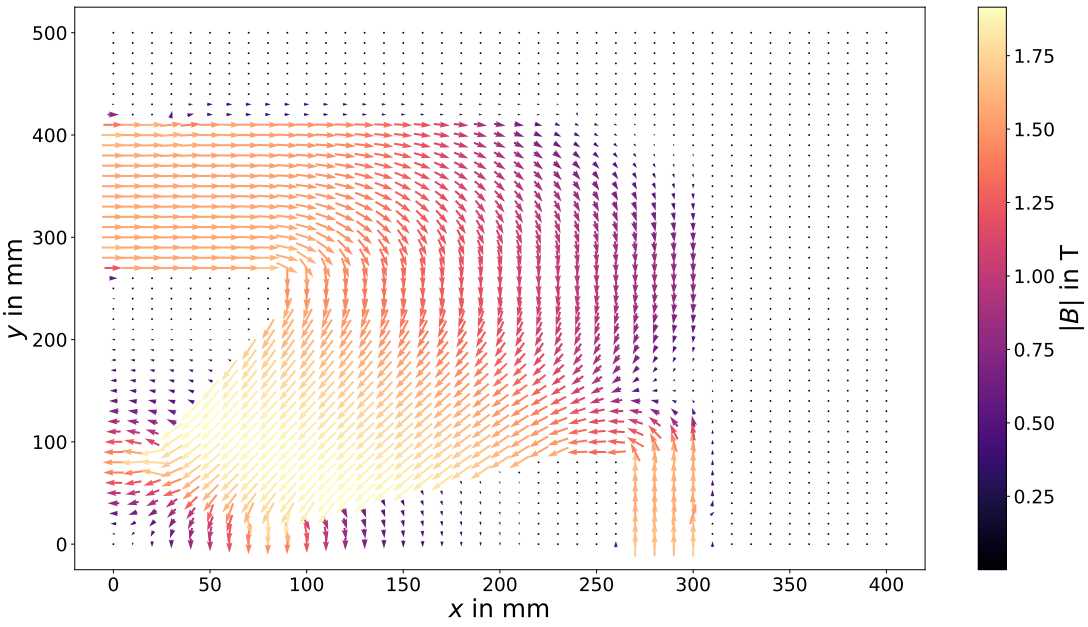

Figure 4.4: Magnetic field map of a QWL (cf. Fig.2.8) for a current of 500 A. The arrows indicate the direction of the magnetic field, whereas the colour scale shows the magnetic flux density at the given locations x and y. The nominal beam goes through (0, 0). On axis, there is no magnetic field and it grows linearly with the distance to the centre. The field map just contains a quarter of the full magnet as it is possible to construct the full map in BDSIM from symmetry considerations.

To be able to use the right field map for the beamline configuration of interest, so-called I to $B^{(\prime)}L$ curves are included, too. They have been measured and parameterised for all the different beamline magnets in the North Area. They allow to calculate the current needed to achieve the bending and focusing strengths for the optical description of the line. By knowing the current, the closest field map can be found. This field map will finally be scaled to the required integrated field for dipoles or integrated gradient for quadrupoles. An example of such a curve is depicted in Fig. 4.5.

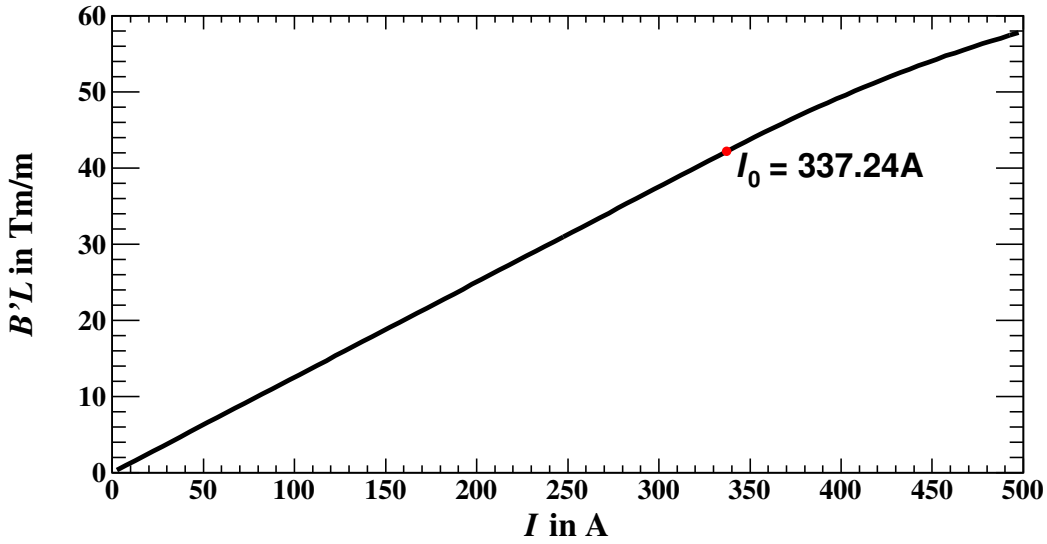

Figure 4.5: $B'L - I$-curve of a QWL-magnet (cf. Fig. 2.8). It shows the available integrated gradient of the magnet as a function of the excitation current. To collect the data the magnetic field has been measured at the pole tip. It is assumed that the gradient is constant over the magnet aperture. To describe this curve the parameterisation (4.1) is used.

The formula

$$B^{(\prime)}L(I) = \begin{cases} aI, & I \leq I_0 \\ cI^2 + \left(a + b - 2cI_0\right) I + I_0 \left(cI_0 - b\right), & I > I_0 \end{cases}, \tag{4.1}$$

has been used to describe the $B^{(\prime)}L - I$-curves, where the parameters a, b, c and I_0 are extracted from fits to measured data. Finally, by looping over all the elements in the optical description extracted from MAD-X, generating the GDML-model, and in case it is a magnet, attaching the field map, the full beamline can be constructed in an automatic fashion. The general workflow is summarized in Fig. 4.6. Within BDSIM it will be ensured that all the different parts in the beamline will be placed correctly because the necessary coordinate transformations between the reference frame following the beam, which is used in the optical description, and the global Cartesian frame in Geant4, are done automatically.

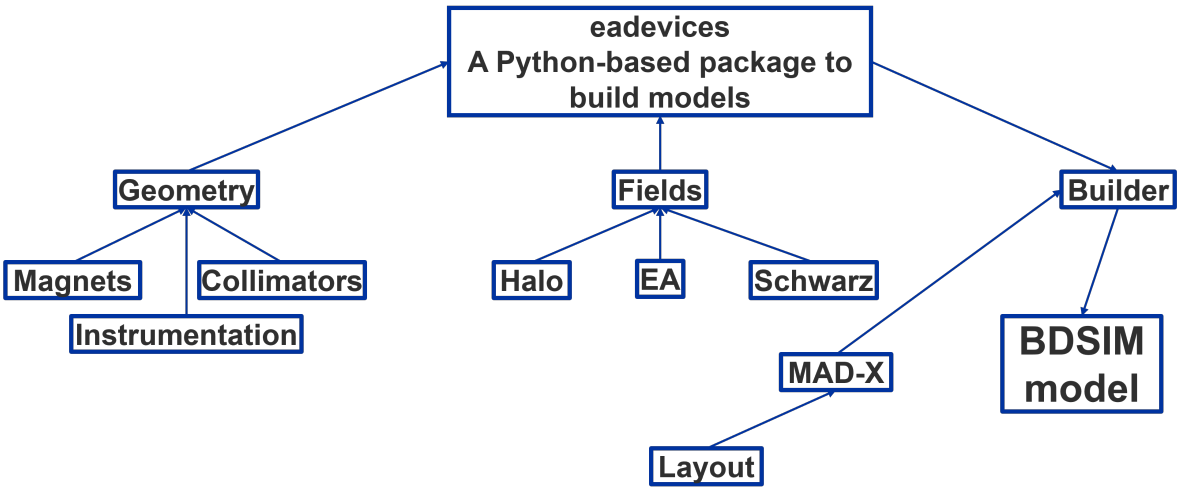

Figure 4.6: Flow chart explaining the combination of the single building blocks to construct a full beamline model [119]. The builder receives the needed information about the beamline from the optical description in MAD-X that is based on the layout database available at CERN. The information is used to construct the necessary geometries and to calculate the needed field maps. The builder puts those different components together to obtain the final BDSIM model.

CHAPTER 5

RF separation

A secondary beam consists of different particle species with various momenta. As the pion is the lightest hadronic particle the vast majority of the beam is made of pions (and protons for positive charge). Therefore, if one calls a beam a hadron beam it is simply a pion beam (or both, pion and proton for positive beam charge).

As the AMBER collaboration is interested in kaon beams in the phase 2 study it is necessary to provide a technique to filter out the unwanted pions.

In a secondary beamline one filters out a certain momentum rather far upstream close to the production target (the way how it is done is explained in section 2.2.2). After this momentum selection all beam particles have the same momentum[1] p. But having the same momentum means that different particle species have different velocities as they differ in their masses because of $p = mv$ with m being the relativistic particle mass and v its velocity. This difference in velocity can be used to filter out a certain particle type one is interested in with the help of the so-called **R**adio-**F**requency RF separation technique, which has already a long standing history at CERN [124] and SLAC [125]. The theoretical description of this method is described in and taken from [124, 125]. Large parts of this chapter have been published in [126, 127].

5.1 Basic idea

The principle of RF separation is based on velocity differences for different particle types at the same momentum. This deviation in velocity manifests as a variation in the time the particles of type 1 and 2 need to take to fly from one point in space to another. In the RF separation case these two points in space are the radio-frequency cavities placed at certain positions along the beamline that deflect the beam transversely, which is illustrated in Fig. 5.1.

With assigning a certain frequency to these cavities, i.e. the radio-frequency itself, one can translate this time difference into a phase difference when travelling from the first to the second cavity. This phase difference is given in Eq. (5.1) with the travel time difference Δt, the distance

[1] There is a certain momentum spread coming from the finite size of the momentum defining collimator slit.

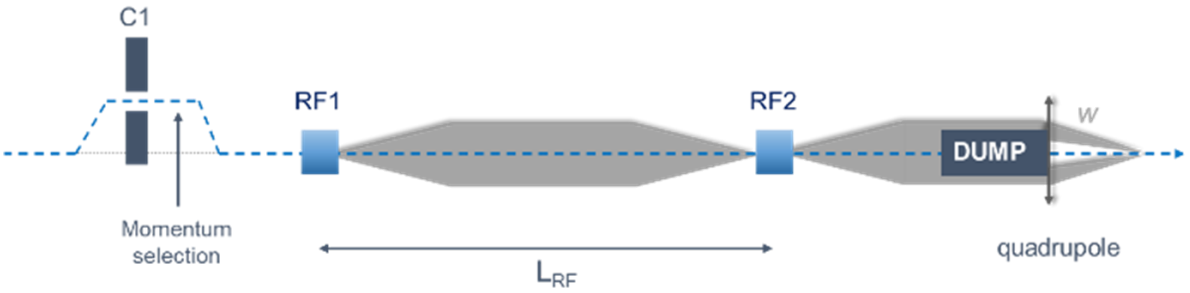

Figure 5.1: Schematic picture showing the basic concept of RF separation [126, 127]. The beam momentum is defined upstream. Afterwards, the beam passes through the separator consisting of the two RF deflectors. The separated beam will be cleaned by a beam dump that will be hit by the unwanted particles. The wanted ones are guided towards the experiment.

between the two cavities L and the velocities $\beta_i c$ of the two species. It is purely dependent on the frequency f and the beam momentum p.

$$\Delta\varphi = 2\pi f \Delta t = \frac{2\pi f L}{c}\left(\frac{1}{\beta_2} - \frac{1}{\beta_1}\right) = \frac{2\pi f L}{c} \cdot \frac{E_2 - E_1}{pc} \approx \frac{\pi f L}{c} \cdot \frac{(m_2 c)^2 - (m_1 c)^2}{p^2}. \tag{5.1}$$

In the last step in (5.1) the relativistic approximation $E \approx pc$ for $p \gg mc$ is applied with the particle mass m. At these energies the beam consists mainly of pions, (anti-)protons and kaons. The phase shifts between those particles are shown in Fig. 5.2.

The phase shift in Eq. (5.1) can now be used to define the beam momentum p for a given frequency f, meaning that one can observe a phase shift of $\Delta\varphi$ between the particles with masses m_1 and m_2. Therefore, it is necessary to solve (5.1) for the beam momentum. The result is given in Eq. (5.2).

$$p = \sqrt{\frac{(m_2 c)^2 - (m_1 c)^2}{\frac{m_1^2 + m_2^2}{m_2^2 - m_1^2} + \frac{\Delta\varphi c}{\pi f L} \cdot \sqrt{1 + \left(\frac{\Delta\varphi c}{2\pi f L}\right)^2 \frac{m_1^2 m_2^2}{\left(m_2^2 - m_1^2\right)^2}}}} \approx \sqrt{\frac{\pi f L}{\Delta\varphi c}\left((m_2 c)^2 - (m_1 c)^2\right)}. \tag{5.2}$$

In the relativistic limit one can see that $p \propto \sqrt{fL}$ meaning that the beam momentum increases only slowly with higher radio-frequencies and distances between the cavities. Fig. 5.3 shows the dependence of the momentum on the frequency for a distance of 830 m between the two cavities.

This Eq. (5.2) can now be used to define the beam momenta for the RF separated beams by requiring a certain phase difference between two particle types. For kaons being the particles

of interest one needs to filter out pions and (anti)protons (depending on the beam charge). The way how it is done is described in detail later in section 5.3. Shortly, it is possible to not deflect the unwanted particles at all, while the species of interest receives a net deflection. In the case of the kaon beam, this can be achieved by requiring $\Delta\varphi_{\bar{p}}^{\pi^-} = \Delta\varphi_{p}^{\pi^+} = 2\pi$ meaning that the (anti)protons reach the second cavity at the RF wave following the arrival of the pions. The kaons would arrive at the second cavity in between the aforementioned types. One obtains a beam momentum of ca. 68.13 GeV/c.

For the $\bar{p}$-beam one could use the same approach forcing $\Delta\varphi_{K^-}^{\pi^-} = 2\pi$. Considering Fig. 5.2 one can see that frequencies larger than 10 GHz would be needed to separate pions and kaons by 2π for momenta as small as 60 GeV/c. Because lowering the energy is not an option and cavities with frequencies of several tenths of GHz do not exist, one needs to follow a different approach. In that case it is needed to require $\Delta\varphi_{\bar{p}}^{\pi^-} = \pi$ to efficiently filter out π^- because they are by far the majority species in the negatively charged hadron beam. The drawback is that one needs to accept that K^- receive a net deflection, too, which is comparably small as one can aim for maximum deflection for the $\bar{p}$ part. The momentum of the RF separated antiproton beam is ca. 96.35 GeV/c.

5.2 Application to M2

The particles of main interest during phase 2 of the AMBER experiment requiring a re-design of the existing M2 beamline, are kaons. This brings up several difficulties compared to the use cases so far when the particles of interest have been mainly pions. Having a look at the production rates of kaons compared to pions, which is described in section 2.2.1, they are approximately an order of magnitude smaller over the full range of secondary beam momenta meaning that there is no preferable momentum, where the production rate of kaons could compete with that of pions. The reason lies of course in the mass of the particles and the composition. Because the pion is the lightest of all hadrons the kinematic phase space for the production of pions is the largest. In addition, as the kaons have a strange quark as one of their two valence quarks there need to be processes taking care of the flavour change making them less likely to happen.

In addition to that kaons have a short decay length compared to pions. The average lifetime of pions is (26.033 ± 0.005) ns and of kaons it is (12.380 ± 0.020) ns [5]. Due to the relativistic time dilation and the smaller mass of pions the average decay length is much different. Here, one has 55.92 m c GeV^{-1} for pions compared to 7.52 m c GeV^{-1} for kaons[2]. Comparing these values, one sees that kaons have a decay length that is smaller by a factor of 7.5.

Taking the production rates discussed in section 2.2.1 and shown in Fig. 2.3(a) and 2.3(b) one can calculate for both beam charges the average particle rates that one could expect at the location of the AMBER target, which is ca. 1.13 km downstream of the production target

[2] The values can be calculated from the average decay length at a given momentum p via time dilation: $l_{\text{Secay}} = \beta\gamma c\tau$ with $p = \beta\gamma mc$.

T6. For this one needs the Atherton parameterisation (2.1) and (2.2), the average number of particles that have decayed and the longitudinal and transverse acceptance of the beamline. The longitudinal acceptance of the RF separated M2 beam is $\frac{\Delta p}{p} = 1\,\%$ and transverse acceptance is 5.6π µsr. After a given distance one can calculate the mean number of particles that has survived with

$$N\left(l\right) = N_0 \exp\left(-\frac{l}{l_{\text{Decay}}}\right). \tag{5.3}$$

Finally, this results in

$$N\left(p,\, l\right) = \frac{\mathrm{d}^2 N}{\mathrm{d}p\,\mathrm{d}\Omega} \cdot \exp\left(-\frac{l}{l_{\text{Decay}}}\right) \cdot 5.6\pi\,\mu\text{sr} \cdot 2p \cdot 1\,\%\,, \tag{5.4}$$

because one needs the actual momentum range that can be transported along the beamline, which is $2\Delta p$. With the distance between T6 and the AMBER target and the quoted decay lengths one can calculate the average number of particles at the experiment (5.4) as a function of the secondary beam momentum p. This is shown for positive and negative beam charge in Fig. 5.4. Of course, protons and antiprotons do not decay. Therefore, the decay term is not used to calculate the number of those.

In Fig. 5.5 the respective shares of the different particles in the beam are calculated.

The numbers depicted in Fig. 5.4 and 5.5 only take decays and the acceptance of the beamline into account. Clearly, there can be more losses due to collimation for instance. This would reduce the rate of particles, but not the beam composition itself because the beam parameters depend only on the particle charge, but not the species. Considering the composition at momenta around 100 to 200 GeV/c, kaons make up approximately 2 % of the total beam (for both, negative and positive beams). As the hall, where the AMBER experiment is located, is an overground building, the allowed rate sent to the building is limited due to radiation protection constraints. The maximum is on the order of 10^8 to 5×10^8 particles per spill (or even 10^9 considering the upgraded shielding described in section 3.5), which depends on the shielding around the AMBER target. Considering the fraction of kaons of 2 % one can calculate the maximal kaon rate, which is 2×10^6 to 2×10^7 kaons per spill.

5.3 RF and particle phases

In the previous section 5.1 the chosen phase difference between the different particles and its influence on the beam momentum have been discussed. But the phase that is used for the separation is not the phase one is aiming to have between two species, but the relative phase of the electric fields in both cavities. The phase that needs to be set between those will be discussed in the following.

The time-component of the electric field in a RF cavity is described by an oscillating function, i.e.

$$E(t) = E_0 \sin\left(\omega t + \phi\right) . \tag{5.5}$$

This immediately implies that the transverse kick θ only depends on the phase the particle arrives at the cavity with respect to the phase of the electric field meaning

$$\theta(t) = \theta_0 \sin\left(\varphi_i(t)\right) , \tag{5.6}$$

with i representing the phase in cavity 1 or 2, respectively. The combined kick of both cavities can be calculated by the sum of both single kicks taking into account the phase α representing the time of flight between both cavities, and $\Delta\varphi_{12}$ being the relative phase between the fields in the cavities. To obtain the total kick, the phase at the second cavity can be written as

$$\varphi_2(t) = \varphi_1(t) + \Delta\varphi_{12} + \alpha . \tag{5.7}$$

This results in[3]

$$\begin{aligned} \theta_{\text{tot}}(t) &= \theta_0 \left(\sin\left(\varphi_1(t)\right) + \sin\left(\varphi_1(t) + \alpha + \Delta\varphi_{12}\right)\right) \\ &= 2\theta_0 \sin\left(\varphi(t) + \frac{\alpha + \Delta\varphi_{12}}{2}\right) \cos\left(\frac{\alpha + \Delta\varphi_{12}}{2}\right) . \end{aligned} \tag{5.8}$$

From Eq. (5.8) one can see that one is able to tune the phase between the two cavities such that the kick can be entirely compensated for a certain species. This can be achieved by tuning $\Delta\varphi_{12}$ in such a way that $\cos\left(\frac{\alpha+\Delta\varphi_{12}}{2}\right) = 0$, which is achieved for $\alpha + \Delta\varphi_{12} = (2n+1)\,\pi$. Another approach would be to maximize the kick for a certain particle type, which can be done by setting $\alpha + \Delta\varphi_{12} = n \cdot 2\pi$. In the following example a K^--beam is considered.

In this case the π^-- and $\bar{p}$-components of the beam should be removed. The time an unwanted π^- travels from the first to the second cavity can be calculated via

$$t_{\pi^-} = \frac{L}{\beta c} = \frac{L}{c}\sqrt{1 + \left(\frac{m_\pi c}{p}\right)^2} . \tag{5.9}$$

This can be translated into a phase at the second cavity, i.e.

$$\alpha_{\pi^-} = \frac{2\pi f L}{\beta c} = \frac{2\pi f L}{c}\sqrt{1 + \left(\frac{m_\pi c}{p}\right)^2} . \tag{5.10}$$

Using Eq. (5.10) in (5.8) one can now calculate the relative phase of both cavities such that the kick for π^- gets compensated, which is demonstrated in Eq. (5.11).

[3] In the following calculations it is made use of sin- and cos-identities as $\cos\left(x+y\right) = \cos(x)\cos\left(y\right) - \sin(x)\sin\left(y\right)$ and $\sin\left(x+y\right) = \sin(x)\cos\left(y\right) + \cos(x)\sin\left(y\right)$ [128].

$$\Delta\varphi_{12} = \pi - \alpha_{\pi^-} = \pi - \frac{2\pi f L}{c}\sqrt{1 + \left(\frac{m_\pi c}{p}\right)^2}. \tag{5.11}$$

Recalling that the beam momentum has been defined by requiring $\Delta\varphi^{\bar{p}}_{\pi^-} = 2\pi$ when flying from the first to the second cavity, one can deduce that the kick is entirely compensated for the $\bar{p}$-component of the beam as well.
Similarly, the kick for the wanted K^--fraction in the beam can be calculated and is shown in Eq. (5.12).

$$\theta^{K^-}_{\text{tot}}(t) = 2\theta_0 \cos\left(\varphi_1(t) + \frac{\pi f L}{c}\left(\sqrt{1 + \left(\frac{m_K c}{p}\right)^2} - \sqrt{1 + \left(\frac{m_\pi c}{p}\right)^2}\right)\right) \sin\left(\frac{\pi f L}{c}\left(\sqrt{1 + \left(\frac{m_K c}{p}\right)^2} - \sqrt{1 + \left(\frac{m_\pi c}{p}\right)^2}\right)\right). \tag{5.12}$$

With (5.8) one can estimate the average kick any species will receive by the separator system. For that one can define the mean kick to be

$$\bar{\theta} = \sqrt{\frac{1}{2\pi}\int_0^{2\pi} \theta^2_{\text{tot}}(\varphi)\,\mathrm{d}\varphi} = \sqrt{2}\theta_0 \left|\cos\left(\frac{\alpha + \Delta\varphi_{12}}{2}\right)\right|, \tag{5.13}$$

resulting in an average kick for K^- of

$$\bar{\theta}_{K^-} = \sqrt{2}\theta_0 \left|\sin\left(\frac{\pi f L}{c}\left(\sqrt{1 + \left(\frac{m_K c}{p}\right)^2} - \sqrt{1 + \left(\frac{m_\pi c}{p}\right)^2}\right)\right)\right|. \tag{5.14}$$

The deflections of the three main species together with the average kicks are shown in Fig. 5.6.

5.4 RF cavities

As deduced from the previous sections, the cavity parameters play a critical role in the performance of the separation. Clearly, a high frequency is needed to separate a beam with high momentum. Another important point is the kick strength itself, which is determined by the electric field in the cavity. Therefore, to reach larger separation, a high gradient is necessary. Last but not least, a large iris is important such that the beam can be transmitted through the cavity.

The performance is better when having a parallel beam, which will be shown in section 5.7. Naturally, this results in a large beam (cf. Liouville's theorem in section 2.2.2) meaning losses in the cavity (or an upstream collimator) if the iris is too small. RF cavities in general and important parameters for the RF separated beam (cf. [126, 127]) are discussed in the present section.

The most famous example of a cavity structure is the so-called Pillbox shown in Fig. 5.7. Its characteristics can be derived analytically.

Generally, the fields in the cavity follow the wave equations

$$\nabla^2 \vec{E} = \frac{1}{c^2} \frac{\partial^2 \vec{E}}{\partial t^2}, \qquad \nabla^2 \vec{B} = \frac{1}{c^2} \frac{\partial^2 \vec{B}}{\partial t^2}, \tag{5.15}$$

which can be derived from Maxwell's equations, so first principles. Those can be derived under the assumption of non-existing space charges and perfectly conducting walls. The solutions are plane waves $\exp(i(\omega t - \vec{k}\vec{r}))$ with the wave-vector $\vec{k}$ defining the direction of propagation of the wave and the frequency $\omega = 2\pi f$. The field vectors fulfill $\vec{E} \perp \vec{B} \perp \vec{k}$. Additionally, so-called dispersion relations are given, i.e.

$$c = \frac{\omega}{|\vec{k}|} = \frac{\lambda}{f}, \tag{5.16}$$

with the wavelength λ. Key input to determine the wavelength and therefore the frequency are the cavity dimensions and the boundary conditions. As cavities have metallic surfaces, there cannot be neither a parallel electric field nor a perpendicular magnetic field. Considering the cavity size given in Fig. 5.7, one can calculate the corresponding solutions to the wave equations (5.15) fulfilling the described boundary conditions. Additionally, propagation is assumed in z-direction. By making use of cylindrical symmetry, one obtains [129, 130]

$$\begin{aligned}
E_r &\propto J'_m\left(k_r r\right) \cos\left(m\varphi\right) \sin\left(k_z z\right) e^{-i\omega t} \\
E_\varphi &\propto \frac{1}{r} J_m\left(k_r r\right) \sin\left(m\varphi\right) \sin\left(k_z z\right) e^{-i\omega t} \\
H_r &\propto \frac{1}{r} J_m\left(k_r r\right) \sin\left(m\varphi\right) \cos\left(k_z z\right) e^{-i\omega t} \\
H_\varphi &\propto J'_m\left(k_r r\right) \cos\left(m\varphi\right) \cos\left(k_z z\right) e^{-i\omega t}
\end{aligned}, \tag{5.17}$$

and

$$E_z \propto \begin{cases} J_m\left(k_r r\right)\cos\left(m\varphi\right)\cos\left(k_z z\right)e^{-i\omega t}, & \text{TM-modes} \\ 0, & \text{TE-modes} \end{cases}$$
$$H_z \propto \begin{cases} 0, & \text{TM-modes} \\ J_m\left(k_r r\right)\cos\left(m\varphi\right)\sin\left(k_z z\right)e^{-i\omega t}, & \text{TE-modes} \end{cases} . \tag{5.18}$$

J_m refers to the Bessel-function of m-th order, whereas J'_m refers to its derivative. When it comes to cavities, one typically defines TM_{mnp}- and TE_{mnp}-modes, with vanishing parallel magnetic fields for TM-modes (transverse magnetic) and vanishing parallel electric fields for TE-modes (transverse electric). The parameters m, n and p define types of those modes: m yields the number of full-periods in azimuthal-direction, n gives the number of radial zeros of the axial fields and p the number of half-periods of the longitudinal fields. With $k^2 = k_z^2 + k_r^2$ and the boundary conditions the dispersion relation reads

$$f_{mnp} = \frac{c}{2\pi}\begin{cases} \sqrt{\left(\frac{j_{mn}}{a}\right)^2 + \left(\frac{p\pi}{L}\right)^2}, & \text{TM-modes} \\ \sqrt{\left(\frac{j'_{mn}}{a}\right)^2 + \left(\frac{p\pi}{L}\right)^2}, & \text{TE-modes} \end{cases} , \tag{5.19}$$

with j_{mn} referring to the n-th root of J_m and j'_{mn} referring to the n-th root of J'_m.

As one can deduce from Eq. (5.18), one can only accelerate in longitudinal direction with a TM-mode. Of course, for the present considerations, field components for transverse acceleration are needed. Transverse deflection can be achieved by both, electric and magnetic fields. Therefore, TE- and TM-modes can be employed such that the beam receives a net deflection in the transverse plane.

One of the key parameters is the radio-frequency f. In section 5.1 the dependence of the momentum p on f is derived showing that the maximum beam momentum is proportional to $\sqrt{f}$. Therefore, the frequency needs to be as high as possible to achieve highest energies. Because the frequency is determined by the cavity shape, the geometry can be optimised to reach highest frequencies. Clearly, another key parameter is the cavity gradient. To minimise the space taken by the cavities itself the gradient needs to be maximised. Having in mind that the proton beam is slowly extracted towards the North Area meaning spill lengths of the order of 5 s, one can deduce that the cavity needs to operate in continuous wave mode (CW). To be still able to have high field gradients, superconducting cavities need to be considered [126, 127]. On the other side, cost is a driving factor. Therefore, to not have exploding costs to develop new, fully customised cavities, ideally an already existing design should be considered. Typically, transverse cavities can be found in collider experiments rotating the

beam in one of the transverse directions to overcome the problem of decreasing luminosity at the interaction point due to finite beam crossing angles. Those types of cavities are referred to as crab cavities. Also, this rotation can be found as crabbing. The **I**nternational **L**inear **C**ollider ILC is currently planning to employ crab cavities to exactly eliminate this problem. The design features high-frequency and high-gradient crab cavities reaching values feasible for the present considerations making use of the dipole TM_{1n0}-modes. A picture of the foreseen 9-cell cavities is shown in Fig. 5.8 with the electric and magnetic field shapes illustrated in Fig. 5.9. Those are able to provide an average transverse gradient of $5\,\mathrm{MV\,m^{-1}}$ and operate at 3.9 GHz. Simultaneously, the design features a reasonable iris with a diameter of 30 mm.

5.5 Aperture influence

As the angle x' with respect to the beam axis grows when travelling through the cavity due to the transverse deflection, the beam size grows accordingly, too. The growth of x' can be calculated via

$$x'(z) = \frac{\frac{\Delta p}{\Delta z}}{p} \cdot z\,, \tag{5.20}$$

where $\frac{\Delta p}{\Delta z}$ is the average cavity gradient, p the momentum and z the longitudinal position along the cavity. By integrating Eq. (5.20) over z the dependence of x follows and is given by[4]

$$x(z) = \frac{\frac{\Delta p}{\Delta z}}{2p} \cdot z^2 + x_0\,, \tag{5.21}$$

which is shown in Fig. 5.10.

This indicates that the beam needs to be small such that it does not get lost at the cavity apertures, which does not only influence the intensity, but can also lead to quenches of the cavities. So, this needs to be avoided by all chances. The maximal size the beam can have at the cavity entrance can be calculated according to Eq. (5.21) requiring that it fills out at most the full iris after traversing the cavity meaning

$$x(L) \overset{!}{\leq} R\,. \tag{5.22}$$

This condition yields the maximal value of x_0 being the maximal acceptable beam size at the cavity entrance, i.e.

$$x_0 \leq \frac{1}{2}\left(2R - \frac{\frac{\Delta p}{\Delta z}}{p} \cdot L^2\right). \tag{5.23}$$

[4] The integration is motivated by $x' = \frac{\mathrm{d}x}{\mathrm{d}z}$. From that step, the integration constant x_0 follows accordingly.

Taking a radius of 15 mm, a gradient of 5 MeV c^{-1} m^{-1}, a momentum of 68.13 GeV/c and a length of 10 m results in $x_0 \approx 11.5$ mm meaning a collimator with such a half opening needs to be installed in front of the first deflector station. Without it, the cavities would appear effectively as collimators, too.

Interestingly, R_{eff} can become zero for a given deflector length. For the present values this would be achieved for $L \approx 20.5$ m. In case the cavities would be longer than this threshold value, the beam would be collimated entirely at the cavity exit.

5.6 Optics considerations

As described in the beginning of the the present chapter, the RF cavities deflect the beam transversely meaning an increase of momentum in the kick direction. The fields assumed and therefore finally the transverse momenta are still small compared to the longitudinal momentum allowing to work in small angle approximation, meaning

$$x' \approx \frac{p_x}{p} \approx \frac{p_x}{p_z}\,, \tag{5.24}$$

with the transverse momentum p_x[5] and the total momentum p, which is basically determined by the longitudinal momentum p_z. From this consideration it gets clear that the RF separation technique works in angular space meaning that after traversing the separator the particle species differ by their angular distributions. Immediately after exiting the second cavity, the different species cannot be filtered by position. As there is no device available that absorbs particles depending on their angle with respect to the beam axis, it is needed to let the beam drift freely in order to translate the angular separation into a spatial one.

As this technique first and foremost separates species by angle it is obvious that it will work most efficiently when having a non-divergent beam meaning that the angular distribution of the beam after exiting the second cavity is purely determined by the field configuration in the cavities. The impacts of a divergent and non-monochromatic beam are qualitatively discussed in the appendix A.1. In the optimal case, i.e. having a parallel, monochromatic beam, the unwanted particles will have a vanishing angle, while the particles of interest have a finite transverse momentum. Of course, creating a parallel beam would therefore be the favourable choice. Having Liouville's theorem in mind, this comes at a cost. A parallel beam, i.e. narrow distribution in x', is large in size, i.e. broad distribution in x. A large beam typically implies losses due to aperture restrictions of various elements along the line. In the RF separated beam case, the critical elements with small apertures are the cavities themselves. High-frequency and high-gradient cavities can be operated with irises of the order of 10 mm. As the ILC crab cavities have been chosen for the present study, the aperture restriction is 30 mm. Clearly,

[5] As the optics have been developed such that the cavities deflect the beam in x-direction, without loss of generality it is assumed that the transverse momentum is purely determined by p_x. This is a fair assumption because no elements in the beamline couple the two transverse directions meaning the cavities do not impact the motion in vertical direction.

having a beam that is larger than the cavity aperture results in a smaller transmission and therefore smaller number of particles at the experiment[6]. This means there is an optimum between beam size and parallelism in terms of number of particles transmitted and efficiency of the separator. The two extreme cases, parallel and focused beam, are shown in Fig. 5.11.

For a parallel beam, the angles of the wanted particles are purely determined by the transverse kick provided by the cavities. Therefore, the wanted particles can be clearly differentiated from the unwanted ones by angle. Of course, this comes at a cost of lower transmission because the beam gets effectively collimated. For a focused, i.e. a divergent beam, the transmission through the cavities is not a concern as the beam size is small compared to the iris. Oppositely, the angular separation is less pronounced because the divergence of the wanted particles after the separator is determined by the kick and the intrinsic divergence still resulting in an overlap in angular space of the wanted and unwanted parts. In the case of an extremely focused beam, the transverse deflection would be only visible as a slight modulation on top of the intrinsic beam divergence.

Finally, the beam optics can be developed based on the aforementioned considerations. One needs to ensure a monochromatic beam as spread in momentum directly impacts the phase relations derived in section 5.3 and ultimately the performance of the separator. The variation $\Delta\alpha$ of the imposed time-of-flight phase α for a particle with mass m, momentum p and energy E due to a finite momentum spread Δp can be calculated based on Eq. (5.10). One obtains

$$\frac{\Delta\alpha}{\alpha} = \left(\frac{mc^2}{E}\right)^2 \frac{\Delta p}{p} = \frac{1}{1+\left(\frac{p}{mc}\right)^2} \frac{\Delta p}{p} \,. \tag{5.25}$$

Clearly, for high-energy beams the effect becomes small as with increasing momentum a small change in momentum is less noticeable than for the low-energy case. Still, the relevant part is the difference in time-of-flight between species as the separator differentiates particles based on this quantity. The impact on the phase difference $\Delta\varphi$ between two particles with masses m_1 and m_2 can be calculated with Eq. (5.1) and is

$$\frac{\Delta(\Delta\varphi)}{\Delta\varphi} = \frac{\Delta p}{p} \left| \frac{\left(m_1c^2\right)^2}{E_1E_2 - E_1^2} + \frac{\left(m_2c^2\right)^2}{E_1E_2 - E_2^2} \right| \approx 2\frac{\Delta p}{p} \,, \tag{5.26}$$

with the high-energy approximation $p \gg m_i c$ applied in the last step. This relation becomes clear when keeping in mind that with increasing momentum the velocity difference between two species becomes smaller. Therefore, the shift in phase in case of a finite energy spread is pronounced more. This motivates the chosen maximum spread of 1 %, which is achieved by

[6] If those particles would be lost in the cavity walls, quenches would be the result. Those would lead to field breakdowns and in the worst case to the destruction of the cavity.

the momentum selecting dipoles and collimator upstream. The momentum spread of the beam as a function of the collimator opening is depicted in Fig. 5.12.

The correlation is linear, which is to be expected as the transmission through the momentum-defining collimator gets smaller with smaller aperture. Finally, only particles with momenta close to design value will be transmitted. Therefore, the relation $\frac{\Delta p}{p} = \delta p_0 + m \cdot \frac{w}{2}$ has been fitted to the data. One obtains a minimal momentum spread of (0.134 ± 0.005) % and a dispersion of $(9.54 \pm 0.07)\,\mathrm{mm}\,\%^{-1}$. With these results (also depicted in Fig. 5.12), one can calculate the opening needed to achieve 1 % to be about ±8.2 mm.

The remaining bending magnets along the beamline make the beam follow the M2 tunnel shape.

Immediately after the momentum definition, the first deflection station is placed to achieve maximum distance between the two sets of cavities. It is located at about $s \approx 170\,\mathrm{m}$. The second station is placed at about $s \approx 1\,\mathrm{km}$ resulting in a distance of ca. 830 m. Various optics have been developed differing in the beam size and parallelism at the cavity positions. In any case, a one-to-one image from the first to the second station is ensured such that the deflection of the unwanted particles can be compensated. Ca. 20 m downstream of the second deflecting station a 5 m long beam dump is placed that will absorb the unwanted particles while the wanted ones circumvent it. Following the dump, a refocusing quadrupole is installed that brings the beam back onto the optical axis.

Finally, a parallel beam at the location of the CEDARs in M2 ($s \approx 1.09\,\mathrm{km}$) used for beam particle identification is setup. From there the beam is finally sent to the AMBER experiment with a focus in the transverse plane at the target. The evolution of the most relevant transfer matrix elements along the beamline is shown in Fig. 5.13.

In Fig. 5.13, the beam size and parallelism at the cavity locations have been optimised. The beam size is dominantly determined by the transfer matrix parameters R_{12} in the horizontal and R_{34} in the vertical direction. One of the constraints that have been imposed concerns the front-end of the beamline. The layout up to the target collimators (TAX) features six large-acceptance quadrupoles that need to stay in their place also for the RF separated beam due to radiation-protection constraints and overall radiation levels in the area close to the target. Therefore, the acceptance of the beamline in its current layout can be used to estimate the maximal value of R_{12} such that the beam still fits through the cavity. The horizontal angular acceptance $\Delta\alpha_{\mathrm{hor}}$ has been estimated by tracing particles with nominal momentum, no offset in position and different angles x'. The maximal value of x', for which particles still reach the end, yields the angular acceptance, which is 2 mrad. As the beamline is in forward direction, the accepted cone is indeed $\Delta\alpha_{\mathrm{hor}} = \pm 2\,\mathrm{mrad}$. Considering the iris of the cavities, the maximal value of R_{12} can be calculated via

$$R_{12} = \frac{d}{\Delta\alpha_{\mathrm{hor}}}\,. \tag{5.27}$$

With $d = 30\,\mathrm{mm}$, one obtains $R_{12} = 7.5\,\mathrm{m\,rad}^{-1}$. The value of R_{12} is modified depending on the actual setting that is under test. In case of a focus, one aims for $R_{12} = 0$, while with higher

values (and $R_{22} = 0$) a more parallel beam is produced.

5.7 Results from simulations

With the different optics settings at hand, the performance of the RF separated beam can be simulated and estimated. The two parameters from the beam perspective that are most relevant for the experiment, are kaon intensity, so number of kaons at the experimental target, and purity, i.e. share of kaons in the beam. The simulations have been performed with the available, internal tracking code in MAD-X version 5.08 [108]. As MAD-X does not include particle-matter interaction, the secondary particle production at T6 needs to be put into the simulation. This is done in the following way: Based on the Atherton parameterisation (2.1), the rates of K^-, π^- and $\bar{p}$ can be calculated. Considering the length of the beamline, one observes a reasonable decay rate, especially for kaons. The decay is taken into account via Eq. (5.3). The positions and angles of the particles escaping the beryllium plates are drawn from Gauß-distributions. x and y are drawn uniformly from a circle with a radius obtained from a normal distribution centered around zero with $\sigma = 1$ mm. Considering the values from the primary proton beam given in Fig. 2.4, i.e. $\sigma \approx 0.4$ mm in y and ± 1.5 mm in x, a spread of 1 mm will yield a reasonable value especially because the main parameter is indeed the angle relative to the beam axis and not the position.

The angles x' and y' are also drawn from a normal distribution centered around zero with $\sigma = 1$ mrad. The Atherton parameterisation yields the particle flux as a function of the solid angle. Therefore, the calculated flux depends linearly on the chosen width of the beam divergence distribution. Having a larger angular distribution will give a higher total number of particles. As the beamline has a certain acceptance, particles with large angles are cut. Again, because MAD-X does not feature particle-matter interaction, the production of particles when a beam particle hits an aperture is not included. Ultimately, because the rate contains the assumption of beam divergence, the choice of the width of the distribution is less critical.

The same holds for the momentum distribution. The flux calculated from the Atherton parameterisation grows linearly with the chosen width of the momentum distribution. Due to the imposed phase relations one aims for a spread of 1 %. Therefore, $\sigma = 1$ % (and $\mu \approx 68\,\mathrm{GeV}/c$ for the RF separated kaon beam) has been chosen for the input of the tracking simulation. Again, because the flux depends linearly on this value, it is less critical in the final evaluation of the intensity because outlying particles would be cut by the beamline, which is shown in Fig. 5.12[7].

The time of production is based on the time distribution of the slowly extracted proton beam. The spill has a flat-top length of 4.8 s [133]. Therefore, the secondary particles are produced in a window ± 2.4 s. The absolute setting of $t = 0$ does not matter as only the relative phase between the fields in both deflecting stations is relevant. In the following, the negative kaon beam is investigated. For the positive kaon beam case everything follows equivalently when considering the fluxes of and shares in the unseparated beam. The nominal momentum of the

[7] All those considerations would be part of a full Geant4 simulation, which would include the secondary beam production in T6.

separated kaon beam achieved with the distance between the two stations of ca. 830 m and the frequency of 3.9 GHz is ca. 68.13 GeV/c.

In the full beamline simulation including the kick response of the cavities a trade-off has been made as MAD-X does not feature fully realistic transverse RF cavities. Therefore, a homogeneous field distribution over the iris is assumed. This is a valid assumption especially for the unwanted particles. Having a non-constant field over the aperture of the cavity implies that the kick a particle experiences depends on the point of passage. Because the optics feature a one-to-one image between the cavities, particles traverse both cavities, to first order, at the same position. For the unwanted particles it is therefore still possible that the deflections cancel. For the wanted species it is expected that the angular distribution is impacted by a transversely varying field as the experienced deflection would be different for particles traversing the cavities at different points $(x,\ y)$ even though the phases at both cavity location would be the same. Secondly, the cavities are simulated with vanishing longitudinal extent. Still, the effect of increasing beam size in the cavity is accounted for by a collimator upstream of RF1 with a half-aperture of about 11.3 mm.

As particles coming out of the separator can be differentiated first only due to their angular distributions, those are the important quantities for the various species in the beam. For the optics setting depicted in Fig. 5.13, so $R_{12} = 7.5\,\mathrm{m\,rad^{-1}}$, the x'-distributions for K^-, π^- and $\bar{p}$ are shown in Fig. 5.14. All plots shown in the following are scaled to 1.5×10^{13} protons on T6.

As imposed by the relative phase between the two deflectors that has been set, π^- and $\bar{p}$ on average do not receive a kick. Oppositely, the distribution of K^- peaks at $x' \approx \pm 1$ mrad. The smearing of the three illustrated distributions is dominantly due to the finite divergence of the beam. The RF separation technique works better the more parallel the beam is as, in the optimal case, the angle is only determined by the deflection. Because the beam has been made as parallel as possible while still fitting through the cavities, one needs to accept a non-vanishing spread of the angles. With Eq. (5.12) one can estimate the maximal expected angle for K^- exiting the separator, which is

$$\theta_{\mathrm{max}}^{K^-} = 2\theta_0 \sin\left(\frac{\pi f L}{c}\left(\sqrt{1+\left(\frac{m_K c}{p}\right)^2} - \sqrt{1+\left(\frac{m_\pi c}{p}\right)^2}\right)\right). \tag{5.28}$$

Plugging in the values for f, L and $\theta_0 = \frac{50\,\mathrm{MeV}/c}{68.13\,\mathrm{GeV}/c} \approx 0.74$ mrad yields $\theta_{\mathrm{max}}^{K^-} \approx 1.07$ mrad (and $\theta_{\mathrm{min}}^{K^-} \approx -1.07$ mrad), which is in excellent agreement with the peak positions illustrated in Fig. 5.14.

As the optics have been designed in such a way that the beam fills out the cavities, the horizontal positions of all species are distributed over the full iris, i.e. between ±15 mm. The trace spaces for K^- and π^- at the end of the second set of cavities are depicted in Fig. 5.15.

After RF2, there follows a free drift that translates the non-vanishing angles of K^- into a clear spatial discrimination against the unwanted species. With the drift length and width of the beam dump installed after that drift one can modulate the intensity and purity of the kaon component in the beam. The resulting trace space distributions of K^- and π^- after ca. 20 m of drift are illustrated in Fig. 5.16 and 5.17.

As the angular distributions of the unwanted particles peak at zero, even after 20 m of drift, their positions are still centered around zero meaning they hit the installed beam dump. Of course, because it is not a sharp peak, but one also finds unwanted particles with large angles, one observes some also circumventing the beam dump. For the wanted K^- the situation looks different. Their positions peak at $\pm 1\,\text{mrad} \cdot l$ with the drift length l. So for 20 m the peaks are at ±20 mm. Still, as the K^- do not populate the peak angles only, one also finds wanted particles with small angles. Those are not able to circumvent the beam dump and are lost. The arrows in Fig. 5.16 and 5.17 indicate the width of the beam dump. They also stress that the width is a parameter to optimise either purity or intensity of the beam. On the one hand, with a smaller dump size more particles will get around it, but not only wanted but also unwanted ones meaning maximal intensity. On the other hand, with a wider dump, less particles, especially unwanted particles are able to circumvent. Ultimately, one will have a beam only consisting of K^-, so maximal purity. In the illustrated example, it has been set to ±20 mm. With such a setting, about 59 % of the wanted K^- would be dumped, while over 92 % of the unwanted π^- (and by design also of $\bar{p}$) hit the beam dump.

Besides the beam dump, the following quadrupole that should refocus the beam onto the optical axis, needs to be respected. Its aperture is indicated by the two tilted lines in Fig. 5.16 and 5.17. Those are tilted because the quadrupole is placed downstream of the beam dump meaning further translation of non-vanishing angles x' into positional offsets x. Clearly, particles being outside of the aperture are lost, too, leading to an uncontrollable loss of intensity and purity as typically wanted particles have larger amplitudes.

The interplay between K^- intensity and purity for various studied beam optics is shown in Fig. 5.18.

The solid red line in Fig. 5.18 represents the maximum allowed rate of about 4×10^8 particles per spill in EHN2. This limitation is set by radiation-protection. Considering this limit, everything above the red line would be forbidden by radiation-protection. When being above the allowed maximum, it would be necessary to collimate the beam to decrease the overall intensity.

The purple points indicate the rate and share of K^- for different beam momenta at the AMBER target, i.e. about 1 150 m downstream of the production target T6. In the calculation, only the production according to Atherton and the average number of decays along the beamline, but no other losses have been considered. As all the three points are above the RP-limit one would need to lower the rate, for example by collimating the beam.

The other data points represent the K^- intensity as a function of the share of K^- in the beam for various beam optics. The green crosses show the performance of the separator achieved with a focus in the center of the two deflector stations. Clearly, the transmission through the

cavities is optimal because the beam is small but it is not possible to reach a high purity above 50 %. The same holds for the red crosses featuring a slightly larger and therefore more parallel beam through the cavities. One can reach a higher purity, but there is still a limit.

The blue circles represent a setting with a highly parallel beam at the cavity locations. With such a beam it is possible to even reach a 100 % share of K^- in the beam. Of course, one needs to sacrifice intensity and to accept low overall transmission. As long as the beam dump is smaller than the cavity iris, one does not gain in terms of purity and only looses intensity because there are still unwanted particles that can circumvent the dump. As soon as it is larger than the aperture, the intensity stays constant with increasing purity. From this one can deduce that it would be beneficial to generate a beam as parallel as possible when aiming for highest kaon purity.

The optimised beam optics are represented by the black crosses. Those settings feature the considerations discussed in section 5.6. In addition, the overall transmission along the beamline has been optimised to make maximal use of the kaon content in the beam. With those optics it is possible to reach a high purity, too, while at intermediate kaon fractions the intensity is still higher than for the parallel beam setup. With the optimised magnet strengths, it would be possible to deliver 10^6 K^- per spill at 40 % purity for 1.5×10^{13} protons on T6. When sacrificing purity for intensity and going down to 20 %, it would be already possible to achieve about 3×10^6 K^- per spill.

5.8 Conclusion

In the present chapter the important steps towards the design of a RF separated beam have been discussed. Key parameters for the performance of the separated beam are the cavity design values. The maximal beam momentum that can be achieved depends on the radio-frequency and length of the separator system, i.e. $p \propto \sqrt{fL}$, meaning one needs to maximise both to reach highest momenta. Clearly, the frequency is limited to values of the order of GHz, and the length of the system cannot be larger than the length of the beamline, which is about 1 km. Therefore, one can reach momenta between 50 to 100 GeV/c depending on the particle of interest. For the **C**ompact **LI**near **C**ollider CLIC a frequency of 11.9942 GHz [134] is currently considered for the crab cavities. Those provide a high transverse gradient of the order of 100 MV m^{-1}, too [135]. Consequently, the cavity aperture is limited to 10 mm diameter [134].

It has been shown that the performance is the highest when the beam is made as parallel as possible when traversing the cavities. Naturally, this is accompanied by a large beam size. Due to the large beam, the iris needs to be large, too, such that the beam is not collimated when passing through. Because high-gradient and high-frequency cavities come with small apertures, a focus in the centre needs to be generated that will ensure high transmission but results in small separation. As the gain in terms of momentum is only proportional to $\sqrt{f}$, the compromise of lower frequency and gradient, but larger iris has been made.

With the cavity design values for ILC, several beam optics have been developed. Their performances in terms of beam intensity and purity have been simulated and estimated. In all

cases, intensity of the wanted species needs to be sacrificed when aiming for a higher share of that one, which is caused by the limited aperture of the cavities. For achieving highest purity, a huge drop of rate needs to be accepted. But consequently, the rate stays constant even when going to a fraction close to one. Having beam optics that optimise transmission, i.e. beam size, and separation, i.e. parallelism, kaon rates of the order of 0.2 to 0.6 MHz at intermediate purities of ca. 20 to 40 % can be achieved. Considering the conventional hadron beam that has a share of about 2 %, one reaches kaon intensities up to 4 MHz depending on the allowed maximum in EHN2 (which is 200 MHz during the spill with the improved shielding concept, at maximum). From this comparison one can see that the gain is not in terms of intensity (especially as the values are obtained for 1.5×10^{13} protons on target, while in the conventional beam case, the maximum can be reached with 1.2×10^{13}), but regarding the kaon fraction. The higher purity makes the pion-kaon separation in the beam particle identification system easier, which is still needed because one has about 60 to 80 % of other particles (mainly pions in the negative beam case) remaining. As the tagging comes with an efficiency of identification, which is smaller than one (cf. chapter 6), the final kaon rate will be even smaller.

Finally, the achieved performance of the RF separated beam needs to be related to the requirements set by the AMBER experiment. Several measurements are foreseen, for which different intensities and energies are needed. All those campaigns require different beam settings in terms of energy and intensity. The program that demands the highest beam rate and energy is the Drell-Yan program. The high intensity is needed because it is a low-probability process, while the high energy is needed to reach the kinematic region, i.e. quark momenta that can be measured by the experiment and where it can be clearly differentiated from background processes. Already considering the energy that can be reached by the RF technique shows that the requirements for the Drell-Yan campaign cannot be achieved. In addition, the rate that can be sent, is also smaller compared to the intensity deliverable by the conventional beam especially as additional shielding is installed such that the intensity can be maximised.

The situation becomes different for instance for the strange spectroscopy program of AMBER, during which the hadron absorber described in section 3.5 cannot be installed[8]. The rate without the additional absorber needs to be limited to about 14 MHz meaning a maximal kaon flux of 0.28 MHz in the conventional hadron beam. The rate of the kaon component in the RF beam is comparable to that value and even slightly higher. In addition, the purity is an order of magnitude higher making beam particle identification easier, which is crucial for the anticipated measurement. Also, the beam momentum is not a critical component to reach the physics goals. Therefore, it would be possible to accept the limited energy.

Overall, parts of the physics program can be served with the RF separated beam, but for other parts the conventional beam needs to be employed.

Of course, when going to a technical design study, a full 3D-model of the cavities including the more realistic field distribution (not only homogeneous in the aperture) needs to be considered. In such a study, the impact of a non-constant field, especially on the wanted species, can be

[8] The upgraded shielding around the CEDAR-area and access chicane also discussed in [102] are kept in place.

estimated. Also, the background particles, like muons that are produced during in-flight decays of pions and kaons, are included. Those might be critical when it comes to cavity operation and possible quenches when the walls are hit by particles. The background generated in the collimator upstream of the deflector needs to be evaluated as it would point into the direction of the cavities. Furthermore, in a study featuring particle-matter-interaction the absorption in the beam dump can be determined. This includes not only background generation in the dump, but also the rate of particles that are able to traverse the dump without being absorbed, which allows a final evaluation of the background.

The implementation of the RF beam has significant impact on the other operation modes, especially the muon mode. The muon beam features magnetic collimators that are used to clean the beam and reduce the halo component. Without those, the beam would have a significantly larger halo that might impact attached experiments. As it will be shown, the longitudinal acceptance of the beamline is maximised in order to make maximal use of the hadronic component that decays into muons. The impact of the installed RF cavities on the longitudinal acceptance, or the halo generation, needs to be evaluated, too, in case one aims for still having the possibility of muon beam operation.

A possible improvement that could be studied alongside the aforementioned points is the impact of circular deflecting cavities, i.e. cavities that provide a kick in both directions x and y. As those would deflect in the whole transverse plane, not only the horizontal beam optics are important, but also the vertical. Estimating the performance of those requires a complete redesign of the beam optics as the current layout has been optimised for deflection in the horizontal direction. Considering the vertical kick, too, is more critical because the tunnel that encloses the beamline is mostly vertical making regular installation of vertically deflecting dipoles necessary. Those dipoles introduce dispersion that needs to be recombined at the cavity locations, which makes the calculation of new beam optics more advanced.

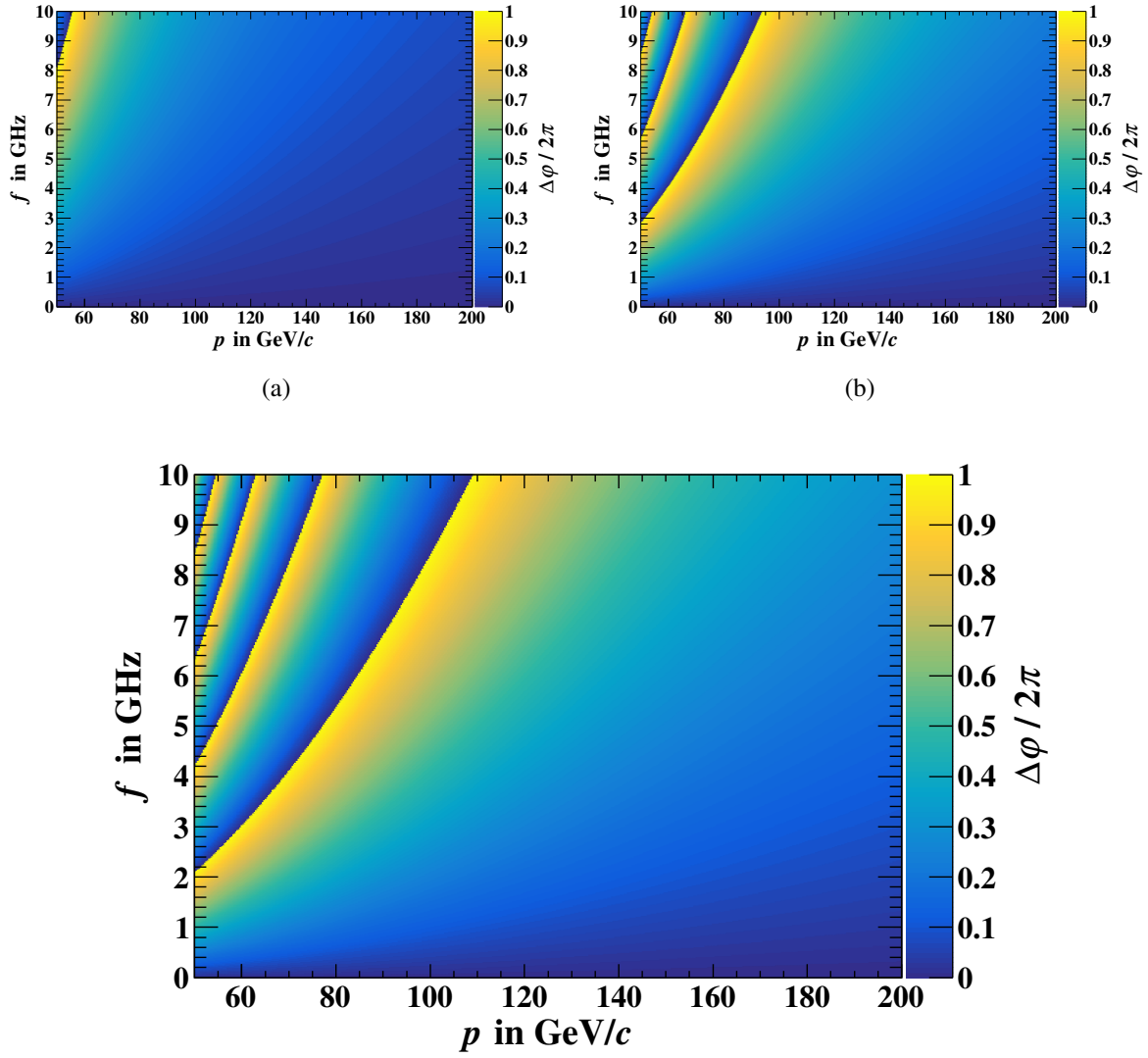

(a)

(b)

(c)

Figure 5.2: Phase differences between pions, kaons and (anti)protons calculated with (5.1) and $L = 830\,\text{m}$. The phase differences are plotted as a function of beam momentum and radio-frequency. Fig. 5.2(a) illustrates the difference between kaons and pions, Fig. 5.2(b) between (anti)protons and kaons, and Fig. 5.2(c) between (anti)protons and pions. From [126, 127]; modified.

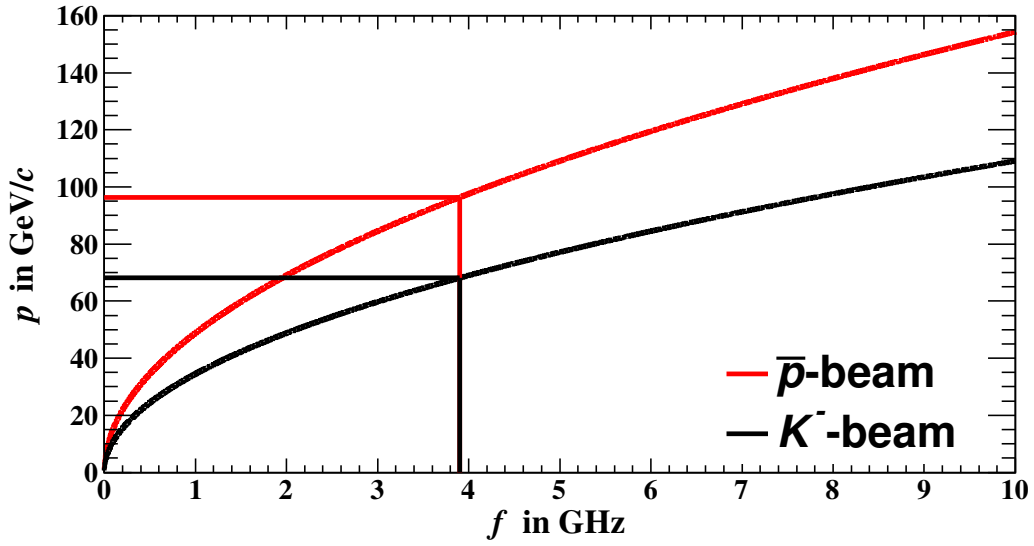

Figure 5.3: Frequency dependence of the beam momentum for a distance between the two RF-cavities of about $L = 830\,\text{m}$. The phase is chosen such that for a kaon beam one gets a phase difference between antiprotons and pions of $\Delta\varphi_{\bar{p}}^{\pi^-} = \Delta\varphi_{p}^{\pi^+} = 2\pi$ and for a $\bar{p}$-beam $\Delta\varphi_{\bar{p}}^{\pi^-} = \Delta\varphi_{p}^{\pi^+} = \pi$. The beam momenta for a kaon and antiproton beam for a frequency of $f = 3.9\,\text{GHz}$ are indicated by the horizontal and vertical red and black lines.

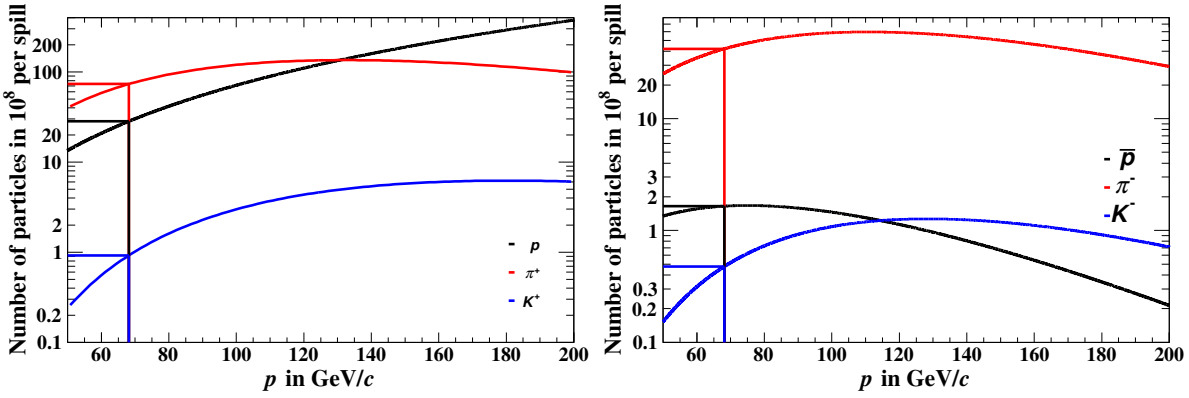

(a) (b)

Figure 5.4: Maximal beam rates that can be sent towards the AMBER target as a function of the beam momentum. The maximum is obtained from the particle production parameterised in Eq. (2.1) and (2.2) together with the average decay rate. Fig. 5.4(a) shows the rate of positive particles and Fig. 5.4(b) illustrates the rate of negative particles. (anti)protons are indicated by the black, pions by the red and kaons by the blue lines. The horizontal lines indicate the flux expected for the momentum of the RF separated beam.

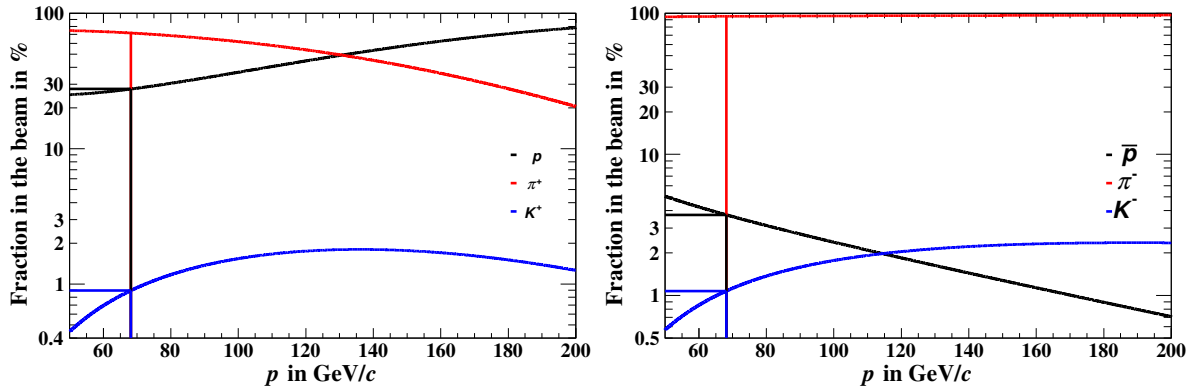

(a) (b)

Figure 5.5: Beam composition at the AMBER target as a function of the beam momentum. The values are obtained from the particle production parameterised in Eq. (2.1) and (2.2) together with the average decay rate. Only the three indicated species are used for the normalisation (muons are not considered here). Fig. 5.5(a) shows the abundances in the positive beam and Fig. 5.5(b) illustrates the shares in the negative beam. (anti)protons are indicated by the black, pions by the red and kaons by the blue lines. The horizontal lines indicate the composition expected for the momentum of the RF separated beam.

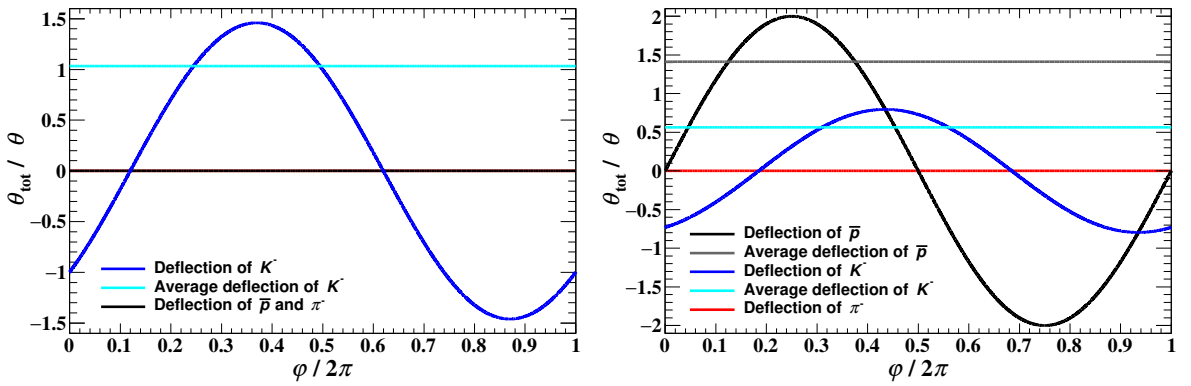

(a) (b)

Figure 5.6: Deflection of particles passing through the RF separator as a function of the phase the particles arrive with relative to the RF wave. Fig. 5.6(a) represents the settings for a separated kaon beam. The black line shows the deflection of (anti)protons and pions, while the blue one illustrates the kick of kaons with the turquoise line representing the average deflection. Fig. 5.6(b) shows the kicks of different particles for a separated antiproton beam. The (average) deflection of antiprotons is plotted in black (grey), the (average) kick of kaons in blue (turquoise) and the deflection of pions in red.

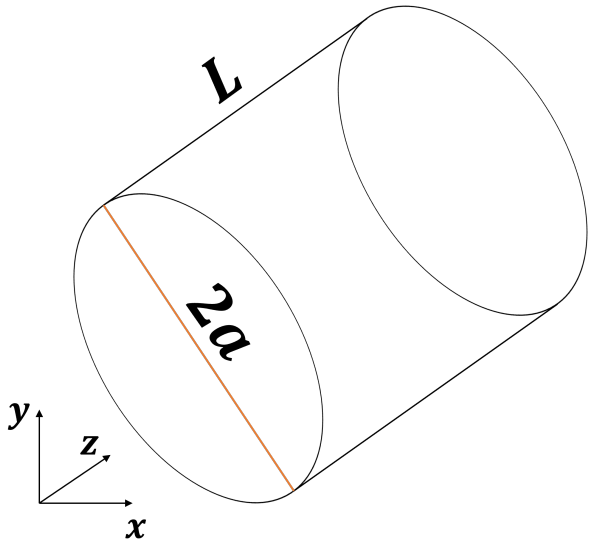

Figure 5.7: Schematic drawing of a Pillbox cavity. Its characteristics can be derived analytically and are purely determined by its shape. In the given example, it has a radius a and a length L. Wave propagation is assumed to be in z-direction.

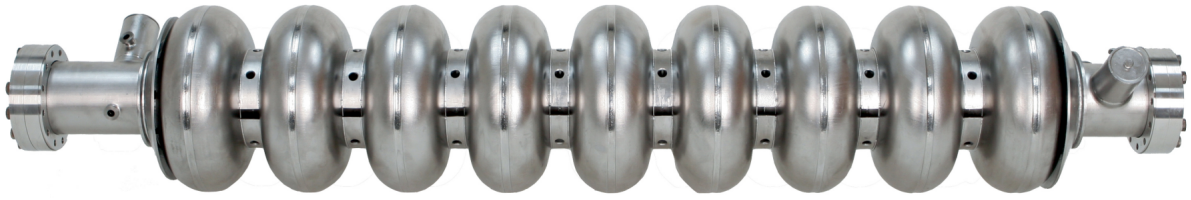

Figure 5.8: Picture of the ILC crab cavities at the design stage in 2013 [131]. At this point, a 9-cell TESLA-style superconducting cavity has been used as a baseline.

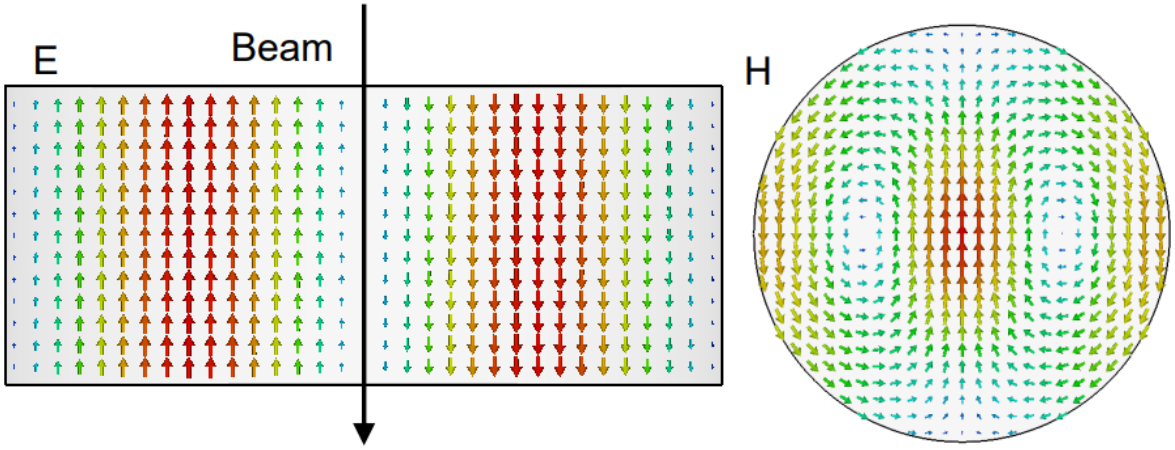

(a) (b)

Figure 5.9: Expected field distribution of the TM_{110}-mode in the ILC crab cavities [132]. The electric field is illustrated in Fig. 5.9(a) (beam is indicated by the black arrow) and the magnetic field in Fig. 5.9(b) (beam goes into the plane).

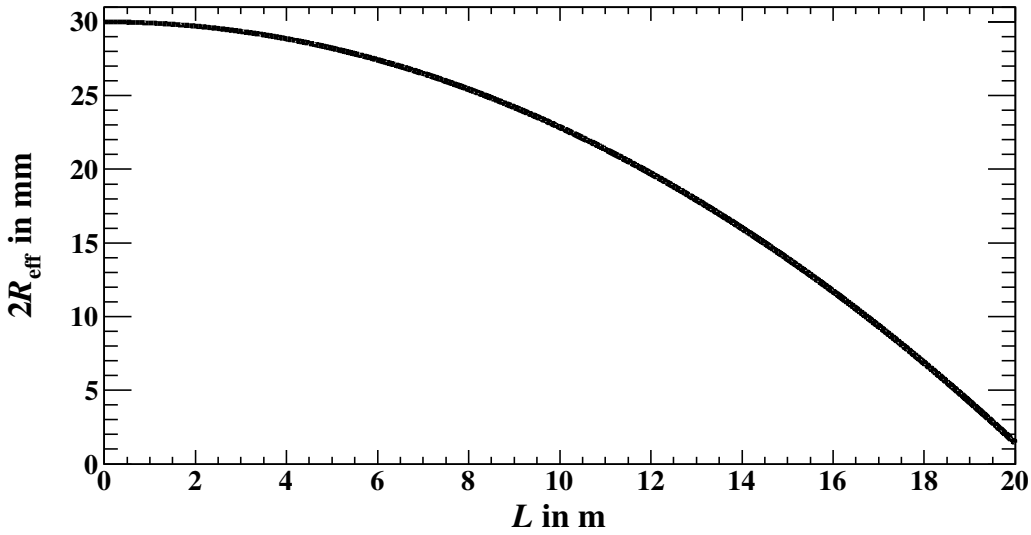

Figure 5.10: Dependence of the effectively usable cavity aperture on the actual length of the cavity itself for a gradient of 5 MeV c^{-1} m^{-1} calculated with Eq. (5.23). The beam momentum is about 70 GeV/c as it would be for the RF separated kaon beam. The full aperture of the RF cavity is 30 mm.

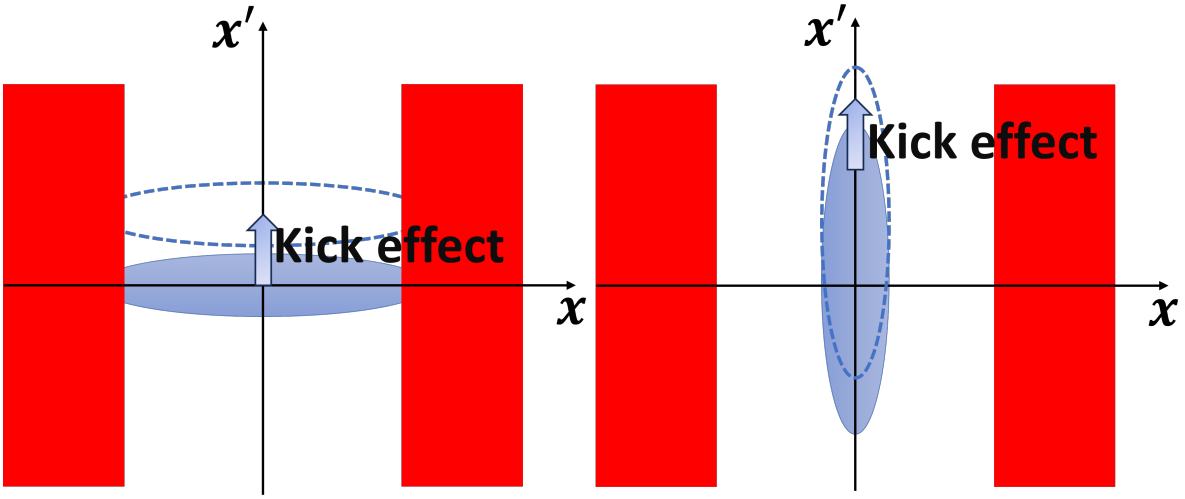

Figure 5.11: Effect of the cavity kick on the transverse trace space (only the kick direction is considered) for the two extreme beam scenarios. On the left, the effect is shown in case the beam is parallel, while on the right it can be seen for a focused beam. From [126, 127]; modified.

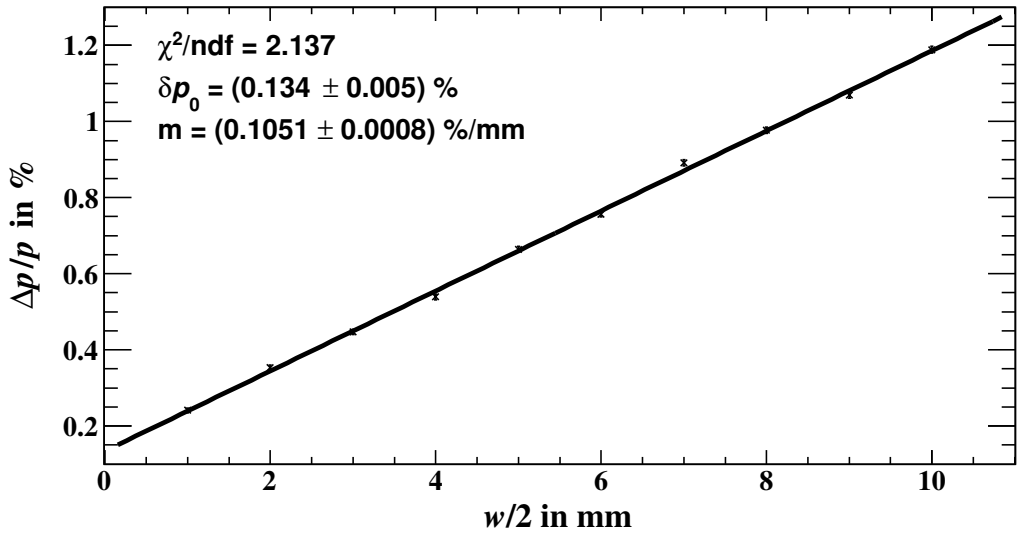

Figure 5.12: Momentum spread of the beam downstream of the momentum-defining bending magnets and collimator as a function of the collimator gap. A linear relation has been fitted to the data.

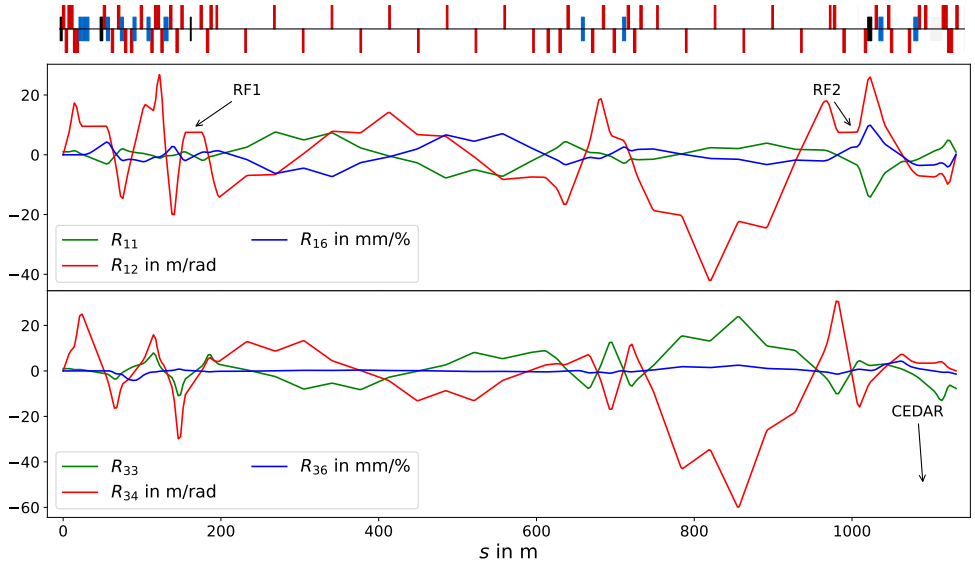

Figure 5.13: Optics for the RF separated beam as a function of the longitudinal position s. In the top half the horizontal direction is shown and in the bottom plot the vertical direction is illustrated. The cavities provide a kick in x-direction. The green lines show the evolution of R_{11} and R_{33}, the red lines represent R_{12} and R_{34}, and the blue ones illustrate the dispersion terms R_{16} and R_{36}.

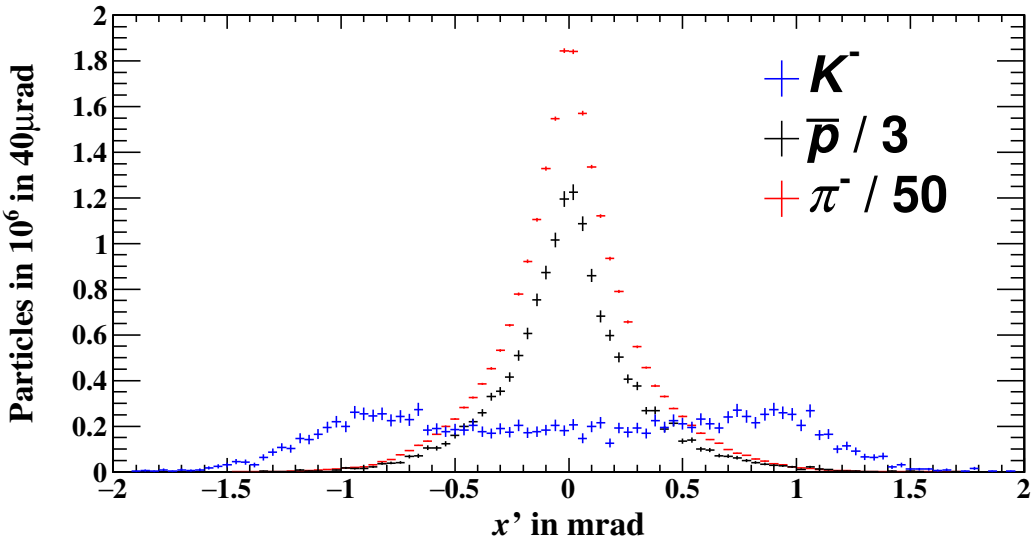

Figure 5.14: Angular distributions of the three main particles species after exiting the second set of cavities. The phase between RF1 and RF2 has been tuned in such a way that π^- (red) and $\bar{p}$ (black) do not receive a kick. Therefore, K^- (blue) experience a net deflection. The number of π^- has been decreased by a factor 50 and the number of $\bar{p}$ by a factor three. From [126, 127]; modified.

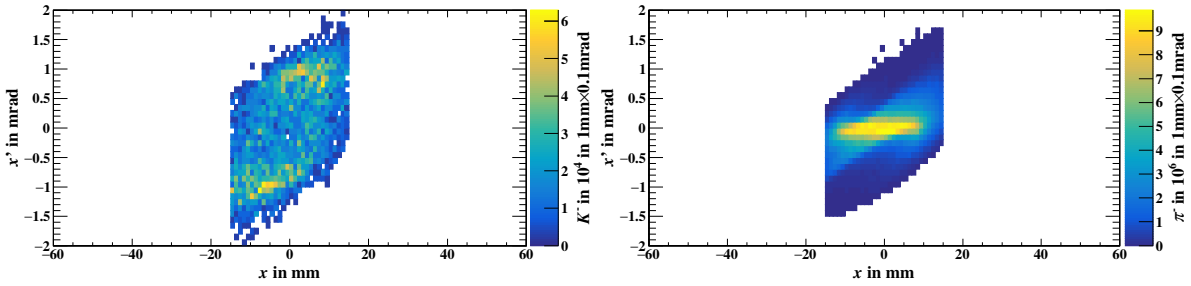

(a) (b)

Figure 5.15: Trace space of K^- (Fig. 5.15(a)) and π^- (Fig. 5.15(b)). The distributions are scored immediately after RF2. By design, the distribution for $\bar{p}$ looks the same as the one for π^-. From [126, 127]; modified.

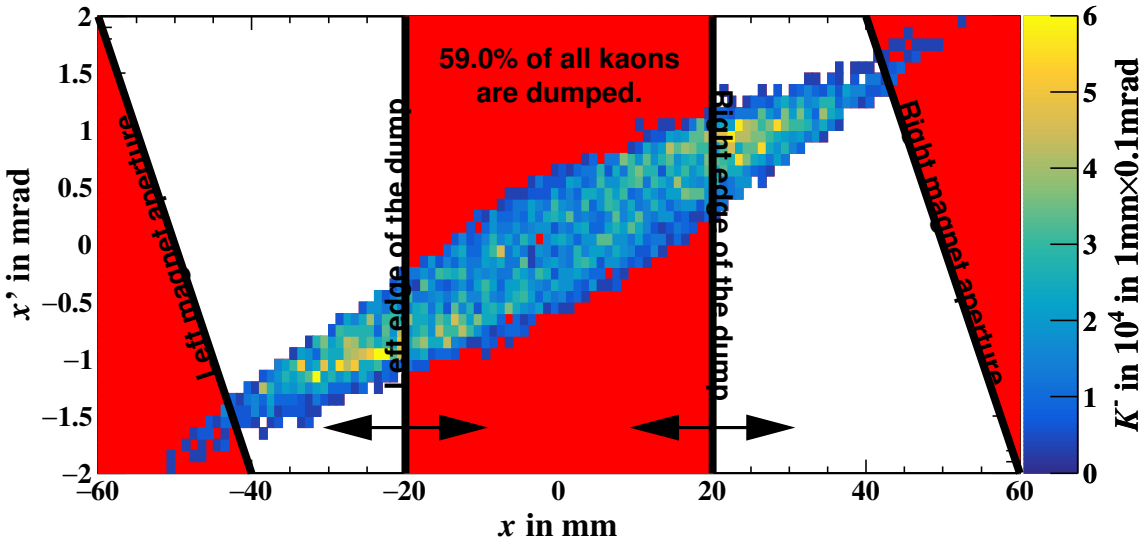

Figure 5.16: Trace space distribution of K^- ca. 20 m downstream of RF2. The inner two lines indicate the width of the installed beam dump. The outer, tilted lines represent the aperture of the refocusing quadrupole. Every particle that is within the red-coloured regions would be lost either in the dump or the magnet aperture. From [126, 127]; modified.

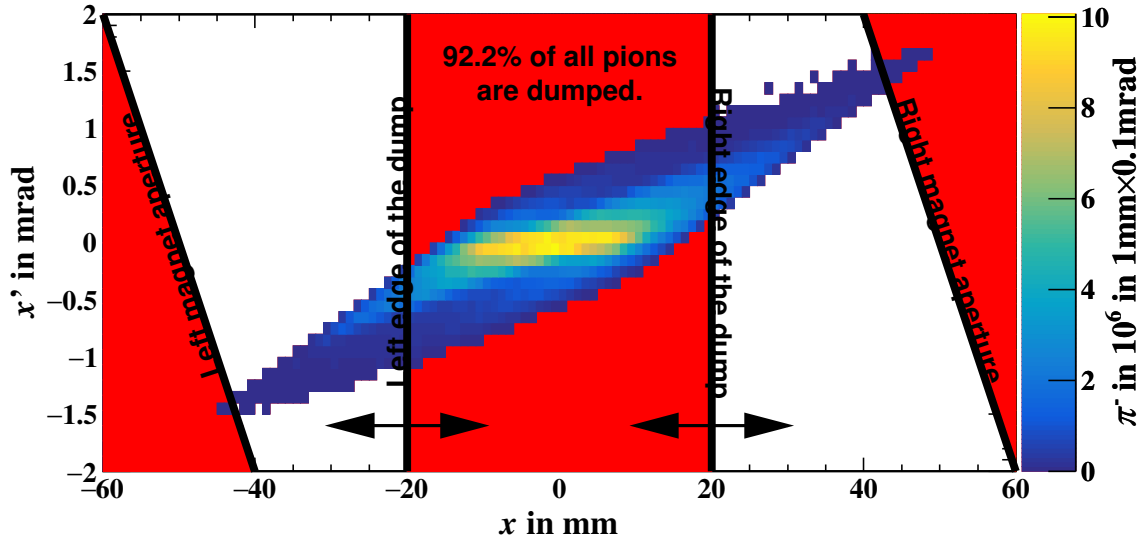

Figure 5.17: Trace space distribution of π^- ca. 20 m downstream of RF2. The inner two lines indicate the width of the installed beam dump. The outer, tilted lines represent the aperture of the refocusing quadrupole. Every particle that is within the red-coloured regions would be lost either in the dump or the magnet aperture. By design, the distribution for $\bar{p}$ looks the same. From [126, 127]; modified.

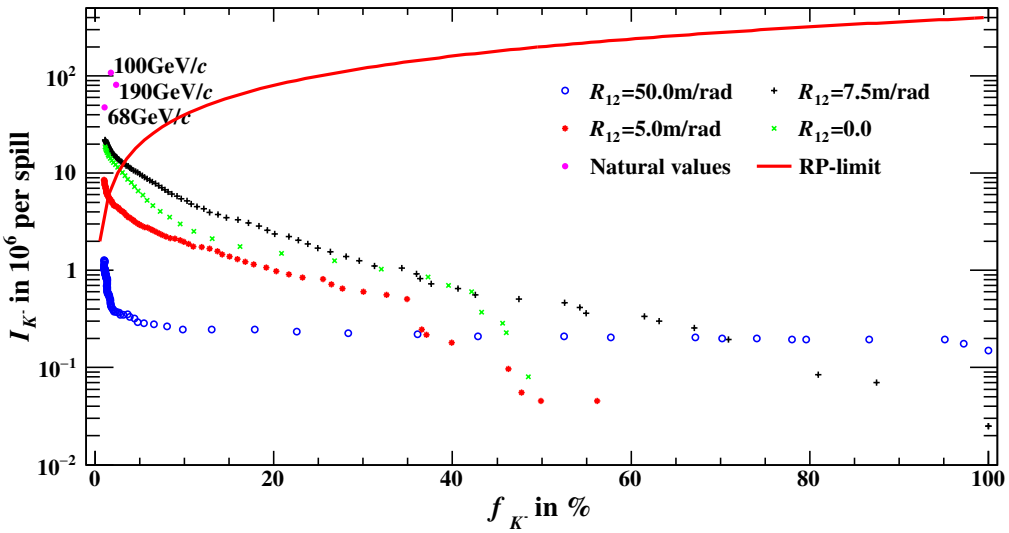

Figure 5.18: Intensity of K^- as a function of the share of K^- in the beam. The solid red line indicates the maximum allowed rate of ca. 4×10^8 particles per spill in EHN2 due to radiation-protection constraints. The natural values refer to the produced flux and fraction of K^- according to the Atherton parameterisation considering only decays in addition. The various colours indicate different optics settings at the cavity locations. From [126, 127]; modified.

CHAPTER 6

Conventional beam optimisation

Having the results of the RF separated beam study at hand, it is necessary to come up with different solutions to increase the hadron beam performance in terms of kaon rate. An easier and faster approach would be modifying the conventional hadron beam. A modification of the beam optics, which are purely determined by the set of magnet currents and positions is a change that requires in the best case no hardware modifications at all (as long as magnets are not moved). Therefore, it is advisable to study the performance increase by improving the beam optics. Additionally, it is also possible to implement hardware changes if necessary, for example changes in magnet positions or collimation schemes. Importantly, in the M2 line one finds vacuum interceptions, where the beam traverses air at atmospheric pressures. The effect of this on the beam quality will also be investigated and the improvement for a full-vacuum setup will be studied. Most of the results presented in this chapter have also been published in [136, 137].

6.1 Current beamline performance

Considering Fig. 5.5 various particle species contribute to the whole hadron beam, mostly (anti-)protons, pions and kaons. Therefore, in periods with hadron beam operation in M2, it is necessary to identify as many particles as possible reaching the experimental hall EHN2. Only particles that have been identified would contribute to the total beam flux meaning the more particles are tagged the higher the accumulated statistics would be. In M2, there is a specified location in the line, where two CEDAR detectors (cf. section 2.2.3) can be installed to do particle identification. This area can found ca. 50 m upstream of the former COMPASS target ($s \approx 1.09\,\mathrm{km}$).

The tagging efficiency of the CEDAR detectors depends crucially on the divergence of the beam, which is described in section 2.2.3. The crucial dependence manifests itself in the need for a very parallel beam at the CEDAR locations in the M2 beamline. The main problem with the current beamline design is that there are a lot of air sections along the line adding up to ca. 100 m. In these sections the beam scatters of the air molecules leading to an incoherent increase of the beam emittance and ultimately the divergence. This increase can be calculated

to first order with the Moliere-formula (6.1) [138, 139], where βc describes the beam particle's velocity, p its momentum, z its electric charge, x the thickness of the traversed material and X_0 the radiation length[1] of the material.

$$\theta_0 = \frac{13.6\,\text{MeV}}{\beta p c} z \sqrt{\frac{x}{X_0}} \left(1 + 0.038 \ln\left(\frac{x}{X_0}\right)\right) . \tag{6.1}$$

For air the radiation length at NTP is 303.9 m [5, p. 144]. The standard hadron beam in M2 has a momentum of 190 GeV/c, in good approximation $\beta = 1$ and is simply charged. For 100 m of air the standard deviation of the angular distribution coming only from multiple scattering can be calculated to be 39.3 µrad. Comparing the contribution of an additional vacuum window, which is typically a 200 µm thick mylar foil in M2 ($X_0 = 28.54$ cm [140]) resulting in 1.4 µrad, one can see the gain in terms of multiple scattering even though one needs to install additional windows.

The multiple scattering is one reason for the beam divergence and therefore for the reduction of tagging efficiency of the CEDAR detectors in M2. Another important, but controllable way of defining the beam angle, are the optics along the line themselves. According to Liouville's theorem the area of the ellipse in the beam's phase space is constant. Because the phase space is defined by the beam size and divergence[2], one can reduce the opening angle of the beam by accepting an increase in transverse size.

As already discussed during the optics design at the cavity locations for the RF separated beam, a parallel beam can be achieved by tuning the transport matrix parameters R_{22} for the horizontal and R_{44} for the vertical plane such that $R_{22} = R_{44} = 0$ at the position of interest, i.e. the CEDAR location. But this is only one part. The two other defining parameters are again R_{12} and R_{34} for both transverse directions. By increasing these parameters, one can enlarge the beam and therefore, one can achieve a more parallel beam. Of course, the limiting factor is the aperture of the CEDARs in this case, similarly as it is aperture of the RF cavities.

Of course, in the remaining part of the beamline between the CEDARs and the target it needs to be possible to focus the beam after the particles have been identified and to guide the beam towards the experiment. This sets another constraint on the beam optics depending on the needs of the experiment: Typically, the optics are tuned in a way to have a focus in the transverse plane at the experiment. In Fig. 6.1 the beam spot 6.1(a) and divergence 6.1(b) are shown.

In the illustrated case 6.1, the beam has been focused on the COMPASS target resulting in $\sigma_x = (8.817 \pm 0.010)$ mm and $\sigma_y = (6.488 \pm 0.007)$ mm assuming a Gaussian beam shape.

The beam rate quantified by the experiment is the number of particles that reach the experiment and have been successfully identified meaning a particle that could not be tagged would be of no use to the experiment. This is illustrated in Fig. 6.2 showing a histogram of the beam

[1] The radiation length is that length a high-energy electron needs to travel in a material to loose all but $\frac{1}{e}$ of its energy by bremsstrahlung.

[2] Correctly, the phase space is defined by the beam size and momentum. Because the transverse momentum is proportional to the angle with respect to the beam axis, the space generate by transverse size and angle is typically referred to as transverse phase space. In the literature, one can often find it as the trace space.

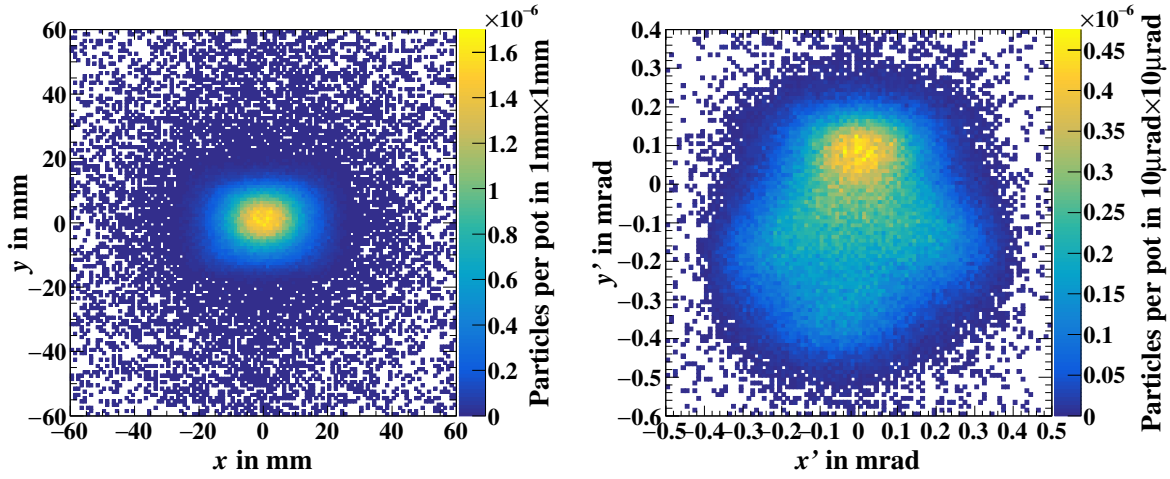

(a) (b)

Figure 6.1: Transverse beam distributions at the COMPASS target achieved with the optics used in the 2018 Drell-Yan run [141]. Fig. 6.1(a) shows the spatial profile of the beam, while the angular profile is plotted in Fig. 6.1(b). No cuts on the simulation have been applied.

divergence.

One can see the divergence of the full beam sample and the drastic reduction the more PMTs in the CEDAR are required to be in coincidence. The maximum number of eight PMTs can only be reached for particles flying through the detector with minimal divergence. This shows the effect of not being able to efficiently identify beam particles on the overall rate that would be seen by the experiment. The overall limited performance and beam intensity due to the CEDAR tagging efficiency need to be overcome. One has several options available to boost the performance:

1. The most obvious one after the initial discussion is the installation of vacuum pipes such that the beam does not traverse air at atmospheric pressure anymore. In the following, primary beam vacuum levels are assumed meaning 10^{-3} mbar, which can be achieved easily. The radiation length scales linearly with the density and therefore with the pressure resulting in around 3×10^{8} m meaning 3.6×10^{-6} radiation lengths of material budget along the whole beamline.

2. In the beam optics that have been used in the past, the beam size has been limited around the CEDAR area resulting in a more divergent beam. The reason for this is again in the missing vacuum along the line. Because multiple scattering incoherently increases the beam emittance clean collimation is only possible in a limited way as the imposed correlations between angle and position in the transverse plane are washed out. Having a beamline under vacuum therefore means that it is finally possible to increase the beam size and limit the divergence resulting in a better performance of the particle identification

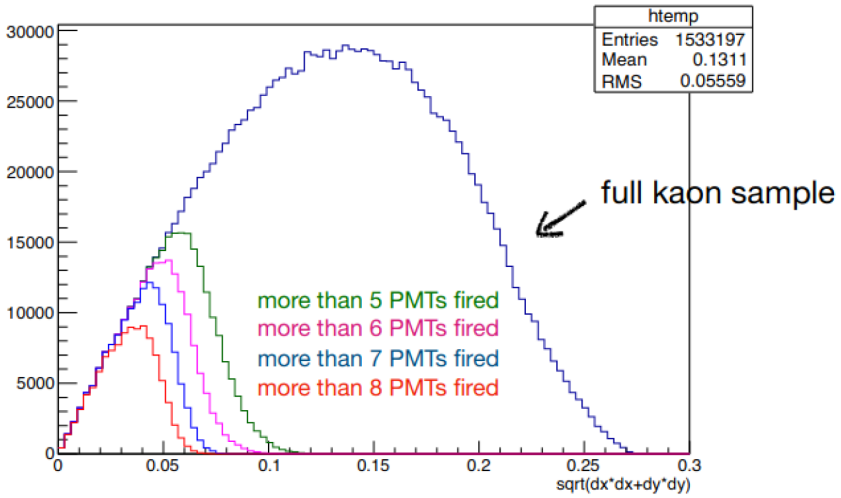

Figure 6.2: Beam divergence at the CEDARs [142]. The light blue histogram is the full beam distribution. By requiring a given number of PMTs to give a signal (indicated by the histograms with other colours) the angular distribution shrinks.

with the CEDARs.

3. Finally, besides the optics themselves, the collimation scheme can also be modified. This is of special importance in case of runs, during which the total rate sent to EHN2 needs to be limited. In such cases, it is crucial to collimate those particles that would not be identified anyway and therefore would not count in the rate measured by the experiment. If they would not be collimated they would of course still count to the total rate important for radiation-protection without being useful for the experiment.

The results presented throughout this chapter are based on simulations done with BDSIM [115], version 1.7, with Geant4 [109] version 10.7.2 and the *FTFP_BERT* physics list.

6.2 Vacuum installation

The improvement needing the highest effort work-wise, will be the installation of additional beam pipes because it requires actual hardware modifications to the beamline. Especially difficult is the incorporation of vacuum pipes in the scraper magnets, which are important for muon beam operation (cf. section 2.2.2 and chapter 7). As those are large magnets and one needs to ensure that the apertures are variable, the design to have them under vacuum is not straightforward because extremely large vacuum chambers would be necessary, which would be costly. Therefore, it is currently foreseen to fix the movable aperture and install a rectangular beam pipe following the shape of the aperture [143]. Additionally, where possible, the scrapers will be put on rails to quickly move them in and out to (de-)install the pipes whenever it is

needed. Of course, before one is able to run in muon-mode again, the beam pipes need to be removed out of the scrapers.

Besides the scrapers there are a few more magnets, where the beam passes through air. In general, the vacuum installation in the magnets is straightforward. Depending on future needs by experiments, the only critical part is the absorber section in M2 (cf. section 2.3). As those parts need to be movable to quickly change between hadron and muon operation, this changeover needs still to be guaranteed even if pipes are installed. Therefore, it is currently investigated if the absorber blocks will be incorporated in the pipes, too, or if this section has to be kept under atmospheric pressure. For the presented studies vacuum pipes are assumed there, too.

Finally, one finds vacuum interceptions at places, where beam instrumentation devices like the COMPASS Beam Momentum Stations [17] are installed.

Simulations comparing the beam quality at the CEDAR location without the completed vacuum with the described modification have been performed. In order to make statements about the beam distributions at various locations, the beamline has been constructed using the automatic model building technique described in section 4.4. The nominal momentum to calculate the needed field maps has been set to 190 GeV/c as it has been used for COMPASS's 2018 Drell-Yan run [141]. An optical description in MAD-X has been existing already, where the necessary locations of vacuum interruptions needed to be added. Those places are described in [143]. The main contribution comes from the scraper magnets, bend4 and 5, and two quadrupoles that are installed in between two of the nine scrapers. Around bend6, one can find beam instrumentation, where the beam passes through air, too. At all these locations beam pipes have been installed in the model to evalute the impact of multiple scattering.

The settings of the five collimators installed along the beamline are given in Tab. 6.1. In the model the XCBV (cf. Fig 2.10(a); it is inside plexiglass under atmospheric pressure) has been put under vacuum, too.

Collimator	Horizontal gap in mm	Vertical gap in mm
XCHV.X0610058	±25	±25
XCHV.X0610070	±25	±25
XCBV.X0610858		±7
XCHV.X0611013	±20	±20
XCHV.X0611054	±20	±20

Table 6.1: Collimator settings as they have been used for the conventional hadron beam simulation. These are the values that are typically used for hadron beam operation [144]. XCHV is referring to a 1 m-long standard four-jaw collimator (cf. Fig 2.10(b)). XCBV is a 1.2 m-long vertical two-jaw collimator (cf. Fig. 2.10(a)).

The beam instrumentation like wire chambers and CEDARs have been kept the same. So indeed, the only difference is the completed vacuum because the magnetic field maps are also

exactly the same.

The beam divergence at the CEDAR position for both case is illustrated in Fig. 6.3. All particles within a square of 10 m × 10 m contribute in the plot.

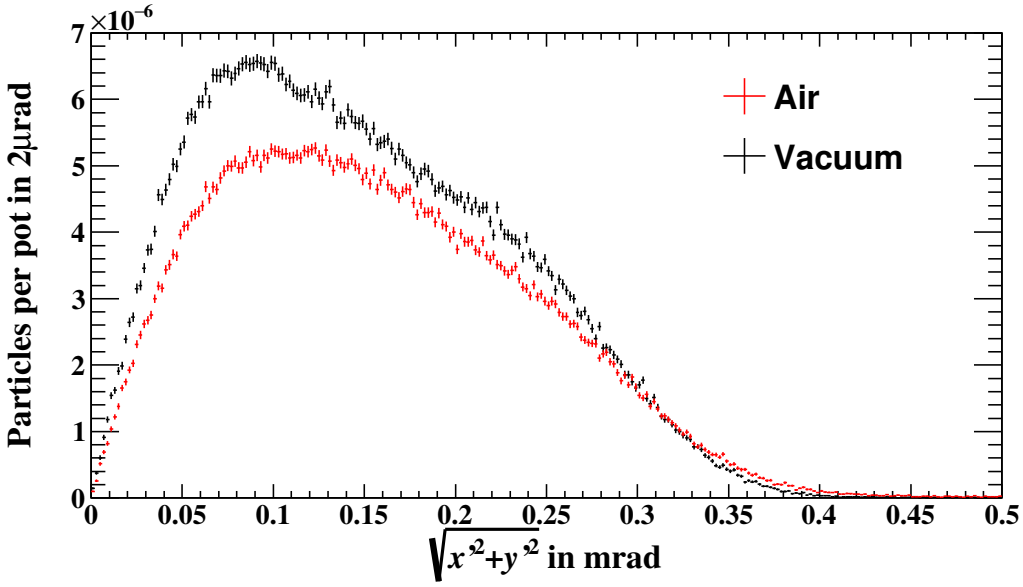

Figure 6.3: Beam divergence at the entrance of the CEDAR location in M2. The beam optics from the Drell-Yan run in 2018 have been used. In red, one can see the implementation as it has been in 2018, compared with a full vacuum setup in black.

Clearly, the overall width of the distribution is not affected by adding more vacuum in the line because it is fully dominated by the outlying background particles. Of course, background particles with large excursions and angles are not seen here as they are outside of the range. But because the plot implies the distributions go to zero anyway. The peak positions of the distributions change visibly. For the current setup, the maximum is at about 120 µrad, whereas it is reduced to 100 µrad for the completed vacuum option. This reduction arises from two effects that have the same reason, which is multiple scattering. Obviously, as there is less material in the beamline, the particles undergo less multiple scattering having less incoherent increase of emittance. The beam divergence is more determined by the beam optics itself. Another effect is an increase in transmission. Just by completing the vacuum, one can see a gain in intensity by 15 to 20 % meaning a total rate increase without sending more protons on T6. Overall, those effects already result in an overall higher total flux of particles including a higher kaon rate, too. Integrating the distributions in Fig. 6.3 yields the total number of particles identifiable by the CEDAR. For the setup in 2018 one gets $(7.477 \pm 0.033) \times 10^{-5}$ particles per proton on target, whereas the full vacuum option yields $(1.016 \pm 0.004) \times 10^{-4}$ considering only particles with a divergence of less than 60 µrad. This gain directly enters the number of kaons observed by AMBER meaning a 36 % increase compared to the COMPASS Drell-Yan measurement.

One could calibrate the numbers with the results obtained from the COMPASS data-taking period in 2018 because the same beamline setup has been simulated, too, to get the absolute particle flux. But this is not necessary as the relative gain is already visible in the particle fluxes mentioned in the paragraph above. Calibration factors would not change this gain factor. Indeed, one can use the obtained performance increase to calculate the intensity as it would have been in 2018 by just completing the vacuum. During the data-taking 1.2×10^{13} protons on T6 resulted in a flux of 4.8×10^{8} hadrons per spill in EHN2. Theoretically, one would reach about 5.6×10^{8} hadrons per spill with the same number of protons as used in 2018 coming from the increased overall flux due to the completed vacuum.

6.3 Improved beam optics

Having the whole beamline under vacuum, i.e. 10^{-6} bar, one can now change the beam optics and collimation scheme. According to Liouville's theorem a beam is more parallel the larger it is in size. This already sets the target for the optics optimisation. To achieve a larger beam one increases the R_{12} and R_{34} terms of the transport matrix of the beamline. To keep the beam parallel R_{22} and R_{44} need to be zero simultaneously just as for the RF beam. Clearly, constraints put by maximal currents of the magnets need to be respected.

The changes in R_{12} and R_{34} compared to the beam optics used in 2018 are shown in Fig. 6.4. The full beam optics are illustrated in Fig. A.6 in the appendix A.2.

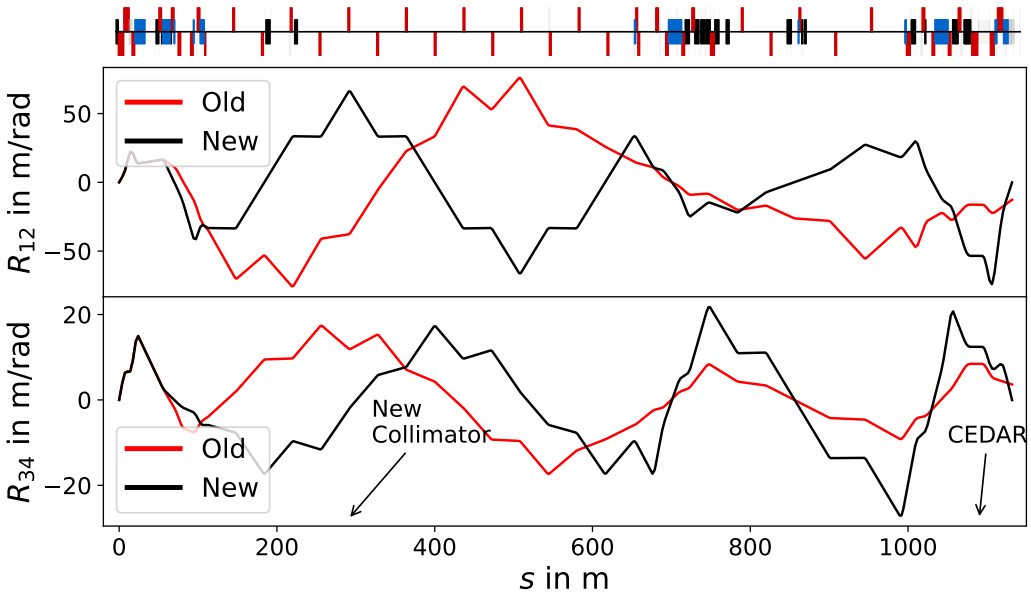

Figure 6.4: Comparison of R_{12} and R_{34} in the old and new optics as a function of the longitudinal position s. Because those terms are the main contribution to the beam size, they have been made larger and constant at the CEDAR location in order to have a more parallel beam. R_{22} and R_{44} are zero to achieve a parallel beam.

The main difference is in R_{12} and R_{34}. Because those determine dominantly the beam size it is important to achieve values as large as possible at the CEDARs still respecting their aperture. Simultaneously, these parameters need to be constant along the CEDAR area meaning no growth in beam size implying a parallel beam. No change in angle is achieved by setting R_{22} and R_{44} to zero.

With this set of magnet currents, the BDSIM model has been generated following the approach described in section 4.4. Of course, the geometry stays the same compared to vacuum implementation studied for the old optics set. Again, the driving quantity is the beam divergence at the CEDAR location. The comparison with the two distributions obtained for the 2018 optics is depicted in Fig. 6.5.

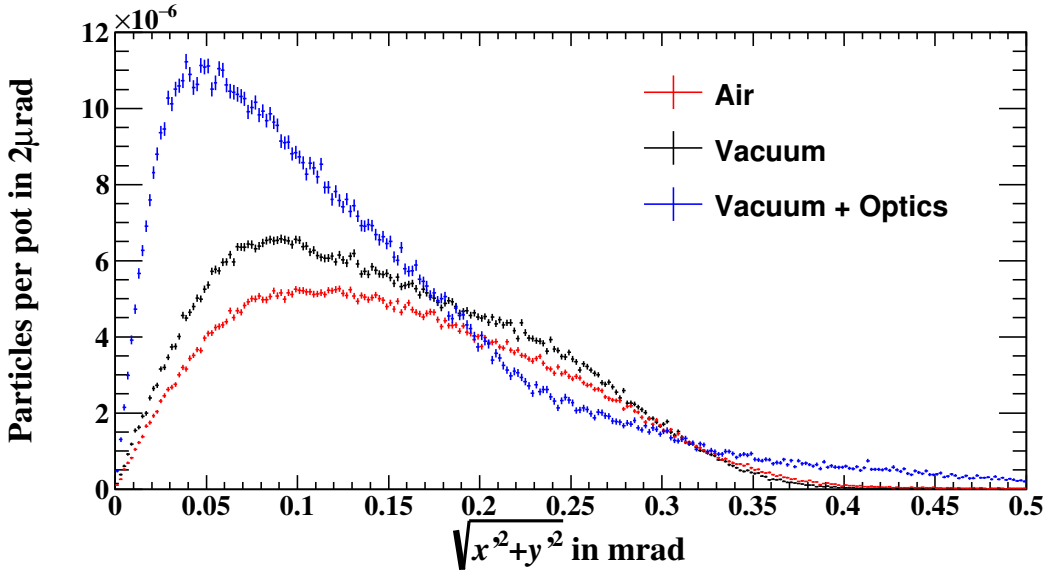

Figure 6.5: Beam divergence at the entrance of the CEDAR location in M2. The beam optics have been improved in a way that the beam is larger at the CEDARs and therefore less divergent. In red, one can see the implementation as it has been in 2018, compared with a full vacuum setup in black. In blue, the divergence expected with the improved optics including completed vacuum is shown. From [136, 137]; modified.

In the optics that have been used up to now, the beam had to be kept small at the CEDAR location to not flood the experiment with background particles coming from downstream collimation close to the target [145]. It has not been possible to collimate the beam while it has still passed through the underground part of the line because the multiple scattering has washed out the imposed correlations between angle and position. Now, without the additional material along the line, the beam can be collimated further upstream and therefore made larger at the CEDARs.

Clearly striking is the shift of the peak position. Now, the maximum is at 50 µrad meaning a reduction by a factor 2.4 compared to 120 µrad for the old setup. Of course, the width of the

distribution is still dominated by mostly background particles with large divergence. Therefore, there is again no clear reduction of it. Again, as it has been already observed by just completing the vacuum, one can see an increase in peak height by nearly a factor two compared to the completed vacuum plus old optics option. But not only the distribution has a higher maximum, again the integral of it up to 60 µrad yields $(2.500 \pm 0.009) \times 10^{-4}$ particles per proton on T6 meaning a gain of 3.344 ± 0.019 in contrast to the version of the line as it has been up to now.

The studies have been performed aiming at highest total intensities. Naturally, when requiring lower rates, one needs to collimate the beam further. With additional collimation, one wants to remove unwanted particles. In the present case, unwanted particles are the ones that are not identified by the CEDARs and do not contribute to the intensity measured by AMBER. So, during runs with limited intensity, either imposed by radiation-protection or the experiment itself, in the best case one should remove those particles. Overall, this would be visible by a shrinking of the overall beam divergence and a gain of intensity in 60 µrad[3] compared to the full intensity. These effects have been studied with an additional horizontal collimator at about $s = 300$ m from T6. The results are shown in Fig. 6.6.

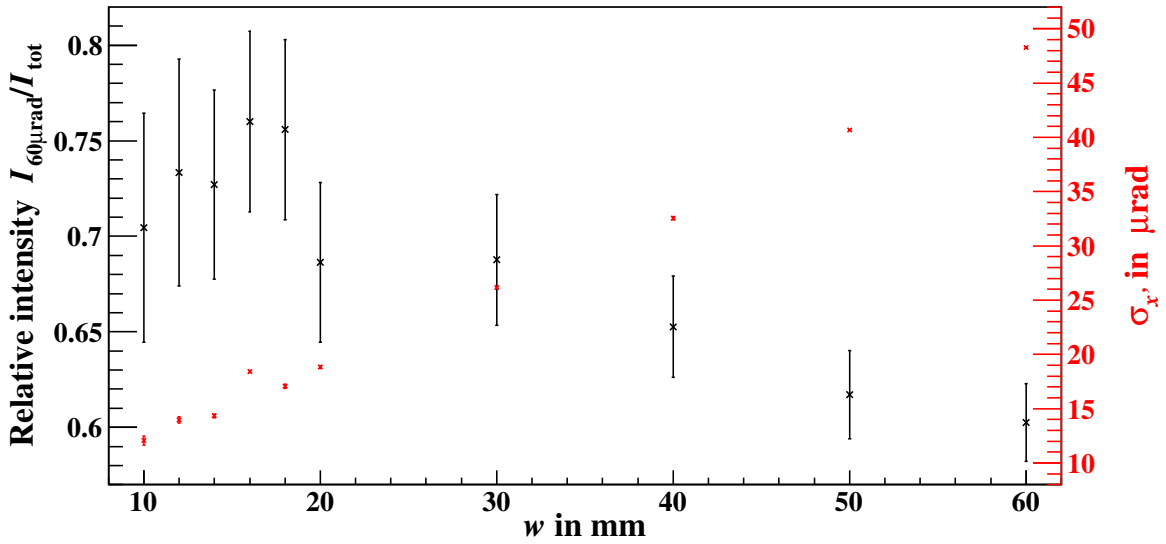

Figure 6.6: Impact of an additional horizontal collimator ($s = 300$ m) on the horizontal divergence at the CEDAR location. The spread of x' is plotted in red. The ratio of intensity in 60 µrad to the full intensity is given in black. Both are estimated for various collimator gaps. From [136, 137]; modified.

To estimate the performance of this collimator, the beam divergence and intensity are scored in front of the CEDAR area in M2 at about 1 090 m downstream from T6. Fig. 6.6 shows exactly the points mentioned before. An additional horizontal collimator helps reducing the horizontal divergence of the beam meaning effectively collimating particles with large

[3] Or more generally, flux of particles with divergence low enough to be detected by the CEDARs.

divergence. Therefore, the relative intensity of particles with small angles goes up compared to the overall observed one at that specific location.

6.4 Beam at AMBER

Finally, the beam distributions at the AMBER target can be investigated for the full vacuum setup and the improved beam optics. The last three quadrupoles between CEDAR area and experiment have been used to generate a focus in the transverse plane at the target location. Considering the gains presented in the previous sections, an improvement of intensity by a factor of three is expected compared to prior COMPASS runs.

Fig. 6.7 illustrates the maximum beam divergence at various momenta to still be able to differentiate pions and kaons. It is based on Fig. 2.16 from [63].

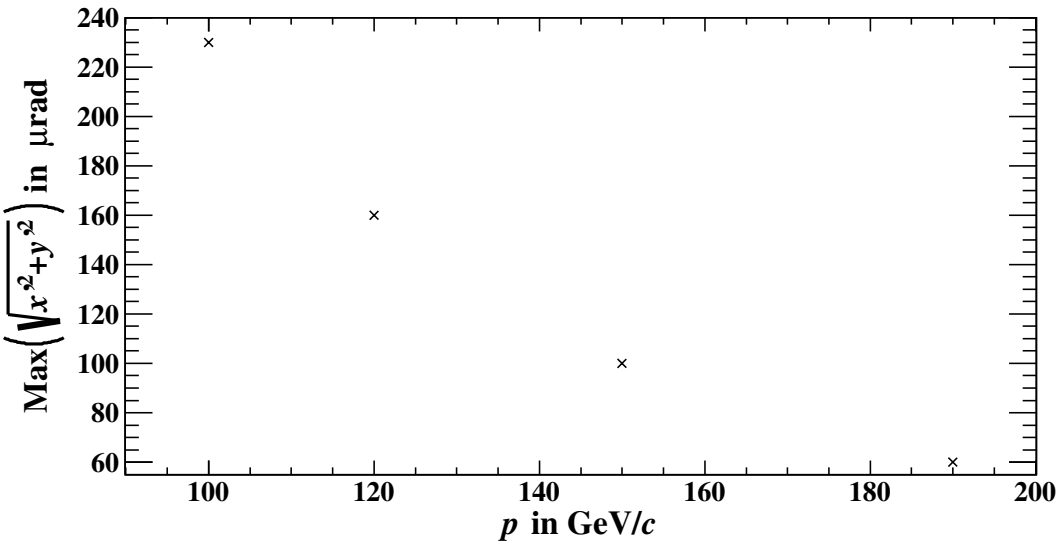

Figure 6.7: Maximum beam divergence in CEDAR-N to be able to separate pions and kaons at various momenta. Based on Fig. 2.16 from [63]. The maximum has been extracted for the four beam momenta that are used below to estimate the AMBER detector performance.

As the difference in velocity increases with decreasing momentum, the difference in Čerenkov angle also increases making pion-kaon separation easier. In the past, a downside of a decreased momentum has been the multiple scattering because it scales inversely with the beam energy. Therefore, a trade-off between multiple scattering and CEDAR efficiency has been necessary. Now, with the decreased amount of material along the beamline, it is possible to consider an optimisation of the beam momentum in terms of particle identification with various systems. To do so, the beam spot and spectra at the AMBER have been simulated at momenta of 100, 120, 150 and 190 GeV/c. As an example, the beam spot and divergence are shown in Fig. 6.8 and the spectrum of hadrons can be seen in Fig. 6.9 for 190 GeV/c.

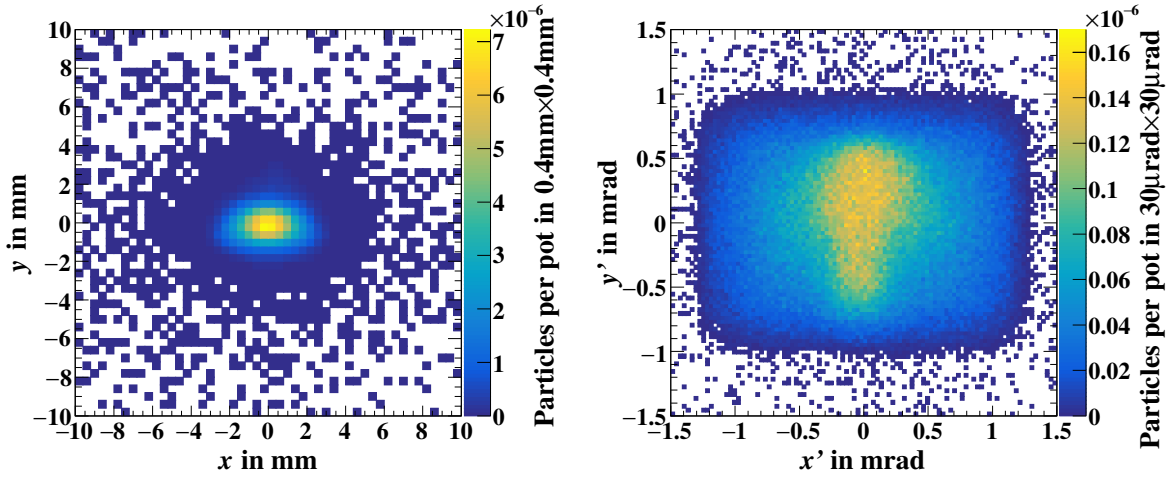

(a) (b)

Figure 6.8: Beam distributions at the AMBER target achieved with the new optics and vacuum at 190 GeV/c beam momentum. Only protons, pions and kaons successfully identified by the CEDARs are included. Fig. 6.8(a) shows the spatial beam profile, while one can see the beam divergence in Fig. 6.8(b).

In the illustrated distributions, only π^+, K^+ and p have been considered. Additionally, a cut on the divergence at the CEDAR location has been made. If it is smaller than the maximal value given in Fig. 6.7, the particle contributes to the plots. The beam is well focused onto the AMBER target with $\sigma_{x,y} \approx 1\,\text{mm}$. Also, the spectra are peaking around the expected 190 GeV/c with $\sigma_p \approx 2\,\text{GeV}/c$, so 1 %. The obtained fractions of K^+ and K^- in the beam at the various momenta are given in Tab. 6.2. They are about 2 % with the maximum around 120 GeV/c. For high energies is decreases again because of the increased fraction of protons. In addition, the fraction of the beam that is inside the maximal divergence is also given in Tab. 6.2. Interestingly, the fraction can be increased by more than a factor three when going from 190 to 100 GeV/c. The beam composition, considering the previously described cuts on the particles and divergence, is illustrated in Fig. 6.10[4].

Comparing the composition to the values obtained from the Atherton formula together with the average decay rates it is in good agreement for the positive beam especially considering that the parameterisation is precise to the order of 10 %. For the negative beam the share of K^- and $\bar{p}$ is different to what one expects from Eq. (2.1) together with decays. At 190 GeV/c one can calculate a fraction of K^- of ca. 2.4 %, while the simulation yields only (0.96 ± 0.15) %. Also, according to the Atherton formula more K^- are expected than $\bar{p}$. Both can be explained by the particle production models used in Geant4. In [44] one can find that one has about (0.55 ± 0.02) % $\bar{p}$ in forward direction at 200 GeV/c coming out of interactions of 400 GeV/c protons with a 500 mm-long beryllium target. Simultaneously, (4.44 ± 0.13) % K^- are expected.

[4] Of course, the cut on the divergence does not influence the composition because the transverse phase space looks the same for the considered particles as they have the same electric charge.

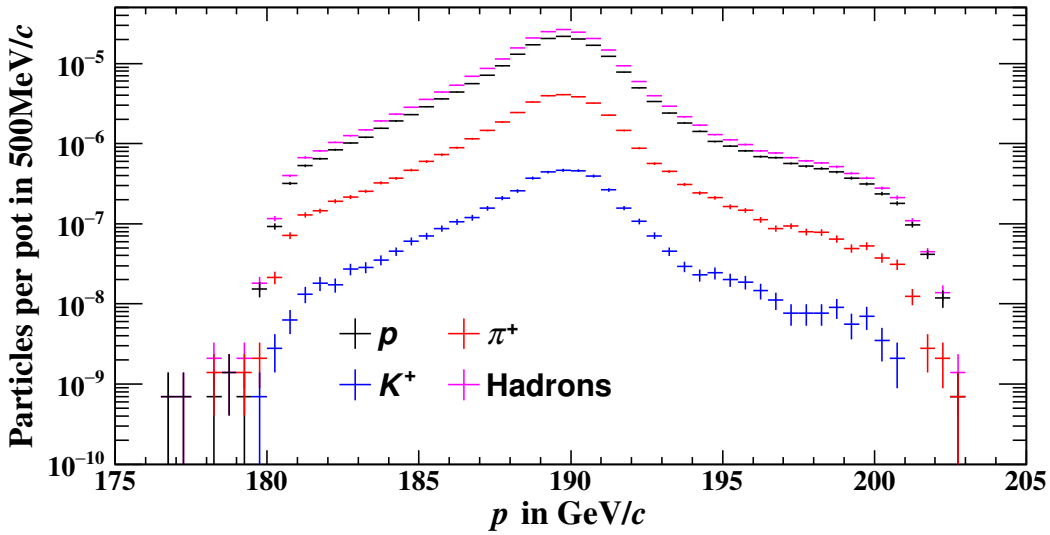

Figure 6.9: Spectrum of hadrons at the AMBER target with a divergence smaller than 60 µrad at the CEDAR location. Kaons are shown in blue, pions in red, and protons in black. The pink histogram is the sum of those three species.

p in GeV/c	Fraction of K^+ in %	Fraction of K^- in %	Identified by the CEDAR in %	RICH efficiency in %
100	2.084 ± 0.020	1.32 ± 0.07	83.28 ± 0.17	80.61 ± 0.31
120	2.206 ± 0.021	1.48 ± 0.08	68.18 ± 0.13	71.10 ± 0.28
150	2.192 ± 0.023	1.25 ± 0.09	45.55 ± 0.12	57.56 ± 0.25
190	1.791 ± 0.023	0.96 ± 0.15	26.21 ± 0.11	44.21 ± 0.21

Table 6.2: The abundance of kaons obtained in the beamline simulation is given for various beam momenta together with the CEDAR and RICH particle identification efficiencies. The muon flux is not included in the normalisation to calculate the kaon fraction.

Estimating the composition directly after T6 in the simulation yields (3.6 ± 0.5) % $\bar{p}$ and (3.3 ± 0.5) % K^-.

The obtained distributions can finally be used to estimate the performance of the AMBER detector mainly meaning the efficiency of the RICH-1 detector (in the following it is referred to just as RICH) responsible for particle identification. AMBER aims at similar data-sets when it comes to strange meson spectroscopy as COMPASS has collected for the pion spectroscopy. Due to the similarity of the processes, the analysis done at COMPASS can be transferred to AMBER with only minor changes.

The AMBER collaboration provides a Geant4-based implementation of the whole setup, called **T**otal **Ge**ometry **an**d **T**racking TGeant [146], originally developed for the COMPASS experiment. The setup is shown in Fig. 3.2.

It is possible to load different configurations for the various data-taking periods. In 2008

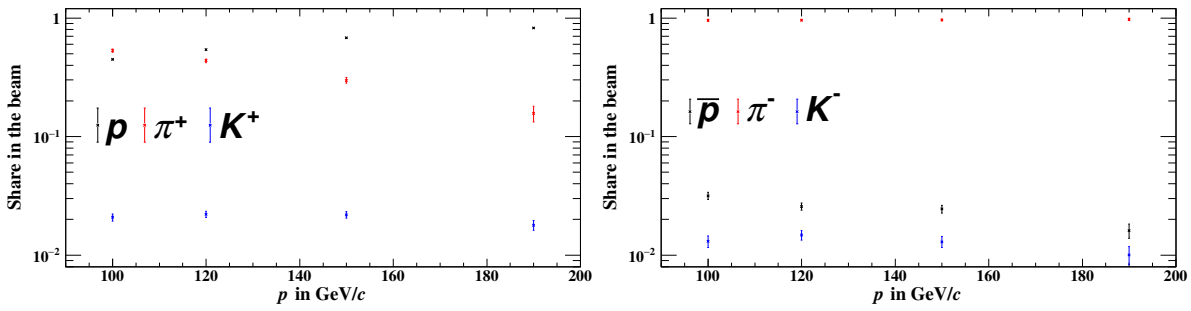

(a) (b)

Figure 6.10: The expected beam composition at the AMBER target coming from the beamline simulation is plotted for various beam momenta. Only (anti)protons, kaons and pions have been considered depending on the beam charge. Muons are not included in the normalisation. Fig. 6.10(a) shows the abundance of protons (black), positive pions (red) and kaon (blue) in the positive beam (error bars are increased by a factor five). In Fig. 6.10(b) the shares of antiprotons (black), negative pions (red) and kaons (blue) in the negative beam are given (error bars enlarged by a factor two).

and 2009, hadron beams have been used to explore spectra of light mesons. A liquid hydrogen target with 400 mm length has been used most of the time [106]. Therefore, the setup as it has been in the mentioned years is used for the following investigations. TGeant offers also the possibility to load realistic beamfiles. Therefore, the distributions obtained from the beamline simulations including the mentioned cuts, are written into a TGeant-readable format. In the following, it is assumed that all particles in those samples are K^+ to better sample the underlying phase space. Afterwards, with the numbers given in Tab. 6.2, it is possible to correct for the fraction of kaons. TGeant also offers a so-called phase space generator of different processes. One can hand over mass- and momentum-transfer distributions of resonances. After defining their decays, the final-state particles are propagated through the setup. The distributions for the process $K^+ + p \rightarrow K^+\pi^+\pi^- + p$ are taken from [59] with the assumption that they look the same as for the case with a K^- as beam particle. For each beam energy, about 10^5 $K^+\pi^+\pi^-$-events are generated with the described approach.

With the **CO**MPASS **R**econstruction **AL**gorithm CORAL [17], the data obtained from the simulation can be digitized and translated into the values as they would be in real data-taking. It also reconstructs the produced events by means of track reconstruction, particle identification etc. Finally, it is possible to analyse the data within the **PH**ysics **A**nalysis **S**oftware **T**ools framework Phast. First of all, certain cuts need to be applied to purify the data to only have events that are surely coming from the process of interest. This is done similarly as it has been done for the three-pion final states in COMPASS [106, 107, 147]. Those cuts will be described shortly. First of all, it is necessary that only one primary vertex has been reconstructed. The reconstructed primary vertex needs to be inside the target to ensure that it has not been an interaction with surrounding material. In addition, the recoil proton detector needs to confirm a recoil proton because it is required to keep the proton intact and just excite the beam kaon.

Furthermore, three charged particles are required to come out of this primary vertex. Naturally, energy, momentum and charge conservation are also enforced. Finally, the RICH detector comes into play. In [59] an approach based on likelihoods has been developed to optimise the efficiency and purity of the particle identification. This is already implemented in the analysis software and can be used. As the final state of interest is $K^+\pi^+\pi^-$ omitting the recoil proton, the RICH needs to successfully identify those three particles. This is different to the three-pion final state, where it is needed to be ensured that no kaon has been reconstructed. From experience obtained in COMPASS, the RICH has a limited performance as soon as a kaon and pion have momenta above ca. 50 GeV/c [59]. Therefore, an interesting quantity to investigate is the correlation between the momenta of the K^+ and π^+ for the different momenta. Due to energy and momentum conservation an increase of acceptance is expected for lower beam momenta because it becomes less likely to have both particles with high energies. The distributions are given in Fig. 6.11.

As mentioned already, with increasing beam momentum there is more momentum available such that the K^+ and π^+ get momenta that make it more difficult to separate those. Consequently, the acceptance decreases. Similarly to the analysis presented in [59], in case the K^+ cannot be differentiated from the π^+, but two positively and one negatively charged particle have been identified, the event is still kept due to the knowledge of the beam particle being a kaon. The values obtained for the RICH efficiency after the aforementioned cuts have been applied are summarized in Tab. 6.2. It goes down from about 80 % for 100 GeV/c beam momentum to 45 % for 190 GeV/c.

Having those values, it is finally possible to estimate the time needed to collect a certain number of $K^+\pi^+\pi^-$-events. To do so, the instantaneous luminosity defined in Eq. (3.2) is important. In the following it is assumed that it stays constant over time meaning that one can calculate the total number of events by just multiplying with the time interval corresponding to the data-taking period. First, one needs to calculate the number of spills coming from the SPS available in one year. The best supercycle has a duration of ca. 30 s with two spills [148]. This would result in 5 760 spills per day. Of course, this is an optimistic assumption keeping downtime of the machine, different users (especially filling of the LHC) and also detector maintenance in mind. If one assumes about one spill every 30 s due to those reasons, one would have about 3 000 spills per day[5] [145]. About 3 000 spills in one day have been communicated by COMPASS for data-taking in 2022 [149]. Typically, operation starts in April and ends in October, meaning half a year. Therefore, 150 d [150] are considered as the maximum number of days for physics data-taking because calibration runs need to be taken and the beamline is shared with other experiments, too. This results in 4.5×10^5 spills per year.

For the COMPASS runs concerning light meson spectroscopy a beam intensity of $5 \times 10^6\ \mathrm{s}^{-1}$, or 2.4×10^7 per spill has been available. For AMBER data-taking it will be possible to go up to 7×10^7 particles per spill in EHN2[6]. Therefore, this intensity is used for the following

[5] Values between 2 500 and 4 000 can be found for instance in the AMBER phase1 proposal [19]. Of course, the number of spills per day is highly dependent on external conditions and can therefore vary by several 10 %.

[6] This is allowed if all heavy materials are removed from the detector setup downstream of the SM2 magnet

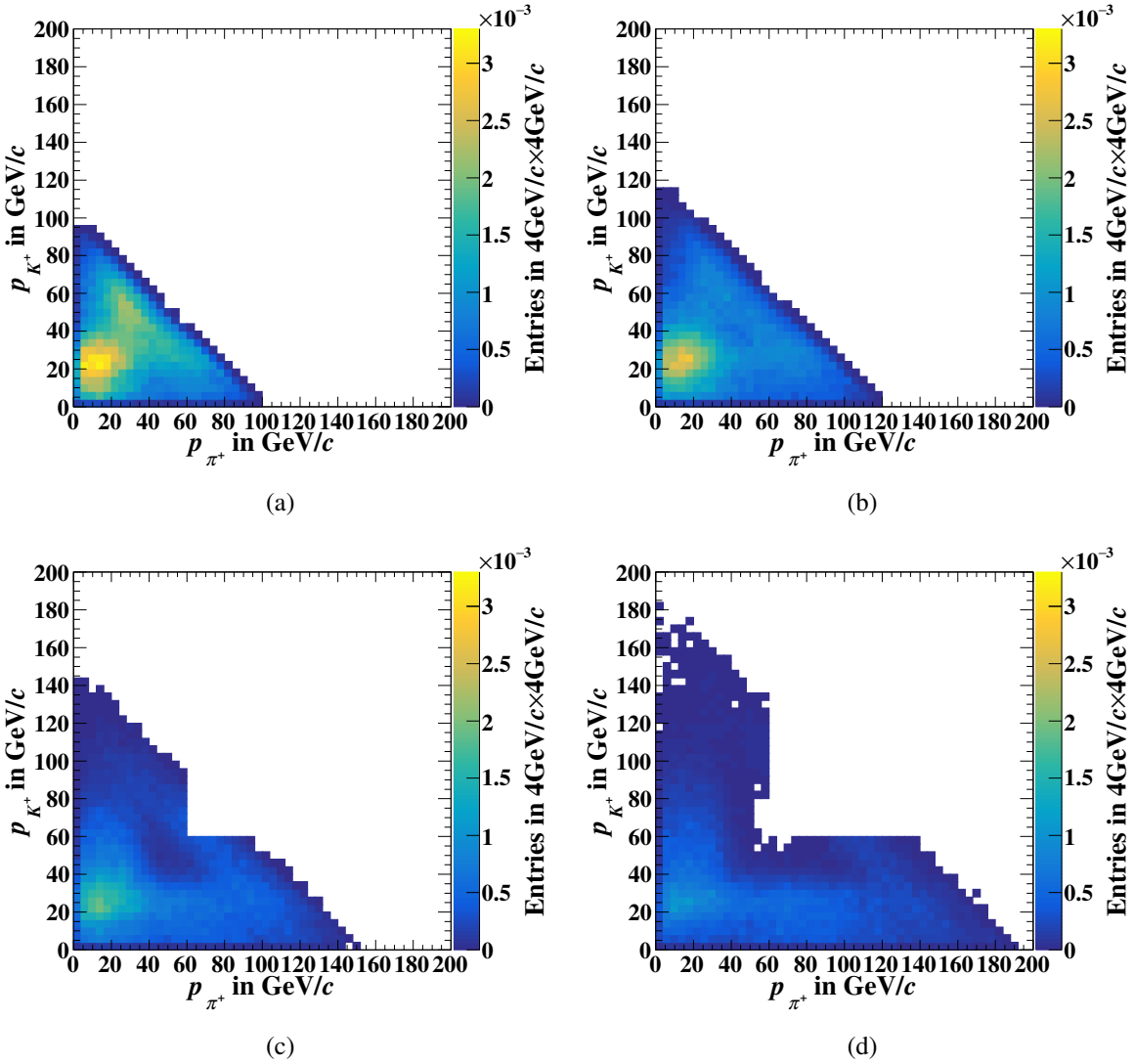

Figure 6.11: RICH efficiency for different beam momenta. All histograms are normalised to the number of simulated events. The unnormalised histograms are given in the appendix A.3. The correlation between the momenta of the outgoing K^+ and π^+ are plotted. Fig. 6.11(a) is obtained at 100 GeV/c beam momentum, Fig. 6.11(b) at 120 GeV/c, Fig. 6.11(c) at 150 GeV/c and Fig. 6.11(d) at 190 GeV/c.

calculations. This number needs to be scaled with the fraction of K^+ in the beam, which is about 2 % depending on the momentum. In addition, the effect of the CEDAR efficiency needs to be taken into account, which goes up from about 25 to 83 % when decreasing the beam momentum. Of course, this assumption is too pessimistic considering the approach developed by COMPASS using track information measured by the spectrometer to get the particle's

because those are sources of hadronic showers.

divergence at the CEDAR position [59–61]. Typically, efficiencies of about 80 % have been achieved for 190 GeV/c, so about a factor three better. This is not considered here meaning the maximum number of data-taking days is estimated. Therefore, by applying more sophisticated analysis techniques the number can only decrease. Additionally, one needs to account for the efficiency of the final-state particle identification, i.e. the RICH efficiency. Overall, with such a spill intensity and detector efficiencies, one gets $3.15 \times 10^{13}\,\mathrm{yr}^{-1} f_{K^+}\epsilon_\mathrm{C}\epsilon_\mathrm{R}$ identified, positive kaons with the fraction f_{K^+} of K^+, the CEDAR efficiency ϵ_C and the RICH efficiency ϵ_R[7]. For 100 GeV/c this results in a flux of K^+ of $4.41 \times 10^{11}\,\mathrm{yr}^{-1}$ and $6.54 \times 10^{10}\,\mathrm{yr}^{-1}$ for 190 GeV/c.

The other important quantity to calculate the luminosity (3.2) besides the flux is the areal number density of the target. Because the employed target consists of liquid hydrogen, the density is $0.0708\,\mathrm{g\,cm}^{-3}$ and the molar mass is $2.016\,\mathrm{g\,mol}^{-1}$ [151]. With the Avogadro number $N_A = 6.022 \times 10^{23}\,\mathrm{mol}^{-1}$ [5] one obtains a number density of $2.116 \times 10^{22}\,\mathrm{cm}^{-3}$. For a 40 cm long target [106] one gets an instantaneous luminosity of $2.6648 \times 10^{37}\,\mathrm{yr}^{-1}\,\mathrm{cm}^{-2} f_{K^+}\epsilon_\mathrm{C}\epsilon_\mathrm{R}$, again assuming about 4.5×10^5 spills per year in total[8].

The goal is to collect a data-set that is comparable in size as the one for the three-pion final state in COMPASS. Therefore, the target set in the letter of intent [18] is 2×10^7 events. For the diffractive excitation of a beam pion of 205 GeV/c and the subsequent decay into the three-pion final state one can find a cross section of $\sigma = (423 \pm 41)\,\mu\mathrm{b}$ [106, 152]. In other sources measuring the $K\pi\pi$-final state at lower energies one finds cross sections of about $(61 \pm 3)\,\mu\mathrm{b}$ at 40 GeV/c [153] and up to $(250 \pm 12)\,\mu\mathrm{b}$ at 63 GeV [154]. [155] shows various cross sections of kaon-induced reactions. For the diffractive excitation, only values measured up to 30 GeV/c are given, but are also of the order of 200 to 300 µb. Due to these various different numbers, an energy-independent cross section of 250 µb is assumed in the following. One obtains $\frac{1\,350.95\,\mathrm{spills}}{f_{K^+}\epsilon_\mathrm{C}\epsilon_\mathrm{R}}$, or $\Delta t = \frac{0.003\,\mathrm{yr}}{f_{K^+}\epsilon_\mathrm{C}\epsilon_\mathrm{R}}$. For the values given in Tab. 6.2, this results in 0.215 yr for 100 GeV/c and 1.447 yr for 190 GeV/c. Of course, the CEDAR efficiency has been higher than the value used in the present analysis for 190 GeV/c. Having about a factor three better CEDAR efficiency as it has been achieved with COMPASS, the run time would be about 72 d. For the low beam momentum, there is not much to gain with an improved tagging by the CEDARs because the efficiency is already above 80 % assuming the mentioned hard cut on the beam divergence. One can deduce already from those numbers that running at lower beam momenta is more beneficial due to easier particle identification. One does not need to do more sophisticated analyses to reject especially the pion-component in the CEDAR and can reach similar efficiencies as they have been achieved with COMPASS.

Besides the mentioned detection efficiencies, one also needs to consider the geometric acceptance of the setup. In previous analyses of the three-pion final state, a value in the range of 40 to 50 % depending on the momentum transfer and resonance mass was obtained [156].

[7] As mentioned already, 1 yr corresponds to 150 d of operation.

[8] One can express the instantaneous luminosity also in terms of the number of spills, too. One obtains about $5.9218 \times 10^{31}\,\mathrm{cm}^{-2}\,\#\mathrm{spills}^{-1} f_{K^+}\epsilon_\mathrm{C}\epsilon_\mathrm{R}$. Doing so, it is possible to estimate the number of spills needed to collect a certain number of events. This is independent of the number of spills the machine can deliver in a given time period.

Additionally, not the full kinematic region is of interest. In the previous analyses in [156] focusing on the three-pion final state and in [59] on the $K\pi\pi$ final state, only momentum transfers t' between 0.1 to 1 GeV^2 c^{-2} and resonance masses between 0.5 to 3 GeV/c^2 have been investigated. Considering the t'-distribution given in [156], i.e. $\exp(-10.8t') + 0.1\exp(-3.9t')$, the number of events in the given range will be only about 41 %. In addition, in the $\pi\pi\pi$ final state, about 85 % of the events have been collected in the mass range of interest. Considering those effects on top, the number of spills that need to be collected and therefore the run time will increase accordingly. One obtains about 7×10^5 spills or 1.54 yr for 100 GeV/c and 4.7×10^6 spills or 10.42 yr for 190 GeV/c (or about 3.5 yr considering the likelihood approach for beam particle identification presented in [59–61]).

The chosen beam charge has an additional impact on the kaon flux. As the allowed number of particles during operation is limited by radiation-protection, the only quantity that matters is the kaon fraction. For both beam charges the kaon fraction is of the order of 2 %. The fraction is slightly higher for lower momenta in the positive beam and for higher momenta in the negative beam. Because the particle identification, both beam and final state, works better for lower momenta, it is favourable from this point of view to use lower momenta as long as the identification cannot be increased significantly. Therefore, it is beneficial to run with the positive hadron beam option, which has an additional advantage. The most challenging part for the beam particle identification is the clear pion-kaon separation, whereas kaon-proton separation is easier, which is shown in Fig. 6.12.

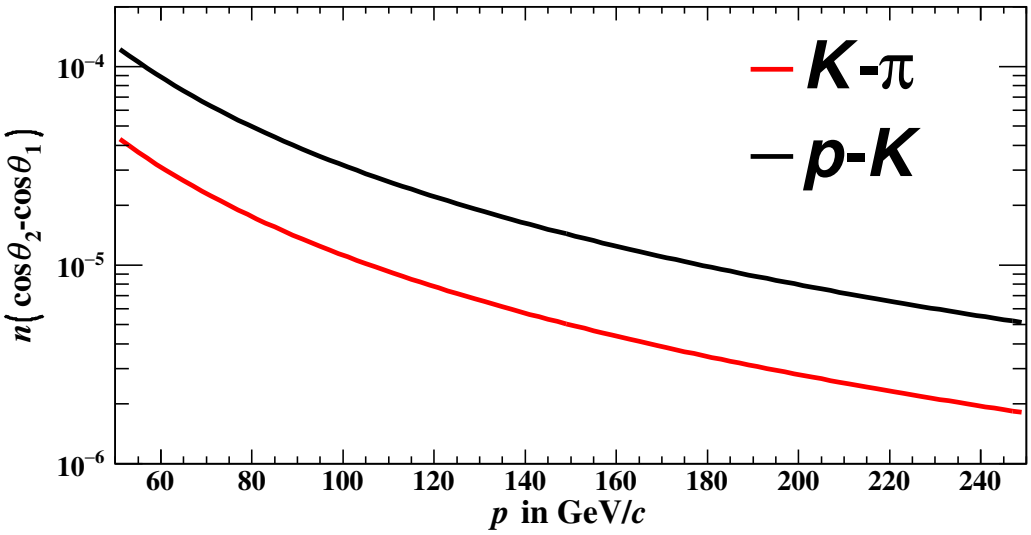

Figure 6.12: Difference in Čerenkov angles for (anti-)protons, kaons and pions based on Eq. (2.23) as a function of the momenta of the particles. n refers to the index of refraction of the detector gas. In red the kaon-pion separation is given. The kaon-(anti)proton separation is plotted in black.

As one has a reasonable proton component in the positive beam ($O(40\,\%)$ for momenta

around 100 GeV/c cf. Fig. 6.10(a)) one can collect a cleaner data sample with the positive beam because the rejection of the proton fraction in the beam is easier. In the negative beam, the pion fraction is always around 95 % meaning one needs to differentiate the kaons from the vast majority of beam particles.

Detection efficiency is not the only key parameter to determine the performance of a setup. Purity of the obtained data sample is also an important quantity. To estimate effects coming from other beam particles like the pion component one would need to do a background Monte Carlo study. If the the other components are wrongly identified as kaons one pollutes the collected sample. With data from other experiments, it is at least also possible to estimate the order of magnitude of this misidentification. For the high beam momentum one can make use of analyses performed by the COMPASS collaboration presented in [59]. For the CEDAR performance for kaon identification at 190 GeV/c one can find misidentification probabilities of about 3 % referring to cases, where a pion was wrongly identified to be a kaon. Therefore, one would need to assume a similar value for the strange-meson spectroscopy at AMBER when running at high beam momenta. Such a rate would imply that the number of pions, which are wrongly identified as kaons, is of the same order of magnitude as the number of correctly identified kaons because the pion rate is a factor 30 higher at high momenta in the negative beam. The NA62 experiment [39] features a high-intensity kaon beam[9] at 75 GeV/c. For beam particle identification a CEDAR detector type West is employed, which can separate pions from kaons up to 150 GeV/c [58]. The collaboration investigated the particle identification performance and communicated efficiencies above 95 % when requiring 4-fold coincidence[10] with a low misidentification probability of 10^{-4} [157]. With such a performance, the pion component in the beam can be rejected successfully having only a minor pollution of the kaon sample.

6.5 Conclusion

The performance of the beamline setup used in 2018 for the COMPASS Drell-Yan run has been investigated. Crucial during hadron operation is the identification of the beam particles reaching the experiment. Because those are tagged with Čerenkov detectors any divergence of beam particles lead to a decrease of identification efficiency. Therefore, the beam needs to traverse the CEDARs as parallel as possible.

A major source of incoherent emittance increase is the multiple scattering that occurs due to vacuum interruptions along the beamline. Those parts, where the beam passes through air at atmospheric pressure sum up to about 100 m, so around 10 % of the full beamline. Of course, some interruptions are needed, for instance around the TAX, which needs to be able to absorb the full primary proton beam extracted towards T6 in case of failures. Because these

[9] The kaon fraction is about 4 % [157].

[10] The coincidence refers to the number of photo-multipliers that give a signal. As they are arranged in a circle around the beam axis, the more PMTs give a signal the cleaner the sample is.

devices need to be movable vertically to have the option of different intensities, no beam pipe can be installed. Still, the major amount of the mentioned 100 m can be put under vacuum. About 50 m are due to in-air installation of the magnetic collimators, called scrapers, which are important for muon operation (cf. chapter 7). Those collimators have variable apertures, which can be tapered, too. Depending on the needs of the experiment, these apertures need to be optimised and changed. Therefore, no vacuum pipes have been installed yet. But by completing the vacuum the total transmission along the beamline can be increased without having more protons on T6. The gain is of the order of 15 to 20 % directly impacting the intensity at the AMBER target. On top, removing the contribution to the beam divergence by multiple scattering increases the number of particles that can be identified by the CEDARs when requiring the full number of PMTs, i.e. eight, to fire, the so-called majority method. Considering the higher transmission and better identification, one would have ca. 36 % more kaons[11].

Another possibility to increase the number of kaons to the experiment is the optimisation of the beam optics. By making the beam larger in size, one can decrease its divergence having a higher tagging efficiency. With those modifications to the magnet settings including the vacuum completion one can gain an overall factor 3.3 compared to previous COMPASS measurements[12]. When lower intensity runs are foreseen, one needs to remove those particles from the beam that would not be seen by the experiment. This is achieved by collimation. The effect of an additional collimator on the horizontal divergence has been investigated. It has been shown that such a collimator can help efficiently removing particles outside of the tagging acceptance reducing the overall width of the angular distribution of the beam. Therefore, such a collimator can be used to reduce the intensity for example considered by radiation-protection without impacting the intensity relevant for the experiment.

Compared to previous COMPASS runs, an improved shielding has been developed by radiation-protection, too [102]. With its installation, it will be allowed to have an instantaneous rate of 10^9 particles per spill (200 MHz) in EHN2 [102] meaning already a factor two gain in terms of kaon rate even without the improvements concerning the beamline. Considering in addition that in the previous runs, typically 1.2×10^{13} protons on T6 have been used, one has 25 % margin when increasing to 1.5×10^{13}. Clearly, this higher primary rate can be used to further collimate the beam and to make optimal use of the allowed intensity in EHN2.

The improved beam optics settings have been used to estimate the performance of the AMBER detector for the strange-meson spectroscopy campaign. For that study several beamfiles have been generated at various momenta that have been used as input for the full simulation of the AMBER setup including event reconstruction. The analysis has shown that lower momenta are preferable when it comes to both, initial- and final-state particle identification. Several analyses performed by COMPASS have shown that with more advanced techniques the beam particle

[11] Only identified particles count to the intensity seen by the experiment.

[12] The gain factor refers to the number of particles in 60 µrad, which is the maximal divergence the particles can have at 190 GeV/c to be still identified.

tagging can be optimised to reach values of 85 % [59–61] at 190 GeV/c. Still, with a momentum of 100 GeV/c this value can be reached already with just the majority method, so just the signal the CEDARs sent. Also, the misidentification probability is expected to be lower because clear separation is easier. With a cross section for the process $K^+ + p \rightarrow K^+\pi^+\pi^- + p$ of the order of 250 µb a period of about 1.5 yr or 250 d is expected to collect a sample with 2×10^7 events.

CHAPTER 7

M2 muon beam

It is also possible to send high-intensity muon beams via M2 in EHN2. The muon beam developed originally for the SMC experiment [158] and later on used by the COMPASS collaboration is described and explained in detail in [90]. Nowadays, it is also used by the MUonE [21] and NA64 collaborations [20, 38]. So far, the muon beam has been studied with the Fortran-based Monte Carlo packages HALO [159] and TURTLE [160]. Those are able to track particles through magnetic fields and estimate halo contributions in muon beams. Particle-matter interactions are not included. Therefore, it is not possible to study beam-induced backgrounds. Dark matter experiments like NA64 are extremely sensitive and rely on a precise knowledge of background processes. Therefore, it is necessary to provide a realistic 3D model in Geant4 of the beamline serving the experiment such that one is able to study possible beam-induced backgrounds.

7.1 Motivation

The development of the muon beam model has been done as an important input for NA64 allowing also to benchmark the simulation with real data. Therefore, the presented study in this chapter has been carried out in close collaboration with them. Details of the NA64 physics program can be found in the proposal [20] and will be shortly summarized here. The aim of the experiment is to look at invisible decays of a dark matter boson Z', which is assumed to couple mostly to muons and tauons. This dark boson could be an explanation for the anomalous magnetic moment of the muon being 3.6σ off from the Standard Model value [161]. The experiment is based on detection of missing momentum. Therefore, the momentum of the incoming muon is measured precisely. It will then scatter of a heavy active target. In case the dark boson exists it could be produced in the scattering of the muon on the target. This process is illustrated in the Feynman diagram 7.1. With such a setup, NA64 will also be able to probe the dark photon A' produced via bremsstrahlung of the scattered muon. In both cases, the signature would be large missing momentum of the scattered muon, independent of the dark matter particle being stable or decaying invisibly (to neutrinos or other dark matter particles).

Of course, if its mass is large enough it could decay into a $\mu^+\mu^-$-pair, so the decay would be visible.

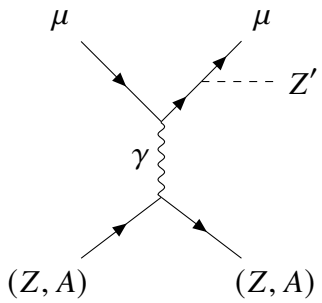

Figure 7.1: Feynman diagram showing the production of the dark matter boson Z'. A high-energy muon scatters off a heavy target and produces the Z'. From [20]; modified.

The general challenge of dark matter searches is the coupling of Standard Model particles to dark matter. In the present case, it is expected to be of the order of 10^{-8} [20]. For comparison, the electromagnetic coupling α, i.e. fine-structure constant, is about $\frac{1}{137} \approx 7.3 \times 10^{-3}$ [5]. From this one can can conclude that for conducting dark matter experiments, precise knowledge of background processes is crucial as the observation of a signal event itself has a low probability. NA64 expects about 10^{-10} background events per reconstructed muon [20] meaning that in ca. one day of data-taking one will observe one background event.

As the NA64 approach is based on missing momentum, it is of great importance to reconstruct the muon momentum precisely. For NA64 an event with a Z' candidate is therefore defined as signal if the scattered muon momentum $p_{\mu'}$ fulfills the criterion $p_{\mu'} < 0.5 p_\mu$ with the incoming muon momentum p_μ [20].

Such a selection implies complicated signal searches when having a low-energy tail in the muon spectrum, which can be vetoed by a high-energy muon selection. Still, such a background contribution needs to be suppressed as much as possible. They can arise from beam-matter interactions with the air that one finds along the line or even vacuum windows. Another contribution for low-energy muons arises from in-flight decays of pions and kaons. The M2 muon beam features a hadron absorber resulting in a low rate of hadrons. Still, a certain number will escape this absorber and may produce unwanted muons. The most critical effect of this is mis-reconstructing a hadron in front of the target that decays afterwards. Naturally, the daughter will have a lower energy. In such a case, one would claim missing momentum to be measured.

7.2 Biasing techniques

7.2.1 Muon biasing

The signal muons that are transported to EHN2 are coming mostly from pion decays, with a small fraction being produced in kaon decays. From operational experience, it is known that about 10^8 muons can be measured in EHN2 for having 10^{13} protons on the production target [144]. While an attenuation factor of 10^{-5} is not prohibitive in terms of computation time, there are possible ways to increase the simulation efficiency. These techniques fall in the category of biasing [109, 162]. In general, biasing refers to influencing intentionally the cross section of a physics process. This results in this process being more or less probable depending on the actual way of biasing. Biasing helps reducing the fluctuations observed in the signal and background regions and is therefore also called variance reduction technique.

In the current example, the possible bias that one could introduce is the enhancement of pion decays by reducing the corresponding mean free path. BDSIM does not only offer Geant4's cross section biasing, it also provides a method called muon splitting [163]. It works in the following way: If any kaon or pion decays into a muon and the corresponding neutrino, or a positron annihilates and produces a muon-pair in the final state, then the physics process during the step, in which the muon is / the muons are produced, gets replayed randomly a defined number of times. It has to be noted that all possible physics processes are considered during this replay. Every time another muon is created it gets stored for further tracking. Because the decays involve two particles in the final state, the angles and momenta of the muon and neutrino[1] follow a distribution, which is introduced by the boost from the mother particle's rest frame into the lab frame. The momentum and angle of the outgoing muon are sampled from those distributions. Even though, one then has more than one muon coming from the same location, one observes multiple muons with various energies flying in several directions. Finally, after the physics processes got replayed the defined number of times, every muon gets a weight attached that corresponds to $\frac{1}{N}$, where N is the number of times, the physics process was resampled[2].

Overall, muon splitting can help to simulate the spectra of muons, especially crucial for background estimations. It is also useful in understanding, where muons are coming from, especially important again in terms of background for experiments.

Surely, when influencing the physics processes in such a way, one needs to verify that one still gets the right observable ensuring that the physics were not impacted wrongly or too heavy. In order to make this statement, the developed model of M2 transporting 160 GeV/c μ^+ has been studied once without activating muon splitting and once with activating it.

The model that has been used for verification, will be described in detail in the following

[1] The produced neutrino will be destroyed immediately and not tracked through the beamline as it does not leave a signal in any of the detectors. Therefore, it would be only unnecessary computing overhead to simulate its path through the model.

[2] It is assumed that no other weighting factor has been introduced yet. Of course, when other biasing techniques are used at the same time, all weights are multiplied accordingly.

section 7.3. Fig. 7.2 shows the spectra of μ^+ in front of bend6 in M2 ($s \approx 1\,020$ m) simulated without muon splitting in red and with it being turned on in blue.

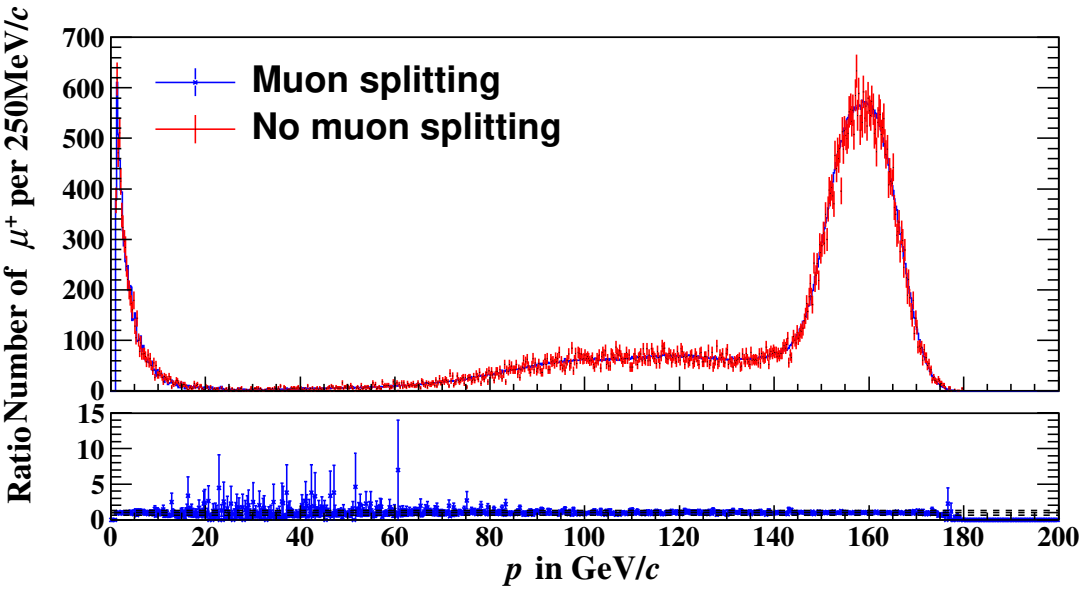

Figure 7.2: Spectrum of positive muons before bend6 in the M2 line. In blue, the spectrum is shown when muon splitting is used in BDSIM. In contrast, the momentum distribution is shown for no muon splitting in red. In addition, the ratio between both distributions is depicted underneath the spectra.

One can clearly see the effect of it being a variance reduction. The error bars get reduced when making use of that feature, whereas the average value in each bin does not change as the ratio of both curves show, which is plotted underneath the spectra. This is ensured by the carriage of the weight when applying the split. In the region between 20 to 40 GeV/c the difference of the average ratio from one can be explained by the low number of muons in those bins for both options. Of course, considering the error bar, it is still within. But the ratio is quite prone to small differences in the number of muons. This effect would be gone in case of having higher statistics. Considering the equality of the spectra for both cases, one can safely make use of that variance reduction technique in the following. Throughout this study, muon splitting will be activated in case the parent particle has a kinetic energy larger than 100 GeV and the multiplication factor is set to 30 meaning in case a muon is produced the process will be replayed 30 times. The energy threshold is chosen like that because the nominal muon momentum is 160 GeV/c. Therefore, particles below around 140 GeV/c will not be properly transported by the beamline. To be not too close to that threshold 100 GeV has been chosen. Therefore, background close to the nominal energy will still be sampled well. This is especially important as such high-energetic muons will be able to traverse large amounts of material and could still reach the overground level around EHN2.

7.2.2 Hadron biasing

As described in section 7.3.1 and visible in Fig. 7.4, the beam is cleaned from hadrons that have not decayed into muons with beryllium absorbers. Those come in 1.1 m-long rods and a maximum of nine can be moved into the beam. Still, with the high rate of the order of 10^{10} secondaries impinging on the absorber, one will still observe hadrons traversing and escaping the beryllium. From a computational point of view, simulating those numbers is not reasonable. Therefore, one can make use of yet another biasing technique, i.e. cross section biasing. In this case, to be able to observe escaping hadrons, it is necessary to bias the probability of inelastic processes that destroy the hadrons. In Geant4, all the inelastic processes are combined in one process per particle called *protonInelastic*, *pi+Inelastic* or *kaon+Inelastic*, of course depending on the particle. In the present case, one needs to actually do inverse cross section biasing of those processes to make them rarer and get hadrons through. The necessity is depicted in Fig. 7.3, in which one can see the distances, π^+ with a momentum of 172 GeV/c are travelling in beryllium until they are destroyed.

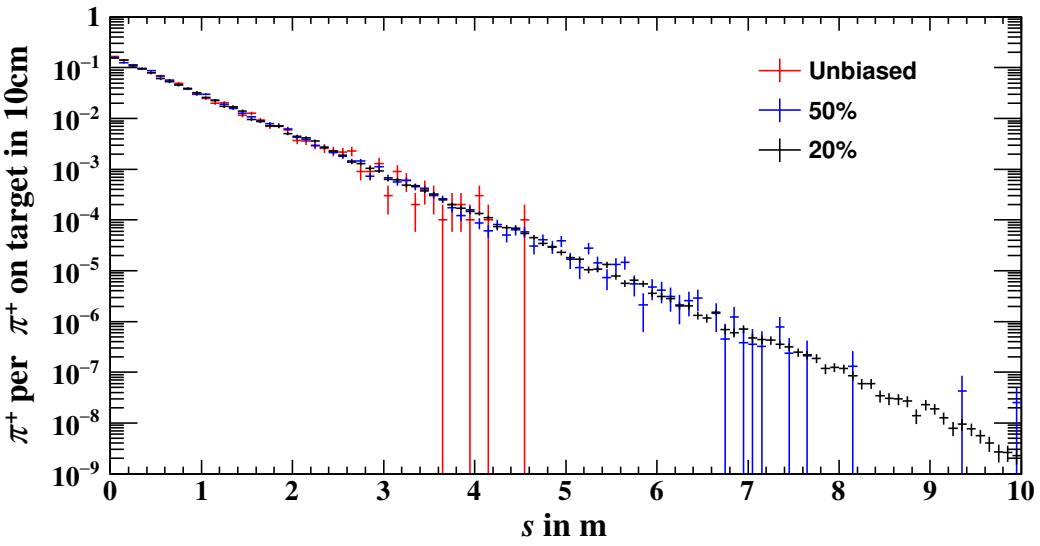

Figure 7.3: Position of last interaction of primary π^+ with 172 GeV/c in 10 m of beryllium. In red, the unbiased simulation is shown. In blue, the results with the cross section for inelastic processes of pions being reduced by a factor two are given. In black, it has been reduced by a factor five.

For Fig. 7.3, 10^4 primary π^+ have been simulated for each of the three distributions. From this number it gets clear that the statistical limit will be 10^{-4} meaning that one can observe only processes happening at this rate or higher, which can be also deduced from the red distribution. To be able to see processes occurring with lower probabilities, in this case seeing hadrons penetrating the beryllium deeper than ca. 4 m, one either needs to simulate a higher number of primaries or one decreases the interaction cross section for inelastic processes. For the blue

curve, it has been reduced to 50 % and for the black one to 20 % of its initial value. Clearly, one can observe deeper penetration depths as the probability of absorption has been reduced. When interfering with the physics processes, one needs to deal with weighting factors in the analysis. From the black distribution in Fig. 7.3 it gets clear that the rate of π^+ fully traversing a 10 m long block of beryllium is ca. one in 10^9 hitting the absorber. Finally, this also implies that it is possible to decrease the statistical limit even without simulating more events. Of course, it is not possible to decrease the number of simulated events arbitrarily and simultaneously also decreasing the interaction cross section because still other processes are happening and also the process of interest still needs to happen.

Clearly, another important point is to not deplete other regions in the plot 7.3. By choosing unsuitable biasing factors, for example too small ones, one will start seeing less events happening with positions of last interaction close to 0, even though, this has naturally the highest probability. By applying the weight, it should still get back to the nominal rate as long as still some events fall in that bin, but one will see increasing error bars because the variance is larger due to smaller number of entries in there. This refers to the variance reduction techniques discussed in 7.2.1. Of course, as soon as the biasing factor is so inappropriate that no entries are observed in those bins, even the weight cannot ensure the right physics results. But from considering all three distributions, one can deduce that none of the investigated factors depletes the region of absorption close to the entrance meaning that they are in principle suitable for all three investigated absorber lengths. This gets especially clear because the bins with small s still have the smallest error bars meaning that those events still happen the most even though a bias has been applied.

7.3 Hadron contamination

Considering the origin of muons in the beam, one feature in regard to the quality is the number of hadrons in the muon beam. The NA64 collaboration [38] has investigated precisely the content of hadrons per incoming muon. In 2023, a measurement of the hadron contamination for different numbers of absorbers in the beamline (cf. Fig 7.4) has been conducted [164]. These measurement results can be used to validate and benchmark the simulation. The model itself, simulation results and validation will be described and explained in the following sections.

7.3.1 Muon beam model

The general features of the muon beam are discussed in section 2.3. Therefore, only important highlights will be discussed. Due to its internal division into two parts, hadron and muon section, the simulation of the beamline is also split up into two parts: the part from T6 to the absorber, and from the absorber to EHN2.

The T6 target is set to 500 mm beryllium to produce the maximum number of hadrons. The target attenuators TAX are also set to their largest opening to guarantee optimal transmission and acceptance. The large momentum spread of about ±5 % around the central value of 172 GeV/c

in the hadron section is produced by the large acceptance dipoles and slightly closed collimators (cf. first two rows in Tab. 7.1) in the hadron section.

Collimator	Horizontal gap in mm	Vertical gap in mm
XCHV.X0610058	±20	±20
XCHV.X0610070	±20	±20
XCMV.X0610190		±30
XCMV.X0610715		±30
XCMH.X0610727	±28	
XCMV.X0610733		±60
XCMV.X0610741		±70
XCMH.X0610752	±28	
XCMV.X0610845		±52
XCBV.X0610858		±90
XCMV.X0610997		±75
XCHV.X0611013	±45	±45
XCMV.X0611050		±30
XCHV.X0611054	±45	±45

Table 7.1: Standard collimator settings for muon beam operation [144]. XCM refers to the magnetic collimators, i.e. scraper magnets, which are used for sweeping away the muon halo. The following letter, V or H, tells the orientation, i.e. vertical or horizontal. The aperture of those can be only varied in the respective direction.

The model that has been implemented to represent the absorber, is illustrated in Fig. 7.4. This is the fourth bending section in the beamline, which deflects the beam in total by 14.4 mrad. The inserts to absorb the hadrons are relatively simple: it is a beryllium rod with 27.5 mm radius, encased in an aluminium box with dimensions 236.0 mm × 64.0 mm. Every insert has a longitudinal extent of 1.1 m.

Taking the investigations discussed in section 7.2.2 into account, biasing factors need to be applied to the absorber inserts, both to the aluminium casing and beryllium rods. Considering the nuclear interaction length of aluminium of 39.7 cm [165], it is a fair assumption to apply the same biasing factor as for beryllium, which has a nuclear interaction length of 42.1 cm [43]. Moreover, this is justified because the beam is focused onto the rods meaning that the majority of particles will traverse the beryllium parts and only few will interact with the casing. The factors that have been multiplied to the inelastic cross sections for protons, positive pions and kaons are presented in Tab. 7.2. Similar plots to Fig. 7.3 justifying the chosen values are given in the appendix A.4.

The momentum of the muon section, which follows after the absorber, is tuned to an average of 160 GeV/c. The full beam optics used for the simulation are illustrated in Fig. 7.5.

The momentum selection is visible as the peak in the horizontal dispersion in Fig. 7.5(a) at around $s \approx 50$ m. There one can find horizontal, large acceptance dipoles and collimators,

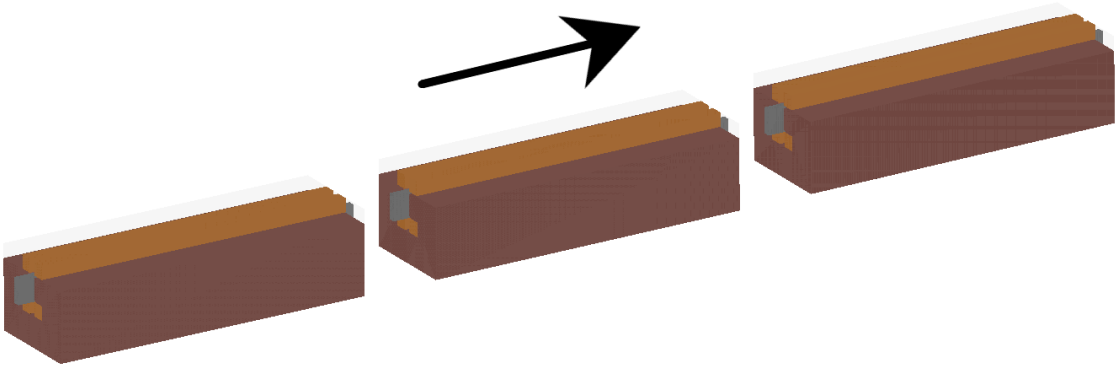

Figure 7.4: Model of the bend4 section in M2 including the absorber inserts made of beryllium. The arrow in the picture indicates the beam direction. Each single bending magnet is 3 m long only considering the iron part, and not the out-coming coils. The grey blocks that come out of the magnets are the beryllium rods (absorber) encased in aluminium boxes.

Absober length in m	p bias	π^+ bias	K^+ bias
3.3	0.7	0.95	0.95
6.6	0.4	0.5	0.5
9.9	0.15	0.2	0.2

Table 7.2: Biasing factors that have been applied to the corresponding inelastic processes for the given particles in the beryllium absorber.

which allow a maximum momentum bite of up to ±10 %. Another striking feature in Fig. 7.5(a) is the FODO-structure between $s \approx 100$ m and $s \approx 650$ m. This part is the decay section, where the parent hadrons can drift freely and have enough time to decay[3]. The remaining part of the line shown in Fig. 7.5(b) transports the produced, tertiary muons towards EHN2 providing either focused or parallel beams at the targets of the installed experiments.

With the described $B^{(\prime)}L - I$-curves (cf. section 4.4) the optics can be converted into currents and finally 2D field maps that are applied in the simulation.

7.3.2 Simulation to the absorber

The proton beam impinging on T6 is illustrated in Fig. 2.4 and has been used in the simulation. Therefore, the spectra of particles escaping the target are the same as in Fig. 2.5. Of course, only a part of the full spectrum will be transported along the line, which is the region around 170 GeV/c. In the present case the beamline has been set to transfer positive particles. The most

[3] Depending on the momentum, around 10 to 20 % of the pions decay, mostly into muons.

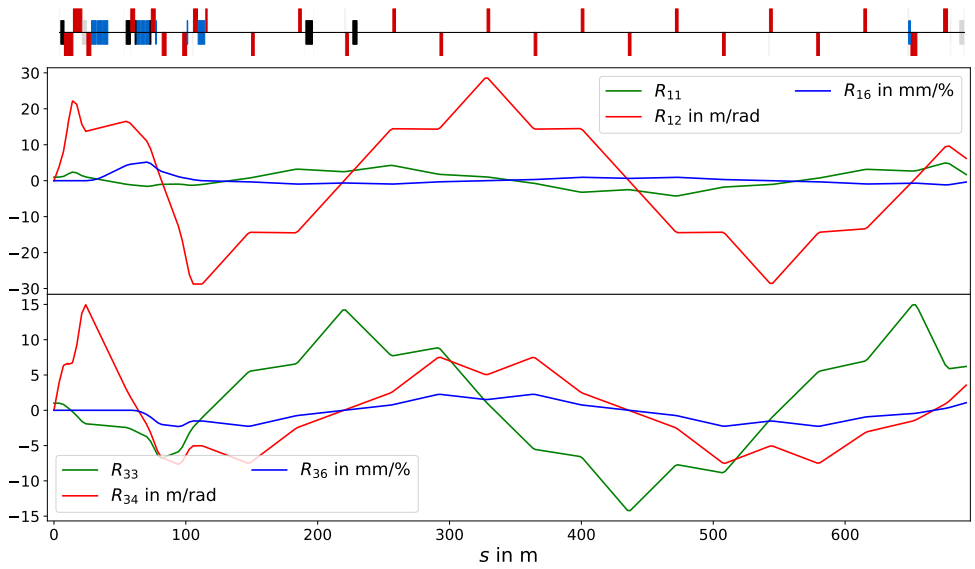

(a)

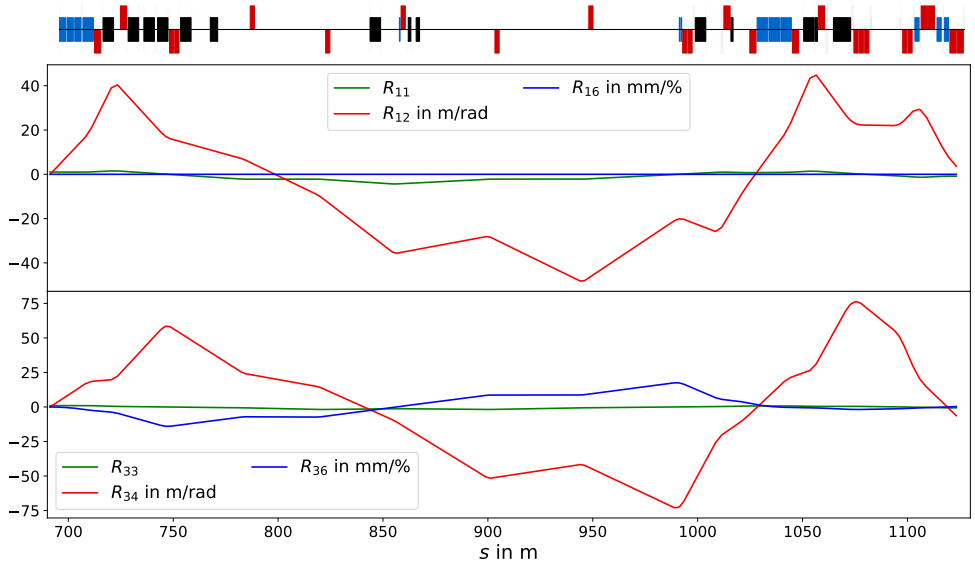

(b)

Figure 7.5: Beam optics used for the muon beam simulation plotted along the beamline. Fig. 7.5(a) shows the hadron section up to the absorber. The muon section is illustrated in Fig. 7.5(b). R_{11} and R_{33} are represented by the green line, R_{12} and R_{34} by the red line and the dispersion R_{16} and R_{36} by the blue one.

relevant part of the hadron section after production is the momentum selection. So, the spectra of hadrons is a good quantity to verify the simulation at this point. Because there are only FODO-sections in between the momentum defining bends and the absorber, the spectra will be

investigated directly in front of the absorber, where the first stage of the simulation finishes. The spectra of π^+ and K^+ are depicted in Fig. 7.6. The results throughout the chapter have been simulated with BDSIM-version 1.7.6, Geant4-version 10.7.2 with the *FTFP_BERT* physics list.

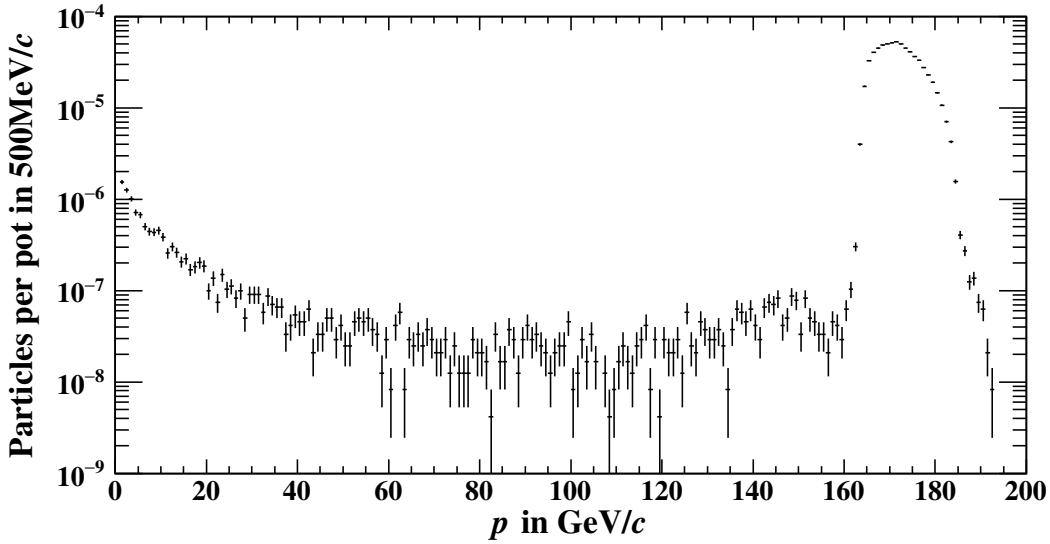

Figure 7.6: Summed spectra of π^+ and K^+ in front of the absorber ($s \approx 700\,\text{m}$). The beamline has been tuned to a nominal momentum of the hadron section of 172 GeV/c. The beamline has a large longitudinal acceptance to make maximum use of the pions and kaons that will decay into muons.

The spectra are normalized to the number of protons on target such that it is easy to calculate the total number of particles for a given number of units on T6. One can see the clear peak around 172 GeV/c in Fig. 7.6. The width of the peak is around ±5 %. The background is also on a reasonable level being at least around two orders of magnitude lower, especially considering that the spectrum is taken over an area of 2 m × 2 m[4].

Another important parameter to look at is the μ^+ spectrum 7.7. It is interesting to note that the distribution is flat between $\approx 90\,\text{GeV}/c$ and $\approx 170\,\text{GeV}/c$. Considering the two-body decay of a pion into a muon and the corresponding neutrino, it can be calculated that the muon will receive at least ≈ 57 % of its parent's momentum [90]. Considering 172 GeV/c pion momentum, this results in 98 GeV/c. According to Fig. 7.6, the spectra of the parent particles are not monochromatic ($\sigma \approx 10.3\,\text{GeV}\,c^{-1}$), the final muon spectrum will be the convolution of the parent spectra with a uniform distribution allowing momenta between 57 % and 100 %[5]. From that spectrum also only a part will be transported down to EHN2. Through the absorber,

[4] The beam pipe has a radius of 100 mm in the FODO section. So, the beam size is of that order. Everything outside of that has interacted with any kind of material, magnet or beam pipe, and will therefore distort the spectrum.

[5] For a kaon decay into a muon and neutrino, the muon will pick up at least 4.5 % of the kaon momentum.

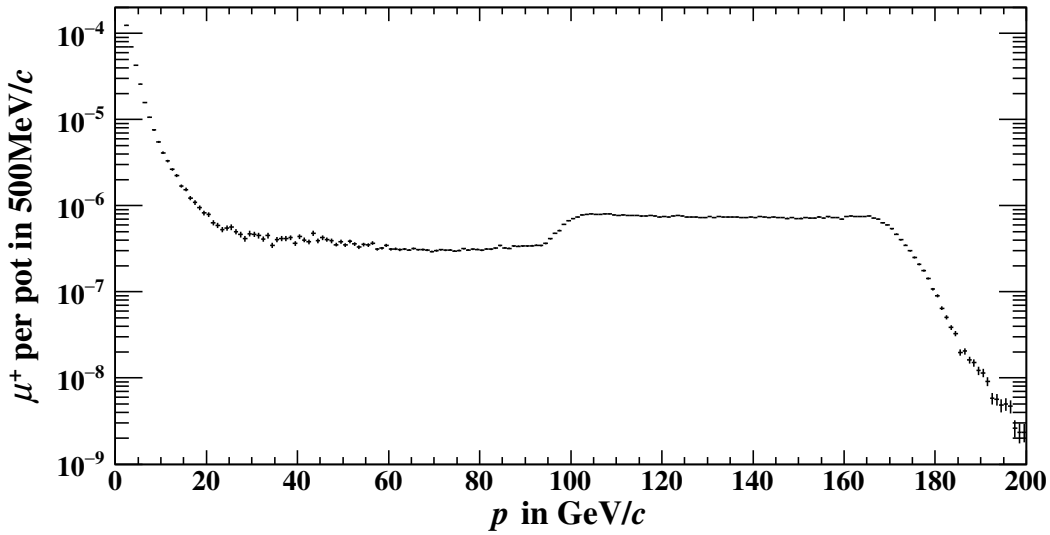

Figure 7.7: Spectrum of μ^+ in front of the absorber ($s \approx 700$ m). Decaying π^+ produce the plateau visible in the μ^+ spectrum.

one will see an average energy loss of 2.444 MeV cm^2 g^{-1} [166], resulting in a total energy loss between about 1.5 to 4.5 GeV depending on the number of absorbers.

7.3.3 Beam contamination

The second stage of the simulation is started in front of the absorber with the samples scored in the first one. Three different configurations have been implemented and studied: three, six and nine absorbers. The biasing factors applied for the three different configurations have been given in Tab. 7.2. Due to that biasing it is possible to draw conclusions about the rate of hadrons passing the absorbers even without simulating unreasonable statistics and despite the survival rate being around one in 10^9. In the first stage of the study approximately 10^9 protons on target have been simulated and the emerging secondaries have been tracked to the absorber. The particles that reach that position have been replayed five times in each simulation of the second stage. For the three absorber settings, the second stage has been rerun up to six times with different random number generator seeds to start with. Several samplers have been placed to score the beam distributions along the remaining part of the line. The two most important ones for the current study are the one at the entrance of the CEDAR area ($s \approx 1\,079.6$ m) and in the middle of that same region ($s \approx 1\,086.1$ m) because the NA64 experiment has been installed in this part of the beamline. Those two positions are used to estimate the hadron contamination that has been described in the beginning of this chapter.

Having the NA64 setup not implemented in the simulation, one needs to come up with a solution to mimic the trigger logic that has been used for analysing the data. The several

triggers and the general setup are described in [164]. The important triggers for estimating the hadron contamination are $\overline{V_0}$, S_0, S_1 and S_2 that have to be true. In the simulation, data has been recorded at the entrance of the CEDAR region approximately at the same position as V_0. Therefore, a loose cut on the radial position of $r < 30\,\text{mm}$[6] has been applied being on the pessimistic side concerning the number of background hadrons. Considering the distance between V_0 and S_2 of ca. 5.3 m and the diameter of S_2 of 35 mm, one can calculate a maximal angle of a beam particle that would fulfill the trigger conditions[7]. With the given numbers, this results in a maximal acceptance of ca. 6.6 mrad. In the data-taking, the particles are recognised in a hadronic calorimeter. A threshold of 1 GeV [167] is applied to make sure that the detected particle is not a muon. This threshold will be applied, too, throughout the analysis of the simulated data.

The spectra of particles, μ^+ and hadrons, are illustrated in Fig. 7.8 for the three different absorber settings. Those spectra will be the basis for the remaining analyses throughout the chapter.

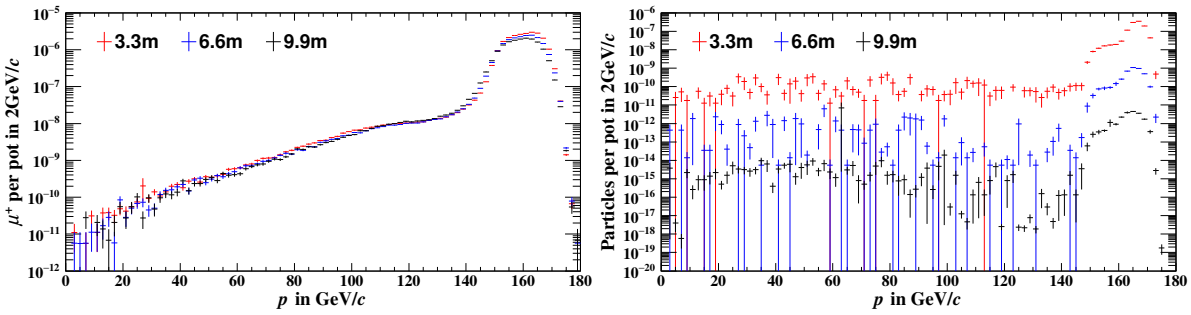

(a) (b)

Figure 7.8: Spectra of μ^+ (Fig. 7.8(a)) and hadrons (Fig. 7.8(b)) that match the trigger conditions discussed in the beginning of this section. They have been obtained for various absorber lengths, i.e. 3.3 m (red), 6.6 m (blue) and 9.9 m (black).

The momentum distributions of μ^+s are peaking at 160 GeV/c with a width of 5.5 GeV/c resulting in a 3.5 % momentum band. For all cases, the rate drops by more than two orders of magnitude outside of 4σ meaning that the flux will be purely determined by muons with nominal momentum. Considering the error bars of the various bins, the spectrum has been determined well down to 40 GeV/c. For lower momenta, the rate starts to fluctuate meaning too few events in those bins. Naturally, when having a higher number of absorbers, the energy loss of muons will also increase. This increase depletes the high-energy part of the spectrum. Another effect is multiple Coulomb scattering of muons in the beryllium rods. This effect is proportional to $\sqrt{\frac{x}{X_0}}$ [5] with x being the length of traversed material and X_0 the radiation

[6] The hole in the trigger V_0 has a diameter of 40 mm.

[7] Again, to be on the pessimistic side in terms of contamination, the maximum angle is calculated considering the full size of S_2.

length. Therefore, it increases with more absorbers. The multiple scattering leads to decreased number of muons being in the acceptance of the muon section of the beamline resulting in less muons for larger absorber lengths.

In Fig. 7.8(b) the spectra of hadrons for the three different absorber lengths are shown. As the number of interaction lengths increases when moving more beryllium blocks in, the rate of hadrons drops because more are absorbed due to inelastic processes. This is the reason for the drop by three orders of magnitude when having 3.3 m of beryllium more, which corresponds to around eight nuclear interaction lengths. On top of having a higher absorption rate, one also observes a higher energy loss of the hadrons resulting in a broader momentum distribution. For less absorbers, the secondary hadron momentum of 172 GeV/c is still very clear, whereas for the maximum number that same peak gets smeared. It is important to note that all particles contributing to the depicted spectra are passing the absorber meaning they are transported close to the beam axis. This can be deduced from the number of particles for 9.9 m being below 10^{-12}. As such a rate implies a number of protons on target that has not been simulated, particles in those events must have passed a region that is biased. In the simulation the only biased parts are the beryllium inserts including the aluminium casing. This gets underlined in addition by Fig. 7.9.

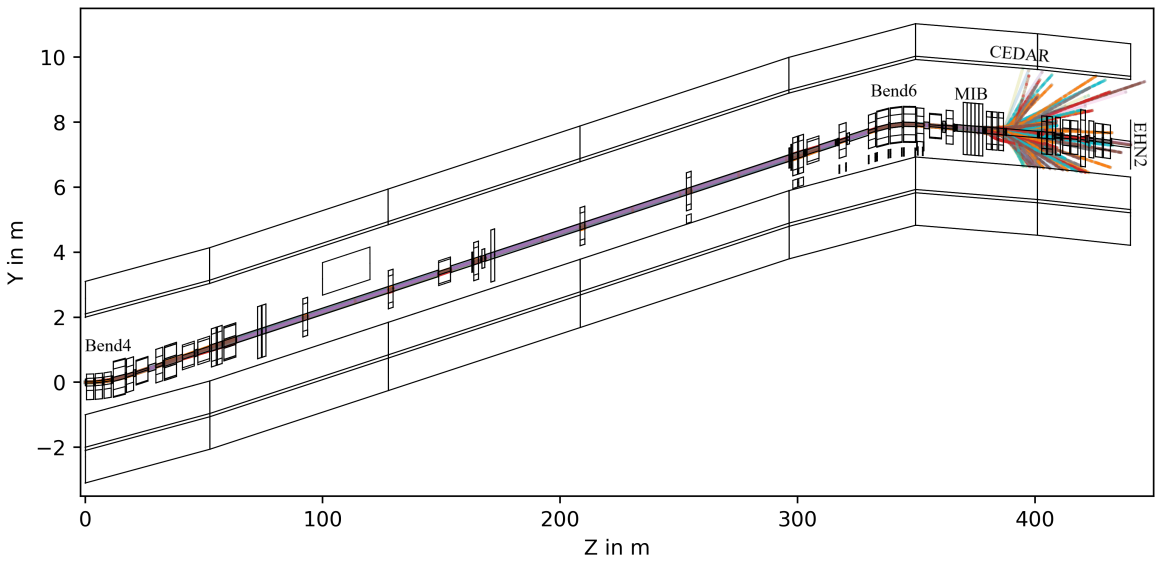

Figure 7.9: Trajectories of particles generating hadronic background. In this representation, the beamline goes down after passing through bend6 at around $Z \approx 350$ m. This is due to the two-stage simulation. As the beam has been scored in local coordinates in front of the absorber, it has been launched into the second part in this coordinate system. Therefore, it is fair to construct the start of the line in the second half straight without considering the vertical angle of 9.5 mrad and horizontal angle of 25.8 mrad because those are contained in the beam distribution. The rectangular block around $Z \approx 100$ to 120 m mimics the part of the line passing the Lion river, where the nominal beam trajectory is close to the tunnel roof.

Fig. 7.9 shows a schematic view of M2 of the second stage of the simulation in the $y-z$-plane. In this part of the beamline, one finds only vertical bending magnets. That is why the $x-z$-plane is of less interest here. Overlaid on the beamline are hadronic events passing the described NA64 filters, so the ones contributing to the spectra in Fig. 7.8(b). Clearly, all those particles are transported within the beam pipe meaning that there momentum is still close enough to the nominal setting of 160 GeV/c. Those are hadrons that loose small amounts of energy in the absorber. As the beam pipes in M2 are large with typically 100 mm radius because the muon beam has a large transverse size, those off-momentum particles can still be guided along the beamline. In the last triplet before entering the CEDAR area in M2 some particles hit the magnet material and produce background events contributing to the low-energy part of the spectra. The ones, which traverse the magnet within the aperture are the ones in the peaks of the distributions.

A validity check of the simulation is the rate of μ^+ that would be visible in the detector considering the described cuts. The muon flux has been measured for two absorber lengths (seven and nine) at the COMPASS experiment for 1.2×10^{13} protons on T6. This is shown in Fig. 7.10 as a function of the muon momentum.

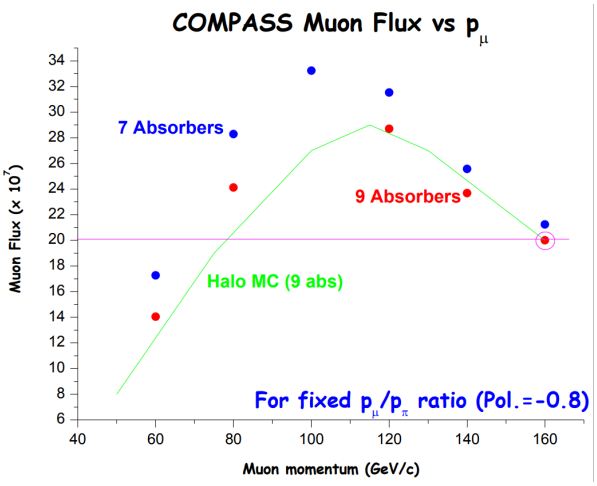

Figure 7.10: Muon flux at COMPASS as a function of the muon momentum for different absorber lengths (9.9 m in red and 7.7 m in blue) [168]. The expectation coming from HALO [159] for 9.9 m is plotted in green.

At a momentum of 160 GeV/c one reaches 2×10^8 muons at the COMPASS target for nine absorbers, whereas one gets 2.2×10^8 for seven. The muon flux obtained in the simulation is illustrated in Fig. 7.11(a) for the 160 GeV/c beam as a function of the absorber length. The rates are calculated via the integral of the muonic spectrum 7.8(a) over the full momentum range.

The flux is shown per proton on target and summarised in Tab. 7.3. Considering the number of protons of 1.2×10^{13}, one will get $(1.9634 \pm 0.0013) \times 10^8$ muons for the full absorber length going up to $(2.7357 \pm 0.0015) \times 10^8$ for 6.6 m. Those values are in good agreement considering

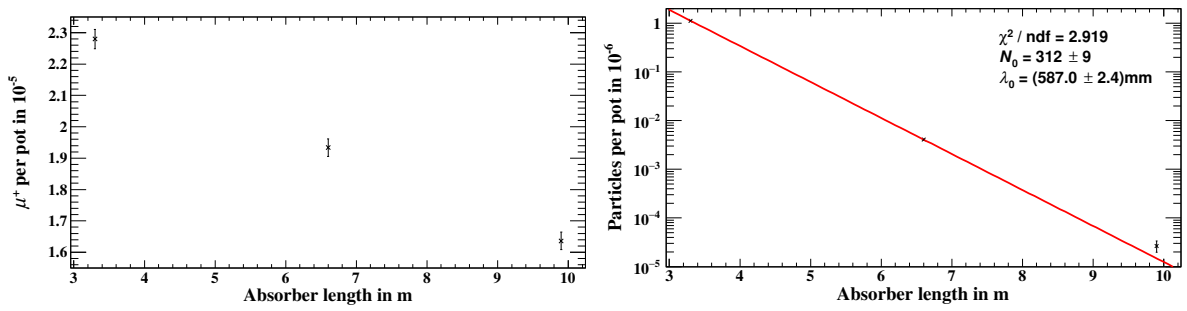

(a) (b)

Figure 7.11: The integrated muon flux is plotted in Fig. 7.11(a) as a function of the absorber length (error bars are enlarged by a factor 25). Fig. 7.11(b) shows the rate of hadrons for different absorber lengths (the errors of the first two data points are of the order of 1 to 2 %). Only particles passing the described filters are considered.

the different position in the beamline ($\Delta s \approx 50$ m) and different trigger conditions.

For the same setup, the flux of hadrons matching the NA64 trigger logic is given in Fig. 7.11(b). As it is expected from the qualitative analysis of the spectra, the rate drops exponentially when inserting more absorbers (y-axis is logarithmic and not linear as in Fig. 7.11(a)). A single exponential $N_0 \exp\left(-\frac{x}{\lambda_0}\right)$ has been fitted to the rate with λ_0 being a measure of the mean free path of inelastic, hadronic processes. Because the traversing hadrons also undergo multiple scattering, loose energy electromagnetically and may decay the result for λ_0 is impacted by those contributions, which impacts especially the hadrons accepted transversely and longitudinally by the second part of the simulation. Therefore, the drop in rate is slightly influenced by those effects, too. The fit yields $\lambda_0 = (587.0 \pm 2.4)$ mm, which is in good agreement with the pion interaction length of 59.36 cm [43].

Having the rates for μ^+ and hadrons at hand, which both take the explained NA64 trigger logic into account, it is possible to determine the ratio of hadrons to μ^+. This ratio is referred to as the hadron contamination, i.e.

$$\text{Hadron Contamination} = \frac{\#\text{Hadrons}}{\#\mu^+} \,. \tag{7.1}$$

It is important to mention again that the full spectrum is used here, meaning that also μ^+ that do not have the nominal momentum will contribute. But this contribution is small. The result is plotted in Fig. 7.12.

As the rate of μ^+ changes only slightly with the number of absorbers, the drop in the hadron contamination mainly originates from the decrease in the hadron flux. The results are summarized in Tab. 7.3.

The contamination goes down to $(1.6 \pm 0.4) \times 10^{-6}$ for 9.9 m. The muon beam has been

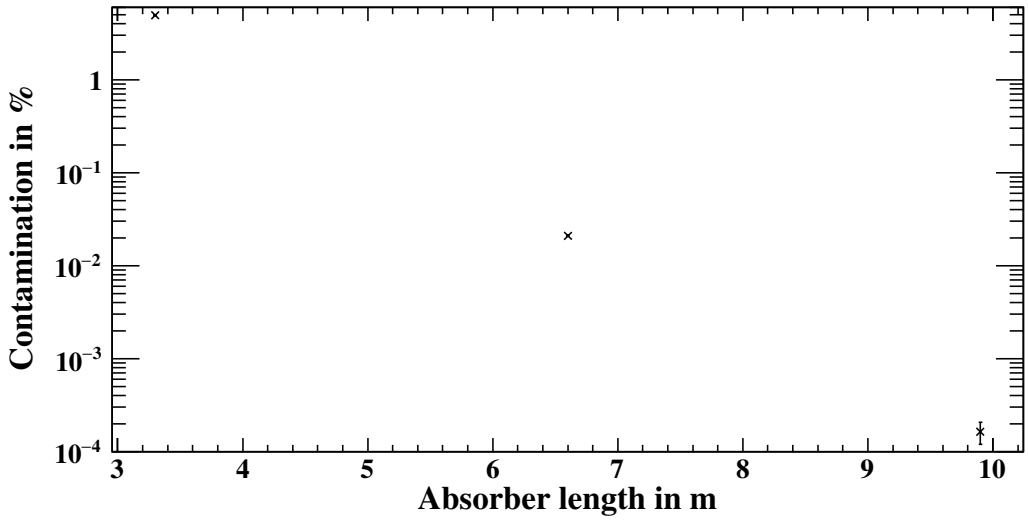

Figure 7.12: The hadron contamination is plotted for different absorber lengths (the errors of the first two data points are of the order of 1 to 2 %). The rates given in Fig. 7.11 are used to estimate the ratio of fluxes of hadrons and muons.

Absober length in m	μ^+ rate in 10^{-5} per pot	Hadron rate per pot	Hadron contamination
3.3	2.2797 ± 0.0012	$(1.128 \pm 0.011) \times 10^{-6}$	$(4.95 \pm 0.05) \times 10^{-2}$
6.6	1.9335 ± 0.0011	$(4.07 \pm 0.09) \times 10^{-9}$	$(2.10 \pm 0.05) \times 10^{-4}$
9.9	1.6362 ± 0.0011	$(2.7 \pm 0.7) \times 10^{-11}$	$(1.6 \pm 0.4) \times 10^{-6}$

Table 7.3: In the table the actual values for the muon and hadron rates, and hadron contamination plotted in Fig. 7.11 and 7.12 are given. All values are normalized to the incident number of protons on T6. Typically, one operates with around 1.2×10^{13} protons on target.

designed to have a maximum hadron contamination of $\frac{\#\pi}{\#\mu} \leq 10^{-6}$ [90]. This matches the value obtained in this study especially considering that in the simulation not only pions have been scored but all hadrons.

NA64 has measured the hadron contamination as a function of the absorber length. They performed runs in step sizes of one beryllium insert from three to nine. The final results have not been published yet, but a hadron contamination of 5×10^{-5} per muon on target [164] for nine absorbers is mentioned. Preliminary results showing the hadronic spectra for three different absorber settings are illustrated in Fig. 7.13 [169].

Interestingly, a plateauing of the contamination from six inserts on is observed meaning no drop in hadron flux when inserting more absorbers. Such a measurement implies additional sources of hadrons downstream of bend4. There are several possibilities that have not been considered in the present study: first and foremost, the NA64 setup including additional tracking

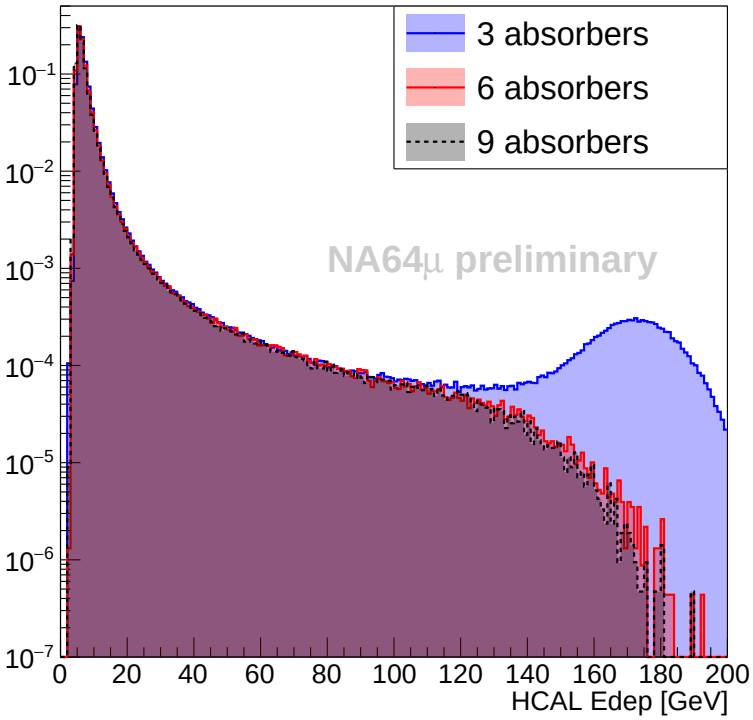

Figure 7.13: Spectrum detected in the NA64 hadronic calorimeter [169]. The energy deposited in the calorimeter is plotted for different absorber lengths; three in blue, six in red and nine in black. No information from the tracking detectors is included.

detectors around bend6 has not been implemented in the simulation. Considering this additional amount of material budget, it is possible to produce further hadrons. Another effect might be the hadron production in the beam momentum stations (BMS) with three modules being placed upstream and three placed downstream of bend6. In the simulation, those detectors have been modelled by pieces of plastic with 16 mm or 20 mm thickness depending on the station. As these modules are put in the beam and are traversed by a huge number of muons, inelastic processes can occur, in which a muon produces a hadron that would be recorded in the actual detectors. Because three stations are on the same level as NA64 it is possible that such particles reach the experiment. Those events are rare and therefore not observed in the simulation. This would be solved by biasing muon interactions in these detectors. Biasing of the BMS is more complex than of the absorbers. In the present case, it is important to sample the hadron production well without depleting the muon spectrum. In Fig. 7.14 one can see the particles that are produced in the interactions of 160 GeV/c μ^+ with 20 mm of plastic for various bias factors applied to nuclear interactions of muons.

For Fig. 7.14, 10^4 μ^+ have been shot on the plastic. Without biasing the simulation, one observes only a small rate of electrons, positrons and photons besides the non-interacting

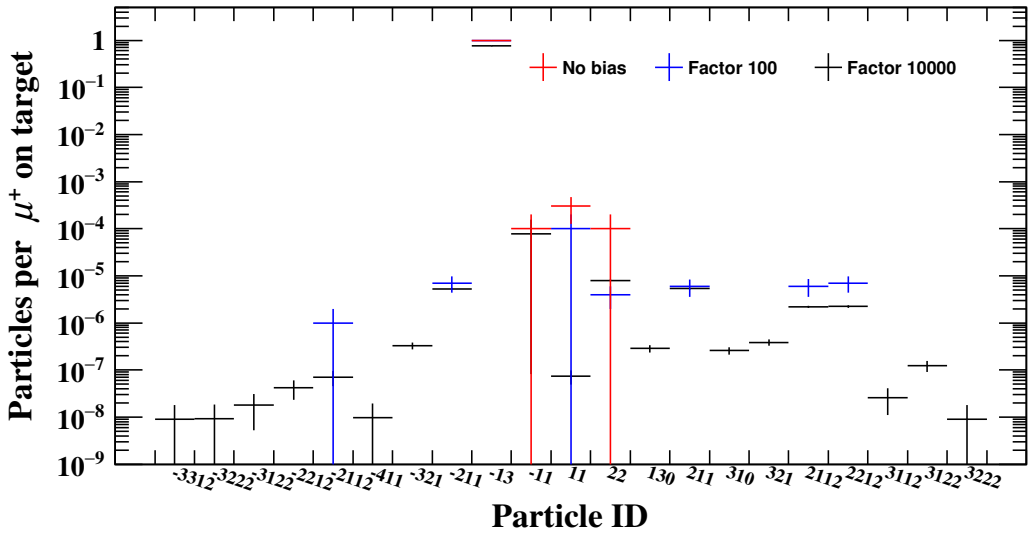

Figure 7.14: Particles that are produced by 160 GeV/c μ^+ interacting with 20 mm of poly-carbonate. The numbers represent the PDG IDs as given in [170]. For example, π^+ has the ID 211 and proton 2 212. The production is given for different biasing factors applied to the nuclear interaction cross section of muons. In blue, the results of the simulation with a cross section increased by a factor 100 are plotted. In the simulation represented in black the factor has been 10 000. The unbiased simulation results are given in red.

muons, but no hadrons at all. As soon as one starts applying reasonably high biasing factors, muons start producing hadrons. Considering the rate of pions and protons being on the order of 10^{-6} to 10^{-5}, it is clear that in an unbiased study, this contribution would not be visible. Additionally, looking at the results with the highest biasing factor, it is noticeable that the muon rate (particle ID is -13) is smaller than for the other two cases meaning that one starts loosing muons. Therefore, a reasonable biasing factor needs an even deeper investigation of the underlying processes. And besides that the present situation is more complicated because there are in total 112 mm of material in the way of the beam requiring a dedicated study including the whole beamline to estimate reasonable biasing factors as one should not deplete the muons in a nonphysical way.

7.4 Discussion

A full 3D model of the M2 line in muon configuration has been implemented. This includes the hadron absorber that is essential for the high quality of the M2 muon beam. This absorber can be used in different configurations determining the number of hadrons that are able to traverse that beamline element. To be able to estimate the rate of surviving hadrons the cross section biasing technique has been used. The fluxes of muons and hadrons have been estimated for

three different configurations showing an exponential drop of the hadron rate by five orders of magnitude with a simultaneous decrease of the muon rate by 25 % when going from three to nine absorbers. Therefore, the performed study also yields a drop by nearly five orders of magnitude in terms of hadron contamination.

As NA64 is observing a different behaviour of the hadron contamination as a function of the number of installed absorbers, it is necessary to investigate further sources, where particles are produced. Locations, where this can happen, are the beam momentum stations. Because those have a small length, the production might not be sampled appropriately in the simulation. Therefore, a deeper investigation of possible biasing techniques needs to be done.

Samples containing the beam distributions, both at the first BMS ($s \approx 995\,\mathrm{m}$) and at the entrance of the CEDAR area ($s \approx 1\,090\,\mathrm{m}$), have been shared with the NA64 experiment to perform a full Monte Carlo simulation of the detector response. The results will be based on the full trigger logic including the geometric acceptance of the setup. As the whole detector is implemented, the production of further hadrons in the setup can be studied yielding a possible answer to the exponential drop in the hadron contamination observed in the presented simulations. The detector simulation and data analysis are currently performed and the results of the whole study, beamline and detector simulation included, will be summarized and published [171].

CHAPTER 8

M2 electron beam

The third and last running option besides the two that have already being discussed is the electron mode. The M2 beamline is capable of transporting electrons, which were used in the past by COMPASS for detector calibration purposes, and were and will be used by AMBER, NA64 and MUonE [21] for the same reason.

MUonE is aiming at measuring the leading hadronic contribution of the electromagnetic coupling constant via muon-electron scattering. The measurement might have a great impact on the understanding of the anomalous magnetic moment of the muon. Currently, the hadronic contribution is one of the leading uncertainties in the determination of the muon magnetic moment. Understanding this source term better may pave the way to Physics Beyond the Standard Model of Particle Physics.

As it is not yet an approved CERN experiment, MUonE is performing several test measurements evaluating detector performances to be able to quantify the impact of the foreseen experiment. One of the test beams has happened at the M2 line in October 2022 [172] partly making use of the available electron mode. Another measurement has been performed at CERN's East Area beamline T09 [172]. During the campaign an electromagnetic calorimeter ($PbWO_4$) has been installed in the CEDAR area in M2 together with silicon tracking detectors [173]. The performance of the calorimeter has been investigated with the transmitted electrons. This measurement will be used to benchmark the simulation that will be discussed in this chapter.

8.1 Simulation approach

From operation experience, it is known that on the order of 10^3 to 10^4 electrons are observed at the CEDAR location in M2 starting from 10^{13} protons on the T6 target [144]. This implies an attenuation factor of 10^{-9}. Therefore, it is necessary to simulate on average 10^9 protons on target to observe one signal electron at the calorimeter location. The ultimate goal naturally would be to simulate one full spill of protons, which is impossible from a computational point of view. Consequently, one needs to come up with another approach to be able to draw quantitative

conclusions from the studies.

Nowadays, biasing techniques are commonly used in physics simulations. Naturally, this would be the go-to approach when such an attenuation factor is involved. To be able to bias the simulation in a proper way without interfering too much with the underlying physics some first investigations have to be done. Those will be described in the following section 8.1.1.

8.1.1 Biasing investigations

As discussed in section 2.3, the electron beam is produced by pair production of photons coming from π^0-decays. Clearly, considering the branching ratio of $\pi^0 \rightarrow 2\gamma$, which is (98.823 ± 0.034) % [174], one does not need to increase the probability for this decay to happen. Also, having 100 GeV/c electrons coming from pair-production, one needs photons with an energy of 200 GeV. Considering Fig. 8.1, one can deduce that also pair-production is the dominant process to happen on this energy scale (cf. κ_{nuc} and κ_e). Again, this means there is no need to interfere with the physics processes producing the high-energy electrons.

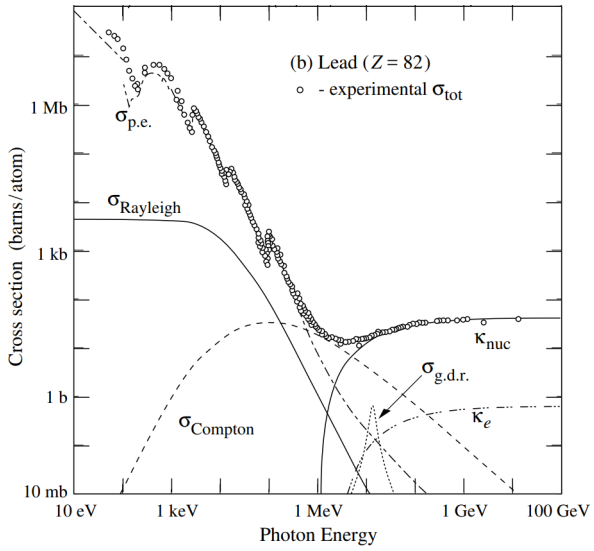

Figure 8.1: Photon interaction cross section in lead [5]. The various interactions contributing to the total cross section as well as the total cross section itself are plotted as a function of photon energy.

Of course, Fig. 8.1 shows the cross section in lead, but this behaviour does only change quantitatively when going to other materials, in this case beryllium. Still, pair-production is the vastly dominating process that happens to photons.

Considering those two general statements, there is only one process in the production-chain that can in principle be biased, which is the production of π^0 in the T6 target. Unfortunately, the production is included in the so-called *hInelastic*, i.e. hadronic inelastic, physics. But this does not include the π^0 production only, but all possible inelastic processes that a hadron can undergo. Biasing this process, which is explained in section 7.2.2, would results in an increase of all processes by the same factor meaning no gain.

The last possibility at the T6 level is looking at the efficiency of photon conversion in the target. To investigate this, a photon beam with energies between 150 to 250 GeV has been shot on a 500 mm block of beryllium. The z-location, where the conversion happened in the material block, is depicted in Fig. 8.2.

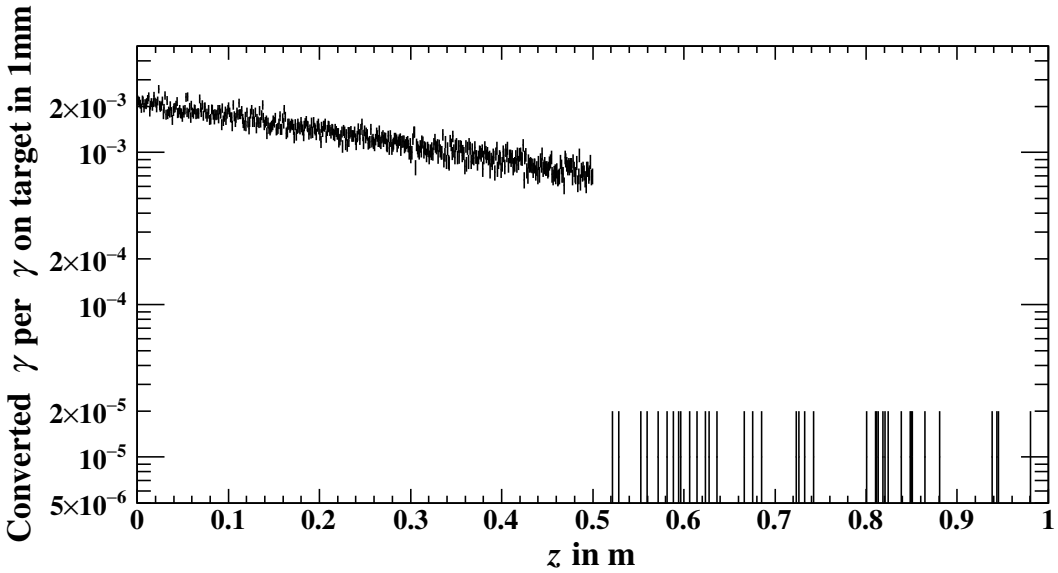

Figure 8.2: z-location of γ-conversion into electron-positron pairs. Only photons that created an electron-positron pair are considered in the plot. Photons undergoing other processes do not contribute.

Integrating the conversion rate over the full target length of 500 mm yields the percentage of photons that will produce an electron-positron pair. For the present case this comes to (66.16 ± 0.26) % meaning that two-thirds of the photons will yield an electron still within the target assuming the π^0s are produced close to the target entrance. One-third will escape the target region or undergo other processes. Considering those numbers, there is no need to force more photons to convert in the target because one will gain at most 50 % in terms of electron rate. This gain would not drastically increase the efficiency of the simulation meaning the attenuation is still the dominating problem.

The presented considerations and investigations have been regarding the T6 target. In addition, there is the so-called electron target, in which the electrons from upstream lose large amounts of energy due to bremsstrahlung while the other particles do not. The final signal electrons will be 40 GeV/c electrons coming from 100 GeV/c upstream with 60 GeV/c-equivalent energy loss. There is the other option that a bremsstrahlung photon pair-converts into e^--e^+. This rate will be evaluated, too. With this secondary target generating a tertiary beam there is another possibility to increase the simulation efficiency by interfering with the physics at that point. To investigate this option, a 100 GeV/c electron beam with a 5 % momentum spread has been fired on a 5 mm lead plate. Potentially, one can change the interaction cross section of bremsstrahlung for electrons. Therefore, the rate of electrons in the intermediate energy range

around 40 GeV needs to be investigated. This is illustrated in Fig. 8.3.

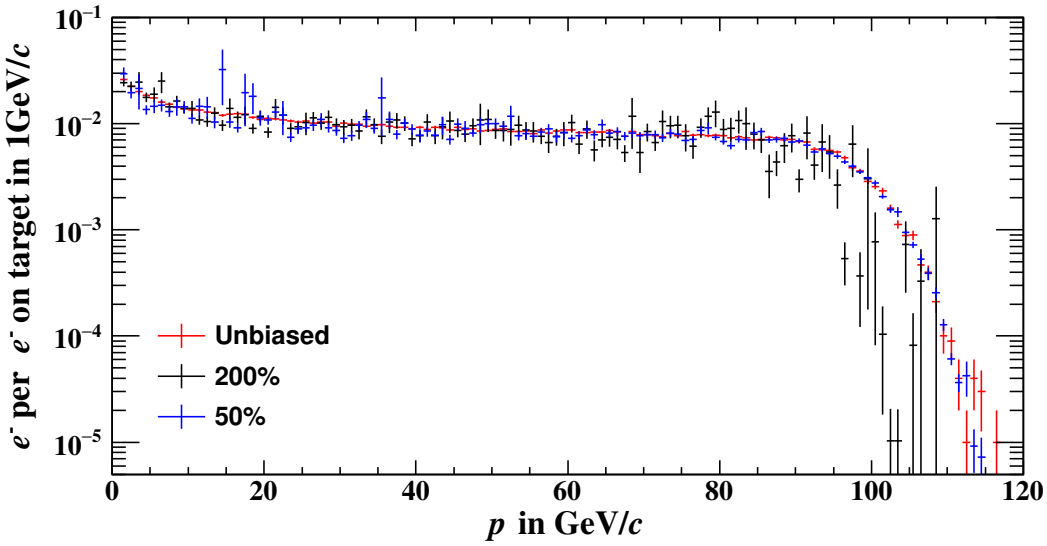

Figure 8.3: Spectrum of electrons (100 GeV/c with a 5 % spread) after traversing a 5 mm-thick lead plate for different biasing factors. The unbiased situation is given in red. In black, the cross section has been increased by a factor two while for the blue one it has been decreased by a factor two.

The red curve shows the unbiased electron spectrum after traversing 5 mm of lead. For the black distribution, the bremsstrahlung cross section has been increased by a factor two, while for the blue one, it has been decreased by a factor two. Clearly, there is no gain in the relevant energy range. One can just observe that by biasing the simulation one depletes certain ranges in the spectrum: when increasing the rate, meaning bremsstrahlung happens more often, one sees less high-energy electrons, while decreasing the cross section results in less low-energy electrons. In the present case it is not useful to bias the production of 40 GeV/c electrons.

Another interesting number is the ratio between electrons coming from upstream of the lead plate and loosing enough energy to be transported through the remaining beamline compared to secondary electrons, typically coming from pair-production of photons coming from bremsstrahlung. Obviously, having a 40 GeV/c electron-positron pair makes a 80 GeV photon necessary. Such photons need to be produced basically in one interaction of an electron from upstream with the secondary target material. The bremsstrahlung cross section for electrons is shown in Fig. 8.4 as a function of the fractional energy transferred to the photon for various electron energies. At the energies of interest around 100 GeV, the cross section peaks at low photon energies. Therefore, most of the photons will not have energies high enough to produce electrons and positrons with 40 GeV/c meaning this effect is expected to be a low contribution. The fraction for the present case is depicted in in Fig. 8.5.

From Fig. 8.5 one can deduce that the rate of primary electrons is an order of magnitude higher compared to secondary electrons. So, having those two results at hand, there is also no

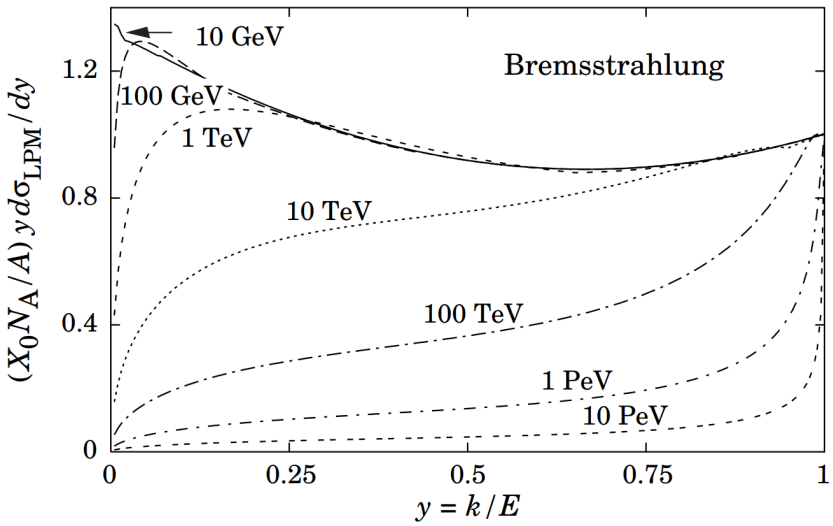

Figure 8.4: Bremsstrahlung cross section in lead shown for various electron energies as a function of the fractional energy transferred to the photon [5]. At the energies of interest around 100 GeV the cross section peaks at small photon energies.

option to bias the production of 40 GeV/c electrons at the location of the secondary target.

8.1.2 Discussion

No biasing techniques are possible because the production of the tertiary electrons is already optimised. Therefore, one needs to accept the large attenuation factor when simulating the electron beam. Considering such a small probability of having a signal electron, there is clearly the need again to have a two-stage simulation as for the muon option already. With this approach, it is again possible to produce a sample at a given location, which will naturally be in front of the secondary target that can be reused multiple times to simulate the remaining part of the beamline and will finally yield the electron spectrum and distribution at the MUonE calorimeter. To speed up the simulation several options will be used. In case a neutrino will be created it will not be tracked because it will not leave any signal in the detector anyways. Therefore, it would be only unnecessary computing time to evaluate the neutrino tracks along the beamline. Because the signal electrons have energies around 40 GeV, it is also not needed to track particles down to low energies. Due to that a kinetic energy cut in the first stage of the simulation of 20 GeV will be applied. This is also reasonable as the background is not of interest in this case. Therefore, only beam particles need to be tracked.

Having such a high-energy electron beam, one might expect a large energy loss coming from synchrotron radiation. The effect of synchrotron radiation can be evaluated, which will be done shortly in the following. In the upstream part of the beamline, up to the converter plate, the beam momentum is 100 GeV/c. This part contains three bending sections: the first one consists of three magnets bending by 5.9 mrad each (L = 3.6 m); the second one is made of

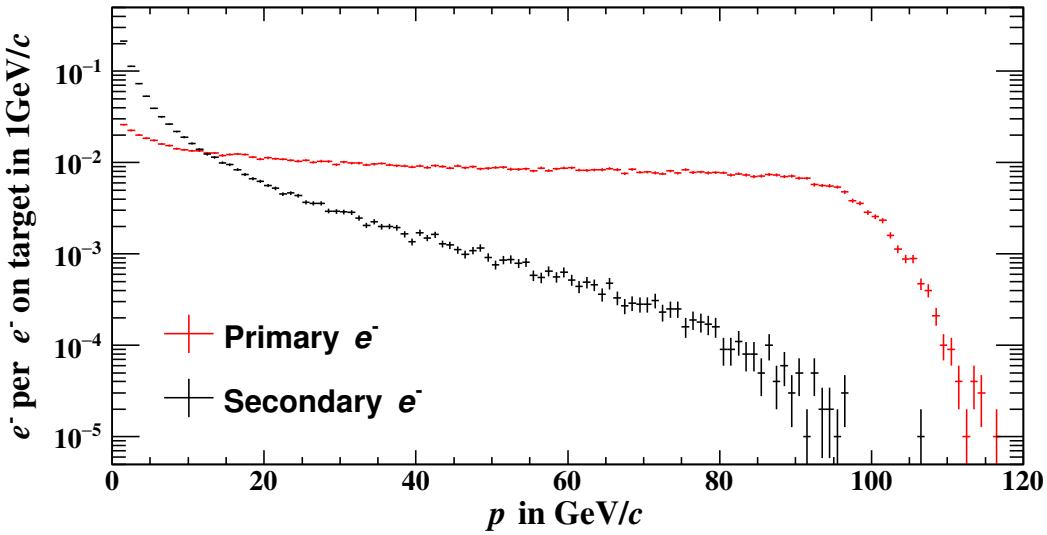

Figure 8.5: Spectra of primary (red) and secondary (black) electrons after traversing a 5 mm-thick lead plate. A particle is still counted as primary if it has not undergone an interaction, where it has been destroyed and created the same particle. For instance, multiple scattering is a process that does not change a primary particle to a secondary.

three magnets with 3.2 mrad per bend ($L = 2.5$ m); and the third station is one magnet bending by 8 mrad ($L = 5$ m). A practical formula to calculate the energy loss ΔE due to synchrotron radiation is given in Eq. (8.1), with the momentum p, the magnet length L and the bending angle θ [53].

$$\Delta E = 1.3935 \times 10^{-2}\,\text{MeV}\frac{\theta^2/\text{mrad}^2 \times p^4/\text{GeV}^4/c^4}{L/\text{m}}\,. \tag{8.1}$$

Evaluating Eq. (8.1) with the given values[1] yields a total energy loss of 75.4 MeV in the first part of the line being ca. 0.08 % of the initial energy.

The part between the secondary target and EHN2 has three magnets bending by 4.8 mrad each ($L = 3$ m), one bending by 9.6 mrad ($L = 5$ m) and again three bending by 10 mrad each ($L = 5$ m). Calculating the energy loss for those values yields 3.9 MeV or 0.01 % of the tertiary momentum 40 GeV/c.

Having those values, one can deduce that it is not necessary to activate synchrotron radiation losses in Geant4 meaning additional saving of computing time.

[1] The beam energy is reduced by the synchrotron loss after each single bending magnet. The energy loss in quadrupoles is neglected in this estimation because the fields are small and the effect is zero anyway for on-axis particles.

8.2 Results

8.2.1 Simulation to the converter

The proton beam depicted in Fig. 2.4 is shot on the 500 mm beryllium plate available in T6 as this yields the highest rate of electrons according to Fig. 8.6. This can be explained by the following: the production of hadrons is proportional to xe^{-x} (cf. Eq. (2.3)), whereas the electron production is roughly given by x^2e^{-x} with $x = \frac{L}{\lambda_0}$ [45]. L corresponds to the material length and λ_0 to its nuclear interaction length. The additional factor of x is caused by the conversion of photons into electron-positron-pairs and in the case of beryllium, radiation length and nuclear interaction length are very close. For both cases one factor x arises from the hadron production, which is also needed because the electrons come from π^0s.

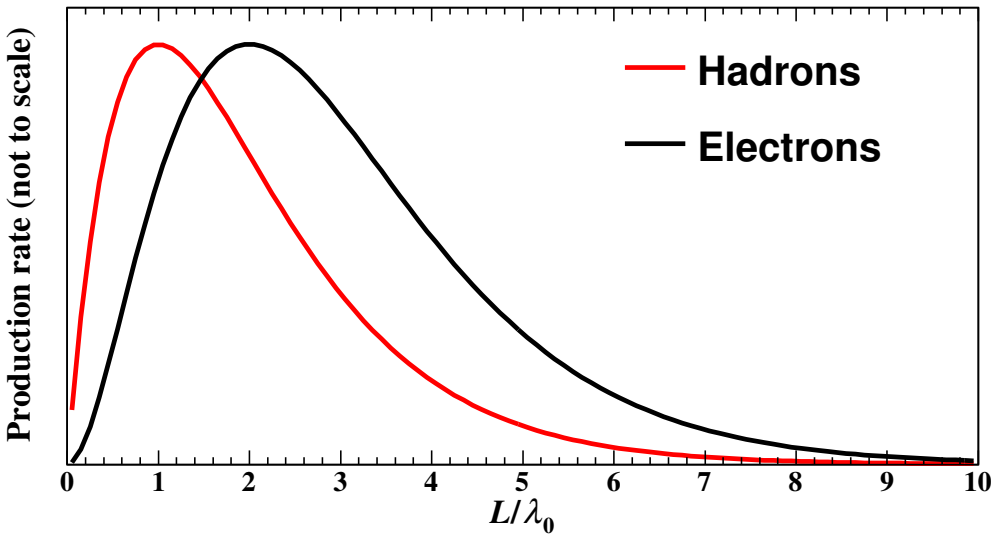

Figure 8.6: Production of electrons (black) and hadrons (red) as a function of the length of the target head expressed in terms of nuclear interaction lengths. Plot after [45].

Again, the large TAX holes have been used for maximal particle flux. The collimator settings are summarized in Tab. 8.1.

For the electron beam mode, there is no particular place in the first part of the beamline that is of special interest. Therefore, the beam distributions are only scored at the position of the converter plate, which is also the hand-over point to the second part of the simulation. The distributions are shown in Fig. 8.7 to 8.9.

From the results, one can see that hadrons and muons get produced and transported to the lead converter more frequently, i.e. by approximately an order of magnitude just considering momenta around the nominal 100 GeV/c of the first part. The main reason is of course the particle production. Considering the mechanism to produce electrons of energies around

Collimator	Horizontal gap in mm	Vertical gap in mm
XCHV.X0610058	±35	±30
XCHV.X0610070	±35	±30
XCBV.X0610858		±20
XCHV.X0611013	±30	-5 +15
XCHV.X0611054	±30	±30

Table 8.1: Collimator settings as they have been used for the electron beam simulation. Those are based on settings that have been used in 2022 [144].

100 GeV (a proton needs to produce a π^0 of 400 GeV that decays into two 200 GeV photons that can produce a 100 GeV electron-positron-pair), it becomes clear that producing hadrons and subsequently muons happens more frequently. Another effect comes into play during the transport. There are vacuum interceptions, and also vacuum windows, where particles undergo interactions like multiple scattering. This effect is of course much worse for electrons than for hadrons and muons meaning one looses more electrons than anything else in case there is material in the beamline.

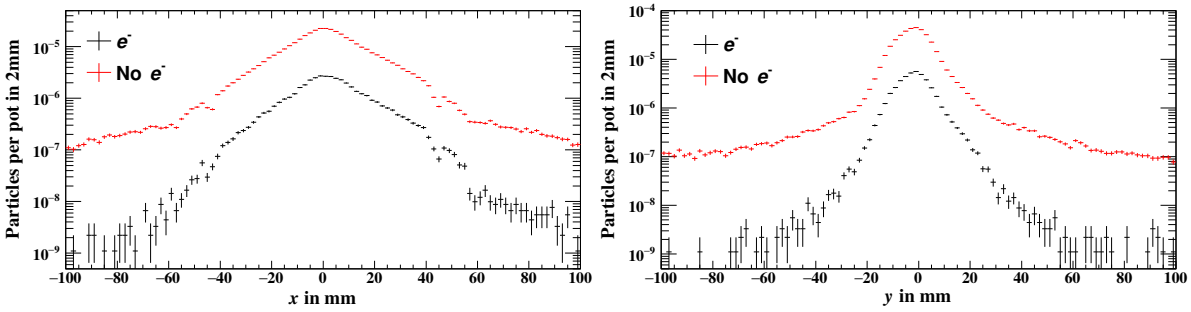

(a) (b)

Figure 8.7: Spatial distributions of the beam at the lead converter. Electrons are plotted in black and the remaining particles in red. The horizontal distribution is illustrated in Fig. 8.7(a) and the vertical in Fig. 8.7(b).

The spatial and angular distributions 8.7 and 8.8 show a beam that is strongly focused on the lead plate, especially in the vertical direction. The reason for that focus is the following: as the converter is placed in the beam way on purpose such that electrons loose large amounts of energy, all the particles will also undergo multiple scattering. The multiple scattering increases the beam divergence incoherently. Therefore, the divergence after the lead plate can be written like $\sqrt{\sigma_0^2 + \sigma_{\mathrm{MS}}^2}$, with σ_0 being the divergence before and σ_{MS} the multiple-scattering contribution. Having a beam that is focused means that the distribution in angle is large. Therefore, adding the multiple scattering term does not impact the total divergence as much as it would do in case

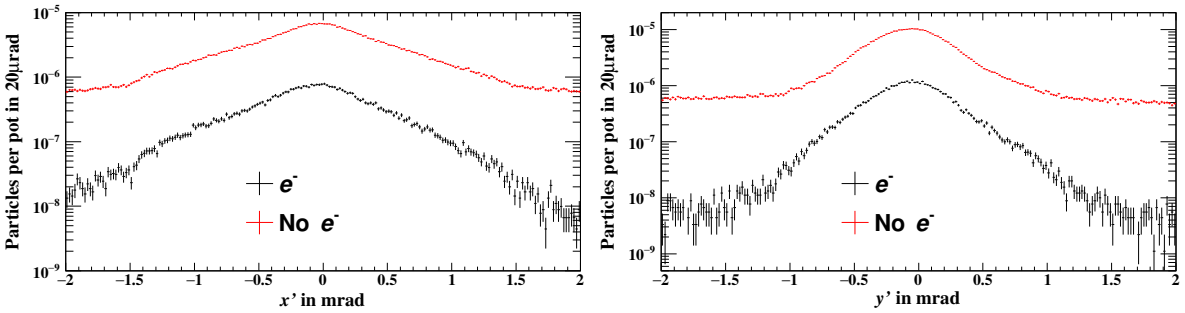

(a) (b)

Figure 8.8: Angular distributions of the beam at the lead converter. Electrons are plotted in black and the remaining particles in red. The horizontal distribution is illustrated in Fig. 8.8(a) and the vertical in Fig. 8.8(b).

one has a parallel beam.

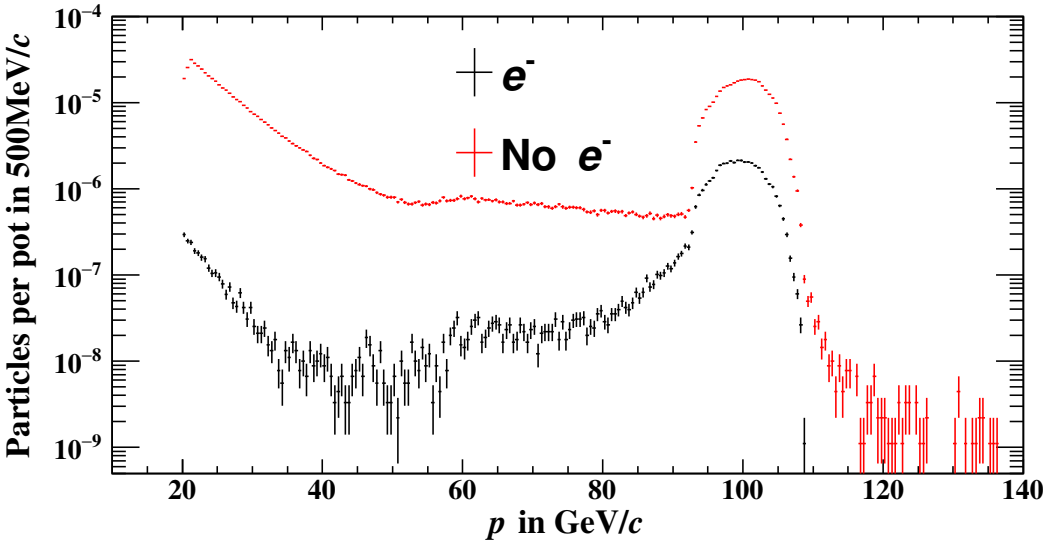

Figure 8.9: Spectrum of the beam at the lead converter. Electrons are plotted in black and the remaining particles in red. For the simulation, a kinetic energy cut has been applied meaning that particles below 20 GeV are destroyed.

The spectra of electrons and all other particles are shown in Fig. 8.9. Those contain all particles within ±5 m meaning also low-energy backgrounds with large spatial amplitudes. Clearly, the kinetic energy threshold set at 20 GeV is visible in the spectra. Of course, this cut has an impact on the low-energy background observed at the MUonE setup because there are no particles in the sample handed over to the second stage that have kinetic energies below 20 GeV.

As the interest is in the beam itself and not the background, the tertiary momentum is set to 40 GeV, so clearly separated from this cut, and such low energy particles are typically not close to the beam axis, the effect of this cut is considered to be negligible.

8.2.2 Simulation to the detector

The presented distributions are used as the input for the second stage of the simulation that starts at the front of the lead converter. During the test run in 2022, the MUonE setup was installed in the CEDAR area. Therefore, the beam distributions shown in the following are scored at this location. The calorimeter that has been in use has a transverse extent of 14.25 cm × 14.25 cm [173]. The beam spot and divergence of the electron component are illustrated in Fig. 8.10. For the test campaign the beam has been fit to the size of the calorimeter, which is clearly the case according to Fig. 8.10(a). Counting all electrons in this area, one gets 4.11×10^{-9} per proton on T6 resulting in around 4 000 electrons for a proton intensity of 10^{13} in one SPS-spill, which is in good agreement with operational experience, during which one observes between 10^{3} to 10^{4} electrons per SPS-cycle [144, 175].

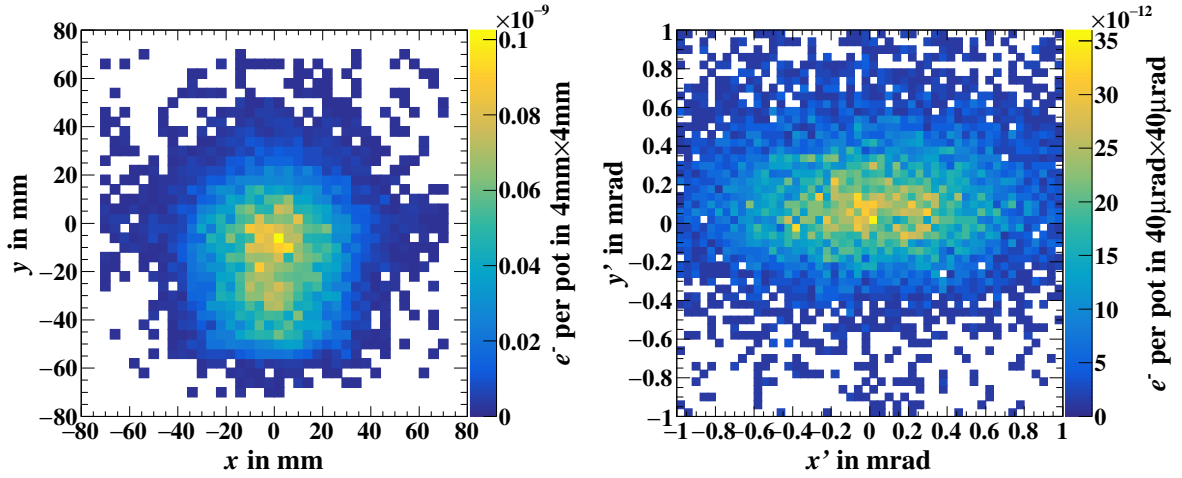

(a) (b)

Figure 8.10: Spatial (Fig. 8.10(a)) and angular ((Fig. 8.10(b))) distributions of electrons at the location of the MUonE calorimeter in the beamline ($s \approx 1.1$ km). A spatial cut of ±7.125 cm was applied in the transverse plane corresponding to the transverse size of the calorimeter.

Of course, the installed calorimeter measures the spectrum of the electrons in the beam. Therefore, the spectrum that has been simulated will be compared with the one obtained by the MUonE collaboration during the test beam campaign. The simulation result is shown in Fig. 8.11.

A Crystal-Ball (8.2) spectrum [176, 177] has been fitted to the simulated data.

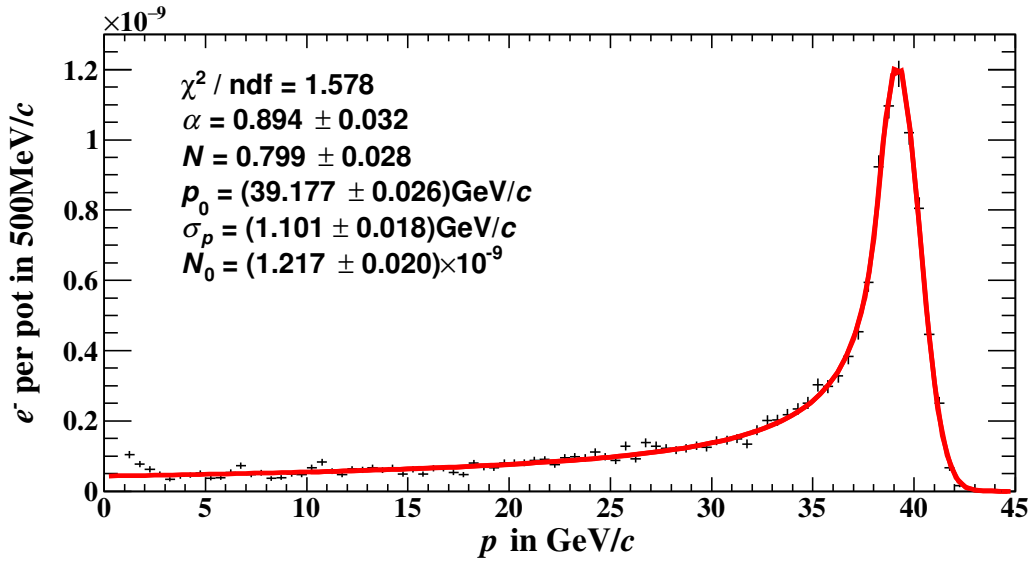

Figure 8.11: Electron spectrum at the location of the MUonE calorimeter in the beamline ($s \approx 1.1\,\mathrm{km}$). A spatial cut of ±7.125 cm was applied in the transverse plane corresponding to the transverse size of the calorimeter. A Crystal-Ball spectrum (Eq. (8.2)) has been fitted to the data.

$$N_0 \begin{cases} \exp\left(-\dfrac{(p-p_0)^2}{2\sigma_p^2}\right), & \dfrac{p-p_0}{\sigma_p} > -\alpha \\ \left(\dfrac{N}{|\alpha|}\right)^N \exp\left(-\dfrac{\alpha^2}{2}\right)\left(\dfrac{N}{|\alpha|} - |\alpha| - \dfrac{p-p_0}{\sigma_p}\right)^{-N}, & \dfrac{p-p_0}{\sigma_p} \leq -\alpha \end{cases} \tag{8.2}$$

The fit yields a mean value p_0 of the Gaussian-part of the spectrum of (39.177 ± 0.026) GeV/c and a standard deviation σ_p of (1.101 ± 0.018) GeV/c, which results in a momentum-resolution of $\frac{\sigma_p}{p_0} = \delta_p = (2.81 \pm 0.04)$ %. Interestingly, the distribution does not peak at 40 GeV, but the maximum is slightly shifted towards lower momenta. As synchrotron radiation is turned off during the simulation this cannot be a possible explanation of this shift. If it would have been turned on, it would also only contribute to ca. 4 MeV which has been derived in section 8.1.2. A main factor is the beam-matter-interaction with material that is in the beams way. A major part here comes from the COMPASS Beam Momentum Stations (BMS) [17], which have been in place during the test beam campaign. Six of those stations were installed making up a total of 11.2 cm of plastic. Considering the energy loss of electrons in polycarbonate of 25.54 MeV cm^2 g^{-1} at 1 GeV kinetic energy given by the ESTAR-database [178] and its density of 1.2 g cm^{-3} [179], one will get a total energy loss of 343.26 MeV. Of course, as the energy loss increases further with higher electron energies it is expected to be even higher at 40 GeV, but the ESTAR-database tabulates values only up to 1 GeV. Another correction arises from the

interaction with the air, where no beam pipes are installed in the beamline. Again, the ESTAR database quotes an energy loss of 26.46 MeV cm^2 g^{-1} [178] resulting in ca. 250 MeV for 80 m of air at 1.205 mg cm^{-3} [180].

The spectrum measured by the MUonE collaboration is depicted in Fig. 8.12.

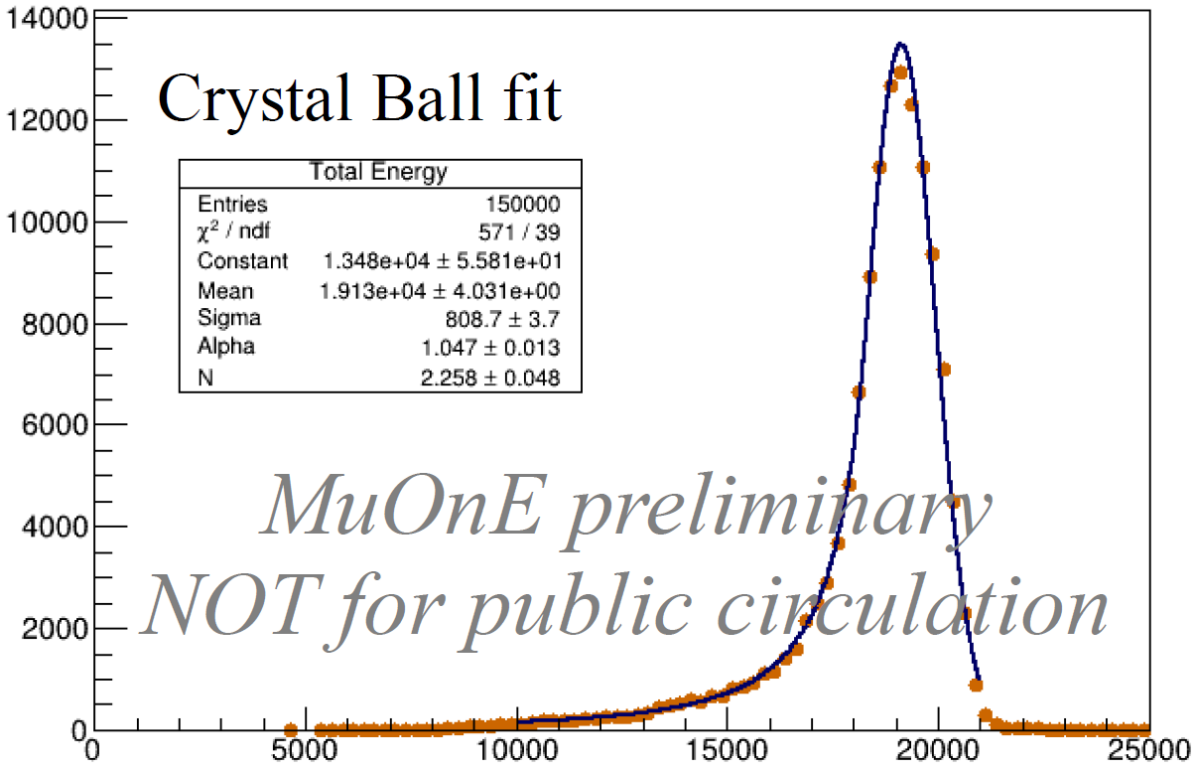

Figure 8.12: Electron spectrum measured by the MUonE calorimeter [177]. The data is not calibrated meaning the spectrum is plotted in analog-to-digital converter (ADC) counts. A Crystal-Ball spectrum (Eq. (8.2)) has been fitted to the data.

A Crytal-Ball distribution has also been fitted to the spectrum. It yields a mean value E_0 of $19\,130 \pm 4$ and a standard deviation σ_E of 809 ± 4, which gives an energy resolution δ_E of (4.227 ± 0.019) %. Compared to the resolution obtained from the simulation one sees a difference of 50 %. Of course, the energy-resolution quoted from the MUonE collaboration contains more source terms than just the energy spread of the beam itself. Clearly, a major contribution is the detector resolution of the calorimeter determined by the device itself and the noise added by the read-out electronics. Because the beam contribution is independent of the detector itself, the total resolution σ_E can be written as $\delta_E = \sqrt{\delta^2_{\text{Beam}} + \delta^2_{\text{Detector}}}$. Considering $\delta_{\text{Beam}} = (2.81 \pm 0.04)$ % and $\delta_E = (4.227 \pm 0.019)$ %, the detector resolution itself would be (3.16 ± 0.05) %. The resolution of the calorimeter is expected to be on the order of 5 to 7 % at an energy of 700 MeV [173]. Assuming a pure $\frac{1}{\sqrt{E}}$-dependence of the resolution, this would mean around 1 % at 40 GeV. Clearly, this simple dependence is not enough to describe the full

calorimeter resolution. Typically, the resolution can be calculated more realistically with

$$\frac{\sigma_E}{E} = \sqrt{\frac{a^2}{E} + \frac{b^2}{E^2} + c^2}, \tag{8.3}$$

[181]. The first term describes the statistically fluctuating number of produced shower particles, the second one the constant electronic noise and the third one represents inhomogeneities in the material or mistakes in the calibration. Considering those additional effects, the value of about 3 % is indeed realistic underlining the excellent agreement between the beamline simulation yielding the pure electron spectrum and the measurement.

CHAPTER 9

Conclusion and outlook

9.1 Summary

Throughout this thesis, the M2 secondary beamline at CERN's SPS has been investigated. The focus has been on the future high-intensity and high-energy hadron beam operation important for the AMBER experiment. Because the beamline is also capable of delivering high-rate, high-energy muon beams used for instance by the NA64 experiment important features of it have been studied. With the third and last operational mode low-energy and low-intensity electrons can be sent to the experimental area. This beam is used for calibration purposes. Therefore, it is necessary to estimate the peak position and width of the momentum distribution. All these points have been studied during the scope of this thesis with Monte Carlo simulation techniques.

To be able to answer questions regarding the fundamental processes of the generation of the hadronic mass, the AMBER experiment relies on high-intensity kaon beams. In chapter 5 and 6 it has been shown that one has two possibilities to overcome the problem of the small abundance of kaons in the secondary beam: either by increasing the purity or the absolute rate.

The latter can be achieved with the RF separation technique. It relies on the velocity differences particles with different masses have at the same momentum. To achieve a separation, a first transversely deflecting RF cavity is used to kick the traversing particles independent of their species. A second one that is placed at a known distance behind the first works as an analysing cavity. Particles coming out of that one have an angular distribution that depends indeed on the particle mass. Simulations of the transmission and separation of the RF beam have shown that it is possible to reach kaon rates up to 600 kHz with a purity of 20 %. But such values are acceptable for only parts of the physics program envisaged by AMBER. A critical constraint enforced by the RF separation is the limitation of the beam momentum. This limit is due to the distance between the cavities and the moderate radio-frequency that one can have while still having reasonable gradients and apertures. For certain measurements like the determination of the parton distribution functions of the kaon via Drell-Yan process a high

beam energy is needed in order to reach a kinematic region that AMBER can cover. Because the process itself has a low probability, a decrease of acceptance due to the low beam energy is unacceptable.

As the increase of kaon abundance is only useful for parts of the AMBER measurements, the absolute rate of kaons needs to be improved. This has been done in the scope of the conventional hadron beam as it has been operated in the past. The flux relevant for the experiment is not the absolute rate reaching the experimental area but the number of particles that are tagged by the particle identification system. Therefore, the efficiency of identification needs to be as high as possible in order to make optimal use of the low kaon fraction in the beam. It has been shown that the remaining ca. 100 m of beamline that are currently not under vacuum reduce the number of identifiable particles by 36 %. Together with improved beam optics resulting in a more parallel beam at the position of identification the vacuum upgrade can increase the rate by a factor 3.3 relative to the current setup of the beamline.

With those improvements of the beam the duration of the strange-meson spectroscopy of AMBER has been estimated. Through Monte Carlo simulations of the full detector response and event reconstruction the acceptance of the setup has been determined. Together with the beam flux the instantaneous luminosity has been estimated finally yielding the run time needed for the anticipated 2×10^7 recorded events. The detector efficiencies regarding particle identification have been simulated for various beam energies. It has been shown that the best performance in terms of PID is expected for lower beam momenta. For 100 GeV/c a period of about 1.5 yr is expected to collect the anticipated data-set.

For the NA64 experiment exploiting the muon beam for dark matter searches knowledge of the hadronic background is crucial. Therefore, the hadron contamination has been evaluated in Monte Carlo simulation. It has been found that for the maximal number of absorbers one has about one hadron in 10^6 muons. To be able to determine such low rates biasing techniques have been investigated. Those help estimating processes with low probability even in a reasonable amount of computing time. Depending on the absorber length different cross section biasing factors have been used. The factors are motivated by the average length particles can travel in the absorber with and without the applied factor reducing the probability for inelastic processes.

Dealing with simulations it is important to benchmark it with real data. The MUonE collaboration has tested an electromagnetic calorimeter with the available electron beam in M2 measuring the spectrum of those. The same has been simulated with the implemented model yielding the peak position and width. A momentum spread of (2.81 ± 0.04) % has been obtained in simulations while the measurement has given (4.227 ± 0.019) %. Clearly, the simulation does not include the calorimeter itself. Therefore, no detector resolutions or fluctuations in the read-out electronics are included. That is why one expects a smaller value coming from the simulation. Considering the width coming from the measurement consisting of the aforementioned contributions together with the intrinsic energy-spread of the beam, one expects an energy resolution of (3.16 ± 0.05) % at 40 GeV, which is of the order of values the MUonE collaboration is communicating [173].

9.2 Future perspectives

The RF beam has not shown a significant increase of the overall beam rate, only of the beam purity. Of course, together with more protons on T6 one could reach kaon intensities that would be suitable for the physics programs. But in order to get there one would need more than an order of magnitude more, which is unrealistic. Considering the low gain together with the huge cost that would need to be invested for the cavities and cryogenics to implement the RF separated beam it is currently out of reach to install it. Clearly, as soon as the RF technology can provide cavities with similar gradients and frequencies but larger apertures, the situation becomes different because the gain would be immediately recognisable.

Together with a larger aperture, which would require a redesign of the beam optics, the effect of a cavity that deflects the beam in the full transverse plane could be investigated. The field of such a cavity is expected to vary less with the azimuthal angle [126] mitigating the problem of a non-constant field over the iris generating a position-dependent cavity kick. Also, a full particle-matter simulation is needed to estimate the absorption capability of the beam dump yielding a realistic determination of the expected background level.

As soon as the proposed beamline upgrades for the conventional beam will be implemented it is important to validate the estimated improvements. Because the gains are already significant only small further enhancements are expected. Because the beam is already close to optimal in the horizontal direction, only changes in the vertical would really help. A possibility to further improve the tagging efficiency is the reduction of the vertical angular dispersion, i.e. R_{46}. M2 is a vertical beamline, which requires the regular installation of vertical bending magnets that introduce dispersion. The corresponding recombination could be studied to get an even further improved set of optics.

Already for the beamline simulation a more realistic implementation of the CEDARs would be helpful. This would include the generation of Čerenkov photons by the particles traversing the active volume of the detector together with the transmissions and reflections through the optical systems consisting of mirrors and lenses. Of course, the simultaneous simulation of the full beamline with the ray-tracing in the CEDARs would be unreasonable in terms of computing time but with realistic beam distributions at the entrance of the detector one could study the full response. Such a model is currently under development within the Experimental Areas group, from which also experiments could profit. As the majority method has been used for the estimation of run time for the spectroscopy program by requiring the beam divergence to be smaller than a given threshold value, the identification efficiency is expected to be determined too pessimistic. With a full simulation of the CEDAR response one could study the actual efficiency together with the rate of wrongly identified particles.

The resulting beam distributions from the muon simulation are currently under study by the NA64 collaboration. They are estimating the detector response in a full Monte Carlo simulation of the complete setup finally yielding the level of hadron contamination. This is important because a measurement of it has been performed in 2023 for different absorber lengths. To be

able to fully compare the simulation with the collected data the model of the detector including response and event reconstruction is needed. This will be provided by the study of NA64. Also, beam-matter interaction with the NA64 setup will be included, which can include locations, where further hadrons are produced.

Preliminary results from measurement do not show the same behaviour of the hadron contamination as it is in the presented simulation. This means further sources of hadrons need to be investigated. Possibilities are the NA64 detectors as well as the thin plastic scintillators, the COMPASS BMS. Because their longitudinal extent is small the production and absorption might not be sampled accurately. To overcome this problem the relevant processes may need to be biased, too, in order to estimate the corresponding contributions. This will help understanding the possible origins of hadrons. When knowing the local sources one can start investigating how to suppress those in order to reduce the hadron contamination even without inserting more absorbers in bend4.

Bibliography

[1] P. W. Higgs, *Broken Symmetries and the Masses of Gauge Bosons*, Phys. Rev. Lett. **13** (16 1964) 508, URL: https://link.aps.org/doi/10.1103/PhysRevLett.13.508 (cit. on p. 1).

[2] F. Englert and R. Brout, *Broken Symmetry and the Mass of Gauge Vector Mesons*, Phys. Rev. Lett. **13** (9 1964) 321, URL: https://link.aps.org/doi/10.1103/PhysRevLett.13.321 (cit. on p. 1).

[3] G. Aad et al., *Observation of a new particle in the search for the Standard Model Higgs boson with the ATLAS detector at the LHC*, Phys. Lett. B **716** (2012) 1, arXiv: 1207.7214 [hep-ex], URL: https://www.sciencedirect.com/science/article/pii/S037026931200857X (cit. on p. 1).

[4] S. Chatrchyan et al., *Observation of a New Boson at a Mass of 125 GeV with the CMS Experiment at the LHC*, Phys. Lett. B **716** (2012) 30, arXiv: 1207.7235 [hep-ex], URL: https://www.sciencedirect.com/science/article/pii/S0370269312008581 (cit. on p. 1).

[5] Particle Data Group, P. A. Zyla et al., *Review of Particle Physics*, Progress of Theoretical and Experimental Physics **2020** (2020), 083C01, ISSN: 2050-3911, eprint: https://academic.oup.com/ptep/article-pdf/2020/8/083C01/34673722/ptaa104.pdf, URL: https://academic.oup.com/ptep/article/2020/8/083C01/5891211 (cit. on pp. 1, 2, 33, 34, 55, 81, 95, 101, 111, 120, 123).

[6] C. D. Roberts, *Empirical Consequences of Emergent Mass*, Symmetry **12** (2020), ISSN: 2073-8994, URL: https://www.mdpi.com/2073-8994/12/9/1468 (cit. on p. 1).

[7] CERN, *Dark matter*, URL: https://home.cern/science/physics/dark-matter (visited on 11/12/2023) (cit. on p. 2).

[8] M. Gell-Mann, *The Eightfold Way: A Theory of Strong Iinteraction Symmetry*, (1961), URL: https://www.osti.gov/biblio/4008239 (cit. on p. 1).

[9] G. Zweig,
"An SU(3) model for strong interaction symmetry and its breaking. Version 2",
Developments in the Quark Theory of Hadrons. Vol. 1. 1964 - 1978,
ed. by D. B. Lichtenberg and S. P. Rosen, 1964 22,
URL: https://cds.cern.ch/record/570209 (cit. on p. 1).

[10] E. D. Bloom et al., *High-Energy Inelastic $e - p$ Scattering at 6° and 10°*,
Phys. Rev. Lett. **23** (16 1969) 930,
URL: https://link.aps.org/doi/10.1103/PhysRevLett.23.930 (cit. on p. 1).

[11] M. Breidenbach et al.,
Observed Behavior of Highly Inelastic Electron-Proton Scattering,
Phys. Rev. Lett. **23** (16 1969) 935,
URL: https://link.aps.org/doi/10.1103/PhysRevLett.23.935 (cit. on p. 1).

[12] J. D. Bjorken, *Theoretical Ideas on Inelastic Electron and Muon Scattering*,
(1967) 109, URL: https://cds.cern.ch/record/2702147 (cit. on p. 1).

[13] Y. Nambu, *Quasi-Particles and Gauge Invariance in the Theory of Superconductivity*,
Phys. Rev. **117** (3 1960) 648,
URL: https://link.aps.org/doi/10.1103/PhysRev.117.648 (cit. on p. 2).

[14] J. Goldstone, *Field Theories with Superconductor Solutions*,
Nuovo Cim. **19** (1961) 154,
URL: https://link.springer.com/article/10.1007/BF02812722
(cit. on p. 2).

[15] C. Han, G. Xie, R. Wang and X. Chen, *An analysis of parton distribution functions of the pion and the kaon with the maximum entropy input*,
The European Physical Journal C **81** (2021), ISSN: 1434-6052, URL:
https://link.springer.com/article/10.1140/epjc/s10052-021-09087-8
(cit. on pp. 3, 40).

[16] W.-C. Chang et al., *Pion PDFs confronted by fixed-target charmonium production*,
AAPPS Bulletin **33** (2023), ISSN: 2309-4710,
URL: https://link.springer.com/article/10.1007/s43673-023-00085-4
(cit. on pp. 3, 40).

[17] P. Abbon et al., *The COMPASS experiment at CERN*,
Nucl. Instrum. Meth. A **577** (2007) 455, arXiv: hep-ex/0703049, URL: https://www.sciencedirect.com/science/article/pii/S0168900207005001
(cit. on pp. 3, 15, 29, 84, 92, 129).

[18] B. Adams et al., *Letter of Intent: A New QCD facility at the M2 beam line of the CERN SPS (COMPASS++/AMBER)*, 2019, arXiv: 1808.00848 [hep-ex]
(cit. on pp. 3, 7, 32, 37, 41, 42, 95).

[19] B. Adams et al., *COMPASS++/AMBER: Proposal for Measurements at the M2 beam line of the CERN SPS Phase-1: 2022-2024*, (2019), URL: http://cds.cern.ch/record/2676885 (cit. on pp. 3, 7, 32, 93).

[20] S. Gninenko et al., *Proposal for an experiment to search for dark sector particles weakly coupled to muon at the SPS*, tech. rep., CERN, 2019, URL: https://cds.cern.ch/record/2653581 (cit. on pp. 4, 100, 101).

[21] G. Abbiendi et al., *Letter of Intent: the MUonE project*, (2019), URL: https://cds.cern.ch/record/2677471 (cit. on pp. 4, 8, 100, 119).

[22] *About CERN*, URL: https://home.cern/node/5011 (visited on 20/09/2023) (cit. on p. 5).

[23] E. Lopienska, *The CERN accelerator complex, layout in 2022. Complexe des accélérateurs du CERN en janvier 2022*, General Photo, 2022, URL: https://cds.cern.ch/record/2800984 (visited on 21/09/2023) (cit. on p. 6).

[24] M. Vretenar et al., *Linac4 design report*, vol. 6, CERN Yellow Reports: Monographs, Geneva: CERN, 2020, URL: https://cds.cern.ch/record/2736208 (cit. on p. 5).

[25] W. Bartmann et al., *CERN PSB to PS Transfer Modifications for the 2 GeV Upgrade*, Conf. Proc. **C1205201** (2012) MOPPD057, URL: https://cds.cern.ch/record/1470565 (cit. on p. 5).

[26] *Proton Synchrotron*, (1959), URL: https://cds.cern.ch/record/1479637 (cit. on p. 5).

[27] *The Proton Synchrotron*, URL: https://home.cern/science/accelerators/proton-synchrotron (visited on 03/10/2023) (cit. on p. 5).

[28] *The Super Proton Synchrotron*, URL: https://home.cern/science/accelerators/super-proton-synchrotron (visited on 03/10/2023) (cit. on p. 6).

[29] J. B. Adams and E. J. N. Wilson, *Design studies for a large proton synchrotron and its laboratory*, CERN Yellow Reports: Monographs (1970), URL: http://cds.cern.ch/record/229225 (cit. on p. 6).

[30] J. B. Adams, *The CERN 400 GeV Proton Synchrotron (CERN SPS)*, (1977), Talk, URL: https://cds.cern.ch/record/2048898 (cit. on p. 6).

[31] *LHC Run 3*, URL: https://home.cern/press/2022/run-3 (visited on 06/02/2024) (cit. on p. 6).

[32] O. S. Brüning et al., *LHC Design Report*, CERN Yellow Reports: Monographs, Geneva: CERN, 2004, URL: https://cds.cern.ch/record/782076 (cit. on p. 6).

[33] *The Low Energy Ion Ring*,
URL: https://home.cern/science/accelerators/low-energy-ion-ring
(visited on 06/02/2024) (cit. on p. 6).

[34] J. Jowett, *Colliding Heavy Ions in the LHC*, (2018) TUXGBD2, URL: https://accelconf.web.cern.ch/ipac2018/doi/JACoW-IPAC2018-TUXGBD2.html
(cit. on p. 6).

[35] L. Gatignon et al., *Report from the Conventional Beams Working Group to the Physics Beyond Collider Study and to the European Strategy for Particle Physics*, (2022),
URL: http://cds.cern.ch/record/2650989 (cit. on p. 7).

[36] L. R. Evans, A. Ijspeert, B. de Raad, W. Thomi and E. Weisse,
The steel septum magnets for beam splitting at the CERN SPS, (1978),
URL: https://cds.cern.ch/record/319349 (cit. on p. 7).

[37] L. R. Evans et al.,
The external proton beam lines and the splitter systems of the CERN SPS,
IEEE Trans. Nucl. Sci. **24** (1977) 1571,
URL: https://ieeexplore.ieee.org/document/4329014 (cit. on p. 7).

[38] S. Andreas et al.,
Proposal for an Experiment to Search for Light Dark Matter at the SPS, 2013,
arXiv: 1312.3309 [hep-ex] (cit. on pp. 7, 8, 100, 105).

[39] A. Ceccucci et al., *Proposal to measure the rare decay $K^+ \to \pi^+ \nu\bar{\nu}$ at the CERN SPS*, (2005), URL: https://cds.cern.ch/record/832885 (cit. on pp. 8, 97).

[40] I. Efthymiopoulos, *Target Station T4 Wobbling - Explained*, (2003), URL: http://sba.web.cern.ch/sba/Documentations/Target/T4/T4Wobbling3.pdf
(cit. on p. 8).

[41] N. Abgrall et al., *NA61/SHINE facility at the CERN SPS: beams and detector system*,
Journal of Instrumentation **9** (2014) P06005, ISSN: 1748-0221, URL:
https://iopscience.iop.org/article/10.1088/1748-0221/9/06/P06005
(cit. on p. 8).

[42] M. Calviani et al., *Specification for the renovated North Area primary targets T2, T4, T6, T10 and associated beam instrumentation*,
URL: https://edms.cern.ch/file/1267311/4.0 (visited on 03/10/2023)
(cit. on pp. 8, 10).

[43] Particle Data Group, *Atomic and nuclear properties of beryllium (Be)*, URL: https://pdg.lbl.gov/2022/AtomicNuclearProperties/HTML/beryllium_Be.html
(visited on 05/10/2023) (cit. on pp. 8, 10, 106, 114).

[44] H. W. Atherton et al., *Precise Measurements of Particle Production by 400 GeV/c Protons on Beryllium Targets*, (1980),
URL: https://cds.cern.ch/record/133786 (cit. on pp. 8, 9, 90).

[45] D. Banerjee et al., *The North Experimental Area at the Cern Super Proton Synchrotron*, (2021), URL: https://cds.cern.ch/record/2774716 (cit. on pp. 10, 24, 28, 29, 125).

[46] *Miniscan on T6*, URL: https://logbook.cern.ch/elogbook-server/GET/showEventInLogbook/3612886 (visited on 05/10/2023) (cit. on p. 11).

[47] H. Wiedemann, *Particle Accelerator Physics*, Springer, 2015, ISBN: 978-3-319-18316-9, URL: https://doi.org/10.1007/978-3-319-18317-6 (cit. on pp. 12, 22).

[48] P. Abbon et al., *The COMPASS Setup for Physics with Hadron Beams*, Nucl. Instrum. Meth. A **779** (2015) 69, arXiv: 1410.1797 [physics.ins-det], URL: https://www.sciencedirect.com/science/article/pii/S0168900215000662 (cit. on pp. 14, 34, 45).

[49] B. J. Holzer, *Lattice Design in High-energy Particle Accelerators*, (2014) 61, 40 pages, contribution to the CAS - CERN Accelerator School: Advanced Accelerator Physics Course, Trondheim, Norway, 18-29 Aug 2013. arXiv admin note: substantial text overlap with arXiv:1303.6514, arXiv: 1601.04913, URL: https://cds.cern.ch/record/1982419 (cit. on p. 17).

[50] V. Stergiou and N. Charitonidis, *User Requirements for the XCSH/V, XCHV and XCBV Collimators*, URL: https://edms.cern.ch/document/2742301/0.3 (visited on 28/09/2023) (cit. on p. 18).

[51] Particle Data Group, *Atomic and nuclear properties of materials: Iron (Fe)*, URL: https://pdg.lbl.gov/2010/AtomicNuclearProperties/HTML_PAGES/026.html (visited on 28/09/2023) (cit. on p. 18).

[52] G. L. D'Alessandro et al., *First "Skin Depth" estimations using GEANT4 and FLUKA based simulations for CERN secondary beamlines*, Nuclear Instruments and Methods in Physics Research Section B: Beam Interactions with Materials and Atoms **512** (2022) 76, ISSN: 0168-583X, URL: https://www.sciencedirect.com/science/article/pii/S0168583X21004055 (cit. on p. 18).

[53] L. Gatignon, *Design and Tuning of Secondary Beamlines in the CERN North and East Areas*, (2020), URL: https://cds.cern.ch/record/2730780 (cit. on pp. 19, 124).

[54] W. Hillert, *Transverse Linear Beam Dynamics*, 2021, arXiv: 2107.02614 [physics.acc-ph] (cit. on pp. 20–22).

[55] J. Liouville, *Note sur la Théorie de la Variation des constantes arbitraires*, fr, Journal de Mathématiques Pures et Appliquées **1e série, 3** (1838), URL: http://www.numdam.org/item/JMPA_1838_1_3__342_0/ (cit. on p. 23).

[56] P. A. Čerenkov, *Visible luminescence of pure liquids under the influence of γ radiation*, Dokl. Akad. Nauk SSSR **2** (1934) 451, URL: https://ufn.ru/ru/articles/1967/10/n/ (cit. on p. 25).

[57] L. Landau et al., *Electrodynamics of Continuous Media*, Second Edition, vol. 8, Course of Theoretical Physics, Amsterdam: Pergamon, 1984 394, ISBN: 978-0-08-030275-1, URL: https://www.sciencedirect.com/science/article/pii/B9780080302751500205 (cit. on p. 25).

[58] C. Bovet, R. Maleyran, L. Piemontese, A. Placci and M. Placidi, *The CEDAR counters for particle identification in the SPS secondary beams: a description and an operation manual*, CERN Yellow Reports: Monographs, Geneva: CERN, 1982, URL: https://cds.cern.ch/record/142935 (cit. on pp. 26, 27, 97).

[59] S. Wallner, *Exploring the Strange-Meson spectrum with COMPASS in the reaction $K^- + p \to K^-\pi^-\pi^+ + p$*, PhD thesis: Technische Universität München, 2022, URL: https://mediatum.ub.tum.de/?id=1632535 (cit. on pp. 26, 44, 45, 92, 93, 95–97, 99).

[60] S. Wallner et al., *CEDAR PID using the Likelihood Approach for the Hadron-Beam*, (2017), URL: https://wwwcompass.cern.ch/compass/notes/2017-1/2017-1.pdf (cit. on pp. 26, 95, 96, 99).

[61] J. Friedrich, *CEDAR performance 2009*, (2010), URL: https://wwwcompass.cern.ch/compass/notes/2010-15/2010-15.pdf (cit. on pp. 26, 95, 96, 99).

[62] *XCED: CEDAR counters*, URL: https://sba.web.cern.ch/sba/Documentations/Informations&Training/Beam_Equipments/XCED_CEDAR_counters/index.htm (visited on 12/01/2024) (cit. on pp. 26, 27).

[63] C. Bovet, S. Milner and A. Placci, *The CEDAR project : Čerenkov differential counters with achromatic ring focus*, Geneva, 1975, URL: https://cds.cern.ch/record/1023286 (cit. on pp. 27, 89).

[64] G. Charpak, R. Bouclier, T. Bressani, J. Favier and Č. Zupančič, *The use of multiwire proportional counters to select and localize charged particles*, Nuclear Instruments and Methods **62** (1968) 262, ISSN: 0029-554X, URL: https://www.sciencedirect.com/science/article/pii/0029554X68903716 (cit. on p. 27).

[65] I. Ortega Ruiz et al., *The XBPF, a new multipurpose scintillating fibre monitor for the measurement of secondary beams at CERN*,
Nuclear Instruments and Methods in Physics Research Section A: Accelerators, Spectrometers, Detectors and Associated Equipment **951** (2020) 162996,
ISSN: 0168-9002, URL: https://www.sciencedirect.com/science/article/pii/S0168900219313737
(cit. on p. 28).

[66] J. Tan et al., *Summing up of instrumentation needs for primary and secondary beams*,
URL: https://edms.cern.ch/ui/file/2870743/1/2019-02-15-Deliverable_2_SBA_BIEA-1_pptx_cpdf.pdf (visited on 13/01/2024)
(cit. on p. 28).

[67] G. Baum et al., *COMPASS: A Proposal for a Common Muon and Proton Apparatus for Structure and Spectroscopy*, (1996),
URL: https://wwwcompass.cern.ch/compass/proposal/pdf/proposal.pdf
(cit. on p. 29).

[68] F. Gautheron et al., *COMPASS-II Proposal*, (2010),
URL: https://wwwcompass.cern.ch/compass/proposal/compass-II_proposal/compass-II_proposal.pdf (cit. on p. 29).

[69] V. Andrieux and B. Parsamyan,
From COMPASS to AMBER: exploring fundamental properties of hadrons,
URL: https://ep-news.web.cern.ch/compass-amber-exploring-fundamental-properties-hadrons (visited on 17/01/2024) (cit. on p. 33).

[70] Y. Fukuda et al., *Evidence for Oscillation of Atmospheric Neutrinos*,
Phys. Rev. Lett. **81** (8 1998) 1562,
URL: https://link.aps.org/doi/10.1103/PhysRevLett.81.1562
(cit. on p. 33).

[71] F. Zwicky, *On the Masses of Nebulae and of Clusters of Nebulae*,
Astrophysical Journal **86** (1937) 217,
URL: https://ui.adsabs.harvard.edu/abs/1937ApJ....86..217Z
(cit. on p. 34).

[72] M. Thomson, *Modern particle physics*, New York: Cambridge University Press, 2013,
ISBN: 978-1-107-03426-6,
URL: https://www.cambridge.org/highereducation/books/modern-particle-physics/CDFEBC9AE513DA60AA12DE015181A948 (cit. on p. 34).

[73] W. Herr and B. Muratori, *Concept of luminosity*, (2006),
URL: https://cds.cern.ch/record/941318 (cit. on p. 36).

[74] S. Fartoukh, S. Kostoglou, M. Solfaroli Camillocci, G. Arduini and H. Bartosik,
LHC Configuration and Operational Scenario for Run 3, tech. rep., CERN, 2021,
URL: https://cds.cern.ch/record/2790409 (cit. on p. 36).

[75] P. A. M. Dirac, *The Quantum Theory of the Electron*,
Proceedings of the Royal Society of London. Series A, Containing Papers of a Mathematical and Physical Character **117** (1928) 610, ISSN: 09501207,
URL: https://royalsocietypublishing.org/doi/10.1098/rspa.1928.0023 (cit. on p. 37).

[76] J. S. Hangst, P. Bowe et al., *ALPHA Proposal*, tech. rep., CERN, 2005,
URL: https://cds.cern.ch/record/814351 (cit. on p. 37).

[77] J. Hangst et al., *Spectroscopic and gravitational measurements on antihydrogen: ALPHA-3, ALPHA-g and beyond*, tech. rep., CERN, 2019,
URL: https://cds.cern.ch/record/2691557 (cit. on p. 37).

[78] E. Anderson, C. Baker, W. Bertsche et al.,
Observation of the effect of gravity on the motion of antimatter, Nature **621** (2023) 716,
URL: https://www.nature.com/articles/s41586-023-06527-1 (cit. on p. 37).

[79] M. Ahmadi, B. Alves, C. Baker et al.,
Characterization of the 1S–2S transition in antihydrogen, Nature **557** (2018) 71,
URL: https://www.nature.com/articles/s41586-018-0017-2#citeas (cit. on p. 37).

[80] R. Battiston,
The antimatter spectrometer (AMS-02): A particle physics detector in space,
Nuclear Instruments and Methods in Physics Research Section A: Accelerators, Spectrometers, Detectors and Associated Equipment **588** (2008) 227, Proceedings of the First International Conference on Astroparticle Physics, ISSN: 0168-9002,
URL: https://www.sciencedirect.com/science/article/pii/S0168900208000727 (cit. on p. 37).

[81] M. Aguilar et al., *Antiproton Flux, Antiproton-to-Proton Flux Ratio, and Properties of Elementary Particle Fluxes in Primary Cosmic Rays Measured with the Alpha Magnetic Spectrometer on the International Space Station*,
Phys. Rev. Lett. **117** (9 2016) 091103,
URL: https://link.aps.org/doi/10.1103/PhysRevLett.117.091103 (cit. on p. 37).

[82] P. Zuccon, *Antiproton cross-section measurements for Dark Matter search*,
URL: https://indico.cern.ch/event/1021402/contributions/4311146/attachments/2234195/3786365/PZ_AMBER_Workshop_April21.pdf (visited on 17/01/2024) (cit. on p. 38).

[83] J. Bernhard, *CEDAR-N* (cit. on p. 39).

[84] E. Albrecht et al., *COMPASS RICH-1*, Nuclear Instruments and Methods in Physics Research Section A: Accelerators, Spectrometers, Detectors and Associated Equipment **478** (2002) 340, Proceedings of the ninth Int.Conf. on Instrumentation, ISSN: 0168-9002, URL: https://www.sciencedirect.com/science/article/pii/S016890020101823X (cit. on p. 39).

[85] E. Rutherford, *LIV. Collision of α particles with light atoms. IV. An anomalous effect in nitrogen*, The London, Edinburgh, and Dublin Philosophical Magazine and Journal of Science **37** (1919) 581, URL: https://www.tandfonline.com/doi/abs/10.1080/14786440608635919 (cit. on p. 37).

[86] R. Frisch and O. Stern, *Über die magnetische Ablenkung von Wasserstoffmolekülen und das magnetische Moment des Protons. I*, Zeitschrift für Physik **85** (1933) 4, URL: https://link.springer.com/article/10.1007/BF01330773 (cit. on p. 37).

[87] P. J. Mohr, B. N. Taylor and D. B. Newell, *CODATA recommended values of the fundamental physical constants: 2014*, Rev. Mod. Phys. **88** (3 2016) 035009, URL: https://link.aps.org/doi/10.1103/RevModPhys.88.035009 (cit. on p. 38).

[88] R. Pohl et al., *The size of the proton*, Nature **466** (2010) 213, URL: https://www.nature.com/articles/nature09250 (cit. on p. 38).

[89] A. Antognini et al., *Proton Structure from the Measurement of 2S-2P Transition Frequencies of Muonic Hydrogen*, Science **339** (2013) 417, ISSN: 0036-8075, URL: https://science.sciencemag.org/content/339/6118/417 (cit. on p. 38).

[90] N. Doble, L. Gatignon, G. von Holtey and F. Novoskoltsev, *The upgraded muon beam at the SPS*, Nuclear Instruments and Methods in Physics Research Section A: Accelerators, Spectrometers, Detectors and Associated Equipment **343** (1994) 351, ISSN: 0168-9002, URL: https://www.sciencedirect.com/science/article/pii/0168900294902127 (cit. on pp. 39, 100, 109, 115).

[91] D. R. Nygren et al., *The Time Projection Chamber*, Phys. Today **31** (1978) 46, URL: https://pubs.aip.org/physicstoday/article/31/10/46/431734/ (cit. on p. 40).

[92] F. Metzger,
Simulations of an active-target TPC for a measurement of the proton charge radius,
MA thesis: Rheinische Friedrich-Wilhelms-Universität Bonn, 2020,
URL: https://cds.cern.ch/record/2905678 (cit. on p. 40).

[93] C. M. G. Lattes, H. Muirhead, G. P. S. Occhialini and C. F. Powell,
Processes involving charged mesons, Nature **159** (1947) 694,
URL: https://www.nature.com/articles/159694a0 (cit. on p. 40).

[94] G. D. Rochester and C. C. Butler,
Evidence for the Existence of New Unstable Elementary Particles,
Nature **160** (1947) 855, URL: https://www.nature.com/articles/160855a0
(cit. on p. 40).

[95] J. Stirling, *Parton Distribution Functions*,
URL: https://indico.cern.ch/event/94815/contributions/1282690/attachments/1106827/1579062/LBLMIT_Stirling_v2.pdf (visited on 10/02/2024) (cit. on p. 40).

[96] S. D. Drell and T.-M. Yan,
Massive Lepton-Pair Production in Hadron-Hadron Collisions at High Energies,
Phys. Rev. Lett. **25** (5 1970) 316,
URL: https://link.aps.org/doi/10.1103/PhysRevLett.25.316
(cit. on p. 40).

[97] S. D. Drell and T.-M. Yan,
Massive Lepton-Pair Production in Hadron-Hadron Collisions at High Energies,
Phys. Rev. Lett. **25** (13 1970) 902,
URL: https://link.aps.org/doi/10.1103/PhysRevLett.25.902.2
(cit. on p. 40).

[98] J. Badier et al., *Experimental Determination of the π-Meson Structure Functions by the Drell-Yan Mechanism*, Z. Phys. C **18** (1983) 281,
URL: https://link.springer.com/article/10.1007/BF01573728
(cit. on p. 40).

[99] J. D. Bjorken, *Asymptotic Sum Rules at Infinite Momentum*,
Phys. Rev. **179** (5 1969) 1547,
URL: https://link.aps.org/doi/10.1103/PhysRev.179.1547 (cit. on p. 41).

[100] V. Andrieux, *π- and K-induced Drell-Yan measurements at M2 beamline motivations and requirements*,
URL: https://indico.cern.ch/event/1133376/contributions/4786342/attachments/2414810/4132363/Andrieux_RF-CB-Workshop20220324.pdf
(visited on 07/12/2023) (cit. on p. 42).

[101] C. Quintans, *Polarized Drell-Yan studies at COMPASS*, EPJ Web of Conferences **66** (2014) 06021, URL: https://www.epj-conferences.org/articles/epjconf/abs/2014/03/epjconf_inpc2013_06021/epjconf_inpc2013_06021.html (cit. on p. 42).

[102] A. Devienne, C. Ahdida and F. Malacrida, *Radiation Protection assessment of shielding improvements at EHN2 for Amber Drell-Yan run*, URL: https://edms.cern.ch/ui/file/2670569/1/EHN2_AMBER_TN.pdf (cit. on pp. 42, 43, 69, 98).

[103] J. E. Augustin et al., *Discovery of a Narrow Resonance in e^+e^- Annihilation*, Phys. Rev. Lett. **33** (23 1974) 1406, URL: https://link.aps.org/doi/10.1103/PhysRevLett.33.1406 (cit. on p. 42).

[104] J. J. Aubert et al., *Experimental Observation of a Heavy Particle J*, Phys. Rev. Lett. **33** (23 1974) 1404, URL: https://link.aps.org/doi/10.1103/PhysRevLett.33.1404 (cit. on p. 42).

[105] M. G. Alexeev et al., *Exotic meson $\pi_1(1600)$ with $J^{PC} = 1^{-+}$ and its decay into $\rho(770)\pi$*, Phys. Rev. D **105** (2022) 012005, arXiv: 2108.01744 [hep-ex], URL: https://journals.aps.org/prd/abstract/10.1103/PhysRevD.105.012005 (cit. on p. 44).

[106] B. Ketzer, B. Grube and D. Ryabchikov, *Light-meson spectroscopy with COMPASS*, Progress in Particle and Nuclear Physics **113** (2020) 103755, ISSN: 0146-6410, URL: https://www.sciencedirect.com/science/article/pii/S0146641020300028 (cit. on pp. 44, 92, 95).

[107] H. C. Pekeler, *Investigation of diffractively produced $\eta\pi$ and $\eta'\pi$ final states in COMPASS*, MA thesis: Rheinische Friedrich-Wilhelms-Universität Bonn, 2019, URL: https://wwwcompass.cern.ch/compass/publications/theses/2019_mst_pekeler.pdf (cit. on pp. 45, 92).

[108] H. Grote and F. Schmidt, *MAD-X: An upgrade from MAD8*, Conf. Proc. C **030512** (2003) 3497, URL: http://cds.cern.ch/record/618496 (cit. on pp. 46, 65).

[109] S. Agostinelli et al., *Geant4—a simulation toolkit*, Nuclear Instruments and Methods in Physics Research Section A: Accelerators, Spectrometers, Detectors and Associated Equipment **506** (2003) 250, ISSN: 0168-9002, URL: https:

//www.sciencedirect.com/science/article/pii/S0168900203013688 (cit. on pp. 46, 83, 102).

[110] J. Allison et al., *Geant4 developments and applications*, IEEE Transactions on Nuclear Science **53** (2006) 270, URL: https://ieeexplore.ieee.org/document/1610988 (cit. on p. 46).

[111] J. Allison et al., *Recent developments in Geant4*, Nuclear Instruments and Methods in Physics Research Section A: Accelerators, Spectrometers, Detectors and Associated Equipment **835** (2016) 186, ISSN: 0168-9002, URL: https://www.sciencedirect.com/science/article/pii/S0168900216306957 (cit. on p. 46).

[112] R. Chytracek, J. Mccormick, W. Pokorski and G. Santin, *Geometry Description Markup Language for Physics Simulation and Analysis Applications*, IEEE Transactions on Nuclear Science **53** (2006) 2892, URL: https://ieeexplore.ieee.org/document/1710291 (cit. on p. 47).

[113] R. Brun and F. Rademakers, *ROOT — An object oriented data analysis framework*, Nuclear Instruments and Methods in Physics Research Section A: Accelerators, Spectrometers, Detectors and Associated Equipment **389** (1997) 81, New Computing Techniques in Physics Research V, ISSN: 0168-9002, URL: https://www.sciencedirect.com/science/article/pii/S016890029700048X (cit. on p. 47).

[114] I. Antcheva et al., *ROOT — A C++ framework for petabyte data storage, statistical analysis and visualization*, Computer Physics Communications **180** (2009) 2499, 40 YEARS OF CPC: A celebratory issue focused on quality software for high performance, grid and novel computing architectures, ISSN: 0010-4655, URL: https://www.sciencedirect.com/science/article/pii/S0010465509002550 (cit. on p. 47).

[115] L. Nevay et al., *BDSIM: An accelerator tracking code with particle–matter interactions*, Computer Physics Communications **252** (2020) 107200, ISSN: 0010-4655, URL: https://www.sciencedirect.com/science/article/pii/S0010465520300400 (cit. on pp. 48, 83).

[116] L. Lönnblad, *CLHEP—a project for designing a C++ class library for high energy physics*, Computer Physics Communications **84** (1994) 307, ISSN: 0010-4655, URL: https://www.sciencedirect.com/science/article/pii/0010465594902178 (cit. on p. 48).

[117] A. Abramov, S. Boogert, L. Nevay and S. Walker,
First Studies of Ion Collimation for the LHC Using BDSIM,
International Particle Accelerator Conference (2018) 341,
URL: http://jacow.org/ipac2018/papers/mopmf090.pdf (cit. on p. 48).

[118] C. Hernalsteens et al.,
A novel approach to seamless simulations of compact hadron therapy systems for self-consistent evaluation of dosimetric and radiation protection quantities,
EPL **132** (2020) 50004, URL:
https://iopscience.iop.org/article/10.1209/0295-5075/132/50004
(cit. on p. 48).

[119] F. Metzger, F. W. Stummer and L. J. Nevay,
Automatic building of 3D models of beamlines, (2024), Publication in progress
(cit. on pp. 50, 52).

[120] S. Boogert, A. Abramov, L. J. Nevay, W. Shields and S. Walker, *Pyg4ometry: A Python library for the creation of Monte Carlo radiation transport physical geometries*,
Comput. Phys. Commun. **272** (2022) 108228,
arXiv: 2010.01109 [physics.comp-ph], URL: https:
//www.sciencedirect.com/science/article/pii/S0010465521003404
(cit. on p. 50).

[121] G. Battistoni et al., *Overview of the FLUKA code*, Annals of Nuclear Energy **82** (2015) 10, Joint International Conference on Supercomputing in Nuclear Applications and Monte Carlo 2013, SNA + MC 2013. Pluri- and Trans-disciplinarity, Towards New Modeling and Numerical Simulation Paradigms, ISSN: 0306-4549, URL: https:
//www.sciencedirect.com/science/article/pii/S0306454914005878
(cit. on p. 50).

[122] C. Ahdida et al., *New Capabilities of the FLUKA Multi-Purpose Code*,
Frontiers in Physics **9** (2022), ISSN: 2296-424X,
URL: https://www.frontiersin.org/articles/10.3389/fphy.2021.788253
(cit. on p. 50).

[123] Dassault Systèmes, *Opera*,
URL: https://www.3ds.com/products/simulia/opera (visited on 20/10/2023)
(cit. on p. 50).

[124] W. Schnell,
Discussion of a radio-frequency particle separator for CERN Proton Synchrotron,
(1961), URL: https://cds.cern.ch/record/278086 (cit. on p. 53).

[125] W. K. H. Panofsky, *A Mass Sensitive Deflector for High Energy Particles*, High-Energy Physics Laboratory Rept. HEPL-82, Stanford University, Stanford, California (1956)
(cit. on p. 53).

[126] A. Gerbershagen et al., *Design of beam optics for RF-separated kaon and antiproton beams in the M2 beam line of the CERN North Area*,
Nuclear Instruments and Methods in Physics Research Section A: Accelerators, Spectrometers, Detectors and Associated Equipment (2022) 168004, ISSN: 0168-9002, URL: https://www.sciencedirect.com/science/article/pii/S0168900222012967
(cit. on pp. 53, 54, 59, 60, 71, 76–79, 134).

[127] A. Gerbershagen et al., *RF-Separated Beam Project for the M2 Beam Line at CERN*, (2022), URL: https://cds.cern.ch/record/2806692
(cit. on pp. 53, 54, 59, 60, 71, 76–79).

[128] I. Bronštejn, K. Semendjajew, H. Mühlig and G. Musiol, *Taschenbuch der Mathematik*, Edition Harri Deutsch,
Verlag Europa-Lehrmittel Nourney, Vollmer GmbH & Company KG, 2016,
ISBN: 9783808557891 (cit. on p. 57).

[129] *CAS - CERN Accelerator School : Radio Frequency Engineering: Seeheim, Germany 8 - 16 May 2000. CAS - CERN Accelerator School : Radio Frequency Engineering*, CERN, Geneva: CERN, 2005, URL: https://cds.cern.ch/record/386544
(cit. on p. 59).

[130] F. Gerigk, *RF cavities, overview, part I*,
Lecture at the CERN Accelerator School about Radio-Frequency 2023,
URL: https://indico.cern.ch/event/1212689/contributions/5377030/attachments/2669006/4639010/RF-Cavities-F-Gerigk%20part%201.pdf
(cit. on p. 59).

[131] C. Adolphsen et al., *The International Linear Collider Technical Design Report - Volume 3.I: Accelerator R&D in the Technical Design Phase*, (2013),
arXiv: 1306.6353 [physics.acc-ph] (cit. on p. 74).

[132] G. Burt, *Transverse deflecting cavities*,
URL: https://indico.cern.ch/event/1212689/contributions/5377903/attachments/2676190/4641806/CAS%20Deflecting.pdf (visited on 01/01/2024) (cit. on p. 75).

[133] B. Balhan et al., *Improvements to the SPS Slow Extraction for High Intensity Operation*, (2019), URL: https://cds.cern.ch/record/2668989 (cit. on p. 65).

[134] A. Dexter, G. Burt, P. Ambattu, V. Dolgashev and R. Jones,
CLIC crab cavity design optimisation for maximum luminosity,
Nuclear Instruments and Methods in Physics Research Section A: Accelerators, Spectrometers, Detectors and Associated Equipment **657** (2011) 45, X-Band Structures, Beam Dynamics and Sources Workshop (XB-10), ISSN: 0168-9002, URL: https://www.sciencedirect.com/science/article/pii/S0168900211010229
(cit. on p. 68).

[135] S. Döbert et al.,
High Power test of a low group velocity X-band Accelerator Structure for CLIC,
tech. rep., CERN, 2008, URL: https://cds.cern.ch/record/1141224
(cit. on p. 68).

[136] F. Metzger et al.,
Kaon beam simulations employing conventional hadron beam concepts and the RF separation technique at the CERN M2 beamline for the future AMBER experiment,
IPAC'23 - 14th International Particle Accelerator Conference (2023) 2357,
ISSN: 2673-5490,
URL: https://indico.jacow.org/event/41/contributions/1785
(cit. on pp. 80, 87, 88).

[137] F. Metzger et al.,
Kaon beam simulations employing conventional hadron beam concepts and the RF separation technique at the CERN M2 beamline for the future AMBER experiment,
Journal of Physics: Conference Series **2687** (2024) 052023, URL: https://iopscience.iop.org/article/10.1088/1742-6596/2687/5/052023/meta
(cit. on pp. 80, 87, 88).

[138] G. Molière,
Theorie der Streuung schneller geladener Teilchen II, Mehrfach- und Vielfachstreuung,
Z. Naturforsch. **3a** (1948) 78,
URL: https://zfn.mpdl.mpg.de/data/Reihe_A/3/ZNA-1948-3a-0078.pdf
(cit. on p. 81).

[139] H. A. Bethe, *Molière's Theory of Multiple Scattering*, Phys. Rev. **89** (6 1953) 1256,
URL: https://link.aps.org/doi/10.1103/PhysRev.89.1256 (cit. on p. 81).

[140] Particle Data Group,
Atomic and nuclear properties of polyethylene terephthalate (Mylar) [(C10H8O4)n],
URL: https://pdg.lbl.gov/2023/AtomicNuclearProperties/HTML/polyethylene_terephthalate_Mylar.html (visited on 18/10/2023)
(cit. on p. 81).

[141] B. Parsamyan, *Transversely polarized Drell-Yan measurements at COMPASS*,
PoS **DIS2019** (2019) 195, arXiv: 1908.01727 [hep-ex],
URL: https://pos.sissa.it/352/195 (cit. on pp. 82, 84).

[142] C. Quintans, AMBER Drell-Yan meeting, 30.11.2021 (cit. on p. 83).

[143] G. Romagnoli, F. Metzger et al., *M2 Vacuum Requirements*, 2023,
URL: https://indico.cern.ch/event/1335909/contributions/5623532/attachments/2735599/4757079/BE-EA_M2%20Under%20vacuum%20Strategy%20for%20EATM-162.pdf
(cit. on pp. 83, 84).

[144] D. Banerjee, Private Communication (cit. on pp. 84, 102, 106, 119, 126, 128).

[145] L. Gatignon, Private Communication (cit. on pp. 87, 93).

[146] T. C. Szameitat,
New Geant4-based Monte Carlo software for the COMPASS-II experiment at CERN,
PhD thesis: Freiburg U., 2017, URL: https://wwwcompass.cern.ch/compass/publications/theses/2016_phd_szameitat.pdf (cit. on p. 91).

[147] H. C. Pekeler, Private communication (cit. on p. 92).

[148] T. Prebibaj, G. Arduini, H. Bartosik and M. A. Fraser,
SPS Operation and Future Proton Sharing Scenarios for the ECN3 facility, (2023),
URL: https://cds.cern.ch/record/2848908 (cit. on p. 93).

[149] B. Parsamyan, *Status and plans of the COMPASS (NA58) Experiment*,
URL: https://indico.cern.ch/event/1337721/contributions/5631300/attachments/2748941/4789644/Parsamyan_20231114-SPSC.pdf (visited on 30/01/2024) (cit. on p. 93).

[150] A. Magnon, *Future Plans of COMPASS*, (2009) 229,
URL: https://cds.cern.ch/record/2626987 (cit. on p. 93).

[151] Particle Data Group, *Atomic and nuclear properties of hydrogen liquid (H2)*,
URL: https://pdg.lbl.gov/2023/AtomicNuclearProperties/HTML/hydrogen_liquid.html (visited on 10/12/2023) (cit. on p. 95).

[152] H. Bingham et al., *Pion and nucleon dissociation in $\pi^- p \to \pi^-\pi^+\pi^- p$ at 205 GeV/c*,
Physics Letters B **51** (1974) 397, ISSN: 0370-2693, URL: https://www.sciencedirect.com/science/article/pii/037026937490238X (cit. on p. 95).

[153] Y. Antipov et al., *Analysis of the reaction $K^- p \to K^-\pi^-\pi^+ p$ at 40 GeV/c*,
Nuclear Physics B **86** (1975) 381, ISSN: 0550-3213, URL: https://www.sciencedirect.com/science/article/pii/0550321375903545 (cit. on p. 95).

[154] C. Daum et al., *Diffractive production of strange mesons at 63 GeV*,
Nuclear Physics B **187** (1981) 1, ISSN: 0550-3213, URL: https://www.sciencedirect.com/science/article/pii/0550321381901140 (cit. on p. 95).

[155] V. Flaminio, W. G. Moorhead, D. R. O. Morrison and N. Rivoire,
Compilation of cross-sections, Updated version of CERN HERA 79-02; contains all data published up to the beginning of 1982, Geneva: CERN, 1983,
URL: https://cds.cern.ch/record/99525 (cit. on p. 95).

[156] F. Haas, *Two-Dimensional Partial-Wave Analysis of Exclusive 190 GeV $\pi^- p$ Scattering into the $\pi^-\pi^-\pi^+$ Final-State at COMPASS (CERN)*,
PhD thesis: Technische Universität München, 2014,
URL: https://mediatum.ub.tum.de/1186008 (cit. on pp. 95, 96).

[157] J. Fry, *KTAG: The Kaon Identification Detector for CERN experiment NA62*, Nuclear Instruments and Methods in Physics Research Section A: Accelerators, Spectrometers, Detectors and Associated Equipment **824** (2016) 96, Frontier Detectors for Frontier Physics: Proceedings of the 13th Pisa Meeting on Advanced Detectors, ISSN: 0168-9002, URL: https://www.sciencedirect.com/science/article/pii/S0168900215013297 (cit. on p. 97).

[158] J. Beaufays, J. Ciborowski and R. Van Dantzig, *Measurement of the spin-dependent structure functions of the neutron and proton*, (1988), URL: http://cds.cern.ch/record/301939 (cit. on p. 100).

[159] F. C. Iselin, *HALO: a computer program to calculate muon halo*, CERN Yellow Reports: Monographs, Geneva: CERN, 1974, URL: https://cds.cern.ch/record/186209 (cit. on pp. 100, 113).

[160] K. L. Brown and F. C. Iselin, *DECAY TURTLE (Trace Unlimted Rays Through Lumped Elements): a computer program for simulating charged-particle beam transport systems, including decay calculations*, CERN Yellow Reports: Monographs, Geneva: CERN, 1974, URL: https://cds.cern.ch/record/186178 (cit. on p. 100).

[161] G. W. Bennett et al., *Final report of the E821 muon anomalous magnetic moment measurement at BNL*, Phys. Rev. D **73** (7 2006) 072003, URL: https://link.aps.org/doi/10.1103/PhysRevD.73.072003 (cit. on p. 100).

[162] *Event Biasing Techniques*, URL: https://geant4-userdoc.web.cern.ch/UsersGuides/ForApplicationDeveloper/html/Fundamentals/biasing.html (visited on 18/08/2023) (cit. on p. 102).

[163] L. J. Nevay et al., *Muon Splitting*, URL: https://www.pp.rhul.ac.uk/bdsim/manual/model_control.html#physics-bias-muon-splitting (visited on 18/08/2023) (cit. on p. 102).

[164] L. Molina Bueno et al., *NA64 status report 2023*, (2023), URL: https://cds.cern.ch/record/2868332 (cit. on pp. 105, 111, 115).

[165] Particle Data Group, *Atomic and nuclear properties of aluminum (Al)*, URL: https://pdg.lbl.gov/2022/AtomicNuclearProperties/HTML/aluminum_Al.html (visited on 27/10/2023) (cit. on p. 106).

[166] Particle Data Group, *Muons in beryllium (Be)*, URL: https://pdg.lbl.gov/2022/AtomicNuclearProperties/MUE/muE_beryllium_Be.pdf (visited on 08/11/2023) (cit. on p. 110).

[167] L. M. Bueno, Private Communication (cit. on p. 111).

[168] L. Gatignon, N. Doble et al., *The M2 Beam Line for the COMPASS Experiment*, URL: http://gatignon.web.cern.ch/gatignon/M2Poster.pdf (cit. on p. 113).

[169] Courtesy from NA64, Preliminary, unpublished results (cit. on pp. 115, 116).

[170] Particle Data Group, *34. MONTE CARLO PARTICLE NUMBERING SCHEME*, URL: https://pdg.lbl.gov/2007/reviews/montecarlorpp.pdf (visited on 17/11/2023) (cit. on p. 117).

[171] F. Metzger et al., *Hadron contamination studies in CERN's secondary M2 muon beam*, (2024), Publication in progress (cit. on p. 118).

[172] C. Matteuzzi, U. Marconi et al., *Status of the MUonE project*, tech. rep., CERN, 2023, URL: https://cds.cern.ch/record/2848505 (cit. on p. 119).

[173] A. Gutierrez, *A prototype electromagnetic calorimeter for the MUonE experiment: status and first performance results*, 2023, URL: https://indico.desy.de/event/34916/contributions/147254/attachments/84329/111700/A%20prototype%20electromagnetic%20calorimeter%20for%20the%20MUonE%20experiment.pdf (cit. on pp. 119, 128, 130, 133).

[174] π^0, URL: https://pdglive.lbl.gov/Particle.action?init=0&node=S009&home=MXXX005 (visited on 11/10/2023) (cit. on p. 120).

[175] *User Guide for the M2 beam*, URL: https://gatignon.web.cern.ch/gatignon/M2manual.html (visited on 11/01/2024) (cit. on p. 128).

[176] M. Oreglia, *A Study of the Reactions $\psi' \to \gamma\gamma\psi$*, PhD thesis: Stanford University, 1980 (cit. on p. 128).

[177] F. Simonetto, Private Communication (cit. on pp. 128, 130).

[178] *Stopping Powers for Electrons and Positrons*, URL: https://physics.nist.gov/PhysRefData/Star/Text/ESTAR.html (visited on 01/12/2023) (cit. on pp. 129, 130).

[179] Particle Data Group, *Atomic and nuclear properties of polycarbonate (Lexan, [OC6H4C(CH3)2C6H4OCO)n*, URL: https://pdg.lbl.gov/2023/AtomicNuclearProperties/HTML/polycarbonate_Lexan.html (visited on 27/10/2023) (cit. on p. 129).

[180] Particle Data Group, *Atomic and nuclear properties of air (dry, 1 atm)*, URL: https://pdg.lbl.gov/2023/AtomicNuclearProperties/HTML/air_dry_1_atm.html (visited on 27/10/2023) (cit. on p. 130).

[181] H. Kolanoski and N. Wermes, *Teilchendetektoren, Grundlagen und Anwendungen*, 1st ed., Springer, 2016, ISBN: 978-3-662-45349-0, URL: https://doi.org/10.1007/978-3-662-45350-6 (cit. on p. 131).

APPENDIX A

Appendix

A.1 Impact of divergence and momentum spread

In the following, the results of a Mickey Mouse Monte Carlo simulation are shown. The purpose of it is seeing the influences of a finite momentum spread and divergence on the RF separation as discussed in section 5.6 and 5.7.

The SPS proton beam is slowly extracted meaning a constant number of protons is sent on T6. The spill length is ca. 4.8 s. Therefore, the times, at which secondary particles are produced are uniformly distributed between ±2.4 s, which is illustrated in Fig. A.1.

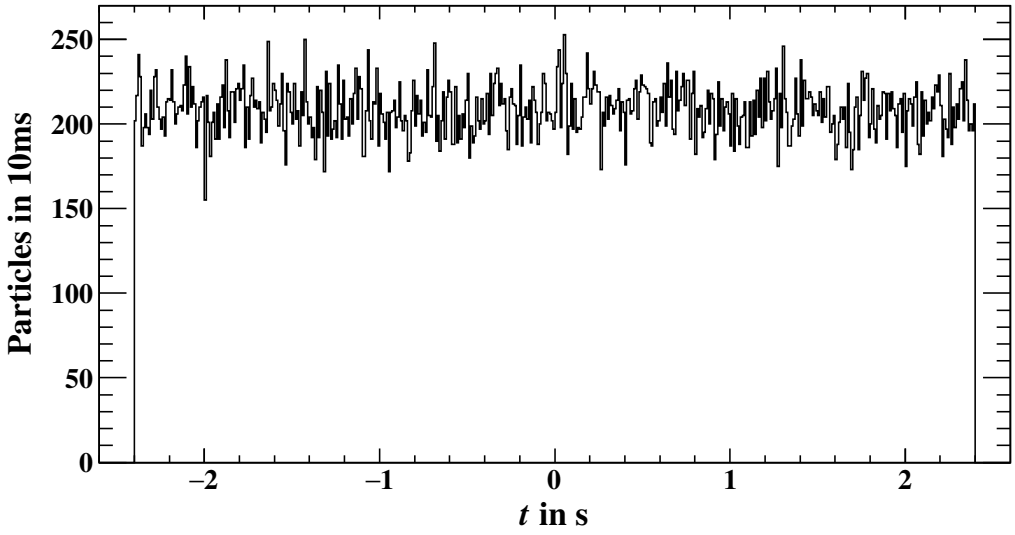

Figure A.1: Time distribution of the slowly extracted proton beam. The secondary particles will be produced in the indicated time window between ±2.4 s.

The different particles receive the kicks at both RF stations, described in chapter 5, which

purely depends on the phase they arrive with relative to the electromagnetic wave. Different scenarios are illustrated. In Fig. A.2 the separation is shown for a monochromatic and parallel beam. Fig. A.3 shows the situation for a parallel beam with a Gaussian momentum spread of $\sigma_p = 1\,\%$. The separation capability for a monochromatic, but divergent beam (Gaussian with $\sigma_{x'} = 0.5\,\text{mrad}$) is plotted in Fig. A.4. Finally, the situation with a divergent, broadband beam (Gaussians with $\sigma_{x'} = 0.5\,\text{mrad}$ and $\sigma_p = 1\,\%$) is shown in Fig. A.5.

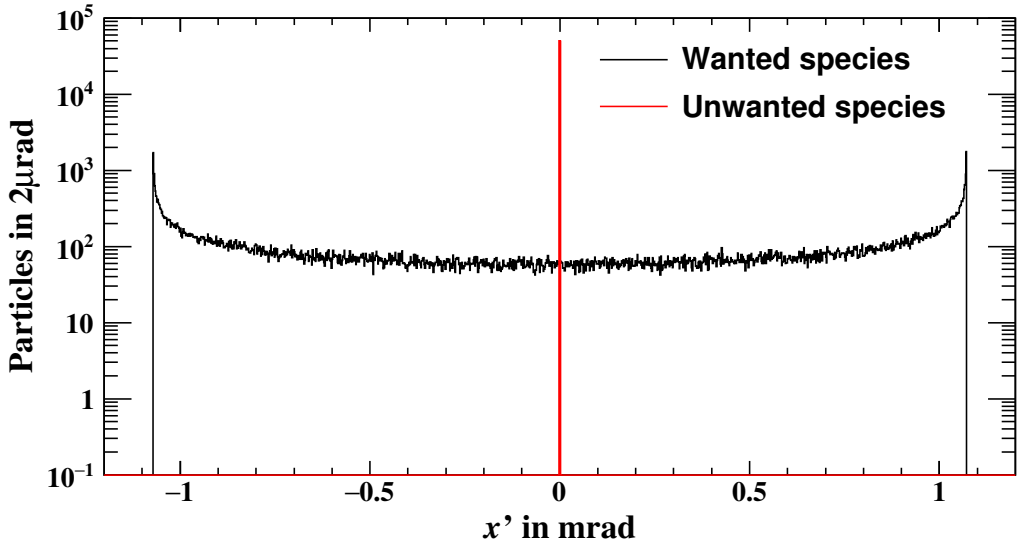

Figure A.2: Angular separation after RF2 for a parallel, monochromatic beam. The wanted particles are shown in black, while the unwanted one are plotted in red.

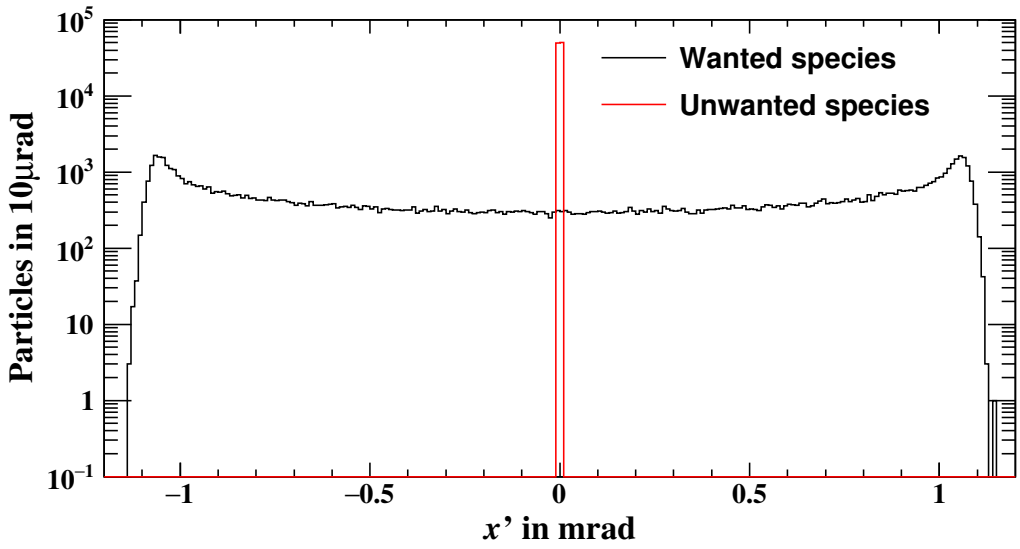

Figure A.3: Angular separation after RF2 for a parallel beam with a Gaussian momentum spread of $\sigma_p = 1\,\%$. The wanted particles are shown in black, while the unwanted one are plotted in red.

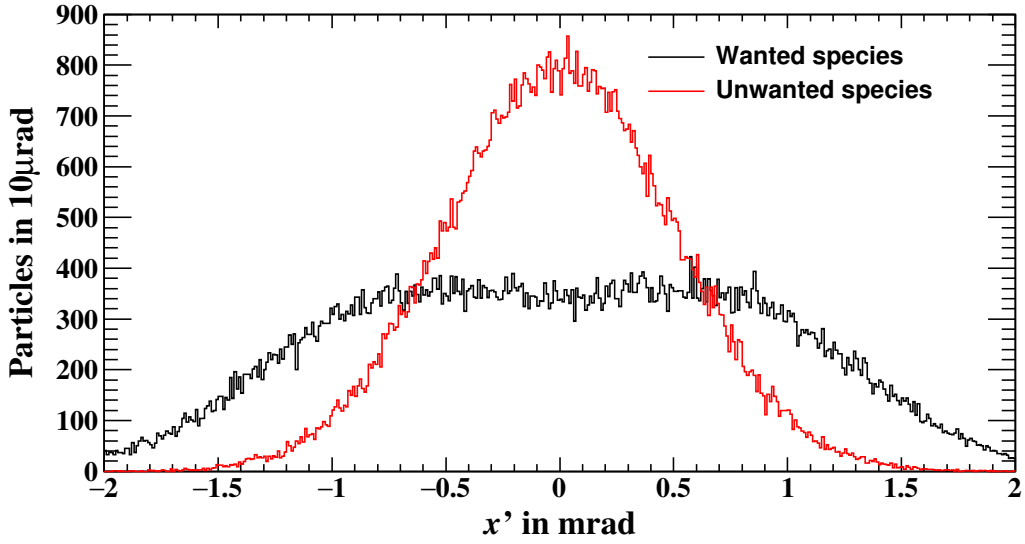

Figure A.4: Angular separation after RF2 for a monochromatic beam with a Gaussian angular spread of $\sigma_{x'} = 0.5\,\text{mrad}$. The wanted particles are shown in black, while the unwanted one are plotted in red.

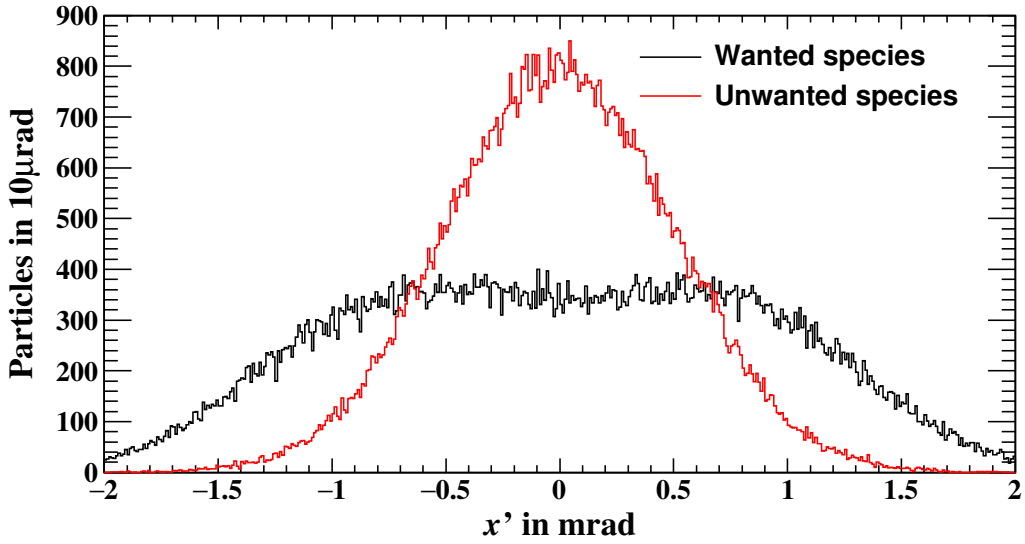

Figure A.5: Angular separation after RF2 for a broadband, divergent beam. Both, angle and momentum, are Gaussian distributed with $\sigma_{x'} = 0.5$ mrad and $\sigma_p = 1$ %. The wanted particles are shown in black, while the unwanted one are plotted in red.

A.2 New hadron beam optics

The transport matrix elements R_{11}, R_{12}, R_{16}, R_{33}, R_{34} and R_{36} of the improved conventional beam optics are illustrated in Fig. A.6.

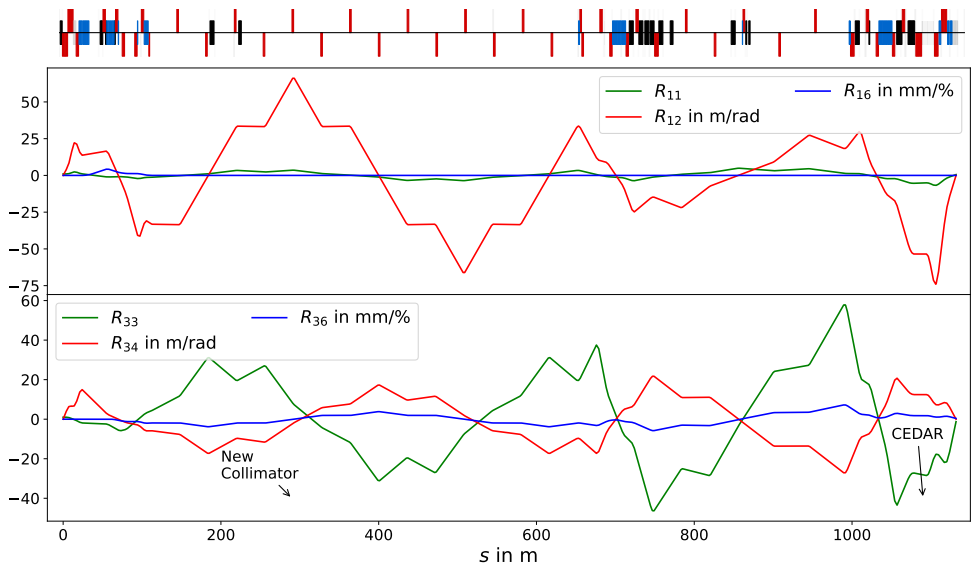

Figure A.6: Plot showing the new optics for hadron operation. A larger and therefore more parallel beam has been achieved at the CEDAR-location for a more efficient beam particle identification.

As the beam size is mostly determined by R_{12} and R_{34}, those parameters are maximised at the CEDAR-position. Simultaneously, to achieve a parallel beam R_{22} and R_{44} are set to zero.

A.3 RICH efficiency

In Fig. 6.11, the particle identification efficiency of the COMPASS RICH1 normalised to the number of simulated events is shown. For comparison purposes the colour scale has been kept constant to see the efficiency increase better. For completeness, the histograms that are not normalised, are plotted in Fig. A.7. Also, the colour scale is not the same for the shown distributions.

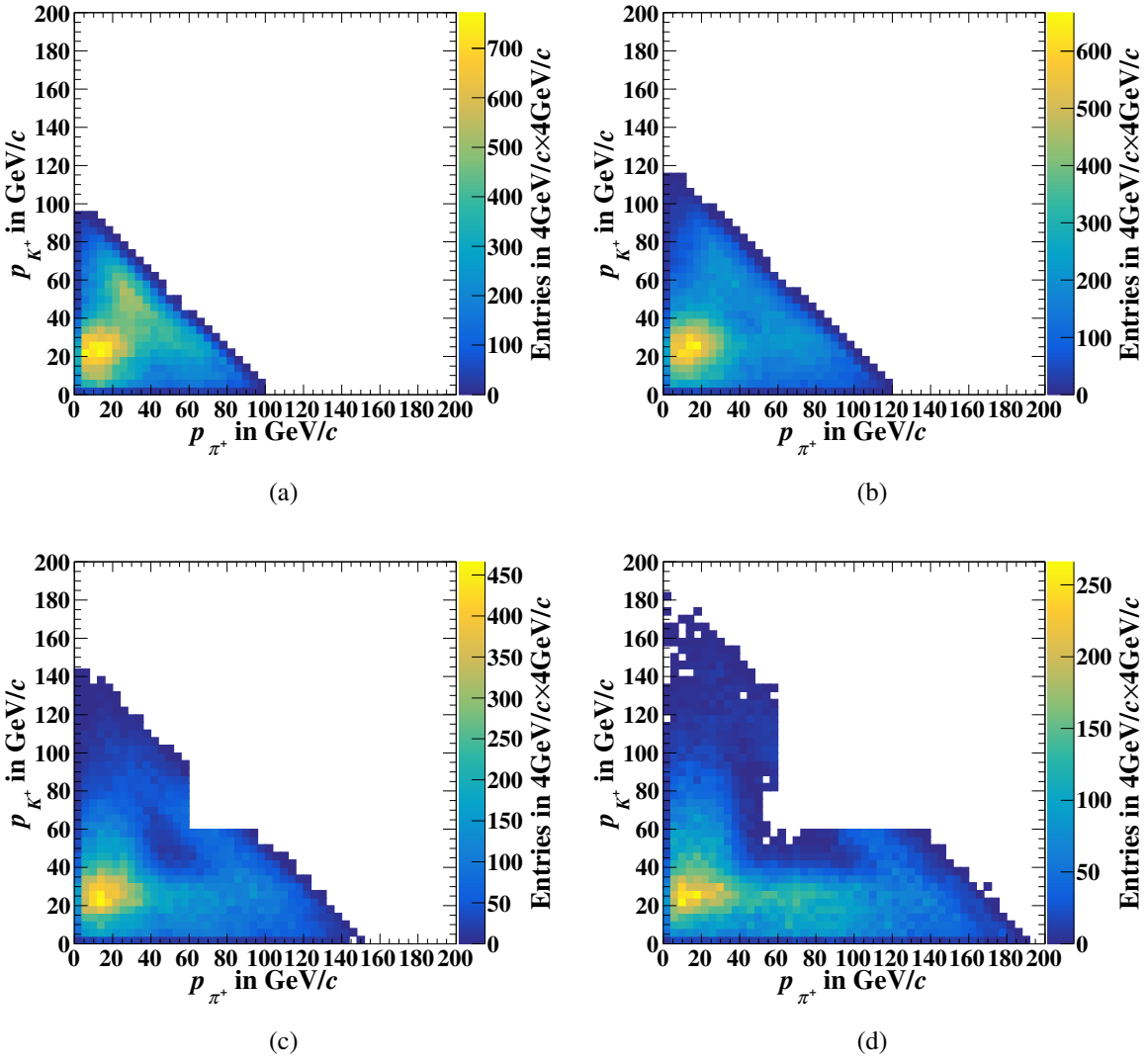

Figure A.7: RICH efficiency for different beam momenta. The correlation between the momenta of the outgoing K^+ and π^+ are plotted. Fig. A.7(a) is obtained at 100 GeV/c beam momentum, Fig. A.7(b) at 120 GeV/c, Fig. A.7(c) at 150 GeV/c and Fig. A.7(d) at 190 GeV/c. The efficiency increases with decreasing beam momentum as it is less likely that both particles have high momenta, where it is more difficult to separate those.

A.4 Biasing factors for the muon beam simulation

The biasing factors for the muon beam simulation discussed in section 7.2 are motivated. Similarly as for π^+ (cf. Fig. 7.3), the s-coordinates of the points of the last interactions are plotted for p in Fig. A.8 and K^+ in Fig. A.9.

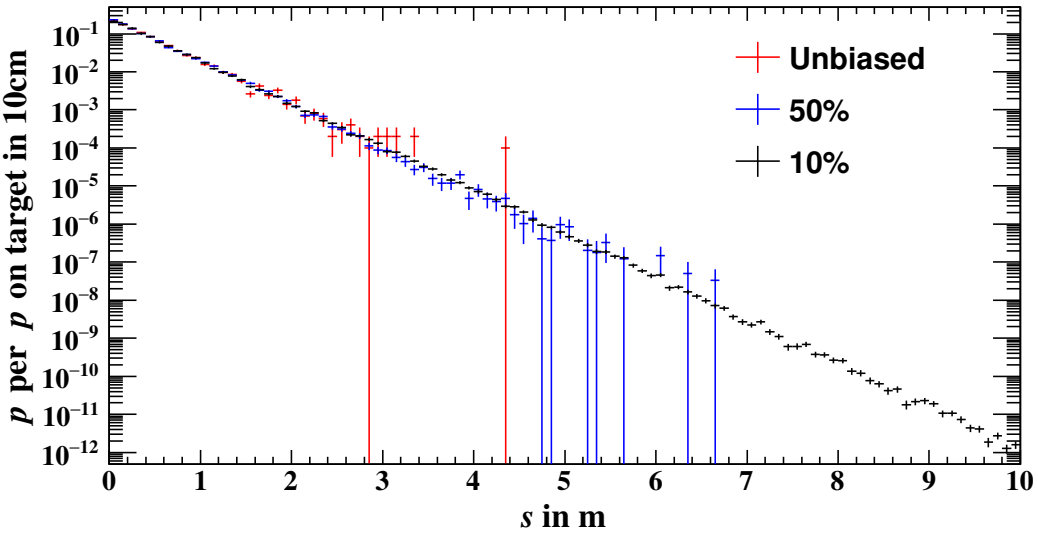

Figure A.8: Position of last interaction of primary p with 172 GeV/c in 10 m of beryllium.

As discussed already for π^+, the choice of the biasing factor is uncritical as the absorption close to the entrance of the beryllium block is still the most probable process. As long as one chooses a factor such that particles escaping the absorber are observed, one can select it in a range from 10 to 50 % depending on the particle.

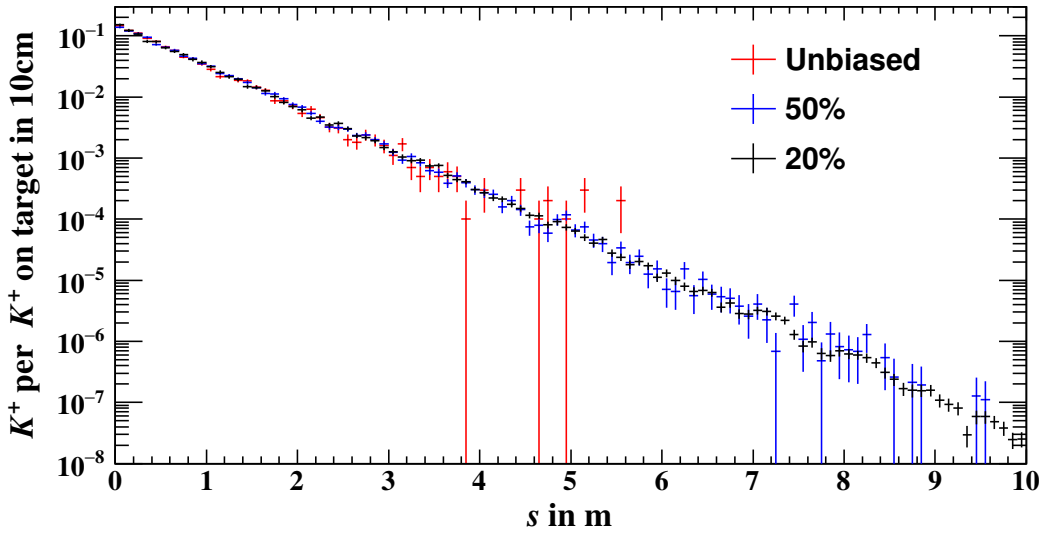

Figure A.9: Position of last interaction of primary K^+ with 172 GeV/c in 10 m of beryllium.

List of Figures

List of Tables